Design, Synthesis and Photophysical Properties of Organic Conjugates of Two-dimensional Layered Nanomaterials for Sensing and PDT Applications

THESIS SUBMITTED TO ACADEMY OF SCIENTIFIC AND INNOVATIVE RESEARCH (**AcSIR**) FOR THE AWARD OF THE DEGREE OF

DOCTOR OF PHILOSOPHY IN CHEMISTRY

UNDER THE FACULTY OF SCIENCE

By

SREEJITH M.

Enrollment No: 10CC12A39002

Under the Supervision of

Dr. JOSHY JOSEPH

PHOTOSCIENCES AND PHOTONICS SECTION

CHEMICAL SCIENCES AND TECHNOLOGY DIVISION

CSIR-NATIONAL INSTITUTE FOR INTERDISCIPLINARY SCIENCE AND TECHNOLOGY (CSIR-NIIST)

THIRUVANANTHAPURAM - 695019, KERALA

APRIL 2018

Dedicated to my beloved Achan, Amma & Chechi ….

DECLARATION

I hereby declare that the matter embodied in the Ph. D. thesis entitled: "**Design, Synthesis and Photophysical Properties of Organic Conjugates of Two-dimensional Layered Nanomaterials for Sensing and PDT Applications**" is the result of an independent work carried out by me at the Photosciences and Photonics Section, Chemical Sciences and Technology Division of the CSIR-National Institute for Interdisciplinary Science and Technology (CSIR-NIIST), Thiruvananthapuram, under the supervision of Dr. Joshy Joseph and the same has not been submitted elsewhere for any other degree or diploma.

In keeping with the general practice of reporting scientific observations, research materials obtained from other investigations has been duly cited and acknowledged in the thesis.

Sreejith M.

Thiruvananthapuram
April 26, 2018

National Institute for Interdisciplinary Science and Technology (CSIR-NIIST)

Council of Scientific & Industrial Research (CSIR)
Industrial Estate P. O., Trivandrum - 695 019
Kerala, INDIA

Dr. Joshy Joseph
Scientist
Chemical Sciences and Technology Division

Tel: +91-471-2515 476
Fax: +91-471-2491 712
E-mail: joshyja@gmail.com, joshy@niist.res.in

April 26, 2018

CERTIFICATE

This is to certify that the work embodied in the thesis entitled: "**Design, Synthesis and Photophysical Properties of Organic Conjugates of Two-dimensional Layered Nanomaterials for Sensing and PDT Applications**" has been carried out by Mr. Sreejith M. under my supervision and guidance at the Photosciences and Photonics Section, Chemical Sciences and Technology Division of the CSIR-National Institute for Interdisciplinary Science and Technology (CSIR-NIIST), Thiruvananthapuram and the same has not been submitted elsewhere for a degree.

(Joshy Joseph)

Thesis Supervisor

ACKNOWLEDGEMENTS

I have great pleasure in placing on record my deep sense of gratitude to Dr. Joshy Joseph, my thesis supervisor, for suggesting the research problem and for his guidance, immense knowledge, endearing care, constant support and motivation, leading to the successful completion of this work.

I would like to express my sincere thanks to Professor M. V. George for his constant help and encouragement during my stay at CSIR-NIIST.

I wish to thank Dr. A. Ajayaghosh, Director and Dr. Gangan Pratap and Dr. Suresh Das, former Directors of the CSIR-National Institute for Interdisciplinary Science and Technology for providing me the necessary facilities for carrying out the work.

I sincerely thank Dr. S. Asha Nair, Dr. P. S. Saneesh Babu, Mr. Manu Prasad and Ms. Rajshree R. Nair, Rajiv Gandhi Centre for Biotechnology (RGCB), Thiruvananthapuram for the help in photobiological experiments.

I sincerely acknowledge Dr. Mangalam S. Nair and Dr. R. Luxmi Varma, former and present AcSIR coordinators for their help in successful completion of the course work.

I am very much thankful to Dr. K. R. Gopidas, Dr. K. N. Narayanan Unni and Dr. K. K. Maiti, my Doctoral Advisory Committee members for their valuable comments and suggestions to improve the quality of my work.

I would like to thank Dr. D. Ramaiah, Dr. C. Vijayakumar, Dr. K. Venugopal, Dr. K. Yoosaf, Dr. Biswapriya Deb and all other scientists of the Photosciences and Photonics Section, Chemical Sciences and Technology Division, for all the help and support extended to me.

I would like to thank Mr. Robert Philip and Mr. Kiran Mohan for general help and TEM analysis and Mrs. Saumini Mathew, Mr. Saran and Mr. Gokul for NMR analysis and

Mrs. Viji, and Ms. Athira for HRMS data, Mr. Aswin, Mr. Vishnu and Mr. Vibhu Darshan for AFM analysis.

I express my sincere thanks to Dr. Adarsh N. and Dr. Nandajan P. C. for their generous support and care throughout my research career and I extend my thanks to Mr. Sandeepa K. V., Mr. Mathews K. M., Ms. Silja Abraham, Ms. Sajena K. S., Ms. Anjali B. R, Ms. Akhila Muhammed, Mr. Ebaston T. M., Ms. Mridula, Dr. Siji Mathew, Ms. Deepika S., Ms. Vijina, Ms. Shibna B., Ms. Nishna N., and Dr. Shanthi Krishna for their valuable help and support. I also thank all M. Sc. project students, Ms. Nasmi, Ms. Shana, Ms. Jahnavi, Ms. Aparna, and Ms. Anagha for their help.

Words are inadequate to express my gratitude to my dear friends Ms. Tanwistha Ghosh, Mr. Muhammed Yoosuf, Dr. Arun Gopi, Mr. Alex Kuriakose, Mr. Sudheesh K. V., Mr. Shameel T., Dr. Ajesh Vijayan, Mr. Naeem K. C., Dr. Sumesh Babu, Dr. Suneesh C. K., Dr. Hari Shankar, Dr. Tony George Thomas and Dr. Rahul Ongugal for their care, love, support and encouragement, which made my life in NIIST memorable. I also thank all the present and former members of the Photosciences and Photonics and other Divisions of CSIR-NIIST for their help and cooperation.

I am deeply indebted to my parents, sister, family members and friends for their support and encouragement. I would also like to extend my thanks and appreciation to all my teachers for their help and blessings.

Finally, I sincerely thank Council of Scientific and Industrial Research (CSIR), and DBT Government of India for financial assistance.

Sreejith M.

CONTENTS

PREFACE

Two dimensional (2D) nanomaterials such as graphene, its chemically modified derivatives and inorganic analogous have emerged as a promising family of nanomaterials for various biological applications due to their unique structural and physicochemical properties. For example, single layer or few layer nanosheets of graphene, graphene oxide (GO) and reduced graphene oxide (rGO) exhibit high surface area and exceptional mechanical, electronic and optical properties, which were utilized in various applications including scaffolds, electrodes and/or active materials for various biosensors, nano-carriers for drug delivery etc. Functionalization of 2D materials with a view to improve its biocompatibility and to tune their optical and electronic properties is another area of research which got great momentum in the past decade. The current thesis makes an effort in utilizing functionalized graphene analogues such as GO and rGO nanosheets, graphene oxide quantum dots (GQDs) and MoS_2 quantum dots (MQDs) for sensing and photodynamic therapy (PDT) applications.

This thesis is organized into four Chapters. The first Chapter introduces the research background with a brief description of the 2D layered nanomaterials such as graphene, MoS_2 etc. and their chemical and physical properties which makes them attractive in various fields of science. Further, this Chapter focuses on different functionalization strategies adopted for improving the material properties suitable for specific biomedical applications. Recent developments in this field and major objectives of the current work are also highlighted in this chapter.

The second Chapter deals with the synthesis and characterization of a pH sensitive, fluorescence 'turn on' sensor based on a graphene oxide–naphthalimide nanoconjugate. These nanoconjugates were synthesized by covalently anchoring picolyl substituted naphthalimide derivatives on GO/rGO surface *via* EDC-NHS coupling strategy and the morphological and photophysical properties were studied in detail. Synergistic effects of π- π interactions between GO and naphthalimide chromophore, and efficient photoinduced electron and energy transfer processes are responsible for the strong quenching of fluorescence of these nanoconjugates, which gets perturbed at acidic pH conditions leading to significant enhancement of fluorescence emission. We have also demonstrated the utility of these nanoconjugates in reporting pH changes in real samples using two examples: i) salt hydrolysis of FeCl3 and ii) enzymatic hydrolysis of acetylcholine, where both reactions reduce the pH of the medium which was efficiently reported by the nanoconjugate through a fluorescence 'turn on' response.

Use of nano-carriers for the delivery of photosensitizer molecules to target cells is a promising strategy to improve the efficacy of PDT based clinical treatment. Graphene Quantum Dots (GQDs), by virtue of its size in the nano domain, physiological solubility, high photostability, easy accumulation in tumor cells and low cytotoxicity, can be used as a suitable platform for the delivery of PDT agents conjugated through covalent and non-covalent strategies. The third Chapter describes synthesis and characterization of Graphene Quantum Dot (GQD) – BODIPY nanoconjugate (GQD-BDPA) with excellent water solubility and high singlet oxygen generation efficiency. Green luminescent GQDs were synthesized from graphene

oxide (GO) *via* a modified acid treatment method, and the amino BODIPY derivative (BDPA) was covalently attached to the GQDs *via* EDC/NHS coupling. These nanoconjugates, with average lateral dimensions of ~50 nm, exhibited characteristic absorption and fluorescence properties of both GQD and BDPA. Triplet quantum yield of GQD-BDPA was found to be 0.94±0.02 with high singlet oxygen generation efficiency (90%), demonstrating the potential of these nanoconjugates for PDT applications. In vitro PDT activity of this nanoconjugate was investigated using MDA-MB-231 cancer cell lines and GQD-BDPA is found to be an efficient system for PDT treatment with an IC_{50} value of 30 nM (sensitizer concentration). The apoptotic cell death was characterized and confirmed by various assays such as Annexin, TMRM, and nuclear condensation on MDA-MB-231 cell lines.

Transition metal dichalcogenides, like MoS_2 have received much attention in recent years, because of the unique properties associated with their ultra-thin thickness and 2D morphology, which makes them a promising candidate for biomedical applications. MoS_2 nanosheets with few nanometers lateral dimension are termed as MoS_2 quantum dots (MQDs), which are known for their bright luminescence, excellent biocompatibility and aqueous solubility. Surface of MoS_2 nanosheets and MQDs can be easily functionalized with photosensitizes *via* various strategies, which will enhance the aqueous solubility and cellular internalization of the photosensitizer, and enhance their photodynamic therapeutic performance. In this Chapter, we describe synthesis and characterization of blue luminescent MQDs conjugated with a diiodo-BODIPY derivative (MQD-BDSH) which showed high triplet quantum yields, excellent singlet oxygen generation efficiencies and aqueous

solubility favourable for PDT applications. We followed an ultra-sonication assisted mixed solvent exfoliation method for the synthesis of few layered MoS_2 nanosheets from bulk MoS_2. These nanosheets were further cut into smaller dimensions (MQDs) *via* a heat treatment method. As synthesized MQDs particles were covalently functionalized with thiol modified diiodo-BODIPY derivative (BDSH) *via* thiol ligand conjugation method. The nanoconjugate, (MQD-BDSH) with average lateral dimensions of ~60 nm and excellent water solubility, exhibited characteristic absorption and fluorescence properties of both MQD and BDSH. Triplet quantum yield of this nanoconjugate was found to be 0.91±0.02 with high singlet oxygen generation efficiency of 81%. In vitro PDT activity of the nanoconjugate was investigated on HSC4 oral cancer cell lines, which shows that MQD-BDSH is an efficient system for PDT with IC_{50} values in low nanomolar concentration range (20 nM, sensitizer concentration). The apoptotic cell death was characterized and confirmed by various assays such as Annexin, TMRM assay, nuclear condensation on HSC4 oral cancer cell lines. These results demonstrate the potential of these nanoconjugates for efficient PDT applications.

LIST OF ABBREVIATIONS

1. AuNRs – Gold nanorods
2. AuNPs – Gold nanoparticles
3. Å - Angstrom
4. AFM- Atomic force microscopy
5. APTES - (3-Aminopropyl)triethoxysilane
6. ATP – Adenosine Triphosphate
7. APS – Average Particle Size
8. AO – Acridine Orange
9. ACh - Acetylcholine
10. ATCh - Acetylthiocholine
11. AChE - Acetylcholinesterase
12. BODIPY - Boron-dipyrromethene
13. ^{o}C – Degree Celsius
14. C_3N_4 – Carbon nitride
15. CVD – Chemical vapor deposition
16. Ce6 – Chlorine e6
17. CT-DNA – Calf thymus Deoxyribonucleic acid
18. CM-H2DCFDA – Chloromethyl 2′,7′-Dichlorodihydrofluorescein diacetate
19. $CDCl_3$ – Deuterated chloroform
20. CH_3CN – Acetonitrile
21. Calcd. – Calculated
22. Cu – Copper

23. DCM – Dichloromethane
24. DNA - Deoxyribonucleic acid
25. DCC - N,N′-Dicyclohexylcarbodiimide
26. DIC - N,N′-Diisopropylcarbodiimide
27. DMSO - Dimethyl sulfoxide
28. DMF - Dimethylformamide
29. DDQ - 2,3-Dichloro-5,6-dicyano-1,4-benzoquinone
30. EDC - 1-Ethyl-3-(3-dimethylaminopropyl)carbodiimide
31. EDX - Energy-dispersive X-ray spectroscopy
32. EtBr - Ethidium bromide
33. *et al.* – *Et allii/alia*
34. ε – Molar extinction coefficient
35. ESI-MS – Electrospray ionoisation mass spectrometry
36. eV – Electron volt
37. ϕ_T – Triplet state quantum yield
38. Φ^1o_2 – Singlet oxygen generation quantum yield
39. FAB-MS – Fast atom bombardment mass spectrometry
40. FTIR - Fourier-transform infrared spectroscopy
41. FITC - Fluorescein isothiocyanate
42. FET - Field-effect transistor
43. FFT - Fast fourier transform
44. FA – Folic acid
45. g - Gram
46. GAs - Graphene analogues

47. GO – Graphene oxide
48. GQDs – Graphene quantum dots
49. GONP – Graphene nanoplatelets
50. GOx - Glucose oxidase
51. h – Hour
52. HOMO – Highest occupied molecular orbital
53. Hg – Mercury
54. HCl – Hydrochloric acid
55. HPPH - (2-[1-hexyloxyethyl]-2-devinyl pyropheophorbide-a
56. HOBT - Hydroxybenzotriazole
57. HA - Hyaluronic acid
58. ICT – Intramolecular charge transfer
59. IR – Infrared
60. ISC – Intersystem crossing
61. IC_{50} - Half maximal inhibitory concentration
62. IgG - Immunoglobulin G
63. K – Kelvin
64. K_{app} - Apparent affinity constant
65. LUMO – Lowest unoccupied molecular orbital
66. λ_{max} – Wavelength maximum
67. LOD – Limit of detection
68. LDHs - Layered double hydroxides
69. M – Molar
70. MUA - 11-Mercaptoundecanoic acid

71. MoS_2 – Molybdenum disulphide
72. MQDs - Molybdenum disulphide quantum dots
73. MTT - (3-(4,5-Dimethylthiazol-2-yl)-2,5-Diphenyltetrazolium Bromide)
74. mg – Milligram
75. mL – Millilitre
76. µM – Micromolar
77. µs – Microseconds
78. µm – Micrometer
79. mM – Millimolar
80. mmol – Millimole
81. nm - Nanometer
82. NMR – Nuclear magnetic resonance
83. ns – Nanosecond
84. NHS - N-Hydroxysuccinimide
85. PL – Photoluminescence
86. PI – propidium iodide
87. PDT – Photodynamic therapy
88. PTT – Photothermal therapy
89. PET – Photo-induced electron transfer
90. PAMAM - Polyamidoamine
91. Φ_F – Quantum yields of fluorescence
92. PNA - Peptide nucleic acid
93. PEG - Polyethylene glycol
94. Pc - Phthalocyanine

95. PAA - Polyacrylic acid

96. QDs – Quantum dots

97. rGO – Reduced graphene oxide

98. ROS – Reactive oxygen species

99. RB – Rose bengal

100. rpm – Rotation per minute

101. SPM – Scanning probe microscope

102. SAED – Selected area electron diffraction

103. SEM – Scanning electron microscope

104. SOG – Singlet oxygen generation

105. s – Seconds

106. TLC – Thin layer chromatography

107. TGA – Thermogravimetric analysis

108. THF – Tetrahydrofuran

109. TMS – Tetramethylsilane

110. τ_f– Fluorescence lifetime

111. TEM – Transmission electron microscope

112. TMDs - Transition metal dichalcogenides

113. TFA – Trifluoroacetic acid

114. TMRM – Tetramethylrhodamin methylester

115. TBAF - Tetra-n-butylammonium fluoride

116. UV – Ultraviolet

117. UCNP – Upconversion nanoparticles

Chapter 1

Layered Two Dimensional Nanomaterials for Sensing and Photodynamic Therapy Applications: An Overview

1.1. Abstract

Two dimensional (2D) nanomaterials such as graphene, its chemically modified derivatives and inorganic analogous have emerged as a promising family of nanomaterials for various biological applications due to their unique structural and physicochemical properties. For example, single layer or few-layer nanosheets of graphene, graphene oxide (GO) and reduced graphene oxide (rGO) exhibit high surface area and exceptional mechanical, electronic and optical properties, which were utilized in various applications including scaffolds, electrodes and/or active materials for various biosensors, nano-carriers for drug delivery, etc. Functionalization of 2D materials with a view to improve its biocompatibility and to tune their optical and electronic properties is another area of research which got great momentum in the past decade. The current Chapter highlights recent developments that are going on in this newly emerging field, and evaluate the potential applications of recently developed 2D nanomaterials.

1.2. Introduction

Ever since graphene isolated in 2004, atomically thin two-dimensional (2D) materials have received a lot of attention in various scientific and engineering subfields. They represent a new class of nanomaterials that possess sheet-like structures with the lateral size of few nanometers, or up to a few micrometers, with single or few-atoms thickness (typically less than 5 nm). 2D nanomaterials are exhibiting exciting physical and chemical properties, which triggered scientific fields to explore them for real technological applications, including energy conversion and storage, optical sensing, drug delivery, DNA sequencing and water purification.[1] We can broadly classify these materials as graphene and analogs of graphene (2D GAs). A number of 2D materials are now available which include semimetals (e.g., graphene, black phosphorus), semiconductors (e.g., transition metal dichalcogenides, TMDs like MoS_2, WS_2, $NbSe_2$, etc.) and insulators (e.g., hexagonal boron nitride). Other classes include carbon nitride (g-C_3N_4), layered double hydroxides (LDHs), MXenes, silicenes, etc.[1] (Figure 1.1)

The layered materials are highly desirable for biomedical applications due to their exclusive structural and physicochemical features compared to nanomaterials of other morphologies such as nanospheres, nanotubes, nanorods, etc. The unique properties of this class of materials originate from their ultrathin thickness and 2D morphological features, such as high surface-area-to-mass ratio and precise physical, electronic, and chemical properties. High surface areas of these materials allow easy regulation to the properties and functionalities by means of surface modification/functionalization, suitable for various applications. The following sections

briefly cover the synthesis, characterization, functionalization and various biological applications of some important 2D layered nanomaterials such as graphene, graphene oxide (GO), reduced graphene oxide (rGO), graphene quantum dots (GQDs) and MoS_2 nanosheets.

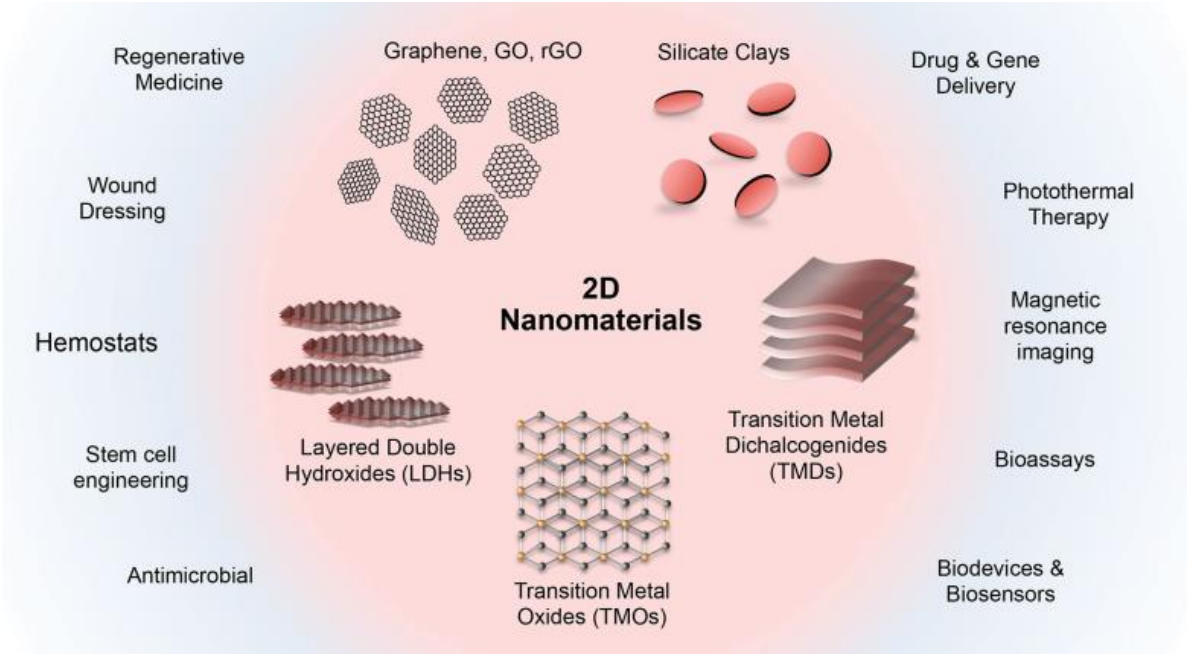

Figure 1.1. Two-dimensional (2D) nanomaterials investigated for biological applications (Adapted from reference 2).

1.3. Graphene

Graphene, an increasingly important 2D nanostructured material with exciting physical, chemical and optical properties, has attracted great interest in the fields of physics, chemistry, biology, medicine and their inter-disciplinary areas.[3] The unique electronic and optical properties of graphene make it one of the most promising materials for various applications.[4] Graphene consist of a single layer planar sheet of sp^2 –hybridized carbon atoms perfectly ordered in a honeycomb lattice.[5,6] It is remarkably

strong (100 times stronger than steel)[7] and it conducts both heat and electricity with great efficiency.[8] While scientists had theorized about graphene for decades, it was first produced in the lab in 2004, by Andre Geim and Konstantin Novoselov at the University of Manchester and they were awarded the Nobel Prize in Physics in 2010 for this remarkable discovery. They mechanically exfoliated graphene layers from graphite and transferred them onto thin SiO_2 in a process called the micromechanical cleavage or the scotch tape technique.[6,9]

Technically graphene is a crystalline allotrope of carbon with 2-dimensional properties and can be considered as a one atom thick layer of graphite. It is the basic structural element of other allotropes, including graphite, charcoal, carbon nanotubes and fullerenes (Figure 1.2).[6] It can also be considered as a large aromatic molecule, the

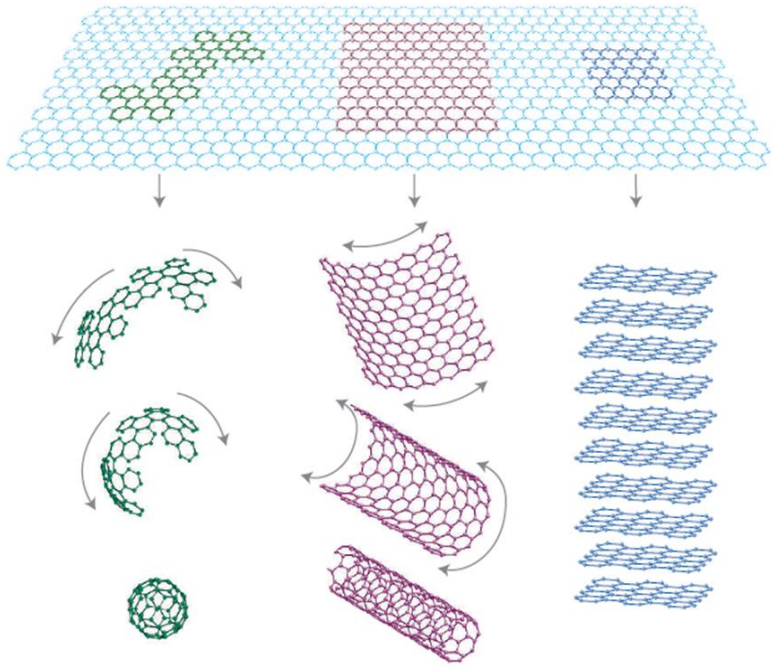

Figure 1.2. Graphene as a precursor to zero-dimensional fullerenes, one-dimensional carbon nanotube and three-dimensional graphite (Adapted from reference 6).

limiting case of the family of flat polycyclic aromatic hydrocarbons. The distance between two neighboring carbon atoms in a single sheet is about 1.42 Å. Individual layers stack together through the van der Waals force to form the graphite, in which the distance between adjacent layers is about 3.35 Å (Figure 1.3).

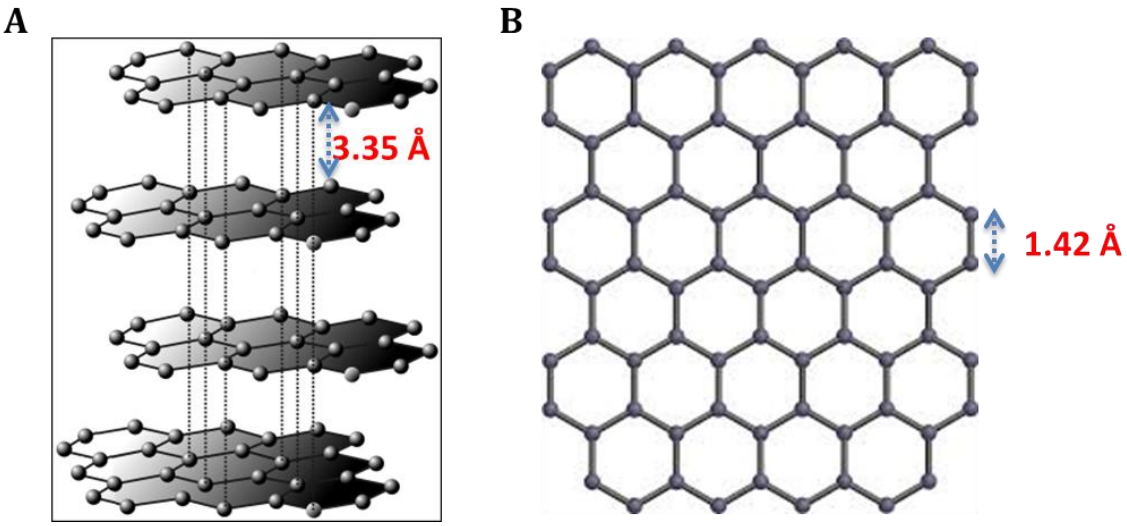

Figure 1.3. A) Schematic structure of graphite showing graphene layers and B) Single layer of graphene showing the bonding pattern of sp^2 carbon atoms.

1.3.1. Graphene Oxide (GO) and Reduced Graphene Oxide (rGO)

Graphene oxide (GO) is a two-dimensional layered material produced by the oxidation of graphene, containing oxygen functional groups such as alcohols, epoxides and carboxylic acids (Figure 1.4). Recently, GO has attracted much attention based on its excellent electronic, thermal, mechanical and photophysical features, as well as its potential applications in synthesizing nanocomposites, fabricating various micro-electrical devices and analyzing biomolecules.[10,11] GO can be considered as the insulating and disordered analog of the highly conducting crystalline graphene.

Chemists are drawn to GO because of its heterogeneous chemical and electronic structures, along with high processibility in solution.

The presence of several types of oxygen-containing functional groups on the basal plane and the edges allow GO to interact with a variety of materials in non-covalent,

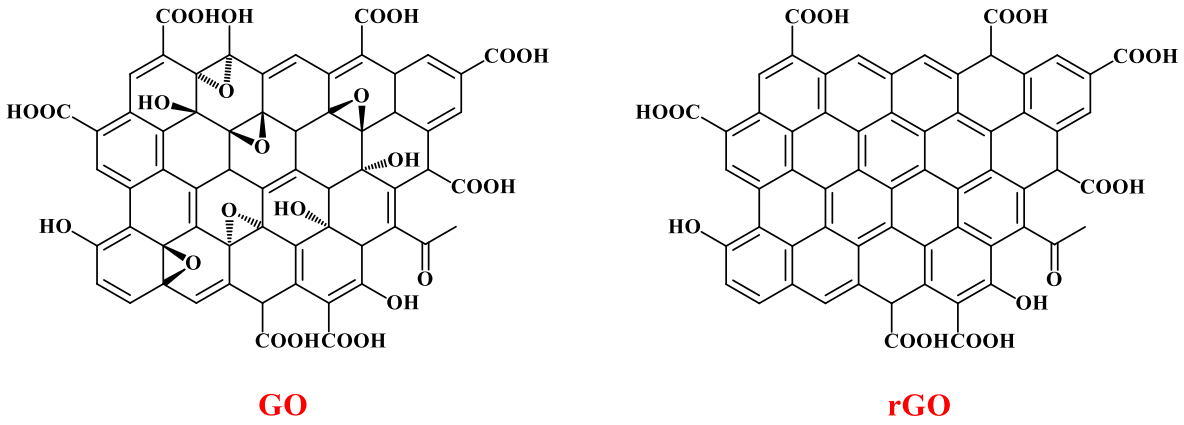

Figure 1.4. Schematic representation of extensively oxidized domains of GO and chemically reduced domains of rGO. The extent of functionalization depends on the chemical modification conditions.

covalent and/or ionic manner so that functional hybrids and composites with exciting properties can be easily synthesized.[12] Furthermore, GO is an electronically hybrid material that features both conducting π states from sp^2 carbon sites and a large energy gap between the sigma states of its sp^3 bonded carbons. Reduced graphene oxide (rGO), synthetically accessed through controlled reduction of GO is another useful graphene analogue which interface between GO and pristine graphene in its physical and chemical properties. Upon reduction of GO to rGO, the ratio of sp^2 to sp^3 fractions increases. This enables us to tune the band gap of GO from an insulator to a

semiconductor and to a graphene like semi-metal and achieves graphene like properties.

1.3.2. Synthesis of Graphene, GO and rGO

The first attempt for the synthesis of monolayer graphene was carried out by Lang *et al.*, in 1975.[13] They showed formation of mono- and multi-layered graphene by thermal decomposition of carbon on single crystal platinum substrates. But due to lack of consistency between properties of such sheets formed on different crystal planes of Pt, authors failed to identify the useful applications of the product. However, in 2004, Andre Geim and Konstantin Novoselov at the University of Manchester succeeded in isolating this material using an exfoliation technique.[6] The synthetic routes for graphene and its chemical derivatives can be broadly categorized into top-down and bottom-up methods (Figure 1.5).

Top-down methods involve exfoliation of individual layers of graphene from bulk graphite using external forces in suitable solvents, which break the van der Waals interactions between the adjacent layers.[14] Exfoliation process can yield millimeter sized graphene sheets with properties close to that of pristine graphene. Coleman and coworkers demonstrated a method to disperse and exfoliate graphite in organic solvents such as *N*-methyl-pyrrolidone.[15] Their method resulted in a monolayer yield of ~1 wt.%, which could improve to 12 wt.% with further processing. Same group developed another strategy to get graphene suspended in water–surfactant solutions with relatively good yields.[16] However many of these techniques suffer from low yield,

time consuming and poor quality which limits its application in laboratory scale. So chemists utilized the possibility of graphite oxide as an alternative precursor for the synthesis of graphene. Synthesis of graphene from oxidation of graphite is becoming a promising method with some advantages such as scalable, high yield and ease of chemical modification.

The oxidation of graphite to GO was first reported by British chemist B. C. Brodie in 1859, using potassium chlorate as an oxidizing agent in presence of HNO_3.[17] Later Hummers and coworkers in 1958, developed an alternative method for synthesis of GO, using $KMnO_4$ as an oxidizing agent in strong H_2SO_4.[18] Here, dimanganese heptoxide (Mn_2O_7) produced from reaction with $KMnO_4$ and H_2SO_4, act as an active oxidative species. This method is slightly modified by several research groups to improve the quality of the synthesized GO, and known as modified Hummers methods.[19,20] GO can be easily treated chemically with hydrazine and/or by thermal annealing, and thus be reduced to graphene, which is generally called reduced GO (rGO). Reduction of GO to reduced graphene oxide (rGO) can be carried out by using reducing agents such as hydroquinone, dimethylhydrazine, hydrazine hydrate, etc.[21] Chemical reduction of GO using hydrazine hydrate yield rGO with reasonably good quality and is the most common strategy adopted for the rGO synthesis. Other methods for reduction of GO include electrochemical reduction,[22] thermal reduction,[23] and photocatalytic reduction.[24]

The bottom up approach depends on the formation of covalent bonds between atoms or suitably designed small molecular building blocks to form 2D network by

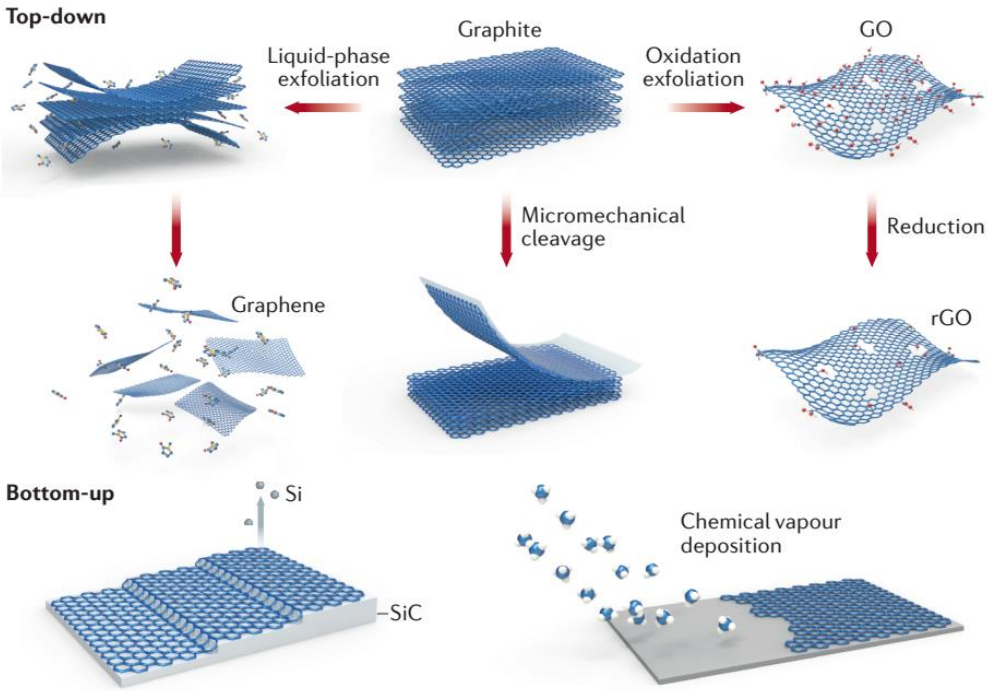

Figure 1.5. Scheme showing the chemical route to the synthesis of graphene derivatives (Adapted from reference 27).

using chemical or physical processes. The most common and efficient bottom-up fabrication methods for graphene sheets are based on epitaxial growth on silicon carbide (SiC) and chemical vapor deposition (CVD) method.[25,26] Graphene sheets can be grown on SiC wafers through the sublimation of Si atoms from the SiC surface and following graphitization of the remaining carbon atoms by annealing at high temperatures. The resulting graphene sheets exhibits crystalline domains reaching hundreds of micrometers in diameter.[25] CVD has been considered as the most promising method for the synthesis of large-area, uniform graphene films. Here, graphene films are formed through thermal decomposition of carbonaceous precursors like CH_4 or solid hydrocarbons, at high temperatures. This process leads to the

assembly of the carbon atoms into graphitic honeycomb structures, mostly on transition metals, such as Cu and Ni.[26]

1.3.3. Graphene Quantum Dots (GQDs)

Nanographenes with smaller sizes (less than ~60 nm) exhibit bandgap with energies that increase with decreasing size due to quantum confinement effect, and are termed as graphene quantum dots (GQDs). Graphene quantum dots are small graphene fragments, where electronic transport is confined in all three spatial dimensions.[28] The presence of oxygen-rich groups make the GQDs soluble in aqueous medium and provides additional advantages for further functionalization. Being a carbon material, GQDs are abundantly available and can be prepared *via* easy synthetic strategies. In addition they have remarkable properties such as low toxicity, high solubility in various solvents and can be equipped with functional groups at their edges and basal planes. These properties make them much more desirable for many applications compared with inorganic semiconductor QDs and fluorescent dye molecules. Photoluminescence of GQDs and semiconductor QDs differs in luminescence bandwidth, which is much wider in GQDs and that their emission maximum shifts to the red and decreases in intensity with increasing excitation wavelength.[29] It also has to be noted that the spectroscopic properties of GQDs may vary depending on the method of preparation and the functional groups at the edges of the particles.[28] More recently, GQDs have been chemically modified and used in applications in the area of energy conversion,[30] bioanalysis, bioimaging, diagnosis and drug delivery.[31-33]

1.3.4. Synthesis of GQDs

Several methods have been developed to fabricate GQDs, which can be classified into top-down and bottom-up methods (Figure 1.6). The top-down methods include electron beam lithography, acidic exfoliation, electrochemical oxidation, microwave-assisted hydrothermal synthesis and so on, which involve the cleavage of carbonaceous materials.[34-38] In addition, GQDs can also be prepared through bottom-up routes, including the solution chemistry and cyclodehydrogenation of polyphenylene precursors.[39] Carbonization of some special organic precursors or, the fragmentation of suitable precursors, like C_{60} are other bottom-up approaches for the synthesis of GQDs.[36] The top-down routes for the preparation of GQDs have the advantages of

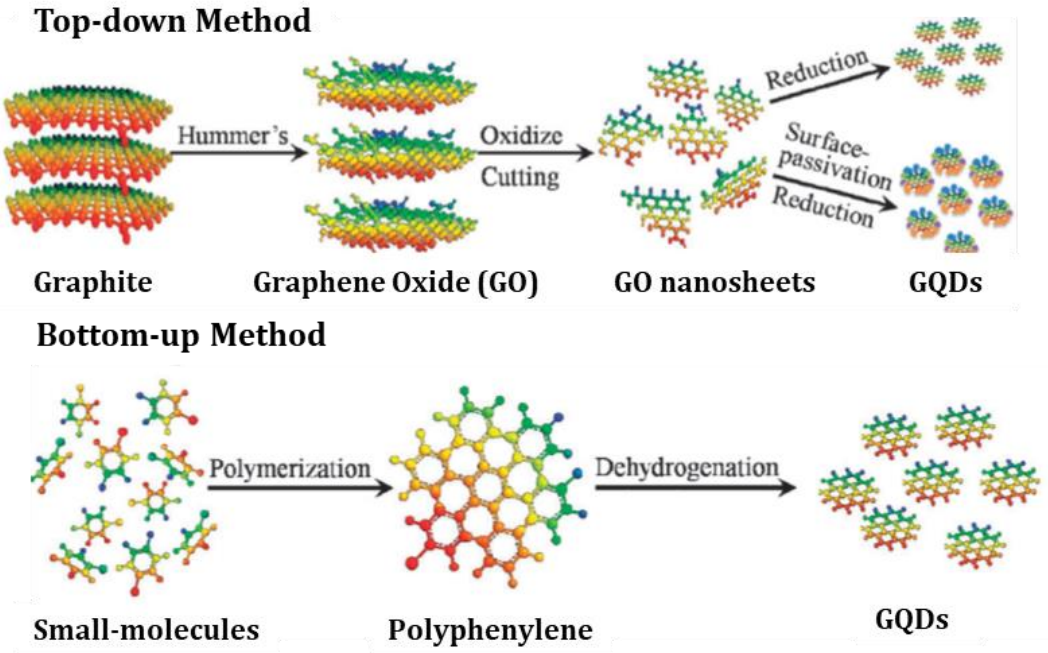

Figure 1.6. Schematic representation of various synthetic approaches for GQDs (Adapted from reference 28).

abundant raw materials, large-scale production, and simple operation. Moreover, the GQDs synthesized *via* top-down methods usually contain oxygen-containing functional groups at the edge, thus facilitating their solubility, functionalization, and passivation.[40]

1.3.5. Organic Functionalization of Graphene

Owing to the outstanding properties of graphene, it is expected to substitute for a variety of classical materials in the near future. However, the strong van der Waals interaction and chemical inertness makes graphene sheets difficult to separate and relatively insoluble in either water or common organic solvents, which is a major obstacle for many of the applications. To overcome this issue, several strategies have been developed to modify the graphene surface with various functional groups. In certain cases, the surface of the graphene requires modification in a desired format, which is especially important in sensing and other biological applications, because the surface charge and wettability are important for attachment and dispersion. The chemical manipulation of graphene is expected to stimulate the development of several new applications in many different fields such as supercapacitors,[41] batteries,[42] fuel cells,[43] optoelectronic devices[44], biomedical applications, etc.

The organic covalent functionalization reactions of graphene include two general methods. The first route utilizes the formation of covalent bonds between free radicals or dienophiles and C=C bonds of pristine graphene and the second method involves the reaction between organic functional groups and the oxygen containing functional groups of GO.[45] In principle, graphene can be functionalized on two surface faces (basal planes) and at the edges. Main examples of organic functionalization

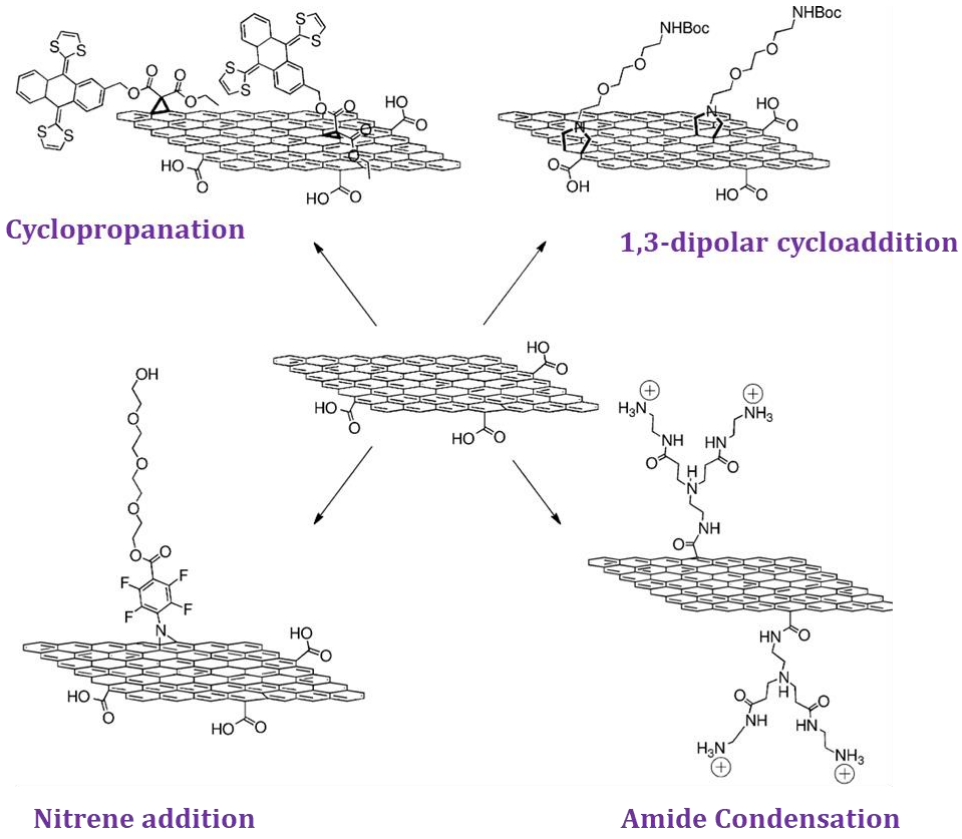

Figure 1.7. Various functionalization strategies for chemical modification of graphene (Adapted from reference 45).

reactions of graphene include 1,3-dipolar cycloadditions, amide condensations, nitrene additions and radical reactions (Figure 1.7). 1-ethyl-3-(3-dimethylaminopropyl)-carbodiimide (EDC) mediated amide coupling is considered to be one of the most successful strategies for efficient functionalization of graphene oxide, due to its high yield and solvent compatibility.[46] Other coupling reagents such as thionyl chloride ($SOCl_2$), *N,N'*-dicyclohexylcarbodiimide (DCC), or 2-(7-aza-1H-benzotriazole-1-yl)-1,1,3,3-tetramethyluronium hexafluorophosphate (HATU) are often used for amide coupling reaction.[47] In the amide condensation reaction, carboxylic groups generated during the oxidation process of graphite are mainly present at the edges of the

exfoliated graphene oxide. The carboxylic acid group can undergo direct coupling with amino functionalities *via* EDC amide coupling strategy. Huang *et al*., developed an immunosensing platform based on graphene oxide by covalently conjugating Immune globulin G (IgG) to GO by EDC-NHS amide coupling strategy.[48]

Liu *et al.*, utilized amide coupling method for the functionalization of GO with oligothiophene.[49] The nanohybrid was synthesized by reacting an amine functionalized oligothiophene and GO in 1,2-dichlorobenzene using 1,3-diisopropyl carbodiimide (DIC) as the coupling reagent. Attachment of oligothiophenes significantly improved the solubility and dispersion stability of the graphene-based material in organic solvents. Chen and coworkers followed $SOCl_2$ reaction to convert acid groups of GO to acid chloride, subsequent coupling with an amine functionalized porphyrin derivatives yield porphyrin–graphene nanohybrids with better optical limiting properties than C_{60}.[50]

Azomethine ylide, which reacts through a 1,3-dipolar cycloaddition, is one of the successful strategies applied in the functionalization of carbon nanostructures such as fullerenes, nanotubes, and nanohorns. This type of reaction affords a variety of organic derivatives, which display interesting applications in several areas. Maurizio Prato and coworkers showed that graphene sheets synthesized from organic dispersion of graphite could be substituted with pyrrolidine rings *via* a 1,3-dipolar cycloaddition of azomethine ylide.[51,52] They synthesized functionalized graphene layers by condensation of a protected amino acid and paraformaldehyde followed by the deprotection of the Boc group. This derivative can be easily integrated with gold nanorods (AuNRs) that can serve as contrast markers for the identification of the reactive sites and produces a

nanocomposite material for various applications. They utilized same reaction to functionalize graphene sheets with a PAMAM Dendron effectively, finding that graphene can be efficiently functionalized all over the surface.[53]

Feringa and coworkers successfully prepared graphene-porphyrin hybrids through one-pot 1,3-dipolar cycloaddition reactions.[54] They observed significant fluorescence and phosphorescence quenching with concomitant decrease in the excited state lifetimes, which confirm the energy and electron-transfer quenching between graphene and the covalently bound porphyrin molecules. Guldi and coworkers recently modified the exfoliated graphite surface by 1,3-dipolar cycloaddition in the presence of an excess of *N*-methyl glycine and 4-formylbenzoic acid.[55] This reaction introduces pyrrolidine ring on graphene surface with an ester group, which on hydrolysis generate carboxylic acid functionality on the basal planes. They further explored EDC/HOBT coupling for covalently anchoring amino functionalized phthalocyanine derivative to the graphene layers. The functionalization of graphene and modified graphene analogs are featured in detail in the recent reviews.[1,11,56]

1.4. Layered Transition Metal Dichalcogenides (TMDs)

Layered TMDs are a class of materials with MX_2 stoichiometry, where M refers to a transition metal typically from Group IV to Group VII (M = Ti, Nb, Ta, Mo, or W) of the periodic table and X refers to a chalcogen such as S, Se, or Te. Approximately 40 different layered TMDs have been identified to date. Bulk 3D crystalline TMDs are stacked structures with strong covalent bonding between metal and chalcogen, and

weak van der Waals interactions between adjacent layers of the MX_2.[57] Each TMD monolayer consists of three atomic layers, in which a transition metal layer is sandwiched between two chalcogen layers. Among the various Layered TMDs reported, molybdenum disulfide (MoS_2) is the most studied nanomaterial and the following section briefly introduces the structure, synthesis and functionalization of MoS_2 nanosheets and MoS_2 QDs.

1.4.1. Molybdenum disulfide, MoS_2

MoS_2, the most common layered TMD, has been well-studied as a semiconductor and received a lot of attention in areas ranging from energy and catalysis to sensing.[58] Bulk MoS_2 has a variety of stacking polytypes. Based on the coordination of Mo atoms within the single layer and the S-Mo-S stacking order of single layers, there are three known polytypes- namely 1T, 2H, and 3R – of MoS_2 (Figure 1.8). Here the former number denotes the crystallographic unit cell, and the latter letter describes the crystallographic structure, where T stands for trigonal, H for hexagonal and R for rhombohedral structure. Of these three polytypes, only 2H-MoS_2 and 3R-MoS_2 are stable and found in nature. Both the 2H and 3R polytypes commonly have trigonal prismatic coordination (D_{3h}) of molybdenum atoms, but they have different stacking order.[59]

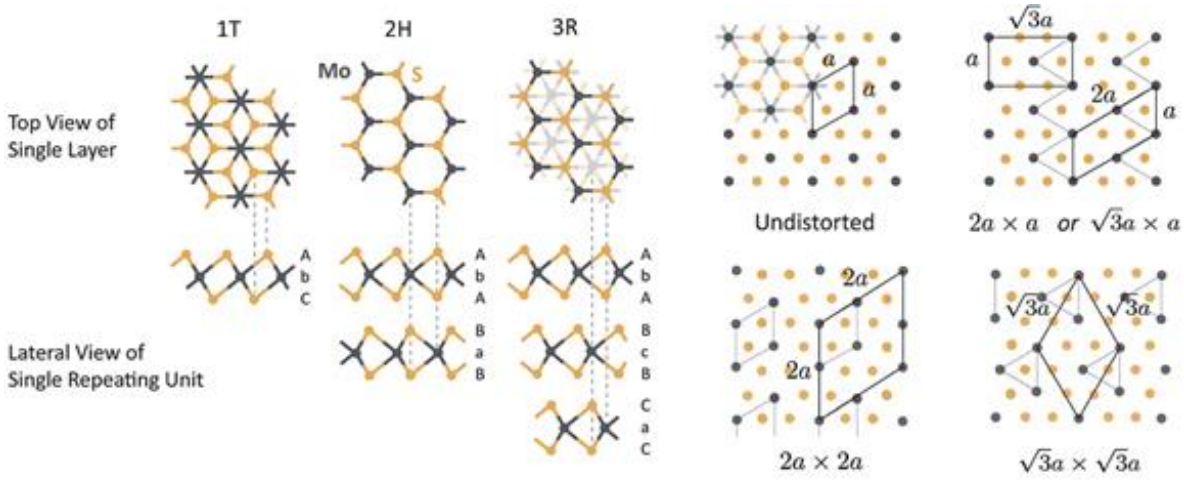

Figure 1.8. Schematic crystal structures of three polytypes of MoS_2-1T, 2H, and 3R (Adapted from reference 59).

Bulk MoS_2 is a semiconductor with an indirect bandgap of about 1.29 eV.[60] Theoretical calculations predicted an indirect to direct bandgap transition in the d-electron system when the bulk MoS_2 is reduced to a single layer. The chemically exfoliated MoS_2 nanosheets undergo a partial transformation from the 2H to the conducting 1T phase, losing its semiconducting properties.[61] Optical absorption is another characteristic which is related to the band structure of a semiconductor. There are usually two absorption peaks observed for thin MoS_2 layers, i.e., peaks at 1.85 eV (670 nm) and 1.98 eV (627 nm), corresponding to the direct excitonic transitions at the Brillouin zone K point. Because of these unique properties and relatively simple synthetic methods, single and few-layered MoS_2 nanosheets have been extensively explored for a wide range of applications in optoelectronics, sensors and energy-storage and conversion devices.[1,2,62]

Several methods have been developed to synthesize single and multilayer 2D MoS_2 nanosheets, which can be classified into two main groups: top-down and bottom-up methods. The top-down methods, which rely on the exfoliation of layered bulk crystals, include the mechanical cleavage method,[63] chemical Li-intercalation[64] and exfoliation with n-butyllithium (BuLi),[65] electrochemical Li-intercalation[66] and liquid phase exfoliation by direct sonication in solvents, and laser thinning technique.[67] Examples of bottom-up approaches are CVD growth and wet chemical synthesis such as hydrothermal reaction.[68]

1.4.2. MoS_2 Quantum Dots (MQDs)

Generally, the electronic band structure of semiconductor materials is relatively sensitive to the quantum size effect. In principle, monolayer MoS_2 with small lateral size can produce novel optical properties due to the quantum confinement effect. Because of quantum confinement and edge effects, MQDs possess unique optical and electronic properties and are potentially applicable in fluorescence sensing, catalysis, bioimaging, etc.[69] We can tune the fluorescence properties of MQDs by following various synthetic strategies. Recently, Xu *et al.*, proposed an efficient method to synthesize MQDs with lateral sizes of few nm by combining sonication and solvothermal treatment of bulk MoS_2 for in vitro cell imaging due to their low cytotoxicity and strong fluorescence.[70] Huang *et al.,* reported a facile one-pot hydrothermal approach to fabricate uniform water-soluble monolayer MQDs by using ammonium molybdate, thiourea, and N-acetyl-

L-cysteine (NAC) as precursors and the capping reagent, which showed promising potential for molecules detection.[71]

1.4.3. Functionalization of MoS_2 nanosheets

The past few years have seen great development in the field of MoS_2 synthesis and functionalization. The unique 2D planar structure and diverse chemical compositions lead to unique properties of these nanomaterials for biomedical applications such as drug delivery, diagnostic imaging, and biosensing. MoS_2 is rather inert and thus face problems for chemical functionalization. However, to further modify the properties of these nanomaterials for various applications, routes towards their chemical functionalization must be identified. Few commonly used functionalization strategies of MoS_2 are shown in Figure 1.9.

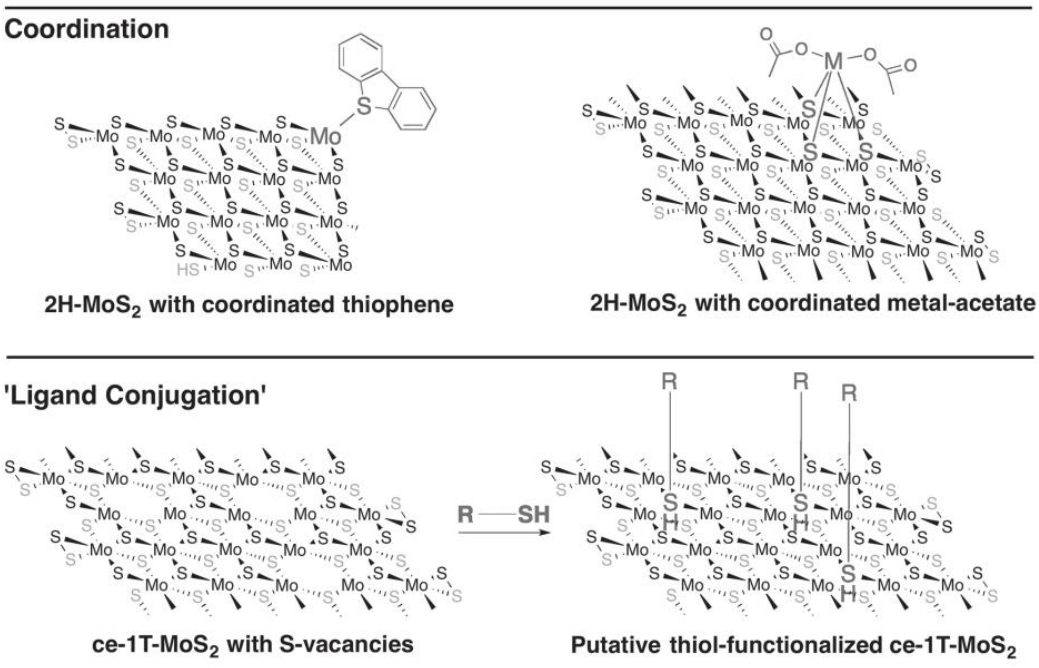

Figure 1.9. Various functionalization strategies for MoS_2 nanosheets.

Vinayak P. Dravid and co-workers reported the first example of an efficient functionalization of 2D TMDs.[72] They have demonstrated ligand conjugation of chemically exfoliated MoS_2 sheets through thiol chemistry (Figure 1.10). They were able to tune the zeta potential and surface functionality of MoS_2 sheets to enable its broad usage as artificial receptors for enzymes such as β-galactosidase. Upon reaction between the 1T-MoS_2 and the organic thiol, a marked change in the zeta-potential of the nanosheets was observed, indicating a change in the 1T-MoS_2 surface properties. XPS analysis showed the presence of surface carbon and oxygen atoms, demonstrating the polyether functional groups were indeed bound to the surface of the 1T-MoS_2. The authors defined this functionalization technique as organic thiol "ligand conjugation," although the exact nature of the thiol/MoS_2 interaction is unclear.

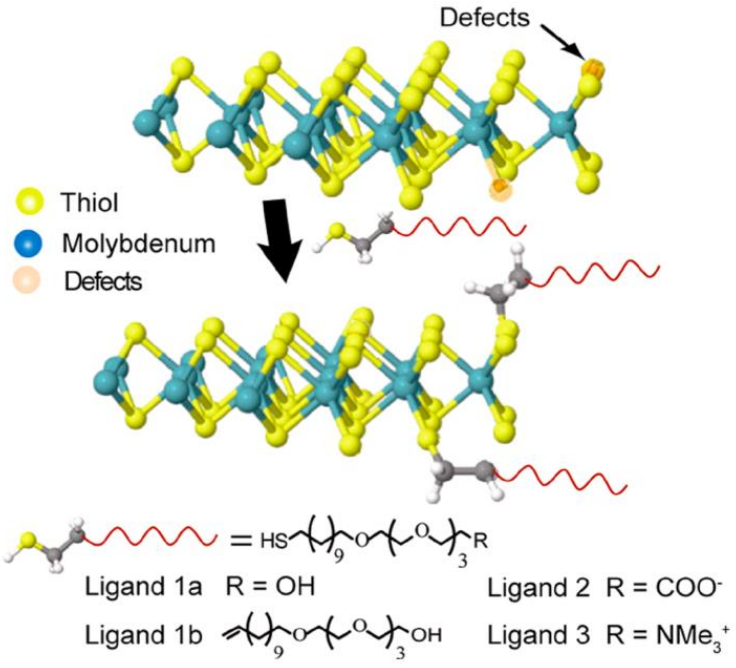

Figure 1.10. Structural models illustrating ligand conjugation of MoS_2 sheets. (Adapted from reference *72*).

Jong-Seon Kim *et al.,* developed a high-performance chemiresistor with a tunable sensor response and high sensitivity for representative volatile organic compounds (VOC) by using molybdenum disulfide (MoS_2) and by conjugating a thiolated ligand (mercaptoundecanoic acid, MUA) to MoS_2 surface (Figure 1.11).[73] Primitive and MUA functionalized MoS_2 sensing channels exhibit different sensor responses toward VOCs. Whereas, the primitive MoS_2 sensor shows positive responses for oxygen-functionalized VOCs, while the MUA-conjugated MoS_2 sensor exhibits negative responses for the same analytes. Such characteristic sensor responses reveal that ligand conjugation successfully introduce thiolated ligand to MoS_2 matrix. This strategy is a promising approach for the construction of a versatile sensor array, by conjugating a

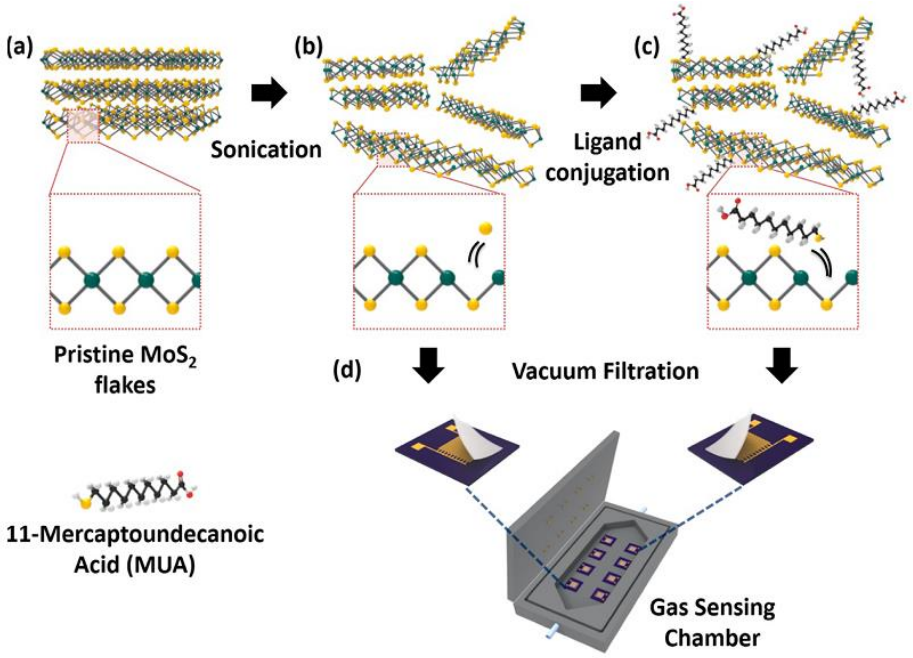

Figure 1.11. Schematic description for the preparation of MoS_2 chemiresistor from powder state material and sensing mechanism for MoS_2 sensing channels with target VOCs molecules (Adapted from reference 73).

wide variety of thiolated ligands on the MoS_2 surface. Furthermore, these MoS_2 sensors in this study exhibit high sensitivity to representative VOCs down to a concentration of 1 ppm.

Another functionalization strategy for 2H-MoS_2 through reaction with organic thiols was reported by Daenecke and co-workers in 2015.[74] They have used various organic thiols such as 4-mercaptophenol, thiophenol, 1-propanethiol, 1-nonanethiol, and 1-dodecanethiol in a fashion similar to Dravid's "ligand conjugation" method. 2H-MoS_2 was exfoliated by grinding and subsequent ultrasonication in ethanol. The exfoliated nanosheets were stirred with a large excess of thiol over a 24 h period followed by dialysis in ethanol/water to give thiol conjugated 2H-MoS_2 in good yields.

1.5. Characterization Techniques for 2D layered Nanomaterials

Due to the rapid progress of nanotechnology, some powerful characterization techniques have been identified for characterizing ultrathin 2D nanomaterials to reveal their composition, size, thickness, crystallinity, defects, and electronic states. The thorough characterization of these materials are of great importance in understanding the correlation between the various synthetic methods and structural properties of materials, as well as in designing 2D layered materials with desired properties for specific applications. The widely used characterization techniques for ultrathin 2D materials include Scanning Probe Microscopy (SPM), Transmission Electron Microscopy (TEM), X-ray Photoelectron Spectroscopy (XPS), and Raman Spectroscopy. The following section introduces few most commonly used characterization techniques for ultrathin 2D layered materials.

1.5.1. Atomic Force Microscopy (AFM)

Atomic force microscopy (AFM) is a powerful characterization tool to measure the thickness of 2D nanomaterials. AFM is a very-high-resolution type of scanning probe microscopy (SPM), with demonstrated resolution in the order of fractions of a nanometer. The successful formation of mono to few layer sheets can be easily probed using AFM morphological analysis. Thickness of single layered materials will always show some differences in theoretical and measured values. For example, measured heights of single-layer graphene on SiO_2/Si substrates vary from 0.5 to 1.0 nm depending on the AFM settings, whereas the thickness of monolayer MoS_2 nanosheet is approximately 1.0 nm, which is larger than the theoretical value of 0.65 nm (Figure 1.12A). AFM also can be used for the study the degradation of many unstable 2D nanomaterial in air. Time dependent morphological images can be used for determining the stability of these materials.

1.5.2. Transmission Electron Microscopy (TEM)

TEM is a powerful technique to characterize the size, crystallinity, phase, and growth direction of a thin material. It is the most widely used tool for the characterization of 2D layered materials. Here electron beam is transmitted through the thin samples and generating an image. Low-magnification TEM images can be used to examine the lateral size of nanosheets and roughly study the thickness. The thickness of nanosheets can be roughly evaluated from the contrast of TEM images. Mono/few layer nanomaterials can be easily detected by characteristic transparent TEM images

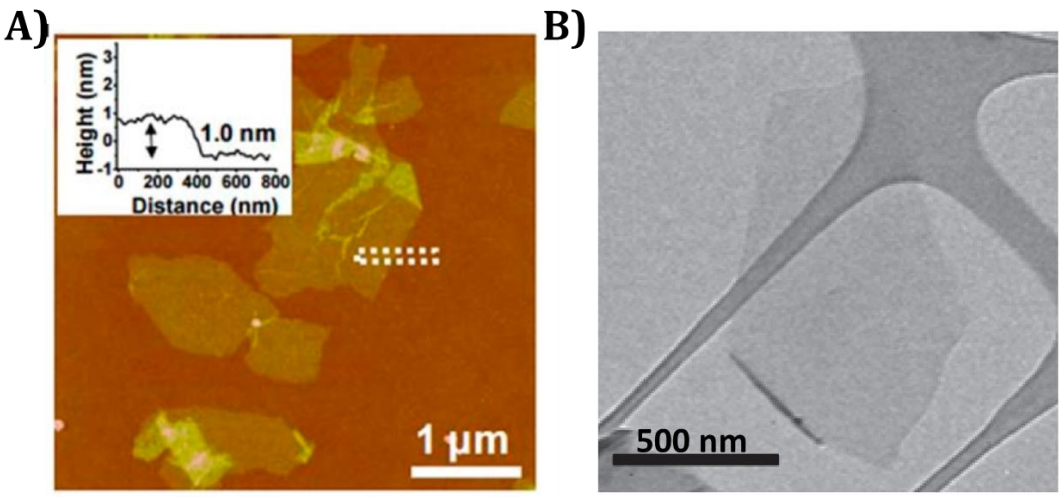

Figure 1.12. A) AFM image and height profile of monolayer MoS_2 nanosheets fabricated through electrochemical Li-intercalation assisted liquid exfoliation method.[75] B) Bright-field TEM images of monolayer graphene flakes[76] (Adapted from references 75 & 76).

(Figure 1.12B), whereas darker contrast indicates the thicker bulk counterpart. The crystallinity of ultrathin 2D nanomaterials can be evaluated from the HRTEM images and corresponding SAED patterns. Single-crystalline nanosheets give continuous lattice fringes with the same orientation and clear bright spots in SAED pattern images, whereas polycrystalline nanosheets give lattice fringes with random orientations and ring-like SAED patterns.

1.5.3. Raman Spectroscopy

Raman spectroscopy is one of the important vibrational spectroscopic techniques used to provide information on molecular vibrations and crystal structures. This technique is utilized to reveal the number of layers, crystalline orientation and phases, strain and doping effects of various ultrathin 2D nanomaterials and their heteronanostructures. Raman spectroscopy is a powerful tool for characterizing

graphene materials, especially for determining extends of defects generated as a result of the oxidation process. Graphene derivatives show a characteristic peak at 1575 cm^{-1}, known as G band due to E_{2g} phonon of sp^2 C atoms (Figure 1.13A).[77] Another major band appears around 1350 cm^{-1}, D band, due to breathing modes and it indicates the presence of disorder in the material due to oxygen incorporation as a result of harsh Hummers oxidation. First example of Raman study on ultrathin 2D TMDs, especially single and few-layer MoS_2 is reported by Lee *et al*. in 2010.[78] Two strong peaks assigned to in-plane (E^1_{2g}) and out-of-plane (A_{1g}) vibrations are observed. E^1_{2g} peaks red shift while A_{1g} peaks blue shift with increasing thickness of MoS_2 (Figure 1.13B).

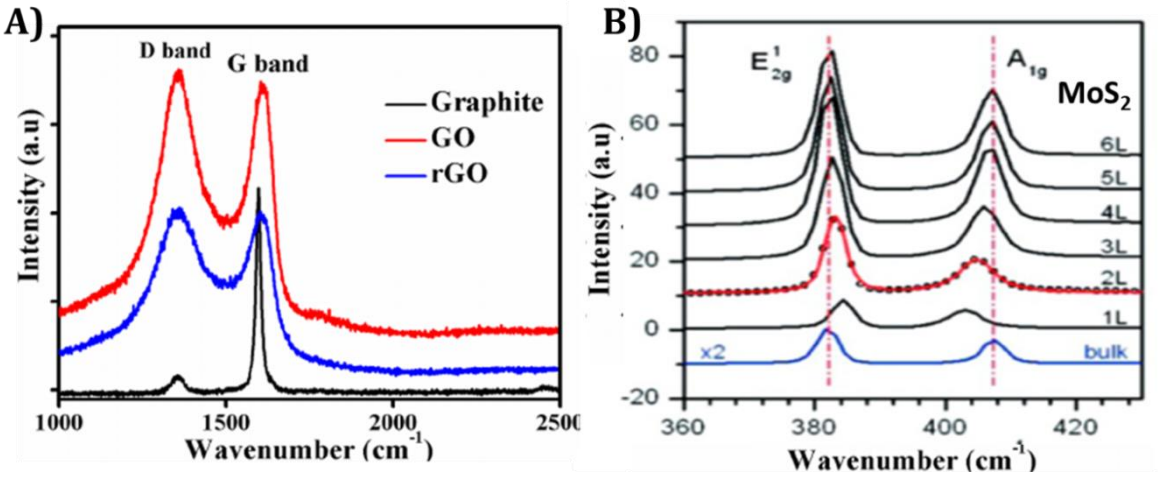

Figure 1.13. A) Raman spectra of graphite, GO and rGO.[79] B) Raman spectra of one layer (1L) to six layers (6L) and bulk MoS_2.[78] (Adapted from references 78 & 79).

1.6. Applications of 2D layered Nanomaterials

Owing to the unique material characteristics and excellent biocompatibility, several research groups are now focusing on various biomedical applications of 2D layered nanomaterials. 2D nanomaterials also possess the highest specific surface areas

of all known materials, which allow these materials to interact with various organic/bio-molecules with great efficiency. The diverse properties make these nanomaterials suitable for a wide range of biological applications, including drug delivery, cancer therapy, tissue engineering, bio-imaging, and biosensors.[1,80] The following section emphasis on various biosensing and photodynamic therapeutic applications of 2D nanomaterials (GO, rGO, GQDs, MoS_2, MQDs, etc.) as well as recent developments that are shaping this emerging field.

1.6.1. Biosensing Applications

2D layered nanomaterials such as graphene and MoS_2 have attracted great attention in the field of biosensing due to its unique properties such as good electron transport properties, high surface area, and high fluorescence quenching efficiency.[80] The partially oxidized form of graphene, GO is also featured with its single atom thickness and shows similar optical properties as graphene. The optical sensors with graphene materials have demonstrated great success because of the following characteristics. (i) The ultra-high luminescence quenching efficiency (ii) the large planar surface which allows simultaneous adsorbing and quenching of multiple probes to achieve multicolor detection in the same solution (iii) the excellent capabilities for direct conjugation with biomolecules due to the stacking and hydrophobic interactions and (iv) presence of oxygen functionalities make it easy to covalently functionalize with various molecules. Sensor assemblies on GO platform have been extensively used for detection of DNA, protein, enzyme activity, metal ions, and other small molecules with promising performances (Figure 1.14).[81,82]

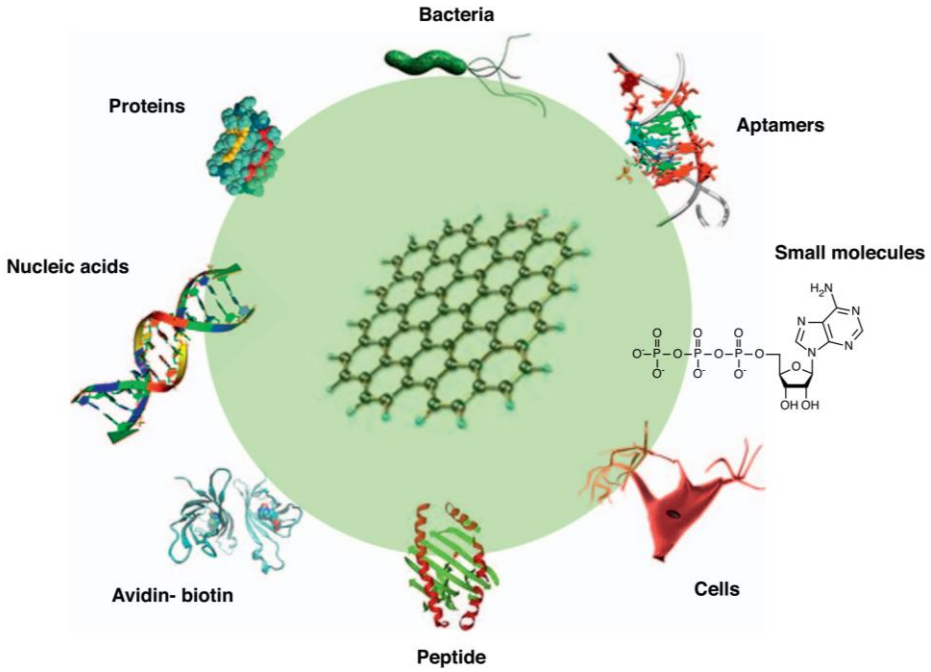

Figure 1.14. Various biomaterials which can interact with graphene (Adapted from reference 83).

1.6.1.1. Fluorescence based sensing

Nucleic acids can be adsorbed onto the surface of graphene materials due to the π-stacking interaction between the ring structures in the nucleobases and the hexagonal cells of graphene. The sensor concept is based on the fluorescence quenching of the dye-labeled ssDNA on binding with graphene materials. This quenching effect originates from fluorescence (or forster) resonance energy transfer, or non-radiative dipole-dipole coupling, between the fluorescent species and graphene materials. In the presence of a target species, the dye-labeled probe DNA forms a duplex with the target molecule so that it becomes rigid, and conformational changes release the duplex from graphene, reversing the quenching effect, resulting in restoration of dye fluorescence (Figure 1.15).[84]

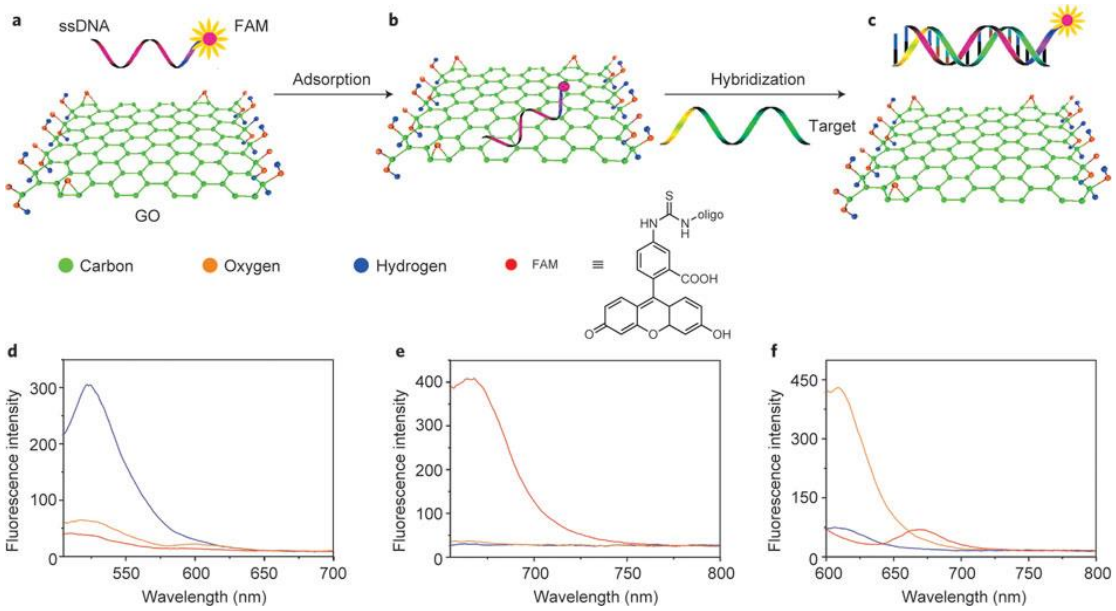

Figure 1.15. **Biosensing by fluorescence quenching in GO.** Schematic illustrating biosensing based on target-induced fluorescence change of the ssDNA-FAM-GO (FAM; fluorescein-based fluorescent dye). The fluorescence of dye-labeled ssDNA is quenched upon absorbing onto GO (b) and can be restored on being subjected to target molecule, (c) owing to the conformation change of the dye-labeled DNA .d-f, Representative fluorescence spectra on the addition of different targets (Adapted from reference 84).

This design could result in detection based on enhanced fluorescence that is sensitive and selective to the target molecule and is used by several research groups for the fabrication of sensors for various analytes.

A graphene oxide-organic dye complex based DNA sensing platform was reported by Kian Ping Loh and coworkers, utilizing ionic interactions between negatively charged GO and positively charged pyrene (PNP) derivative.[85] The dye can also undergo π–π interactions with GO *via* its pyrene moiety, which results in strong fluorescence quenching *via* charge-transfer interactions. Interaction of DNA with this complex can bring back the fluorescence and they demonstrated that GO–dye complex

could be used as an optical sensor for DNA, for which it is selective over a variety of commonly used surfactants and biomolecules (Figure 1.16).

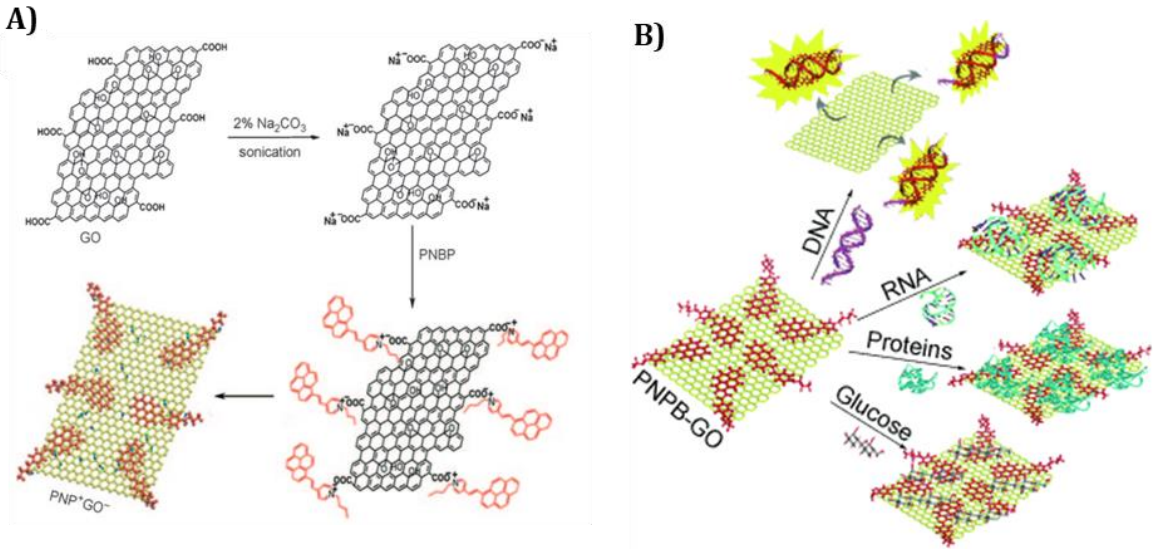

Figure 1.16. A) Schematic representation of synthesis of PNP+GO. B) Interaction of PNPB-GO with various biomolecules such as DNA, RNA, proteins and glucose (Adapted from reference 85).

Koninti *et al.* have presented graphene oxide based molecular switching of ellipticine (E) to probe its efficient loading onto GO and subsequent release to intra-cellular biomolecules like DNA/RNA at physiological pH.[86] The green fluorescence of E switches to blue in GO and switches back to green with polynucleotides. The intensified blue emission of the ellipticine–GO (E–GO) complex with human serum albumin (HSA), switches to a bluish green upon addition of dsDNA (Figure 1.17). Electron microscopy reveals the formation of distinctive 3D assemblies involving GO and biomolecules probably through non-covalent interactions and this is primarily responsible for the biomolecules assisted fluorescence-switching of E.

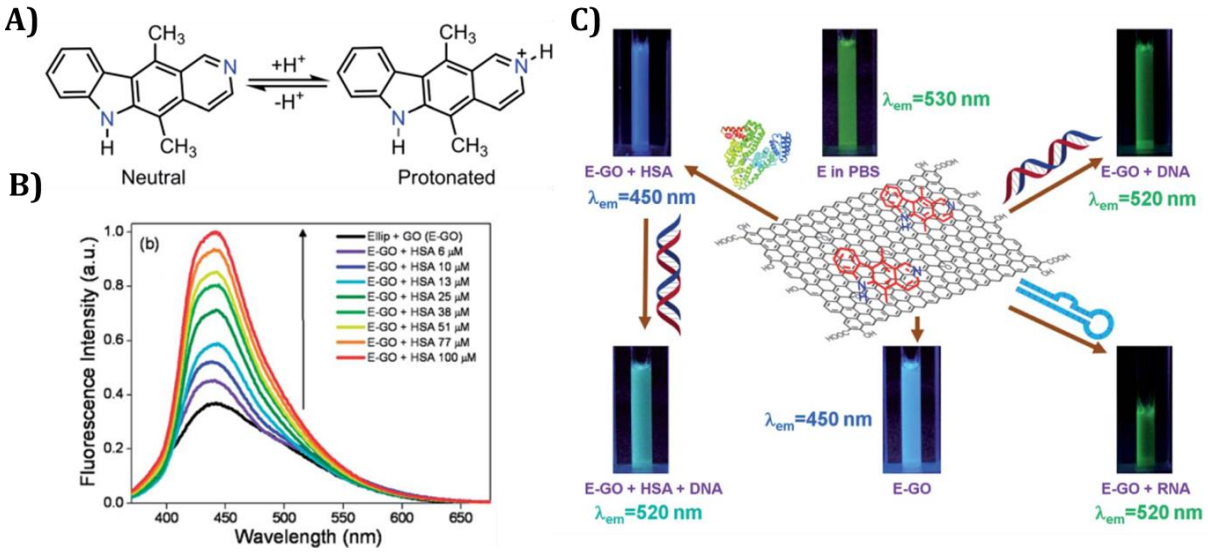

Figure 1.17. A) neutral and protonated form of ellipticine (E), B) fluorescence enhancement of E–GO with HSA (0–100 uM) and C) Fluorescence-switching of ellipticine in the presence of GO with various bio-macromolecules (HSA/dsDNA/RNA) (Adapted from reference 86).

Zhang and coworkers reported a homogeneous assay format for DNA and small molecules by using single-layer MoS_2-based fluorogenic nanoprobes.[87] The single-layer MoS_2 nanosheet was synthesized by exfoliating bulk MoS_2 using the electrochemical lithium-intercalation method. Single-layer MoS_2 nanosheet exhibits high fluorescence quenching ability and different affinity toward ssDNA versus dsDNA similar to that of graphene derivatives. As a proof of concept, they have successfully exploited MoS_2 nanosheet as a sensing platform for the detection of DNA and small molecules (Figure 1.18).

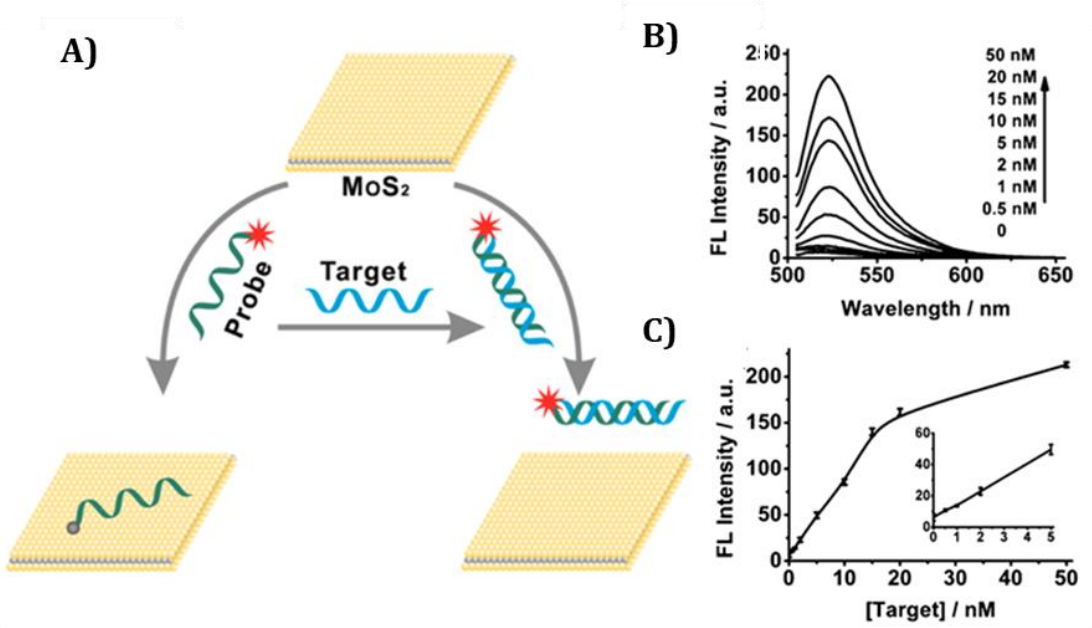

Figure 1.18. A) Schematic Illustration of the Fluorimetric DNA Assay B) Fluorescence spectra of MoS_2-DNA (15 nM) in the presence of different concentrations of target DNA. C) Calibration curve for DNA detection (Adapted from reference 87).

1.6.1.2. FET based sensing

Biosensors based on field-effect transistors (FETs) have attracted much attention, as they offer rapid, inexpensive, and label-free detection.[88] The detection in FET devices is based on the conductance change of the channel material, which is induced by the interaction between the target analytes and the channel material. A typical FET device contains a semiconducting channel between the electrodes (drain/source). We can modulate the conductance of the channel by varying the gate voltage through the dielectric layer. Exposure of channel material to specific analyte allows interactions between them, which leads to a change in conductance of the channel, making them promising platforms for sensing applications.[89] 2D nanosheets are considered to be a better candidate for field effect transistor (FET)-based

biosensors, because of their unique electronic states and ultra-thin planar morphology.[1,90]

The high carrier mobility and unique band structure of graphene make it extremely useful for FETs application. Park *et al.,* in 2012 described the scalable and facile fabrication of reduced graphene oxide FETs (rGO FETs) with the capability of the label-free, ultrasensitive electrical detection of a prostate cancer biomarker, prostate specific antigen/a1-antichymotrypsin (PSA-ACT) complex.[91] The rGO channel in the device was formed by reduction of graphene oxide nanosheets networked by a self-assembly process. Immunoreaction of PSA-ACT complexes with PSA monoclonal antibodies on the rGO channel surface caused a linear response in the shift of the gate voltage, which act as a transducer signal for the detection. This biosensor showed a high specificity to other cancer biomarker in the phosphate buffered saline solutions as well as in the human serum.

Lee and coworkers in 2013 developed a solution-gated reduced graphene oxide field-effect transistors (rGO FETs) for pH sensing and biochemical sensing applications.[92] A channel of a networked rGO film formed by self-assembly was incorporated as a sensing layer into a solution-gated FET structure for pH sensing and the detection of acetylcholine (ACh) through enzymatic reactions. The fabricated rGO FET was sensitive to protons with a pH sensitivity of 29 mV/pH, which is due to changes in the surface potential caused by the interaction of protons with OH surface functional groups present on the rGO surface (Figure 1.19). They further utilized the

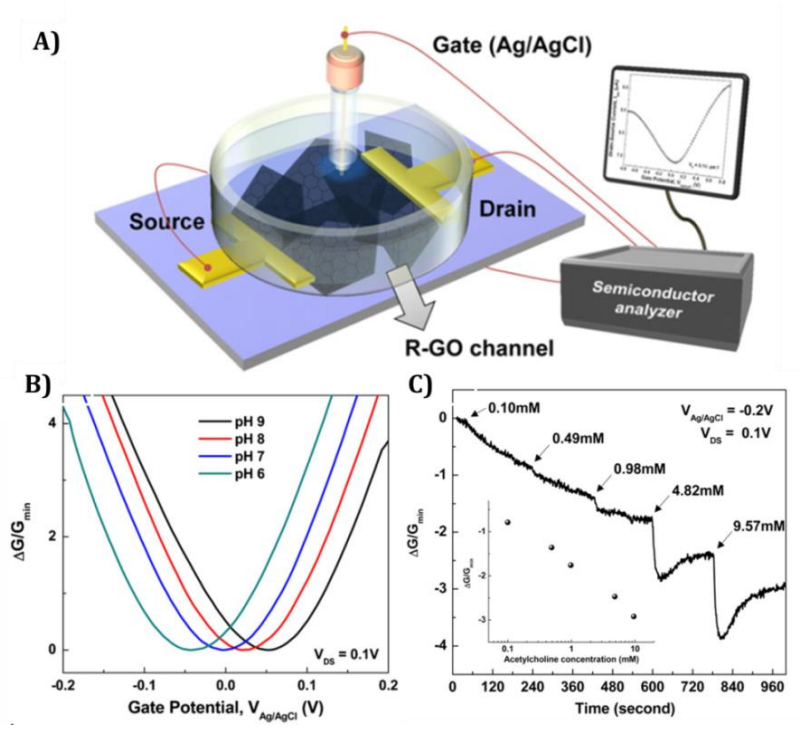

Figure 1.19. A) Experimental set-up employed for the measurement of H^+ and biosensing using the solution-gated rGO FET. B) The transfer characteristics obtained at a source–drain voltage of 0.1 V show the changes in the channel conductance by varying the gate potential. C) An increase of the Ach concentration induces a conductance decrease due to increased H^+ ion generation from the increased enzymatic reaction (Adapted from reference 91).

sensing strategy for the detection of acetylcholine in the concentration range of 0.1–10 mM by sensing protons generated during the enzymatic reactions with immobilized acetylcholinesterase (AChE) on rGO FET.

A reduced graphene oxide based FET biosensor for ultrasensitive label-free detection of DNA *via* peptide nucleic acid (PNA)-DNA hybridization is reported by Zhang and coworkers.[93] FET biosensor was fabricated by drop-casting the rGO suspension onto the sensor surface and DNA detection was performed through PNA-

DNA hybridization by the rGO FET biosensor with a detection limit as low as 100 fM (Figure 1.20). Moreover, the rGO FET biosensor was able to distinguish the complementary DNA from one-base mismatched DNA and noncomplementary DNA.

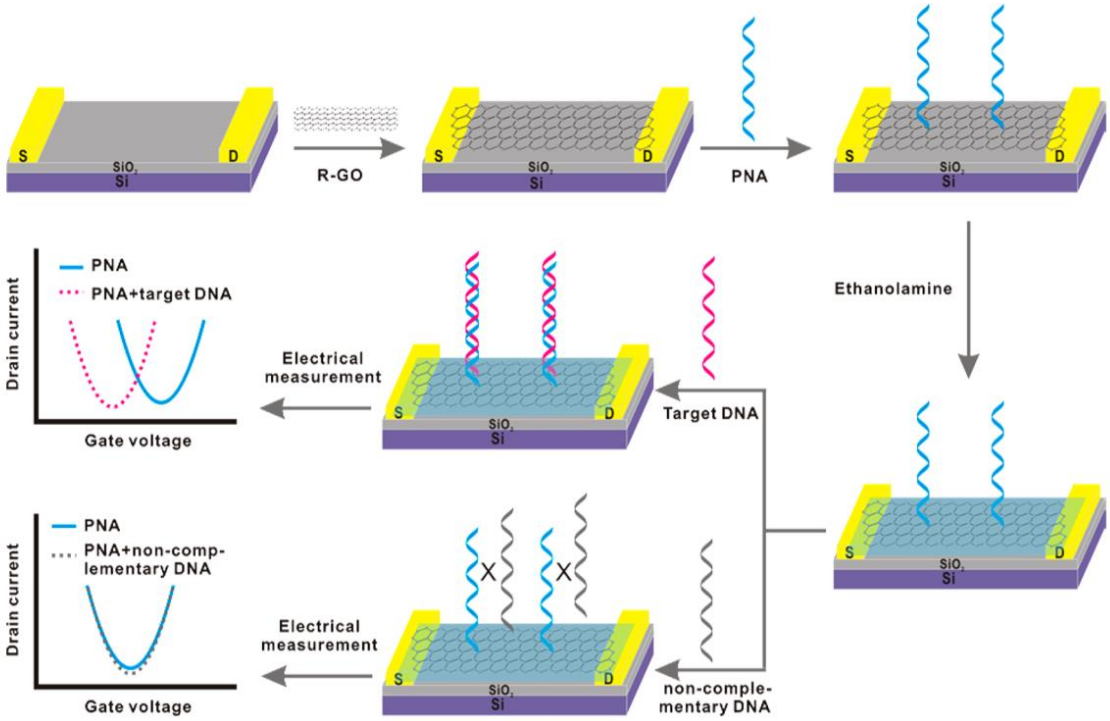

Figure 1.20. Schematic illustration of the rGO FET biosensor for detection of DNA based on PNA-DNA hybridization (Adapted from reference 93).

Banerje and co-workers have demonstarted the fabrication of a FET sensor by using mechanically exfoliated MoS_2 nanosheet as the channel material for pH and biomolecule detection.[94] Here MoS_2 provide excellent electrostatics and sensitivity due to its atomically thin nature along with the presence of a band gap. As fabricated MoS_2-based pH sensor showed sensitivity as high as 713 for a pH change by 1 unit along with efficient operation over a wide pH range (3-9) and exhibited specific protein detection limit of 100 fM (Figure 1.21). Lee *et al.,* developed a FET with few-layer MoS_2 as a

sensing-channel material and demonstrated the label-free electrical detection of DNA hybridization. The MoS_2-channel pattern was selectively formed through the chemical reaction of the Mo layer with H_2S gas and the fabricated FET is stable in electrolytes and inert to pH changes. The results indicate that the MoS_2 bio-FETs can be used to detect target DNA molecules with a low detection limit of 10 fM, with high sensitivity of 17 mV/dec.

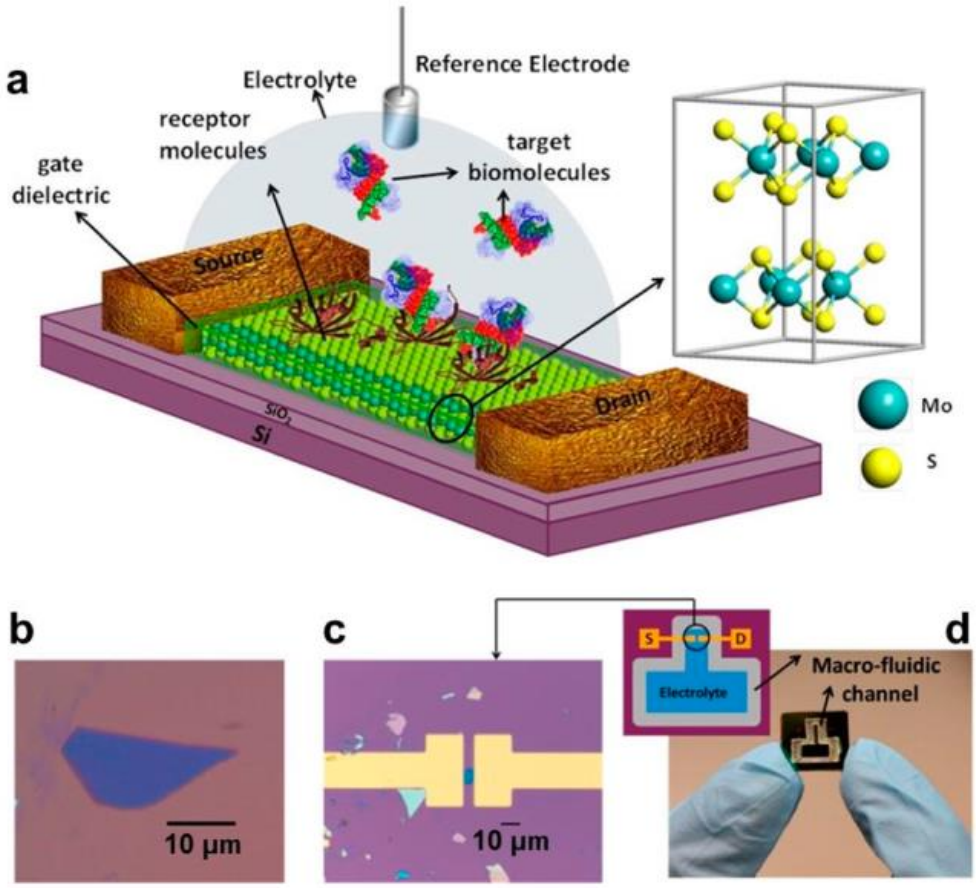

Figure 1.21. (a) Schematic illustration of the MoS2-based FET biosensor. (b) Optical image of a MoS_2 flake on a SiO_2/Si substrate. (c) Optical image of the MoS2-based FET biosensor device. (d) Photograph and scheme (inset figure) of the fabricated chip (Adapted from reference 94).

1.6.1.3. Electrochemical sensing

Electrochemical sensors have been utilized for the detection of various kinds of analytes because of their low cost, good sensitivity, and selectivity.[95] The detection mechanism in electrochemical sensors is mainly based on electron transfer between the active material coated on a working electrode and the target analytes in a three-electrode working system. Owing to the extraordinary electronic properties and electron transport capabilities, 2D layered nanomaterials have recently attracted great attention in the field of electrochemical sensors. Graphene and its derivatives are the most widely explored ultrathin 2D nanomaterials for electrochemical sensors.[96]

Liu *et al.,* in 2010 developed a graphene based electrochemical biosensor for glucose by covalently attaching carboxyl acid groups of GO sheets with glucose oxidase (GOx) *via* amide coupling.[97] The electrochemical performance of the GO electrode decreases after the introduction of GOx because of the weak electron transferring nature of GOx. The covalently linked GOx-GO enzyme electrode shows broad linearity, good sensitivity, excellent reproducibility and storage stability, suggesting GO to be a highly efficient biosensor electrode for efficient sensing of glucose. Kang *et al.*, developed GOx–graphene–chitosan nanocomposite for glucose sensing applications.[98] The immobilized enzyme retains its bioactivity, exhibits a surface confined, reversible two-proton and two-electron transfer reaction, with a fast heterogeneous electron transfer rate. The biosensor exhibits a wider linearity range from 0.08 mM to 12 mM glucose with a detection limit of 0.02 mM.

Pumera and coworkers utilized graphene oxide nanoplatelets (GONPs) as electroactive labels for DNA analysis.[99] The reduction of the oxygen-containing groups present on the surface of GONPs can provide the signals for sensing. The differential ability of the GONPs to conjugate to DNA hybrids obtained with complementary, noncomplementary, and one-mismatch sequences allows the discrimination of single-nucleotide polymorphism correlated with Alzheimer's disease (Figure 1.22). The authors followed a simple and rapid protocol for the detection of DNA hybridization and polymorphism using disposable screen-printed electrodes.

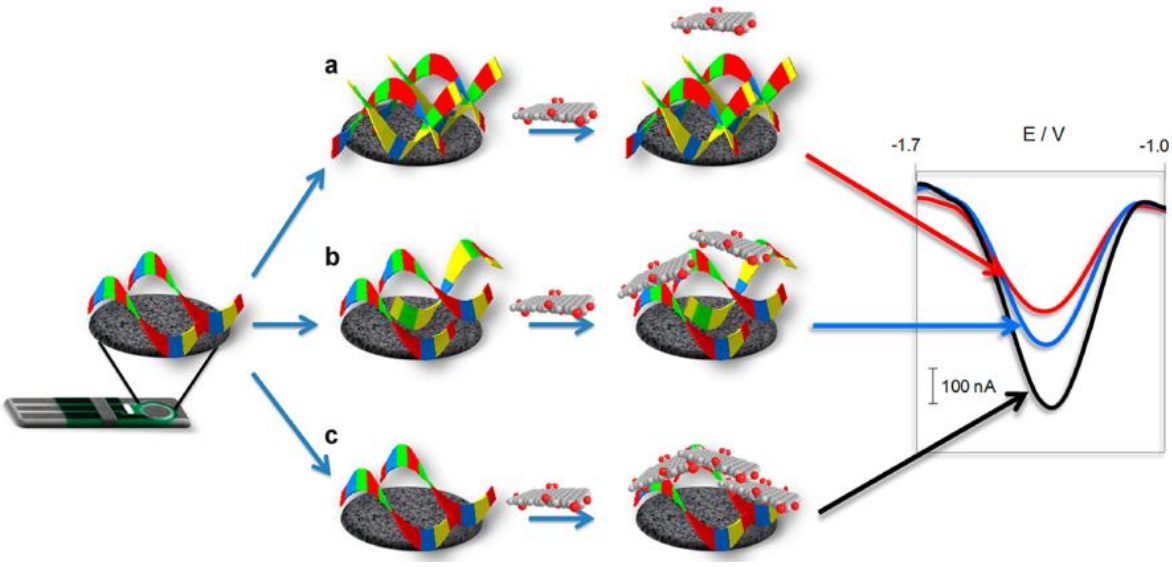

Figure 1.22. Schematic of the graphene oxide nanoplatelets (GONPs) as electroactive labels for DNA analysis. (a) The hybridization step was performed with complementary target; (b) one-mismatch target; and (c) noncomplementary target. (Adapted from reference 99).

Rohaizad *et al.*, recently developed a second generation electrochemical glucose biosensor using chemically exfoliated TMDs (MoS_2, $MoSe_2$, WS_2, and WSe_2).[100] Exfoliation of bulk TMDs were done using t-BuLi as the intercalating agent and used for

sensor fabrication as shown in Figure 1.23. These sensors exhibited superior heterogeneous electron-transfer properties. Characterization data revealed the prominence of metallic 1T phase, a polymorph responsible for the improved electrocatalytic properties. The developed and optimized 1T TMDs-based biosensors achieved excellent selectivity, wide linear ranges, as well as low limits of detection and quantification.

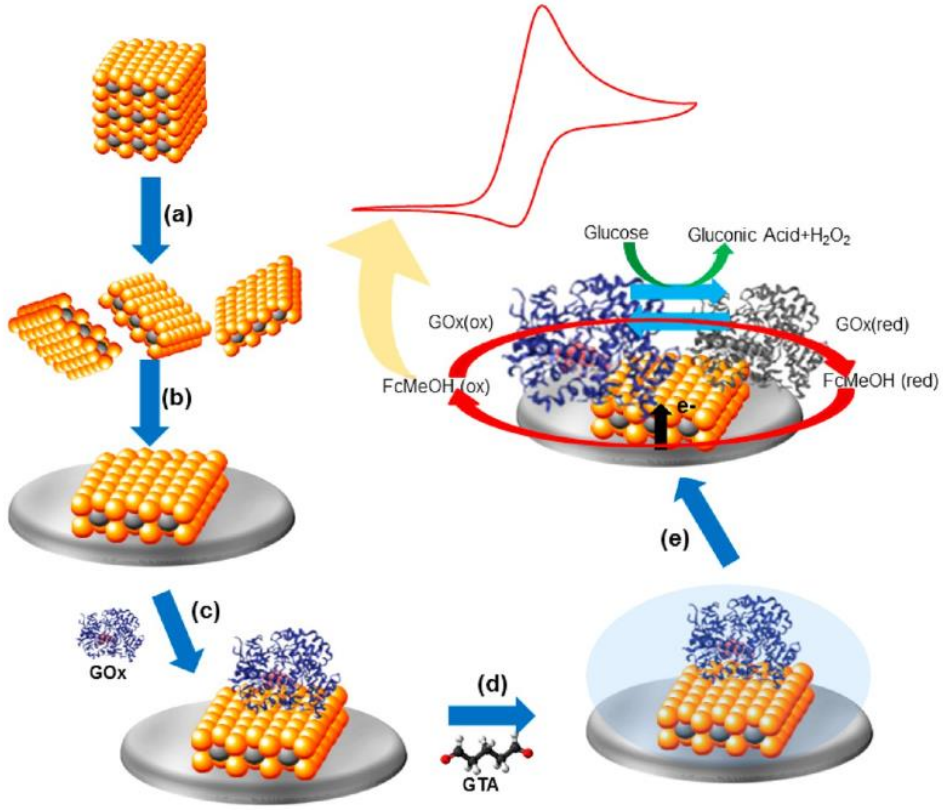

Figure 1.23. Schematic representation illustrating (a) Exfoliation of bulk TMDs employing t-BuLi as the intercalating agent; (b) Construction of the biosensor electrode by drop casting exfoliated TMDs onto bare GC electrode, Followed by (c) GOx, (d) Cross-linking using GTA; (e) Electrochemical detection mechanism of glucose (Adapted from reference 100).

1.6.2. Photodynamic Therapy (PDT) Applications

Photodynamic therapy (PDT), a non-invasive modality for the treatment of cancer, involves the combined interaction of oxygen, light and a photosensitizing agent and cause local destruction of cancerous cells through the generation of reactive oxygen species (ROS).[101-104] In PDT the patient receives an intravenous injection of a photosensitizer. A period of incubation is needed during which the normal cells get rid of photosensitizer and the malignant cells accumulate it. After the incubation time the patient is exposed to light of appropriate wavelength. When sensitizers are illuminated

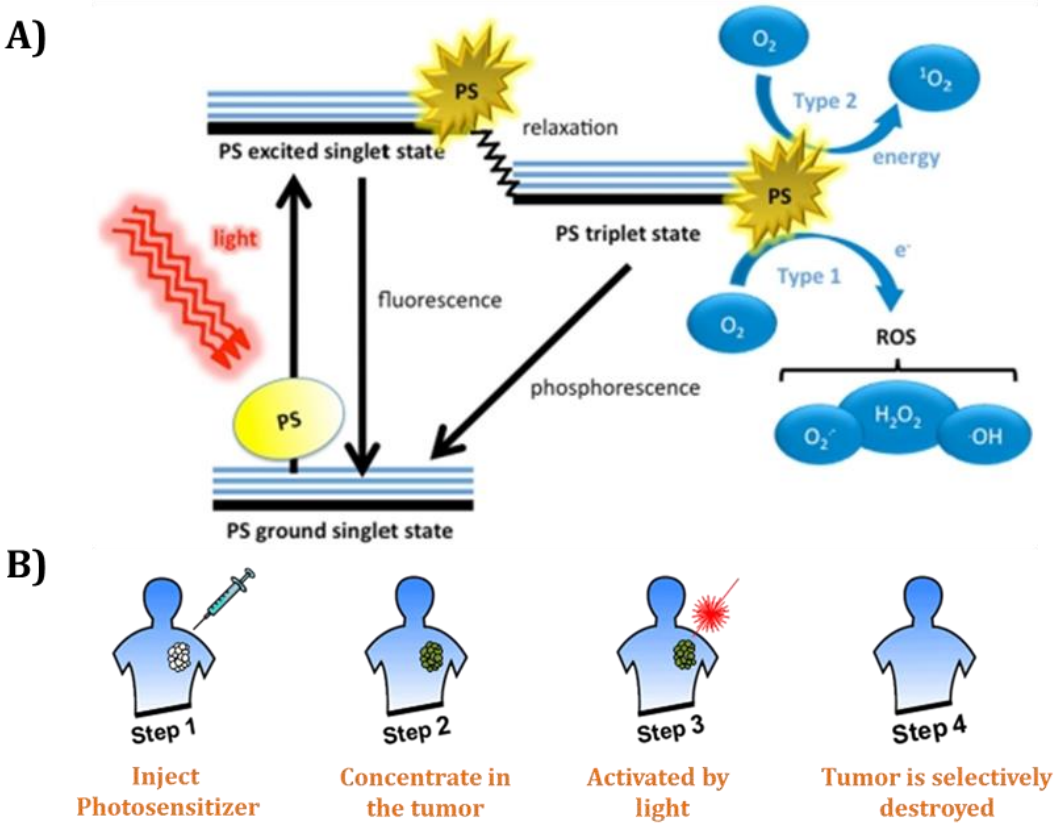

Figure 1.24. A) Jablonski diagram illustrating the various photophysical processes that occur upon irradiation of a PDT photosensitizer.[107]B) Steps involved in the PDT treatment (Adapted from reference 107).

by light, they absorb energy and transfer it to molecular oxygen. The energy transferred by the photosensitizer transforms triplet oxygen to singlet oxygen, an extremely reactive species that ultimately leads to the destruction of targeted cells.[105,106] The generation of singlet oxygen can be explained using Jablonski diagram as shown in Figure 1.24.[107] PDT has many advantages over other modes of treatments. It has minimum long-term side effects when used properly and less invasive than surgery. It is target specific and can be repeated many times at the same site if needed and usually takes a short time and less cost.[108]

Photosensitizer (PS) plays an important role in the outcome of the PDT. Some of the desirable attributes of the PS are its ability to generate reactive oxygen species, cellular internalization and biodistribution, and long wavelength (preferably in the red and near IR regions) absorption because of its better tissue permeability and cellular non-toxicity. Singlet oxygen has been proven to be the main cytotoxic agent of PDT to cause biological effects among reactive oxygen species.[109] The lifetime of singlet oxygen in cells is short and has a limited diffusion distance. Thus singlet oxygen generated in a cell may not damage neighboring cells which provides high selectivity for PDT treatment.[109]

Currently, combination therapies of nanoplatforms for cancer treatment are receiving more and more attention. Among various nanomaterials, graphene and its analogs could be an ideal platform for drug delivery applications.[110] 2D nanomaterials possess ultrahigh surface area, which is available for efficient loading of PDT drug molecules *via* noncovalent as well as covalent approaches. In case of graphene, chemical

modifications can be done easily by introducing functional groups *via* oxidation. Functional groups, such as epoxy, hydroxyl, and carboxylic acid moieties, attached to graphene oxide (GO) sheets facilitate easy modification with biomolecules that could improve the stability, solubility and biocompatibility.[111] So graphene and its derivatives have been extensively used as the targeted deliverer of PDT sensitizers both *in vitro* and *in vivo*.[112]

Zhuang Liu *et al*., reported that graphene with unique physical and chemical properties could have various potential applications in biomedicine.[113] In his work, a photosensitizer molecule, Chlorin e6 (Ce6), is loaded on polyethylene glycol (PEG)-functionalized graphene oxide *via* supramolecular π-π stacking. The obtained GO-PEG-Ce6 complex shows excellent water solubility and can generate cytotoxic singlet oxygen under light excitation for photodynamic therapy (PDT). Owing to the significantly enhanced intracellular trafficking of photosensitizers, this GO-PEG-Ce6 complex offers a remarkably improved cancer cell photodynamic destruction effect compared to free Ce6. More importantly, the photothermal effect of graphene can be utilized to promote the delivery of Ce6 molecules by mild local heating when exposed to a near-infrared laser at a low power density, further enhancing the PDT efficacy against cancer cells (Figure 1.25). This work highlights the promise of using graphene for potential multifunctional cancer therapies.

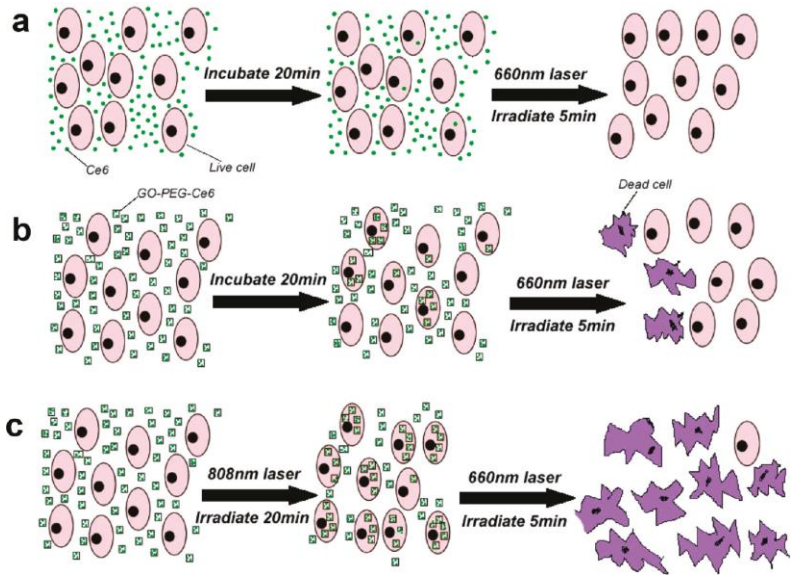

Figure 1.25. Schematic representation of photothermally enhanced photodynamic therapy on KB cells, incubated with free Ce6 (a) and GO-PEG-Ce6 (b) for 20 min in the dark and then irradiated by the 660 nm laser in control experiments (c) (Adapted from reference 113).

Xing-Can Shen and co-workers presented a new and facile one-step method for the fabrication of a water-soluble graphene–phthalocyanine (GR–Pc) hybrid material by simply sonicating graphene with a hydrophilic phthalocyanine, tetrasulfonic acid tetrasodium salt copper phthalocyanine (TSCuPc).[114] In the resultant hybrid material, TSCuPc is coated on the skeleton of pristine graphene *via* non-covalent $\pi - \pi$ interaction (Figure 1.26). The obtained Graphene–Pc hybrid (GR–TSCuPc) is applied for photothermal therapy (PTT) and photodynamic therapy (PDT). In this PTT/PDT system, both Graphene and TSCuPc operate as multifunctional agents, where graphene acts as a photosensitizer carrier and PTT agent, while TSCuPc acts as a hydrophilic PDT agent. Furthermore, the results of cell viability show that the phototherapy effect of GR–TSCuPc is observably higher than that of free TSCuPc, indicating that combined non-invasive PTT/PDT exhibits better anti-cancer efficacy in vitro.

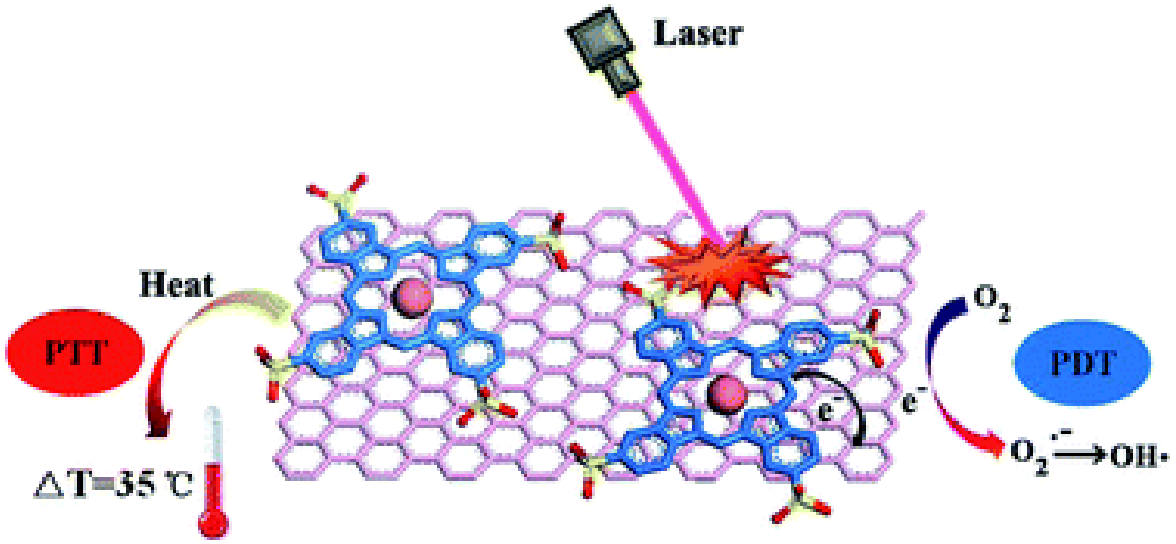

Figure 1.26. Schematic illustration of graphene-phthalocyanine conjugates for PDT and PTT (Adapted from reference 114).

In a recent report by Xiaoyuan Chen and coworkers, a photosensitizer molecule, 2-(1-hexyloxyethyl)-2-devinyl pyropheophorbide-alpha (HPPH or Photochlor®), is loaded onto polyethylene glycol (PEG)-functionalized graphene oxide (GO) *via* supramolecular π-π stacking.[115] The synthesized GO-PEG-HPPH complex displays high drug loading efficiency. As-synthesized nanohybrid offers dramatically improved photodynamic cancer cell killing efficacy compared with free HPPH, due to the increased tumor delivery of sensitizer (Figure 1.27). They have studied the role of graphene as a carrier of PDT agents to improve PDT efficacy and increase long-term survival following treatment.

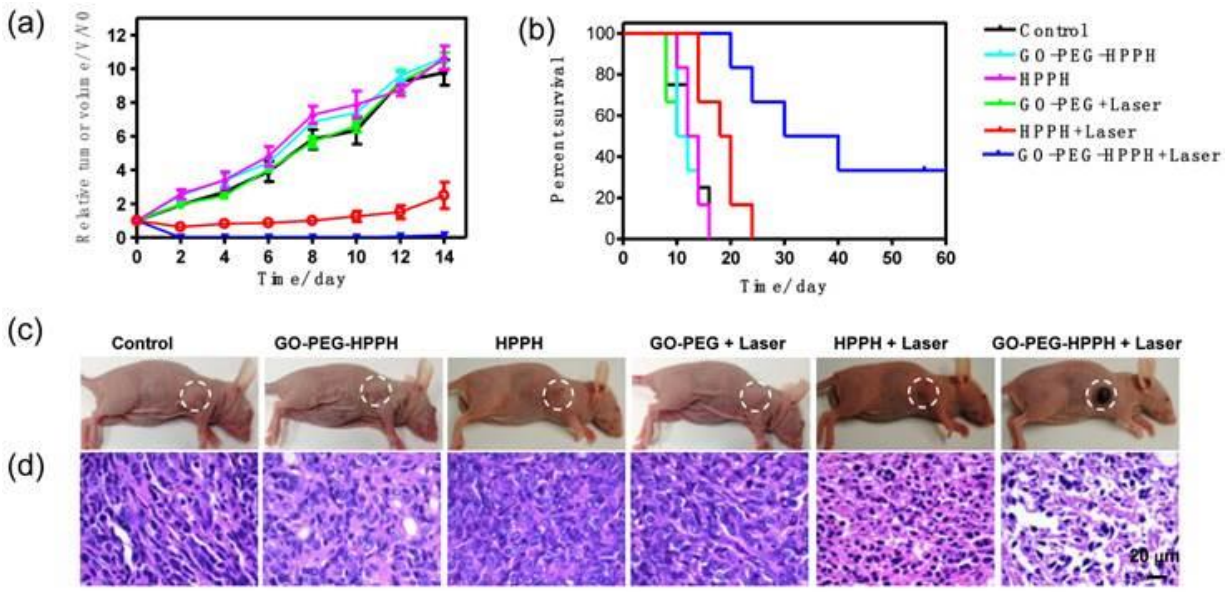

Figure 1.27. a) Tumor growth curves and b) Kaplan-Meier survival curves of different groups of tumor-bearing mice after treatment. c) Representative photos of tumor-bearing mice from different groups 14 days after treatment. d) H&E stained tumor sections collected from different groups of mice 24 hr post-treatment (Adapted from reference 115).

Char *et al.*, reported a Hyaluronic acid (HA) – graphene oxide (GO) conjugates, with a high loading of photosensitizers, Ce6, for cancer cell targeted and photoactivity switchable nanoplatform for photodynamic therapy (PDT).[116] The physical adsorption of Ce6 onto HA–GO nanocarriers were mainly due to the π - π stacking as well as hydrophobic interactions. They found that the cellular internalization of Ce6 carried with HA–GO conjugates were much more effective than that of free Ce6. Zhen *et al.,* reported a new strategy to combine C_{60} with graphene for targeting phototherapy applications.[117] Folic acid (FA) and polyethylene glycol (PEG) were conjugated onto graphene oxide (GO) *via* an imide linkage. The FA–GO–PEG/C_{60} nanohybrid was prepared using nucleophilic addition reaction. This platform of FA–GO–PEG with C_{60}

dramatically improved tumor targeting, which has been demonstrated by a cellular uptake assay.

Zhao *et al.,* have shown that GO is an ideal singlet oxygen generation (SOG) controller, which can reversibly quench and recover SOG depending on the interaction intensity between GO and a photosensitizer.[118] GO is used as a carrier for the efficient loading and delivery of the photosensitizers to cancer cells. They synthesized a novel nanohybrid consisting of GO, a photosensitizer, and an aptamer. Thus, during the delivery process, SOG of the nanohybrid can be completely inhibited by the quenching capacity of the GO even though there is light present. When the nanohybrid enters into

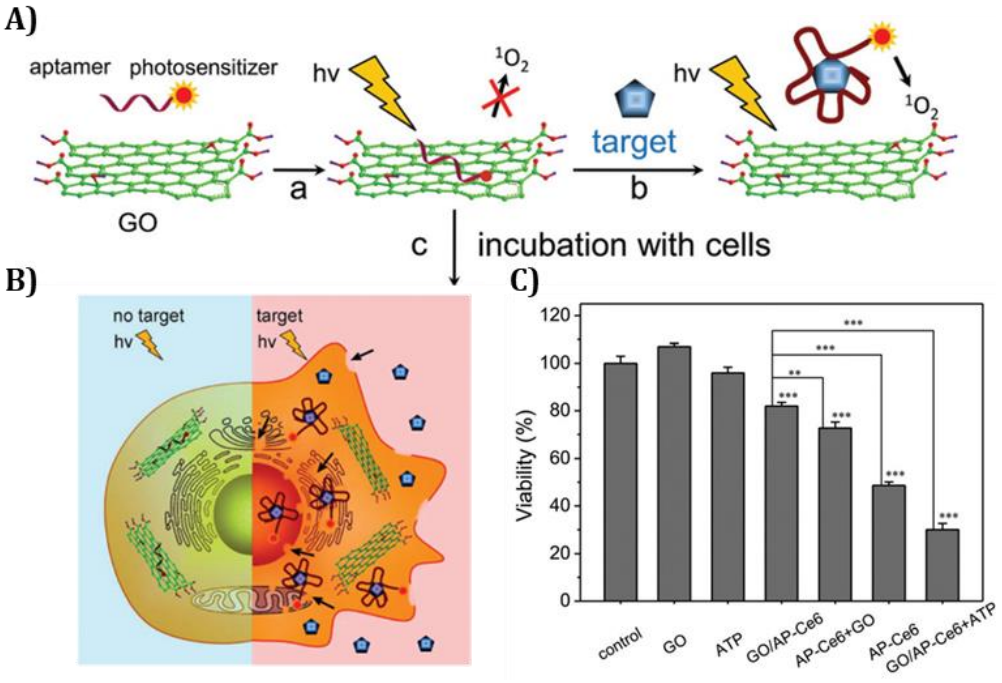

Figure 1.28. A) Schematic representation of the nanohybrid and B) regulation of SOG upon target binding in solution and in cells. C) The cellular viability of HepG2 cells treated with light (Adapted from reference 118).

cancer cells where target molecules are present, SOG is triggered by a target binding event, and singlet oxygen is reversibly released from the nanohybrid, ultimately inducing significant cell death in the presence of light (Figure 1.28).

Markovic and coworkers investigated the ability of gamma irradiation to enhance the photoluminescence properties of graphene quantum dots (GQDs).[119] They have used different doses of γ-irradiation on GQDs to examine the change in structural and optical properties and found that the photoluminescence quantum yield was increased six times. Results indicate that the structural changes caused by γ-irradiation have a direct impact on the irradiated samples compared to the nonirradiated material. As treated GQDs shows the ability to produce singlet oxygen and are photo-stable under

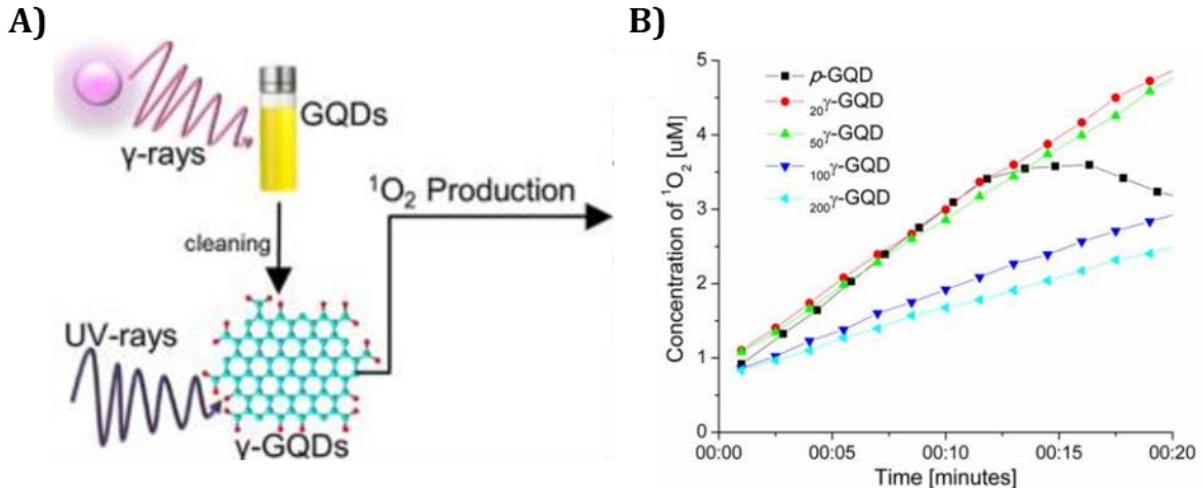

Figure 1.29. A) Schematic representation of γ-ray irradiation of **GQDs** and B) singlet oxygen formation (measured with TEMPO) as a function of UV illumination time for 20 min, in an ethanol solution containing GQDs, irradiated at various dose of γ-rays (Adapted from reference 119).

prolonged UV illumination, which make them promising candidates for photodynamic therapy (Figure 1.29).

IR-808 dye-sensitized upconversion nanoparticle (UCNP) with a Ce6 functionalized silica layer was developed by Yang and coworkers for efficient imaging-guided PDT applications.[120] The nanoparticles with optimal IR-808 sensitization and core-shell structure can efficiently transduce the 808 nm photons to super bright visible light. The APTES-modified Ce6 was covalently conjugated along with the growing process of mesoporous silica shell, and then the silica surface was modified with amino groups and coupled to MoS_2 nanosheets (Figure 1.30). The adopted drug loading

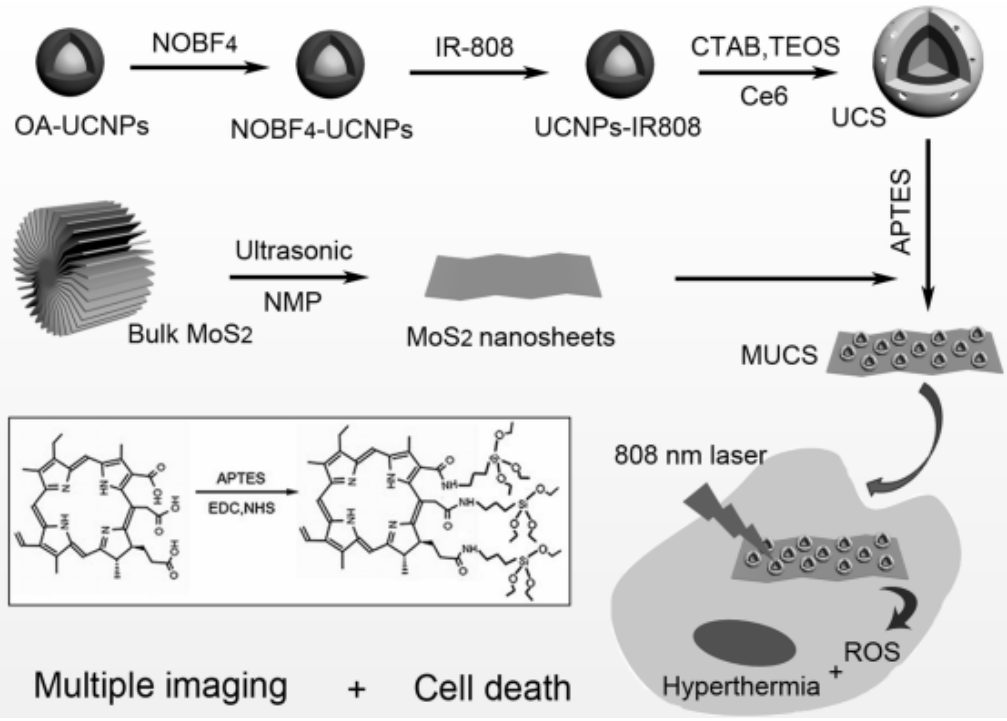

Figure 1.30. Schematic illustration for the synthesis of MUCS and the imaging-guided phototherapy (inset is the synthetic process of the APTES-modifed Ce6) (Adapted from reference 120).

process can ensure the high loading content, avoiding the undesired leakage, and decrease the distance between the energy donor and the acceptors. The experimental results confirm that the innovated nanostructure (MUCS) exhibit higher antitumor activity than those of single treatment mode.

Li Liu *et al*., recently developed an antitumor nanocomposite (PEG-MoS2–Au–Ce6), by adsorbing **Ce6** to the gold nanoparticle (AuNPs)-decorated molybdenum disulfide (PEG-MoS_2) nanosheets.[121] The NIR photosensitizer Ce6 was adsorbed onto the PEG-MoS_2–Au hybrids *via* π–π stacking and hydrophobic interactions, where Ce6 remained in its quenched state due to the surface plasmon resonance capacity of

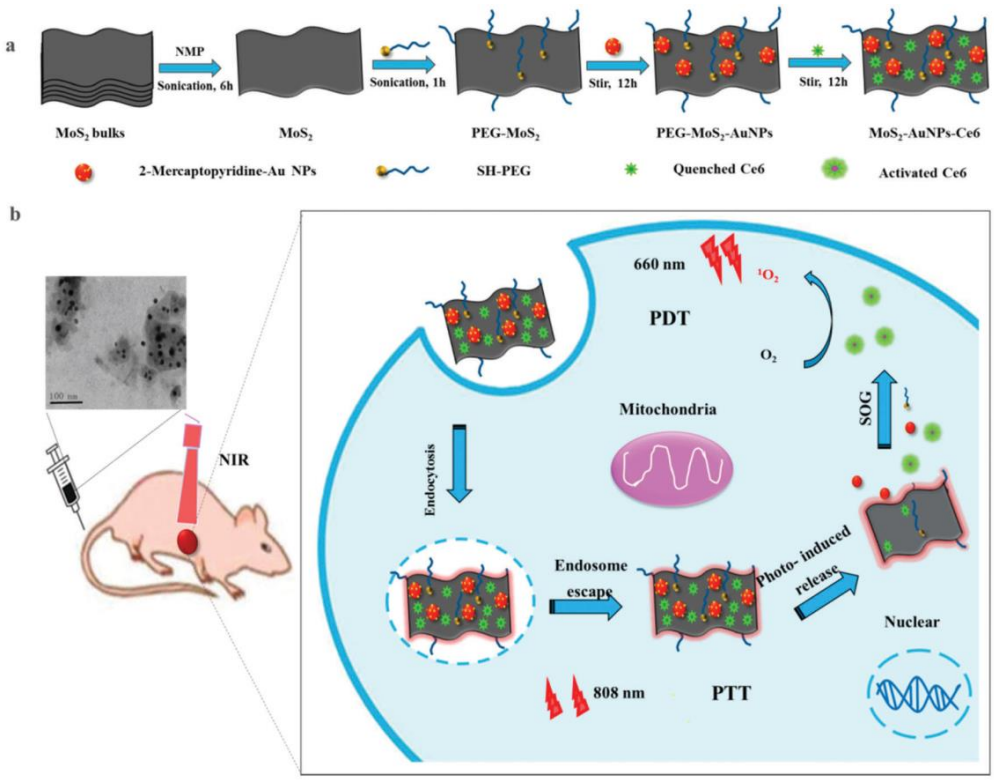

Figure 1.31. Schematic for the preparation procedure and working mechanism of **PEG-MoS_2–AuNPs–Ce6** nanocomposites (Adapted from reference 121).

AuNPs, as well as the coupling interaction with PEG-MoS_2 nanosheets. The drug, Ce6 was dequenched and boosted strong NIR fluorescence signals after being released from the surface of PEG-MoS2–Au hybrids upon heat generation, thus producing the PDT effect for anti-tumor therapy which is confirmed from *in vitro* and *in vivo* PDT analysis under 808 nm laser irradiation (Figure 1.31).

1.7. Objectives of the Present Investigation

Inspired by the recent progress in the design of nano-drug delivery systems based on biocompatible 2D layered nanomaterials and their conjugates, we have planned to explore the possibility of utilizing organic conjugates of Graphene/MoS_2 for sensing and therapeutic applications. It has been demonstrated that these 2D nanosheets present relatively high biocompatibility and low cytotoxicity and thus the biological effect and behaviour of these 2D nanosheets are also now under extensive exploration. The current thesis makes an effort in utilizing functionalized graphene analogues such as GO and rGO nanosheets, graphene oxide quantum dots (GQDs) and MoS_2 quantum dots (MQDs) for sensing and photodynamic therapy (PDT) applications.

Our first objective was to develop a biosensing platform based on GO/rGO by covalently grafting naphthalimide chromophore on the sides as well as basal planes. These stimuli responsive organic conjugates of graphene can be effectively utilized for biosensing applications. Further we planned to design a diiodo-BODIPY conjugate of graphene quantum dots for PDT applications. From the literature background, we envisaged that the diiodo-BODIPY core would improve the singlet oxygen generation

efficiency of the system and the GQDs part will act as a solubilizing as well as a better cellular internalization agent. In this way, an efficient PDT system can be achieved. The green fluorescing property of GQDs can be further explored for image guided PDT applications. Efficiency of PDT activity can be further improvised by using other nanocarriers which is better biocompatible than graphene materials. In this line, we have utilized the possibility of using MoS_2 quantum dots as a fluorescing nanocarrier for diiodo-BODIPY drug for enhanced PDT activity.

1.7. References

(1) Tan, C.; Cao, X.; Wu, X.-J.; He, Q.; Yang, J.; Zhang, X.; Chen, J.; Zhao, W.; Han, S.; Nam, G.-H.; Sindoro, M.; Zhang, H. *Chem. Rev.* **2017**, *117*, 6225.

(2) Chimene, D.; Alge, D. L.; Gaharwar, A. K. *Adv. Mater.* **2015**, *27*, 7261.

(3) Rao, C. N. R.; Matte, H. S. S. R.; Subrahmanyam, K. S. *Acc. Chem. Res.* **2013**, *46*, 149.

(4) Chung, C.; Kim, Y. K.; Shin, D.; Ryoo, S. R.; Hong, B. H.; Min, D. H. *Acc. Chem. Res.* **2013**, *46*, 2211.

(5) Rao, C. N.; Matte, H. S.; Subrahmanyam, K. S. *Acc. Chem. Res.* **2013**, *46*, 149.

(6) Geim, A. K.; Novoselov, K. S. *Nat. Mater.* **2007**, *6*, 183.

(7) Lee, C.; Wei, X.; Kysar, J. W.; Hone, J. *Science* **2008**, *321*, 385.

(8) Stankovich, S.; Dikin, D. A.; Dommett, G. H.; Kohlhaas, K. M.; Zimney, E. J.; Stach, E. A.; Piner, R. D.; Nguyen, S. T.; Ruoff, R. S. *Nature* **2006**, *442*, 282.

(9) Geim, A. K. *Science* **2009**, *324*, 1530.

(10) Georgakilas, V.; Tiwari, J. N.; Kemp, K. C.; Perman, J. A.; Bourlinos, A. B.; Kim, K. S.; Zboril, R. *Chem. Rev.* **2016**, *116*, 5464.

(11) Chen, D.; Feng, H.; Li, J. *Chem. Rev.* **2012**, *112*, 6027.

(12) Georgakilas, V.; Otyepka, M.; Bourlinos, A. B.; Chandra, V.; Kim, N.; Kemp, K. C.; Hobza, P.; Zboril, R.; Kim, K. S. *Chem. Rev.* **2012**, *112*, 6156.

(13) Lang, B. *Surf. Sci.* **1975**, *53*, 317.

(14) Li, D.; Muller, M. B.; Gilje, S.; Kaner, R. B.; Wallace, G. G. *Nat. Nanotechnol.* **2008**, *3*, 101.

(15) Coleman, J. N. *Acc. Chem. Res.* **2013**, *46*, 14.

(16) Barwich, S.; Khan, U.; Coleman, J. N. *J. Phys. Chem. C* **2013**, *117*, 19212.

(17) Brodie, B. C. *Phil. Trans. Roy. Soc. London B* **1859**, *149*, 249.

(18) Hummers, W. S.; Offeman, R. E. *J. Am. Chem. Soc.* **1958**, *80*, 1339.

(19) Chen, J.; Li, Y. R.; Huang, L.; Li, C.; Shi, G. Q. *Carbon* **2015**, *81*, 826.

(20) Marcano, D. C.; Kosynkin, D. V.; Berlin, J. M.; Sinitskii, A.; Sun, Z.; Slesarev, A.; Alemany, L. B.; Lu, W.; Tour, J. M. *ACS Nano* **2010**, *4*, 4806.

(21) Chua, C. K.; Pumera, M. *Chem. Soc. Rev.* **2014**, *43*, 291.

(22) Toh, S. Y.; Loh, K. S.; Kamarudin, S. K.; Daud, W. R. W. *Chem. Eng. J.* **2014**, *251*, 422.

(23) Gao, X.; Jang, J.; Nagase, S. *J. Phys. Chem. C* **2010**, *114*, 832.

(24) Akhavan, O.; Ghaderi, E. *J. Phys. Chem. C* **2009**, *113*, 20214.

(25) Mishra, N.; Boeckl, J.; Motta, N.; Iacopi, F. *physica status solidi (a)* **2016**, *213*, 2269.

(26) Muñoz, R.; Gómez-Aleixandre, C. *Chem. Vap. Deposition* **2013**, *19*, 297.

(27) Wang, X.-Y.; Narita, A.; Müllen, K. *Nat. Rev. Chem.* **2017**, *2*, 0100.

(28) Bacon, M.; Bradley, S. J.; Nann, T. *Part. Part. Syst Charact.* **2014**, *31*, 415.

(29) Changzheng, L.; Yanan, Y. *Nanotechnology* **2014**, *25*, 435703.

(30) Zhang, Z.; Zhang, J.; Chen, N.; Qu, L. *Energy Environ. Sci* **2012**, *5*, 8869.

(31) Yuen Yung, H.; Chia-Liang, C.; Huan-Cheng, C. *J. Phys. D: Appl. Phys.* **2010**, *43*, 374021.

(32) Depan, D.; Misra, R. D. K. *Nanoscale* **2012**, *4*, 6325.

(33) Sun, H.; Wu, L.; Wei, W.; Qu, X. *Mater. Today* **2013**, *16*, 433.

(34) Sun, Y.; Wang, S.; Li, C.; Luo, P.; Tao, L.; Wei, Y.; Shi, G. *PCCP* **2013**, *15*, 9907.

(35) Peng, J.; Gao, W.; Gupta, B. K.; Liu, Z.; Romero-Aburto, R.; Ge, L.; Song, L.; Alemany, L. B.; Zhan, X.; Gao, G.; Vithayathil, S. A.; Kaipparettu, B. A.; Marti, A. A.; Hayashi, T.; Zhu, J.-J.; Ajayan, P. M. *Nano Lett.* **2012**, *12*, 844.

(36) Chua, C. K.; Sofer, Z.; Šimek, P.; Jankovský, O.; Klímová, K.; Bakardjieva, S.; Hrdličková Kučková, Š.; Pumera, M. *ACS Nano* **2015**, *9*, 2548.

(37) Tang, L.; Ji, R.; Li, X.; Teng, K. S.; Lau, S. P. *Part. Part. Syst Charact.* **2013**, *30*, 523.

(38) Liu, R.; Wu, D.; Feng, X.; Müllen, K. *J. Am. Chem. Soc.* **2011**, *133*, 15221.

(39) Liu, Y.; Wang, R.; Lang, J.; Yan, X. *PCCP* **2015**, *17*, 14028.

(40) Shen, J.; Zhu, Y.; Yang, X.; Zong, J.; Zhang, J.; Li, C. *New J. Chem.* **2012**, *36*, 97.

(41) Liu, C. G.; Yu, Z. N.; Neff, D.; Zhamu, A.; Jang, B. Z. *Nano. Lett.* **2010**, *10*, 4863.

(42) Yoo, E.; Kim, J.; Hosono, E.; Zhou, H.; Kudo, T.; Honma, I. *Nano. Lett.* **2008**, *8*, 2277.

(43) Qu, L. T.; Liu, Y.; Baek, J. B.; Dai, L. M. *Acs Nano* **2010**, *4*, 1321.

(44) Bonaccorso, F.; Sun, Z.; Hasan, T.; Ferrari, A. C. *Nat. Photonics* **2010**, *4*, 611.

(45) Quintana, M.; Vazquez, E.; Prato, M. *Acc. Chem. Res.* **2013**, *46*, 138.

(46) Cho, Y.; Choi, Y. *Chem. Commun.* **2012**, *48*, 9912.

(47) Dreyer, D. R.; Park, S.; Bielawski, C. W.; Ruoff, R. S. *Chem. Soc. Rev.* **2010**, *39*, 228.

(48) Cheeveewattanagul, N.; Morales-Narváez, E.; Hassan, A. R. H. A.; Bergua, J. F.; Surareungchai, W.; Somasundrum, M.; Merkoçi, A. *Adv. Funct. Mater.* **2017**, *27*, 1702741.

(49) Liu, Y.; Zhou, J.; Zhang, X.; Liu, Z.; Wan, X.; Tian, J.; Wang, T.; Chen, Y. *Carbon* **2009**, *47*, 3113.

(50) Xu, Y.; Liu, Z.; Zhang, X.; Wang, Y.; Tian, J.; Huang, Y.; Ma, Y.; Zhang, X.; Chen, Y. *Adv. Mater.* **2009**, *21*, 1275.

(51) Georgakilas, V.; Bourlinos, A. B.; Zboril, R.; Steriotis, T. A.; Dallas, P.; Stubos, A. K.; Trapalis, C. *Chem. Commun.* **2010**, *46*, 1766.

(52) Bourlinos, A. B.; Georgakilas, V.; Zboril, R.; Steriotis, T. A.; Stubos, A. K. *Small* **2009**, *5*, 1841.

(53) Quintana, M.; Spyrou, K.; Grzelczak, M.; Browne, W. R.; Rudolf, P.; Prato, M. *Acs Nano* **2010**, *4*, 3527.

(54) Zhang, X.; Hou, L.; Cnossen, A.; Coleman, A. C.; Ivashenko, O.; Rudolf, P.; Wees, B. J. v.; Browne, W. R.; Feringa, B. L. *Chem. Eur. J* **2011**, *17*, 8957.

(55) Ragoussi, M. E.; Malig, J.; Katsukis, G.; Butz, B.; Spiecker, E.; Torre, G. d. l.; Torres, T.; Guldi, D. M. *Angew. Chem. Int. Ed.* **2012**, *51*, 6421.

(56) Georgakilas, V.; Otyepka, M.; Bourlinos, A. B.; Chandra, V.; Kim, N.; Kemp, K. C.; Hobza, P.; Zboril, R.; Kim, K. S. *Chem. Rev.* **2012**, *112*, 6156.

(57) Chhowalla, M.; Liu, Z.; Zhang, H. *Chem. Soc. Rev.* **2015**, *44*, 2584.

(58) Chen, X.; McDonald, A. R. *Adv. Mater.* **2016**, n/a.

(59) Song, I.; Park, C.; Choi, H. C. *RSC Adv.* **2015**, *5*, 7495.

(60) Mak, K. F.; Lee, C.; Hone, J.; Shan, J.; Heinz, T. F. *Phys. Rev. Lett.* **2010**, *105*, 136805.

(61) Voiry, D.; Goswami, A.; Kappera, R.; SilvaCecilia de Carvalho Castro, e.; Kaplan, D.; Fujita, T.; Chen, M.; Asefa, T.; Chhowalla, M. *Nat. Chem.* **2015**, *7*, 45.

(62) Li, X.; Zhu, H. *J. Materiomics* **2015**, *1*, 33.

(63) Magda, G. Z.; Pető, J.; Dobrik, G.; Hwang, C.; Biró, L. P.; Tapasztó, L. *Sci. Rep.* **2015**, *5*, 14714.

(64) Xiong, F.; Wang, H.; Liu, X.; Sun, J.; Brongersma, M.; Pop, E.; Cui, Y. *Nano Lett.* **2015**, *15*, 6777.

(65) Jawaid, A.; Nepal, D.; Park, K.; Jespersen, M.; Qualley, A.; Mirau, P.; Drummy, L. F.; Vaia, R. A. *Chem. Mater.* **2016**, *28*, 337.

(66) Wang, H.; Lu, Z.; Xu, S.; Kong, D.; Cha, J. J.; Zheng, G.; Hsu, P.-C.; Yan, K.; Bradshaw, D.; Prinz, F. B.; Cui, Y. *Proc. Natl. Acad. Sci. U.S.A.* **2013**, *110*, 19701.

(67) Zhang, X.; Lai, Z.; Tan, C.; Zhang, H. *Angew. Chem. Int. Ed.* **2016**, n/a.

(68) Jeon, J.; Jang, S. K.; Jeon, S. M.; Yoo, G.; Jang, Y. H.; Park, J.-H.; Lee, S. *Nanoscale* **2015**, *7*, 1688.

(69) Arul, N. S.; Nithya, V. D. *RSC Adv.* **2016**, *6*, 65670.

(70) Xu, S.; Li, D.; Wu, P. *Adv. Funct. Mater.* **2015**, *25*, 1127.

(71) Huang, H.; Du, C.; Shi, H.; Feng, X.; Li, J.; Tan, Y.; Song, W. *Part. Part. Syst Charact.* **2015**, *32*, 72.

(72) Chou, S. S.; De, M.; Kim, J.; Byun, S.; Dykstra, C.; Yu, J.; Huang, J.; Dravid, V. P. *J Am Chem Soc* **2013**, *135*, 4584.

(73) Kim, J.-S.; Yoo, H.-W.; Choi, H. O.; Jung, H.-T. *Nano Lett.* **2014**, *14*, 5941.

(74) Nguyen, E. P.; Carey, B. J.; Ou, J. Z.; van Embden, J.; Gaspera, E. D.; Chrimes, A. F.; Spencer, M. J. S.; Zhuiykov, S.; Kalantar-zadeh, K.; Daeneke, T. *Adv. Mater.* **2015**, *27*, 6225.

(75) Zeng, Z.; Yin, Z.; Huang, X.; Li, H.; He, Q.; Lu, G.; Boey, F.; Zhang, H. *Angew. Chem. Int. Ed.* **2011**, *50*, 11093.

(76) Hernandez, Y.; Nicolosi, V.; Lotya, M.; Blighe, F. M.; Sun, Z.; De, S.; McGovern, I. T.; Holland, B.; Byrne, M.; Gun'Ko, Y. K.; Boland, J. J.; Niraj, P.; Duesberg, G.; Krishnamurthy, S.; Goodhue, R.; Hutchison, J.; Scardaci, V.; Ferrari, A. C.; Coleman, J. N. *Nat. Nanotechnol.* **2008**, *3*, 563.

(77) Ferrari, A. C.; Meyer, J. C.; Scardaci, V.; Casiraghi, C.; Lazzeri, M.; Mauri, F.; Piscanec, S.; Jiang, D.; Novoselov, K. S.; Roth, S.; Geim, A. K. *Phys. Rev. Lett.* **2006**, *97*, 187401.

(78) Lee, C.; Yan, H.; Brus, L. E.; Heinz, T. F.; Hone, J.; Ryu, S. *ACS Nano* **2010**, *4*, 2695.

(79) Perumbilavil, S.; Sankar, P.; Thankamani, P. R.; Philip, R. *Appl. Phys. Lett.*, **2015**; Vol. 107.

(80) Chen, Y.; Tan, C.; Zhang, H.; Wang, L. *Chem. Soc. Rev.* **2015**, *44*, 2681.

(81) Pumera, M. *Mater. Today* **2011**, *14*, 308.

(82) Barua, S.; Dutta, H. S.; Gogoi, S.; Devi, R.; Khan, R. *ACS Appl. Nano Mater.* **2018**, *1*, 2.

(83) Zhang, Q. P.; Li, Q. L.; Xiang, S. D.; Wang, Y.; Wang, C. Y.; Jiang, W.; Zhou, H.; Yang, Y. W.; Tang, J. *Polymer* **2014**, *55*, 6044.

(84) Lu, C. H.; Yang, H. H.; Zhu, C. L.; Chen, X.; Chen, G. N. *Angew. Chem. Int. Ed.* **2009**, *48*, 4785.

(85) Balapanuru, J.; Yang, J. X.; Xiao, S.; Bao, Q.; Jahan, M.; Polavarapu, L.; Wei, J.; Xu, Q. H.; Loh, K. P. *Angew. Chem. Int. Ed.* **2010**, *49*, 6549.

(86) Koninti, R. K.; Sengupta, A.; Gavvala, K.; Ballav, N.; Hazra, P. *Nanoscale* **2014**, *6*, 2937.

(87) Zhu, C.; Zeng, Z.; Li, H.; Li, F.; Fan, C.; Zhang, H. *J. Am. Chem. Soc.* **2013**, *135*, 5998.

(88) Bergveld, P. *Biosensors* **1986**, *2*, 15.

(89) Liu, S.; Guo, X. *NPG Asia Mater.* **2012**, *4*, e23.

(90) Zhan, B.; Li, C.; Yang, J.; Jenkins, G.; Huang, W.; Dong, X. *Small* **2014**, *10*, 4042.

(91) Kim, D.-J.; Yung Sohn, I.; Jung, J.-H.; Yoon, O. J.; Lee, N.-E.; Park, J. S. *Biosens. Bioelectron.*, **2012**; Vol. 41.

(92) Sohn, I.-Y.; Kim, D.-J.; Jung, J.-H.; Yoon, O. J.; Nguyen Thanh, T.; Tran Quang, T.; Lee, N.-E. *Biosens. Bioelectron.* **2013**, *45*, 70.

(93) Cai, B.; Wang, S.; Huang, L.; Ning, Y.; Zhang, Z.; Zhang, G.-J. *ACS Nano* **2014**, *8*, 2632.

(94) Sarkar, D.; Liu, W.; Xie, X.; Anselmo, A. C.; Mitragotri, S.; Banerjee, K. *ACS Nano* **2014**, *8*, 3992.

(95) Kimmel, D. W.; LeBlanc, G.; Meschievitz, M. E.; Cliffel, D. E. *Anal. Chem. **2012**, 84, 685.*

(96) Pumera, M.; Ambrosi, A.; Bonanni, A.; Chng, E. L. K.; Poh, H. L. *TrAC, Trends Anal. Chem.* **2010**, *29*, 954.

(97) Liu, Y.; Yu, D.; Zeng, C.; Miao, Z.; Dai, L. *Langmuir* **2010**, *26*, 6158.

(98) Kang, X.; Wang, J.; Wu, H.; Aksay, I. A.; Liu, J.; Lin, Y. *Biosens. Bioelectron.* **2009**, *25*, 901.

(99) Bonanni, A.; Chua, C. K.; Zhao, G.; Sofer, Z.; Pumera, M. *ACS Nano* **2012**, *6*, 8546.

(100) Rohaizad, N.; Mayorga-Martinez, C. C.; Sofer, Z.; Pumera, M. *ACS Appl. Mater. Interfaces* **2017**, *9*, 40697.

(101) Dougherty, T. J.; Gomer, C. J.; Henderson, B. W.; Jori, G.; Kessel, D.; Korbelik, M.; Moan, J.; Peng, Q. *JNCI: J. Natl. Cancer Inst.* **1998**, *90*, 889.

(102) Henderson, B. W.; Dougherty, T. *J. Photochem. Photobiol.* **1992**, *55*, 145.

(103) Lucky, S. S.; Soo, K. C.; Zhang, Y. *Chem. Rev.* **2015**, *115*, 1990.

(104) Moan, J.; Peng, Q. *Anticancer Res.* **2003**, *23*, 3591.

(105) Dolmans, D. E. J. G. J.; Fukumura, D.; Jain, R. K. *Nat. Rev. Cancer* **2003**, *3*, 380.

(106) Maiya, B. G. *Resonance* **2000**, *5*, 6.

(107) Tegos, G.; Dai, T.; Fuchs, B.; Coleman, J.; Prates, R.; Astrakas, C.; St Denis, T.; Ribeiro, M.; Mylonakis, E.; Hamblin, M. *Front. Microbiol.* **2012**, *3*.

(108) Brown, S. B.; Brown, E. A.; Walker, I. *Lancet. Oncol.* **2004**, *5*, 497.

(109) DeRosa, M. C.; Crutchley, R. J. *Coordination Chemistry Reviews* **2002**, *233*, 351.

(110) Liu, J.; Cui, L.; Losic, D. *Acta Biomaterialia* **2013**, *9*, 9243.

(111) Quintana, M.; Vazquez, E.; Prato, M. *Acc. Chem. Res.* **2013**, *46*, 138.

(112) Rong, P. F.; Yang, K.; Srivastan, A.; Kiesewetter, D. O.; Yue, X. Y.; Wang, F.; Nie, L. M.; Bhirde, A.; Wang, Z.; Liu, Z.; Niu, G.; Wang, W.; Chen, X. Y. *Theranostics* **2014**, *4*, 229.

(113) Tian, B.; Wang, C.; Zhang, S.; Feng, L. Z.; Liu, Z. *Acs Nano* **2011**, *5*, 7000.

(114) Jiang, B. P.; Hu, L. F.; Wang, D. J.; Ji, S. C.; Shen, X. C.; Liang, H. *J. Mater. Chem. B* **2014**, *2*, 7141.

(115) Rong, P.; Yang, K.; Srivastan, A.; Kiesewetter, D. O.; Yue, X.; Wang, F.; Nie, L.; Bhirde, A.; Wang, Z.; Liu, Z.; Niu, G.; Wang, W.; Chen, X. *Theranostics* **2014**, *4*, 229.

(116) Li, F.; Park, S.; Ling, D.; Park, W.; Han, J. Y.; Na, K.; Char, K. *J. Mater. Chem. B* **2013**, *1*, 1678.

(117) Hu, Z.; Li, J.; Huang, Y.; Chen, L.; Li, Z. *RSC Advances* **2015**, *5*, 654.

(118) Yan, L.; Chang, Y.-N.; Yin, W.; Tian, G.; Zhou, L.; Liu, X.; Xing, G.; Zhao, L.; Gu, Z.; Zhao, Y. *Biomater. Sci* **2014**, *2*, 1412.

(119) Jovanović, S. P.; Syrgiannis, Z.; Marković, Z. M.; Bonasera, A.; Kepić, D. P.; Budimir, M. D.; Milivojević, D. D.; Spasojević, V. D.; Dramićanin, M. D.; Pavlović, V. B.; Todorović Marković, B. M. *ACS Appl. Mater. Interfaces* **2015**, *7*, 25865.

(120) Xu, J.; Gulzar, A.; Liu, Y.; Bi, H.; Gai, S.; Liu, B.; Yang, D.; He, F.; Yang, P. *Small* **2017**, *13*, 1701841.

(121) Liu, L.; Wang, J.; Tan, X.; Pang, X.; You, Q.; Sun, Q.; Tan, F.; Li, N. *J. Mater. Chem. B* **2017**, *5*, 2286.

Chapter 2

Design, Synthesis and Characterization of Graphene Oxide – Naphthalimide Hybrids for pH Sensing Applications

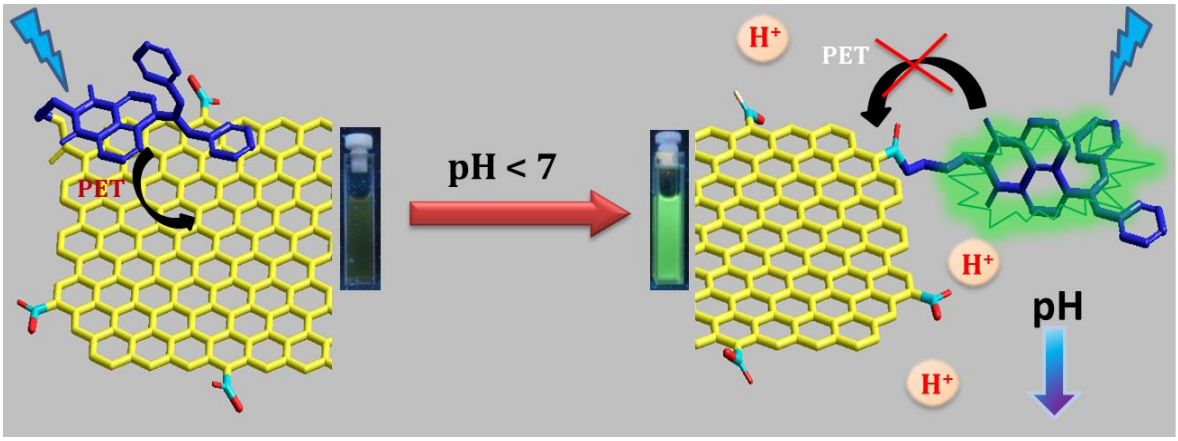

2.1. Abstract

Graphene and its chemically modified analogues are extensively used for various applications ranging from electronics to drug delivery due to their remarkable electronic, mechanical, optical, and chemical properties. Covalent and non-covalent functionalization of GO and rGO with various organic and biomolecules is a key requirement for tailoring the chemical and electronic properties of these nanomaterials for specific applications. Graphene oxide (GO) and reduced graphene oxide (rGO) - naphthalimide nanoconjugates with pH-responsive fluorescence emission are demonstrated in this chapter. These nanoconjugates were synthesized by covalently anchoring picolyl substituted naphthalimide derivatives on GO/rGO surface via EDC-NHS coupling strategy and characterized using AFM, TEM, FTIR, Raman, and TG analyses. These nanoconjugates exhibited a chromophore loading of ~5-7%, which is estimated using TG analysis. The

detailed photophysical characterization revealed strong quenching of fluorescence (>90%) of chromophore in nanoconjugates, which indicates the strong electronic interaction between GO/rGO and covalently attached chromophore. Synergistic effects of π-π interactions and efficient photoinduced electron and energy transfer processes are responsible for the strong quenching of fluorescence of these nanoconjugates, which gets perturbed at acidic pH conditions leading to significant enhancement of fluorescence emission. We have also demonstrated the utility of these nanoconjugates in reporting pH changes in real samples using two examples: i) salt hydrolysis of $FeCl_3$ and ii) enzymatic hydrolysis of acetylcholine, where both reactions reduce the pH of the medium which was efficiently reported by the nanoconjugate through a fluorescence 'turn on' response.

2.2. Introduction

Graphene, an increasingly important nanostructured material with exciting physical, chemical and optical properties, has attracted great interest in the fields of physics, chemistry, biology, medicine and their inter-disciplinary areas.[1-3] Graphene oxide (**GO**), an oxidized analogue of graphene is particularly useful for chemical and biological applications due to its enhanced solubility in aqueous media, colloidal stability and biocompatibility.[4] The presence of oxygen functionalities such as aldehyde, hydroxyl, epoxide, carboxylic group, etc on the edges and basal planes make **GO** a suitable candidate for facile chemical functionalization *via* various strategies.[5,6] Reduced graphene oxide (**rGO**), synthetically accessed through controlled reduction of **GO** is another useful graphene analogue that is intermediate between **GO** and pristine graphene in its physical and chemical properties.[7,8] Covalent and non-covalent

functionalization of **GO** and **rGO** with various organic and biomolecules is a key requirement for tailoring the chemical and electronic properties of these nanomaterials for specific applications.[9,10]

The complete absence of fluorescence in most of the chromophores interacting with the **GO** surface is attributed to the 'super quenching' ability of **GO** and its analogs due to the strong π-π interactions and efficient energy as well as electron transfer processes between the nanomaterial and fluorophores.[11,12] A key property of the fluorescence quenching by graphene is its strong distance dependence, which has been exploited by many research groups in building fluorescence-based sensors.[13] Design of stimuli-responsive fluorescence 'turn on' probes on graphene surface is a challenging task, which requires a stimulus which can perturb the strong interaction between the fluorophore and graphene. Comparing non-covalent and covalent approaches of surface modifications, the possibility of non-specific binding is low in covalently linked systems, and hence sensor probes covalently attached to graphene are more desirable. Although there are many reports on graphene-chromophore covalent derivatives which exhibit better electronic and optical properties,[14,15] very few reports are available on stimuli-responsive fluorescence enhancement of covalently linked fluorophores on graphene surface without detaching the probes to the bulk of the solution.[16-18]

Graphene and its conjugates have been used in the design of pH-responsive probes *via* different strategies.[19-21] For example, Palermo and co-workers reported a pH-sensitive terthiophene-grafted **GO**-nanohybrid, which exhibits reversible pH-dependent emission properties (Figure 2.1).[18] They have covalently attached dye on

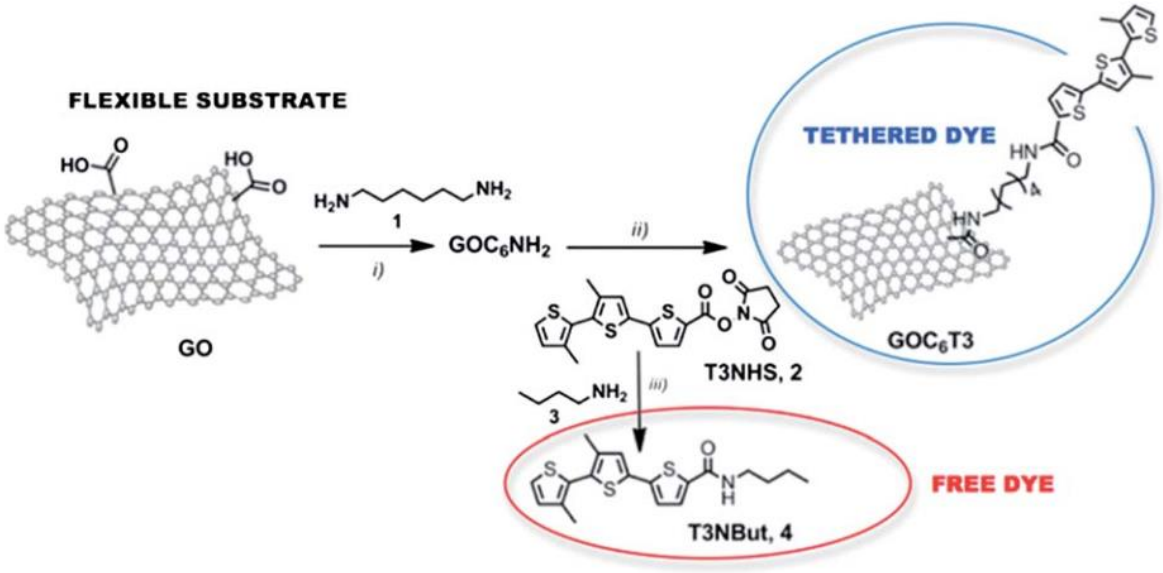

Figure 2.1. Schematic representation of pH responsive terthiophene-grafted **GO**-nanohybrid (Adapted from reference 18).

graphene oxide surface through amide coupling which does not perturb the absorption and emission properties of the dye. They could achieve ~5 % loading of dye on the **GO** by the reported procedure. This method makes **GO** sheets photoluminescent and senstive to pH switching, obtaining the same properties of the free dye.

Another approach towards the development of an efficient colorimetric pH sensor is based on pH-responsive polymer modified quantum dots, integrated on graphene oxide *via* non-covalent interactions, which respond to a wide range of pH changes.[22] Here **GO** provide an excellent signal-to-noise ratio and high dispersion stability in water. The distances between the two color-emitting QDs and the **GO** were controlled independently *via* two linkers of pH-responsive PAA and P2VP, resulting in colorimetric responses over a wide range of pH values (Figure 2.2).

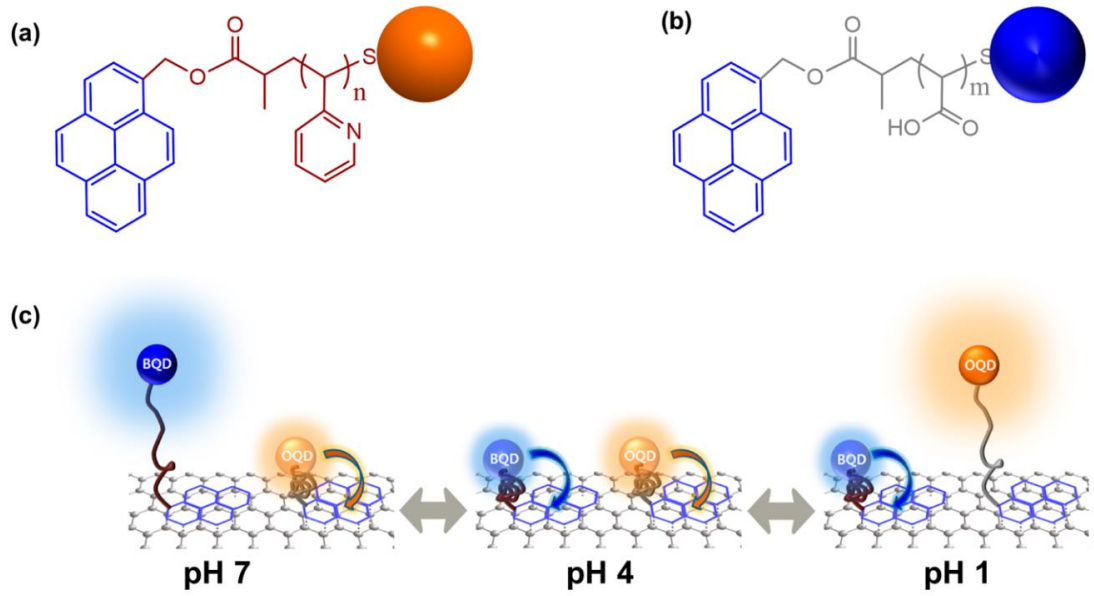

Figure 2.2. pH-responsive polymer modified quantum dots (Adapted from reference 22).

More recently, Kim *et al.,* reported the pH-sensitive enhancement of inherent fluorescence in phenoxy-dextran modified **GO** where they demonstrate the optical detection of enzymatic activity of acetylcholinesterase (AChE) based on its fluorescence 'turn on' response upon protonation.[23] **GO** was non-covalently functionalized with phenoxy-modified dextran (PhO-dex-GO) through hydrophobic interaction; the resulting hybrid showed excellent colloidal stability and intense fluorescence in various aqueous solutions as compared to pristine **GO**. The fluorescence of PhO-dex-GO remarkably increased as AChE catalyzed the hydrolysis of acetylthiocholine (ATCh) to give thiocholine and acetic acid (Figure 2.3). The nanoconjugate was able to report kinetic and thermodynamic parameters involving a maximum velocity, a Michaelis constant, and an inhibition dissociation constant for AChE activity and inhibition.

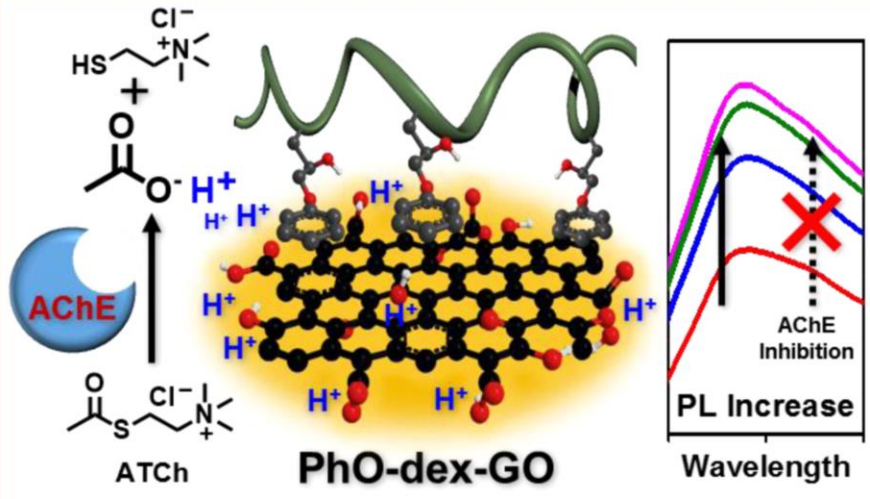

Figure 2.3. Schematic illustration for the detection of acetylcholinesterase (AChE) activity and inhibitors through the fluorescence response of phenoxy dextran-functionalized **GO** (PhO-dex-GO) (Adapted from reference 22).

In the present work, we demonstrate a new strategy for the design of pH-responsive fluorescence 'turn on' sensors using a picolylamine substituted naphthalimide derivative (**NI**) covalently attached to **GO** and **rGO** surfaces (**GO-NI** and **rGO-NI**, respectively; Figure 2.4) *via* two different coupling strategies. These nanoconjugates exhibited negligible fluorescence emission consequent to the synergistic quenching effects of the π-π interaction with **GO** surface and intrinsic PET-based quenching pathways in the naphthalimide chromophore. At lower pH conditions, both **GO** and the naphthalimide chromophores get protonated which perturb both the strong π-π interactions between **GO** and the chromophore, and the PET quenching pathways within the chromophore leading to significant enhancement in the emission. This strategy has been successfully demonstrated both in **GO-NI** and **rGO-NI** nanoconjugates, with the former showing a greater extent of fluorescence enhancement at lower pH conditions. Further, we have shown the utility of the **GO-NI** nanoconjugate

in reporting the pH changes of aqueous solutions using the dissolution of $FeCl_3$ as a representative example, where significant selectivity towards Fe^{3+} could be achieved. The pH-responsive fluorescence 'turn on' strategy was further exploited for the detection of acetylcholine (**ACh**) in the neurophysiological range by the enzymatic reaction with acetylcholine esterase (**AChE**), which convert **ACh** to choline and acetic acid[24,25] resulting in the reduction of the pH of the aqueous solution.

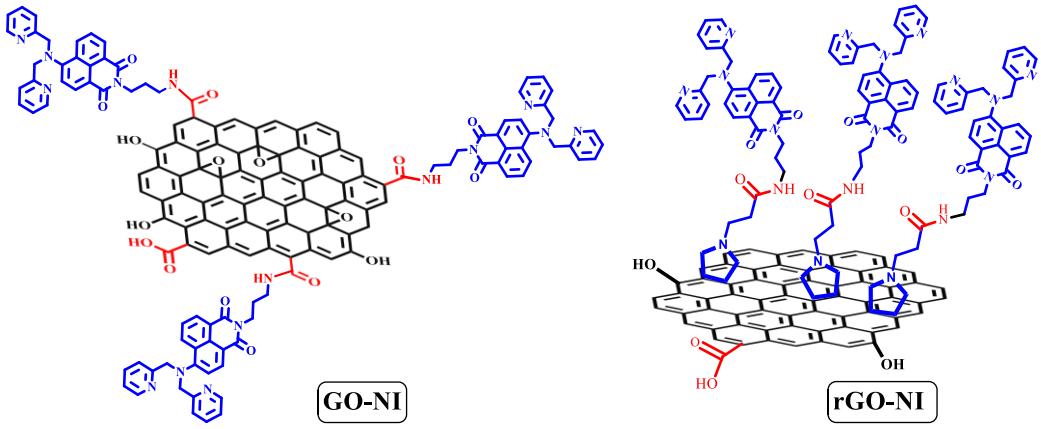

Figure 2.4. Schematic representation of **GO-NI** and **rGO-NI.**

2.3. Results and Discussion

2.3.1. Synthesis and characterization of GO

Synthesis of graphene oxide from graphite was carried out according to a modified Hummers' method. The graphene layers are packed in a 3-dimensional manner in graphite and oxidation introduces functional groups such as carboxylic acid (-COOH), carbonyl (>C=O), hydroxyl (-C-OH) and epoxide (-C-O-C-) in the graphite layers. The hydroxyl and epoxide groups tend to be concentrated more on either side of

its basal plane, while carboxyl groups are located mostly at the edges.[26,27] The oxidized graphite oxide is dispersed in water and subjected to exfoliation to **GO** layers by sonication for 20-30 minutes. The presence of hydrophilic groups and the negatively charged surface of the graphene oxide, due to the presence of carboxylate anions, contribute to the stability of the colloidal solutions of **GO** in water.[28] Figure 2.5 shows the absorption spectrum and image of graphene oxide suspension in water which is found to be stable for several weeks.

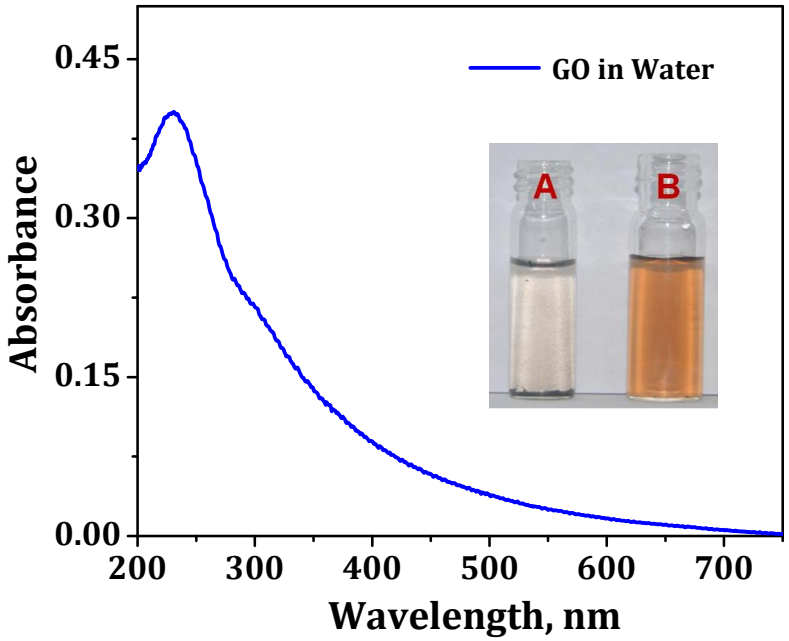

Figure 2.5. The absorption spectrum of exfoliated graphene oxide (**GO**) sheets in water. Inset shows the photographs of graphite oxide before (A) and after (B) exfoliation in water.

GO nano-sheets have been characterized by AFM, TEM, FT-IR and TG analyses. AFM is one of the most direct methods to quantify the degree of exfoliation level of a graphene sheet. A representative AFM image of as-prepared **GO** sheets in tapping mode and the corresponding height profiles are shown in Figure 2.6, which was obtained by coating **GO** on a freshly cleaved mica surface using 0.1 mg/mL aqueous solution of **GO**.

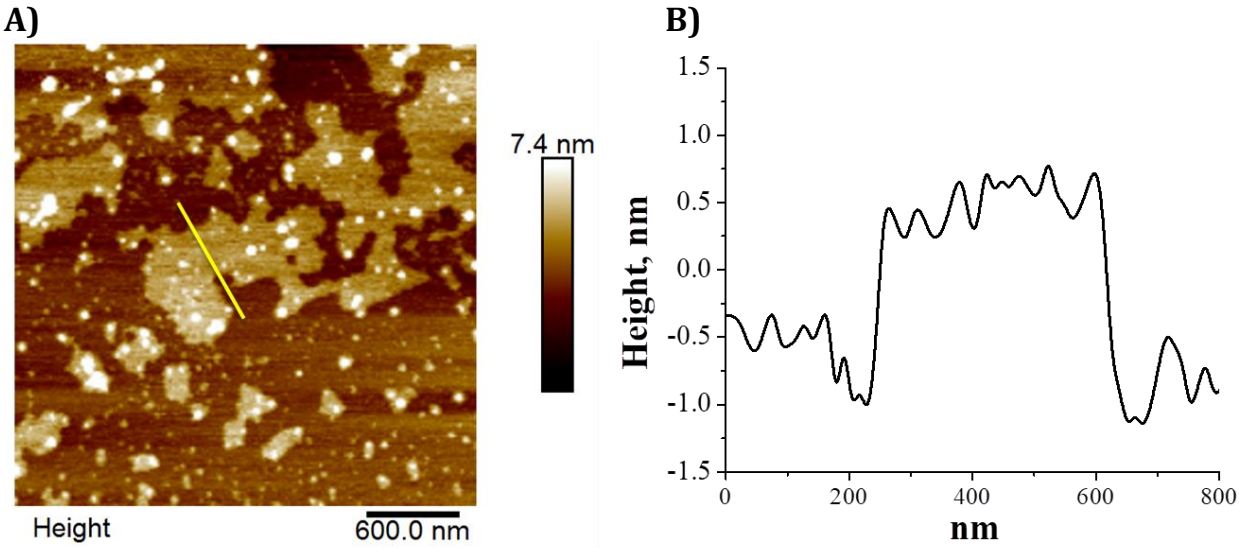

Figure 2.6. A) Tapping mode AFM image and B) the corresponding height profile of as-prepared **GO** nano-sheets. The images were obtained by coating **GO** on a freshly cleaved mica surface using 0.1 $mgmL^{-1}$ aqueous solution of **GO**.

The thickness of various **GO** nano-sheets range between 1 nm and 2 nm, which shows that the exfoliation of graphite oxide down to one or two layers **GO** sheets was achieved under the current synthetic conditions.

TEM image of **GO** obtained by depositing as-prepared **GO** nano-sheets (0.1 mg/mL) on a TEM copper grid is presented in Figure 2.7. Mostly monolayer sheets appear in TEM images, the size of which varies from few nanometers to micrometers. The tendency of the edges to curl and the existence of several folded regions are indicative of the single/bi-layer nature of the deposited graphene oxide sheets. Selected area electron diffraction (SAED) of the few-layer regions of these graphene sheets yielded spot patterns indicating the presence of crystalline order and is consistent with hexagonal lattice, matching those expected for individual graphene-based sheets.

Moreover, the sheet-like structures observed in TEM images are transparent indicating that we have successfully synthesized single/bi-layer nano-sheets of **GO**.

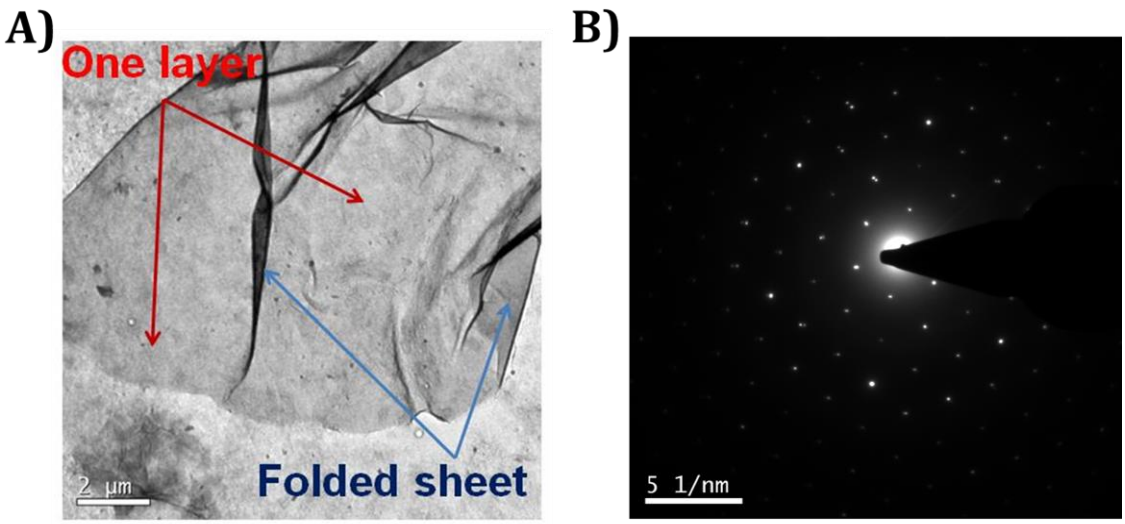

Figure 2.7. A) TEM image of as-prepared **GO** sheets obtained by drop-casting a 0.1 mg/mL water solution of **GO** on a Cu grid; B) SAED pattern of the same sample.

The FT-IR spectrum of **GO** showed characteristic vibrations corresponding to carboxylic acid and hydroxyl groups (Figure 2.8A) which further confirmed the successful oxidation of graphite. For example, peak around 1690 cm^{-1} indicates the presence of carbonyl (>C=O) group and the broad peak around 3200 cm^{-1} is due to O-H stretching arising from carboxyl and hydroxyl functionalities. Peaks around 1600 cm^{-1} and 1200 cm^{-1} corresponds to skeletal vibrations from unoxidized graphitic domains and C-OH stretching vibrations, respectively.

Results of thermogravimetric analysis (TGA) of **GO** is presented in Figure 2.8B which shows weight loss of sample as a function of temperature. The sample is heated from room temperature to 900 ˚C at a heating rate of 5 ˚C/ min under argon atmosphere. Initial weight loss around 100 ˚C is due to the presence of adsorbed water

in the sample. The mass loss (~20%) from 200 ˚C to 220 ˚C was caused by pyrolysis of oxygen containing functional groups. The major weight loss from 500 ˚C onwards is due to the burning of graphitic C atoms.

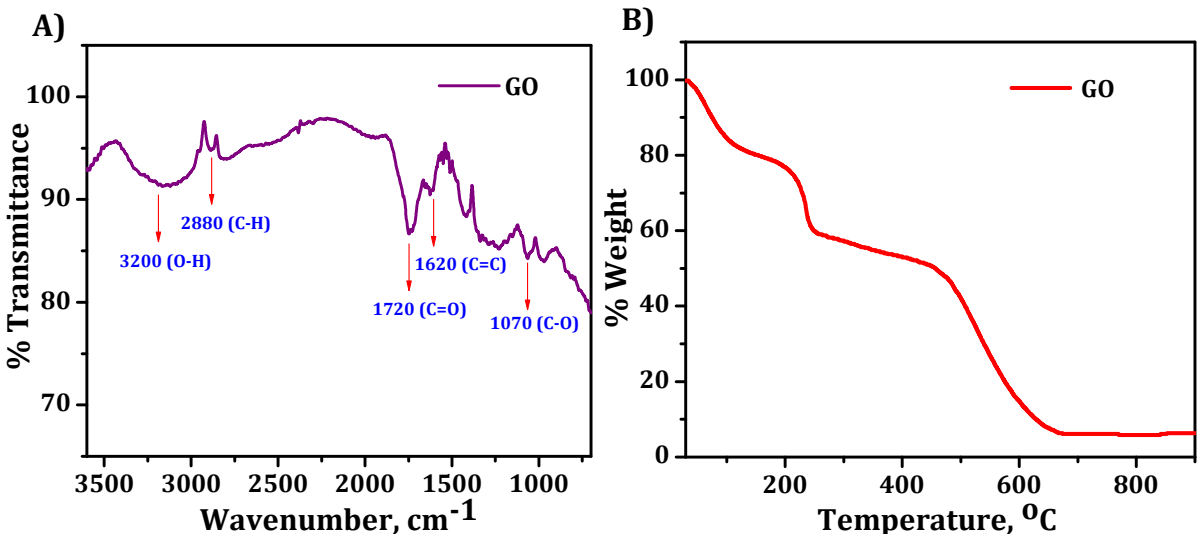

Figure 2.8. A) FT-IR spectrum and B) TGA curve of as-prepared **GO**.

2.3.2. Synthesis and characterization of rGO-COOH

GO is reduced to give reduced graphene oxide, **rGO** by refluxing at 100 °C with hydrazine hydrate, which partly restores the structure and properties of graphene**.** The solubility of **GO** in water is lowered after reduction. However, the resulting **rGO** is highly soluble in polar organic solvents like DMF, DMSO etc. We have synthesized an *N*-carboxylic acid modified alanine and coupled to **rGO** *via* 1, 3-dipolar cycloaddition along with formaldehyde (Scheme 2.1). This reaction introduces pyrrolidine rings on the surface of graphene with end carboxyl functionality (**rGO-COOH**).[29,30] The free carboxylic acid groups allow further functionalization of **rGO** with chromophores having a terminal amine *via* EDC mediated amide coupling. As-synthesized **rGO-COOH**

forms a stable suspension in water where **rGO** showed negligible dispersion even after sonication for hours. The enhanced solubility of **rGO-COOH** compared to **rGO** is attributed to the carboxyl functional groups which help in dispersing in aqueous medium.

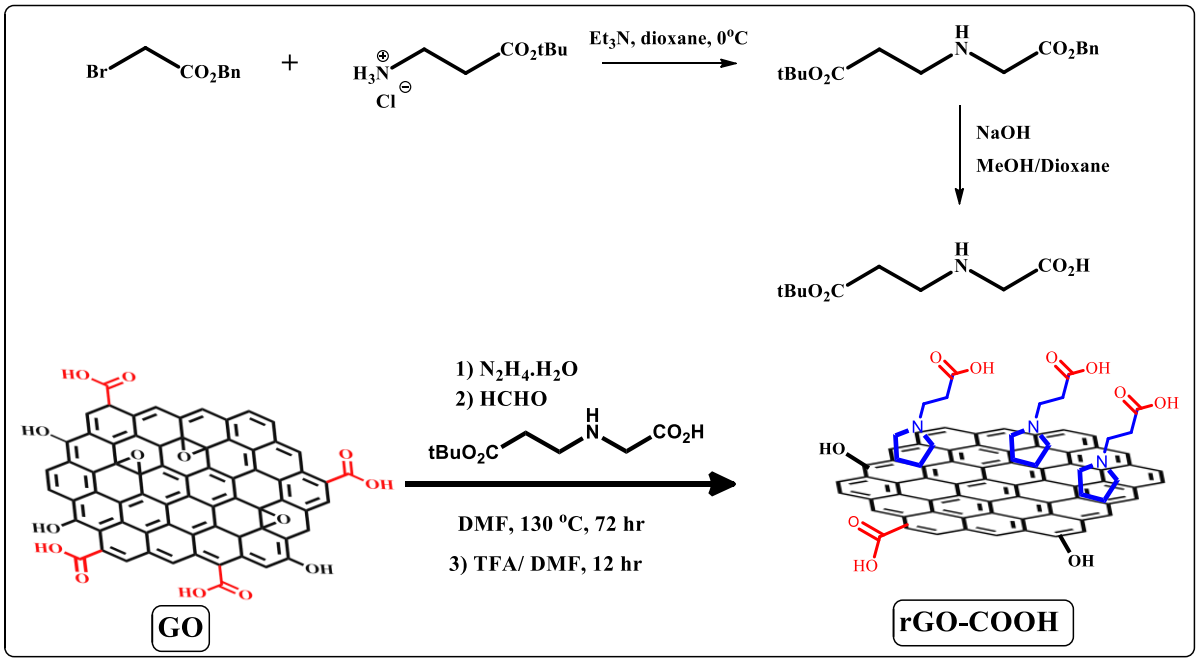

Scheme 2.1. Synthesis strategy adopted for **rGO-COOH**

2.3.3. Synthesis of naphthalimide derivative, NI

The synthesis of naphthalimide derivative, **NI** is carried out as per Scheme 2.2. The synthesis started from the bromo derivative **1**, which upon reaction with *N*,*N*-bis(2-picolyl)amine in 2-methoxyethanol under reflux conditions gave the corresponding bis(2-picolyl)amine derivative, **2** in moderate yield. The amino moiety was introduced by coupling *tert*-butyl (3-aminopropyl)carbamate with **2** and subsequent deprotection of the Boc- protecting group as per standard protocols. **NI** was characterized using ^{1}H NMR and mass analysis and used for further reaction with **GO/rGO-COOH**.

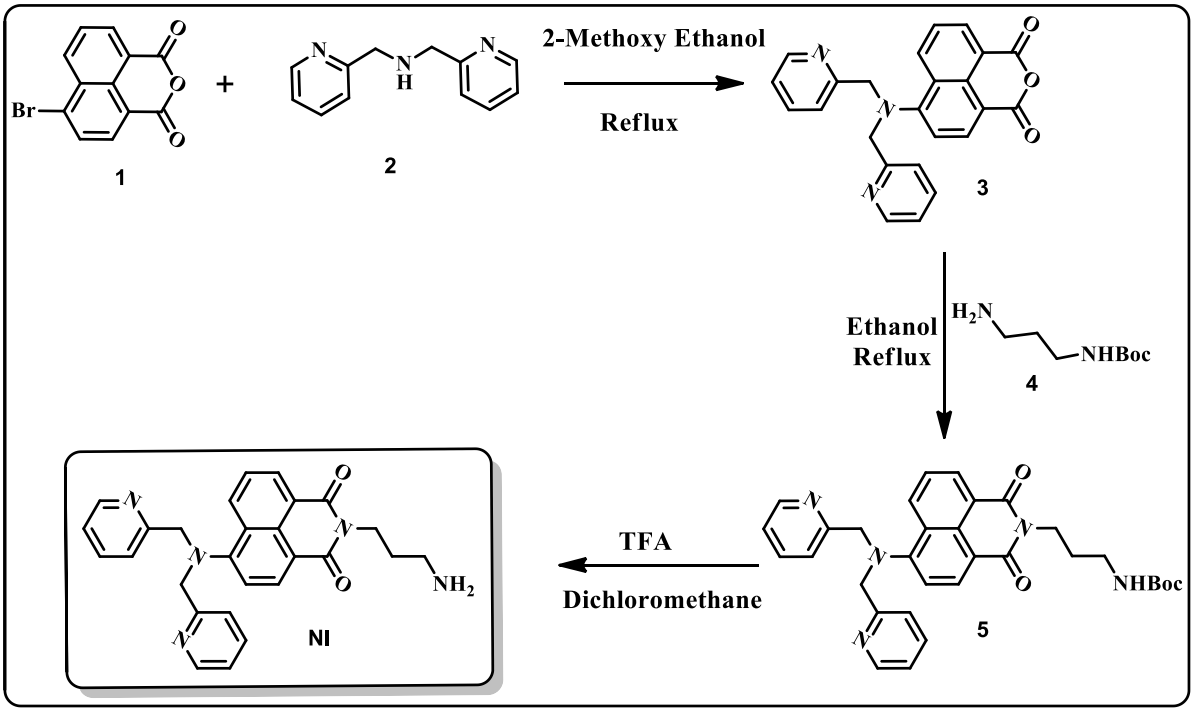

Scheme 2.2. Synthesis of **NI**.

2.3.4. Synthesis of GO-NI and rGO-NI

The 1,8-naphthalimide based fluorophore with a picolyl moiety at the fourth position (**NI**) was introduced to **GO** and **rGO** *via* two different synthetic strategies as shown in Scheme 2.3. In the first approach, **GO** was directly functionalized with **NI** chromophore *via* EDC-NHS coupling with carboxylic acid present on the few-layer **GO** nanosheets. Modification of **rGO** was achieved *via* the introduction of carboxylic acid groups in the basal planes through 1,3-dipolar cycloaddition reaction with a Boc-protected α-amino acid and formaldehyde followed by EDC-NHS coupling with **NI**.[29,30] Both **GO-NI** and **rGO-NI** form stable suspensions in water and in common organic solvents such as acetonitrile, DMF, and DMSO. These nanoconjugates were well

characterized using various spectroscopic and microscopic techniques, and their structural and photophysical properties were investigated in detail.

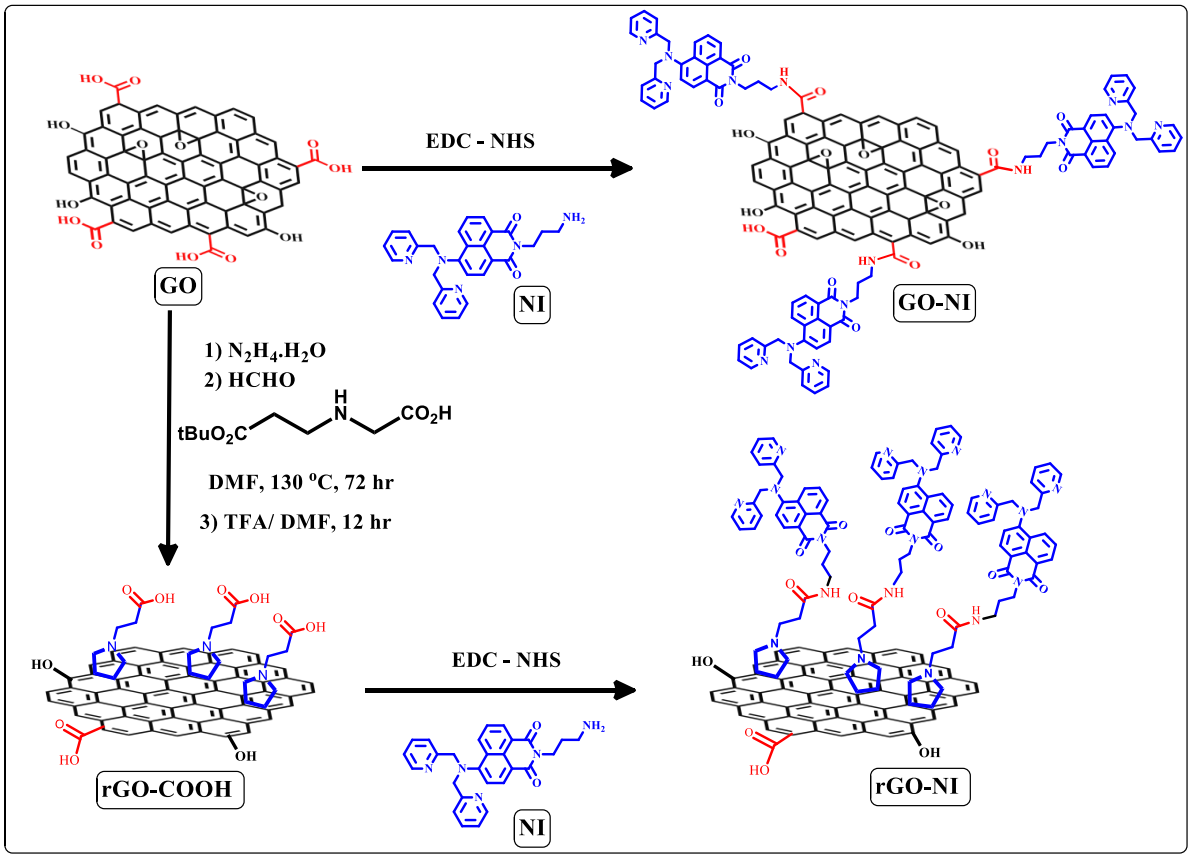

Scheme 2.3. Schematic representation of synthesis of **GO-NI** and **rGO-NI**

2.3.5. Material Characterization of Nanoconjugates

The colloidal stability of the samples decrease in the order **GO** (several months) > **GO-NI** (few weeks) > **rGO-NI** (few days) which directly correlates with the availability of free carboxylic acid groups and other oxygen functionalities on the surface and with the measured zeta potential values of -48 mV, -34 mV, -35 mV and -26 mV, respectively for **GO**, **GO-NI, rGO-COOH** and **rGO-NI** (Figure **2.9**). **rGO** on other hand could not be suspended in water for zeta-potential measurements. The observed decrease in the

surface potential values of nanoconjugates is a clear indication of the successful coupling of **NI** with the carboxylic acid groups present on the **GO**/**rGO** surface.

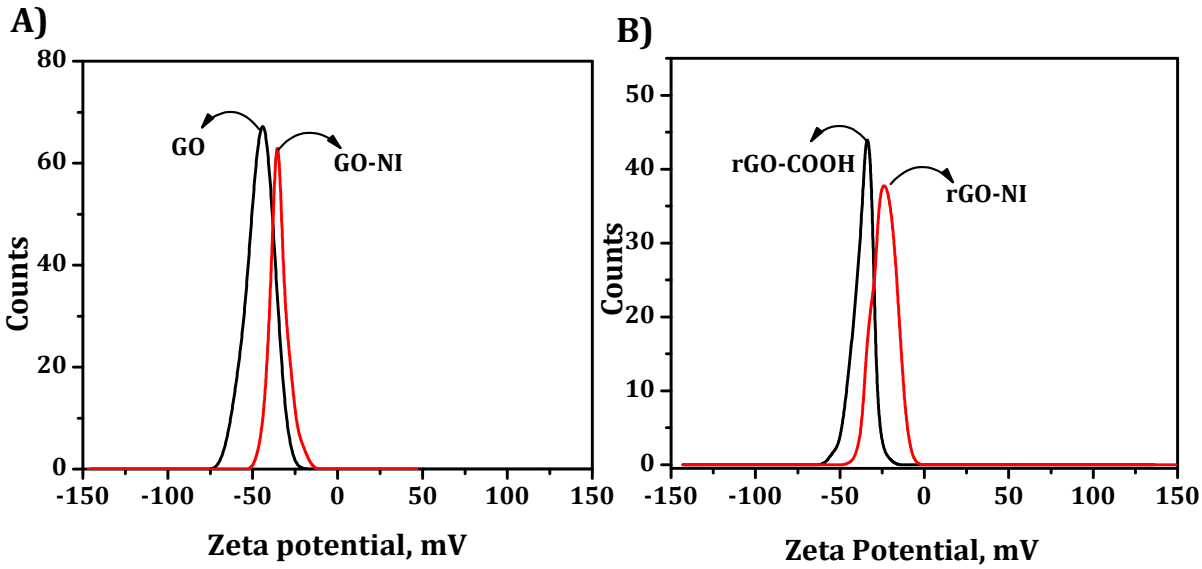

Figure 2.9. A) Zeta potential measurements of **GO** and **GO-NI**; B) **rGO-COOH** and **rGO-NI**

Spectroscopic evidence for the efficient covalent coupling was obtained from the FT-IR measurements which shows additional peaks for **GO-NI** and **rGO-NI** corresponding to the **NI** chromophore along with a change in the carbonyl stretching frequency from 1740 cm^{-1} in **GO** to ~1640 cm^{-1} in the nanoconjugates (Figure 2.10A). Similarly, FT-IR spectrum of **rGO-NI** shows peaks corresponding to **NI** with an amide carbonyl stretching frequency at 1650 cm^{-1} (Figure 2.10B).

Additional proof for covalent functionalization of **GO** with **NI** chromophores was obtained from Raman spectroscopy as shown in Figure 2.11. Typically, the ratio of the intensities of D and G bands (I_D/I_G) provides an idea of the extent of oxidation in the graphene samples.[31] **GO** showed D band at 1340 cm^{-1} and G band at 1590 cm^{-1} with an I_D/I_G ratio of 1.15. The G band of **GO-NI** was observed at the same wavenumber region

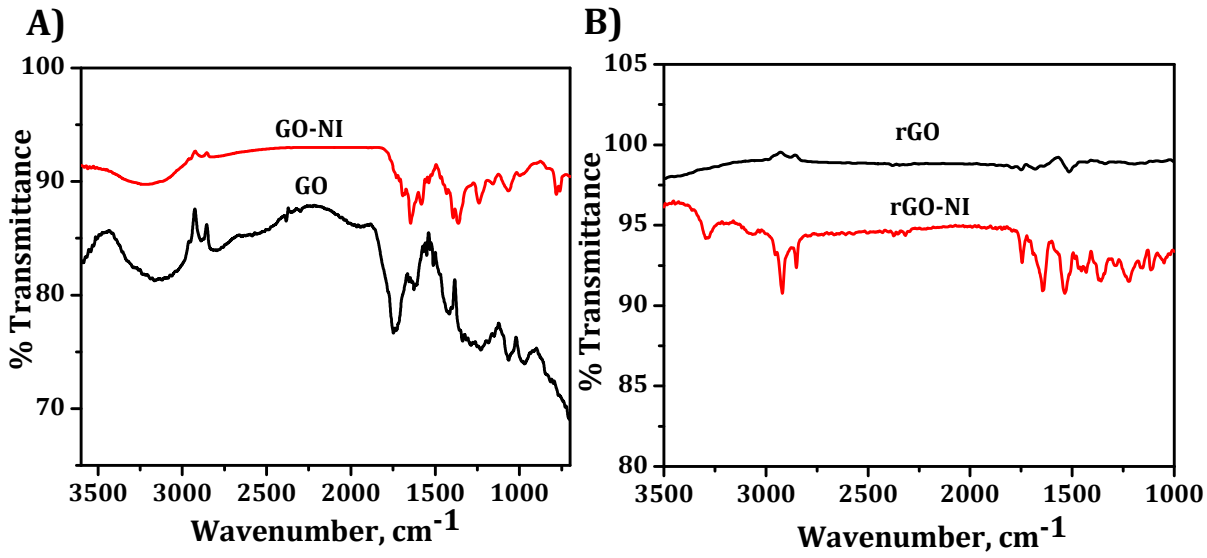

Figure 2.10. A) FT-IR spectra of **GO** and **GO-NI** and B) FT-IR spectra of **rGO** and **rGO-NI.**

while the D band was shifted to 1330 cm^{-1}. This redshift (~10 cm^{-1}) is in accordance with a slight increase in the number of sp^3 carbon atoms in the sample as a result of functionalization with **NI** chromophores. In addition, **GO-NI** showed a slightly larger

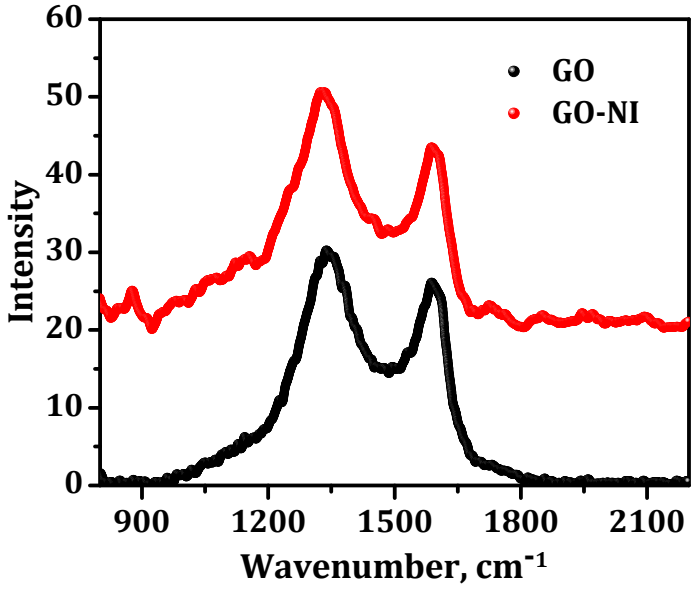

Figure 2.11. Raman spectra of **GO** and **GO-NI**

I_D/I_G ratio of 1.28 due to the increased distortions on **GO** surface by covalent functionalization with **NI** chromophores.[32,33]

The approximate **NI** chromophore loading in these nanoconjugates after the coupling reactions were estimated using thermogravimetric analysis (TGA) and the values were found to be 6.2 wt% for **GO-NI** and 5.6 wt% for **rGO-NI**. For example, a comparison of TG curves for **GO** and **GO-NI** showed a difference of ~7.5% in the weight loss after 200 ˚C corresponding to the loss of functional groups such as carboxylic acid groups (Figure 2.12). Further, an enhanced weight loss is observed for **GO-NI** in the 250-400 °C regions which can be attributed to the degradation of the coupled **NI** chromophores.

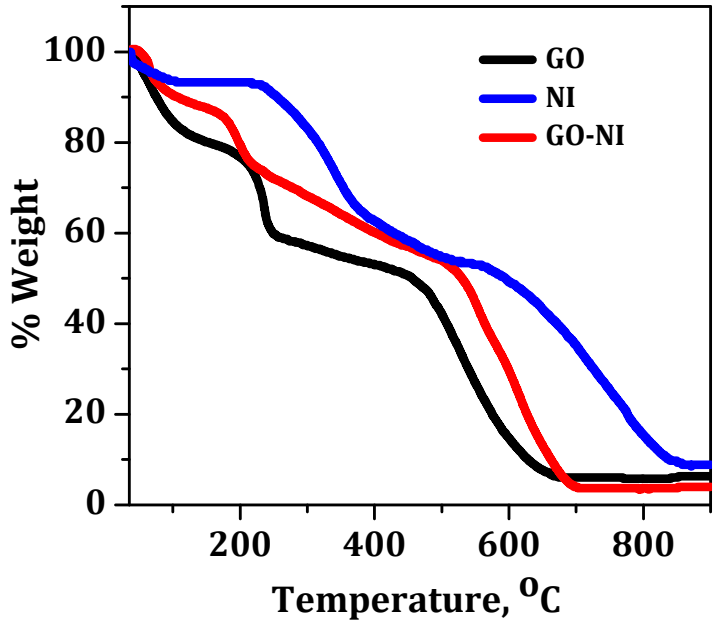

Figure 2.12. TG analysis of **GO, NI** and **GO-NI**.

GO and nanoconjugates have been characterized by AFM and it is one of the most direct methods to quantify the degree of exfoliation level of a graphene sheet. A representative AFM image of as-prepared **GO** and **GO-NI** sheets in tapping mode and the corresponding height profiles are shown in Figure 2.13. The thickness of various **GO** nanosheets range from 1 nm to 2 nm, indicating the exfoliation of graphite oxide down to one or two layer **GO** sheets under the current synthetic conditions. **GO-NI** exhibited few micrometer lateral size with a thickness of 2-3 nm indicating the formation of few layer nanosheets.

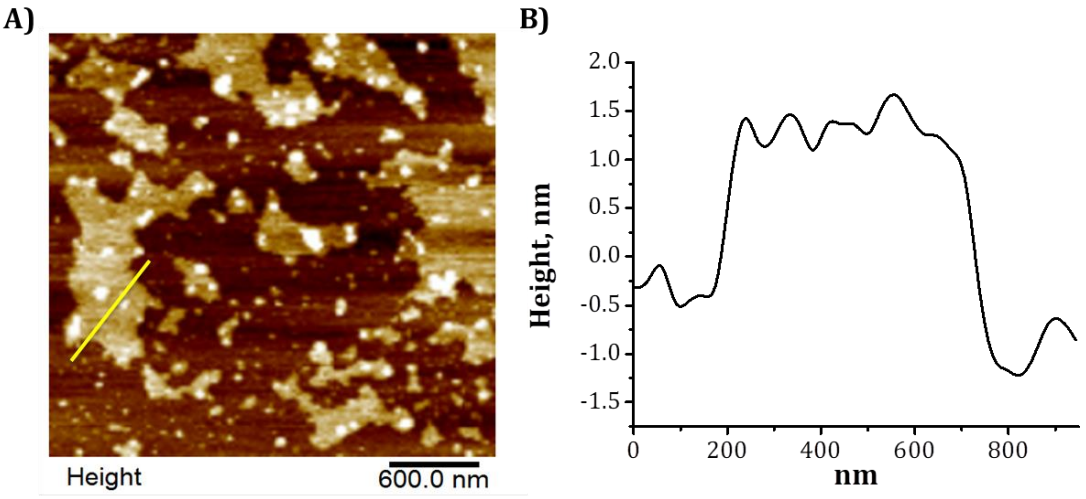

Figure 2.13. A) Tapping mode AFM image and B) the corresponding height profile of **GO-NI** nanosheets.

TEM image of samples obtained by depositing as-prepared nanosheets (0.1 mg/mL) on a TEM copper grid is shown in Figure 2.14. HR-TEM images and corresponding selected area electron diffraction (SAED) patterns (Figure 2.14B) confirmed the nanosheet structure and hexagonal honeycomb lattice features characteristic to chemically modified graphene derivatives. The nanoconjugates, **GO-NI**

and **rGO-NI** also showed similar sheet-like structures indicating the intact nature of the graphene sheets even after coupling reactions with **NI**.

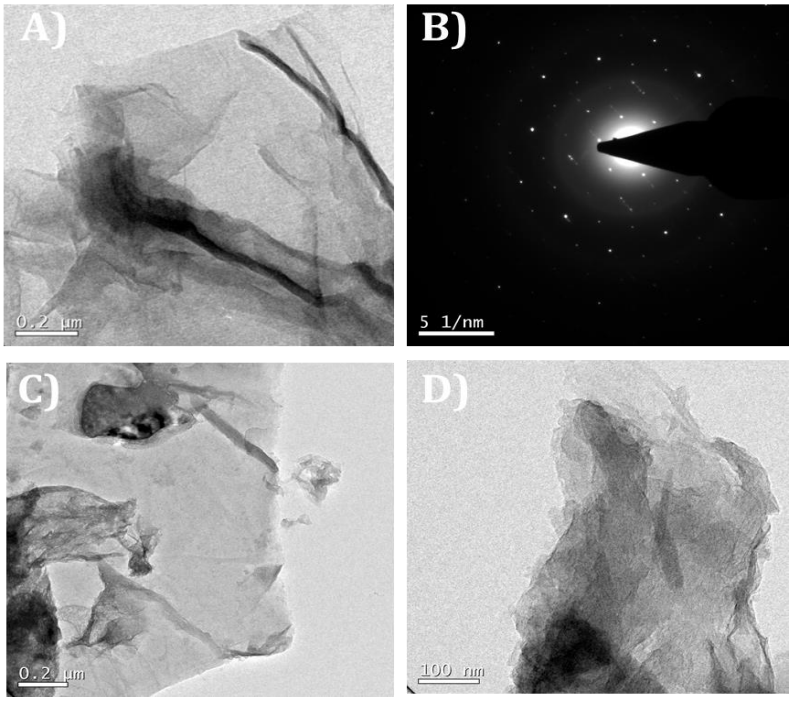

Figure 2.14. TEM images of A) **GO-NI,** and B) corresponding SAED pattern, C) **rGO-COOH** and D) **rGO-NI** nano-sheets.

2.3.6. Photophysical Characterization of Nanoconjugates

The UV-visible absorption spectra of aqueous dispersions of as-synthesized **GO** showed characteristic features of few-layered **GO** nanosheets with an absorption maximum around 230 nm and a broad tail-end absorption extending up to 600 nm (Figure 2.15).[34] The nanoconjugate **GO-NI** exhibited absorption features of both **GO** and **NI** chromophore with shoulder peak maxima around 433 nm and 258 nm. The absorption maximum around 433 nm corresponding to **NI** chromophore showed a redshift of 8 nm compared to the absorption maximum of **NI** chromophore alone (425 nm), which could be due to a possible ground state interaction between **GO** and **NI**

chromophore in the nanoconjugate. UV-visible spectroscopic analysis after a control experiment with **GO** and **NI** in the absence of the coupling reagents, under otherwise similar synthetic and subsequent washing conditions, did not show typical **NI** absorption bands.

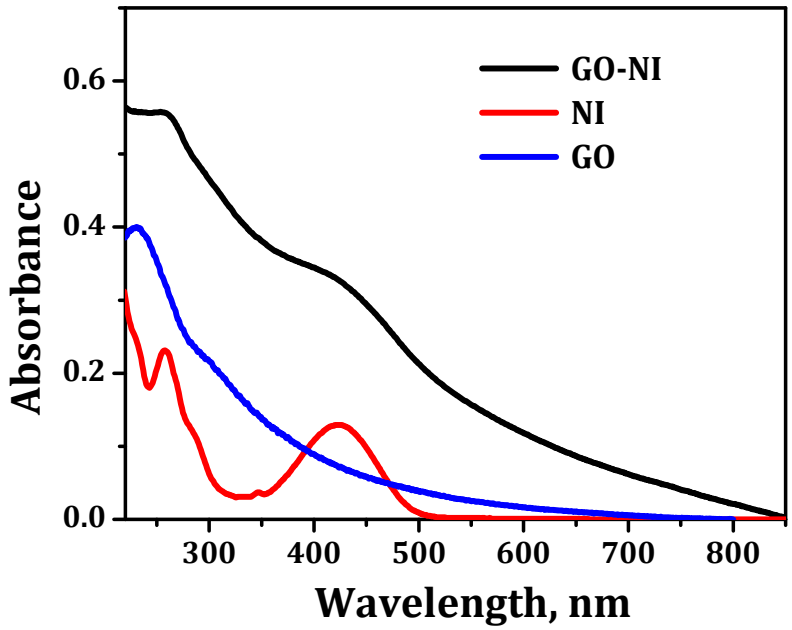

Figure 2.15. Absorption spectra of **GO**, **NI** and **GO-NI**.

The naphthalimide derivative, **NI** showed a fluorescence emission spectrum in the 450 nm - 700 nm range with a maximum around 540 nm and a fluorescence quantum yield of 7.1% in water (Figure 2.16A).[35] On the other hand, fluorescence spectrum of an optically matching solution of the nanoconjugate **GO-NI** revealed a highly quenched emission (quantum yield of 0.42%) corresponding to the **NI** chromophore. A similar, but less pronounced fluorescence quenching compared to **NI** chromophore was observed in the case of **rGO-NI** nanoconjugate (Figure 2.16B).

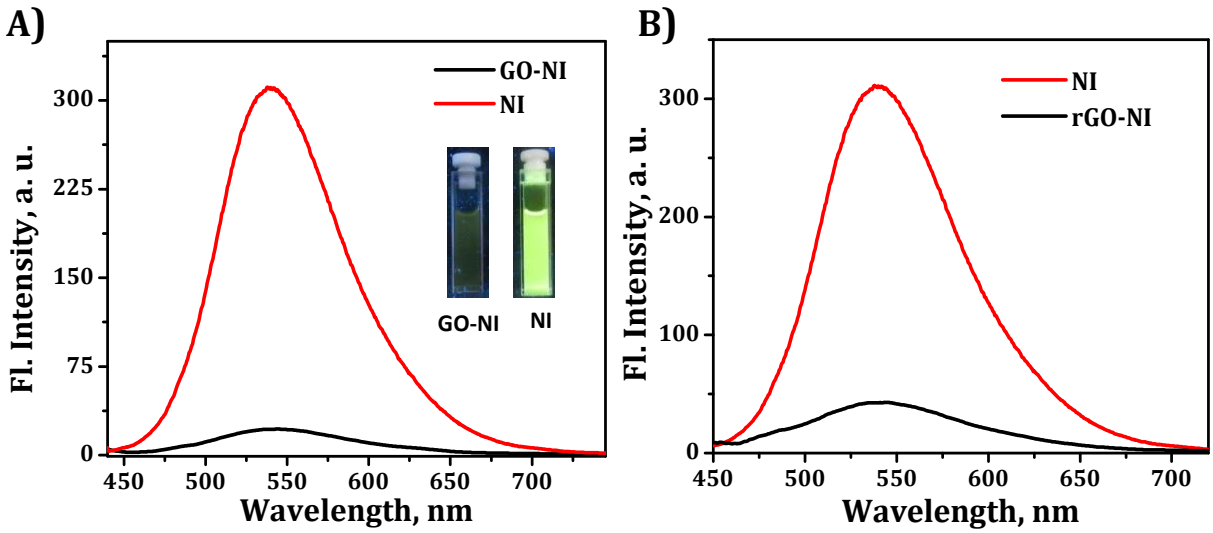

Figure 2.16. Emission spectra of optically matching aqueous solutions of A) **NI** and **GO-NI** and B) **NI** and **rGO-NI** (Excitation wavelength, λ_{exc}, 420 nm).

The **NI** chromophore in aqueous solutions showed a bi-exponential decay with an average fluorescence lifetime of 3.4 ns, whereas the nanoconjugates, **GO-NI** and **rGO-NI** showed multi-exponential decays with significantly reduced fluorescence lifetimes (Figure 2.17; Table 1). The strong quenching of **NI** chromophore fluorescence in **GO-NI** and **rGO-NI** could be attributed to the possible energy and electron transfer processes facilitated by the strong π-π interaction between **GO** and the chromophores.[36,37]

Table 1. Fluorescence lifetimes of **NI**, **GO-NI** and **rGO-NI**.

Sample	T1(ns)	T2(ns)	T3(ns)
NI	5.64 (51%)	1.77 (49%)	-
GO-NI	4.74 (44%)	1.30 (39%)	0.16 (17%)
rGO-NI	5.42 (45%)	1.67 (49%)	0.12 (5%)

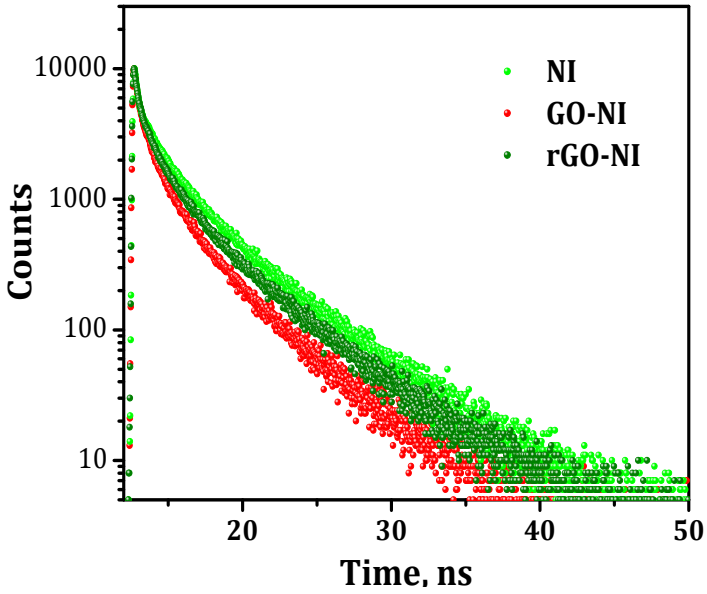

Figure 2.17. Fluorescence lifetime spectra of **NI**, **GO-NI** and **rGO-NI**

The intermolecular interactions between **GO** and **NI** chromophores were probed by titrating **GO** against the **NI** chromophore in aqueous solutions at pH 7. The absorption spectra showed signatures of ground state interactions between **GO** and **NI** (Figure 2. 18A). The corresponding emission spectra showed >90% quenching of the fluorescence of **NI** chromophore upon addition of 30 µg/mL of **GO** (Figure 2.18B).

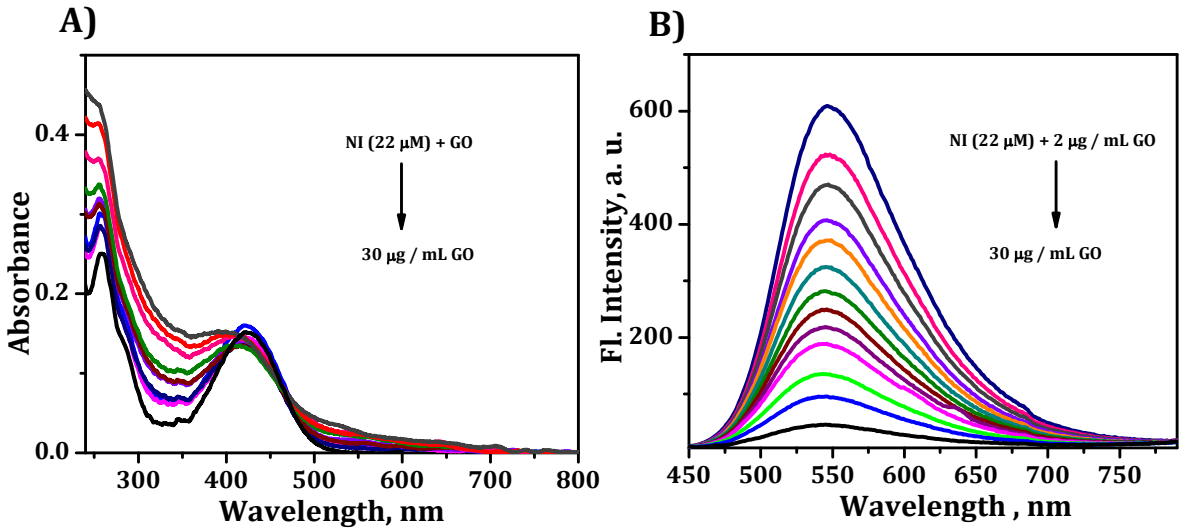

Figure 2.18. Absorption and emission spectra of titration of **NI** with **GO.**

The corresponding Stern-Volmer plot shows an upward curvature indicating the involvement of both dynamic and static quenching pathways (Figure 2.19). The corresponding absorption spectra also showed signatures of ground state interactions between **GO** and the **NI** chromophore (Figure 2.18A).

This observation was further confirmed by the fluorescence lifetime quenching experiments which showed a gradual decrease of the fluorescence lifetime corresponding to dynamic quenching with an increase in the amplitude of the short-lived component representing the static quenching in the **GO-NI** chromophore complex (Figure 2.20; Table 2).

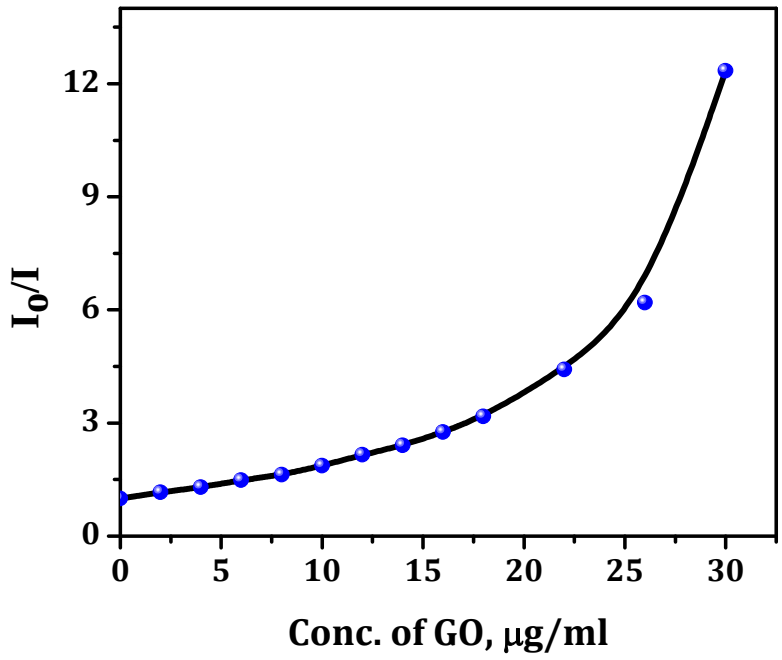

Figure 2.19. Fluorescence quenching efficiency of **GO** on **NI** at pH 7 (Stern-Volmer plot).

Table 2. Fluorescence lifetime changes of **NI** with various addition of **GO** (Excited at 401 nm).

Sample	T1(ns)	T2(ns)	T3(ns)
NI	5.64 (51%)	1.77 (49%)	-
NI + 10 µg/mL **GO**	5.34 (45%)	1.74 (46%)	0.24 (9%)
NI + 20 µg/mL **GO**	5.31 (43%)	1.72 (44%)	0.28 (13%)
NI + 30 µg/mL **GO**	5.27 (42%)	1.70 (43%)	0.26 (15%)

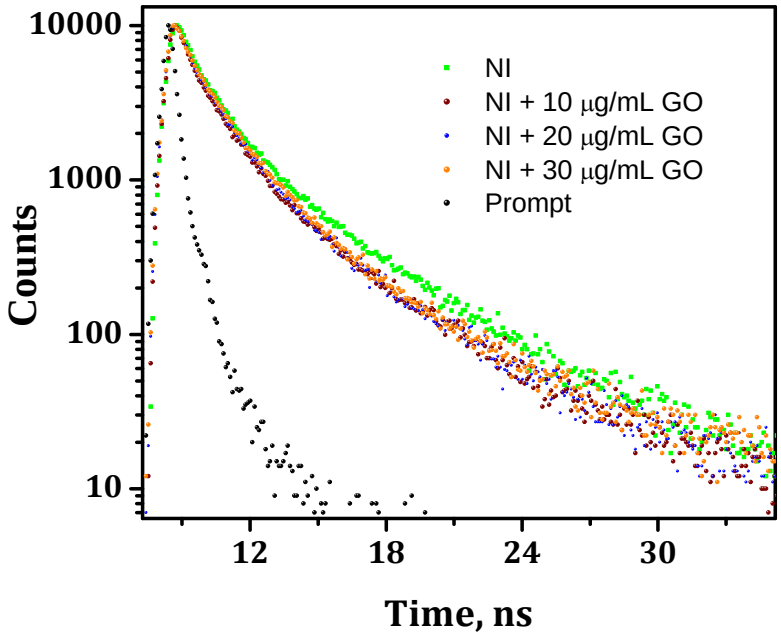

Figure 2.20. Fluorescence lifetime changes of **NI** with various concentration of **GO** up to 30 µg/mL.

2.3.7. pH dependent fluorescence enhancement

The fluorescence spectra of as synthesized nanoconjugates were found to be highly sensitive towards the changes in the pH of the aqueous solution, as shown in the pH dependent fluorescence emission spectra of **GO-NI** and **rGO-NI** (Figure 2.21). For example, the fluorescence intensity corresponding to the **NI** chromophore of **GO-NI**

doubles upon decreasing the pH of the aqueous solution from 7 to 6 and upon further decreasing the pH to 2, a ~7.3 times fluorescence enhancement was observed. Similar observations were made in the case of **rGO-NI** where a ~5 fold enhancement in fluorescence intensity was observed upon decreasing pH from 7 to 2. The observed pH dependent enhancement in fluorescence emission in these nanoconjugates could be explained as follows.

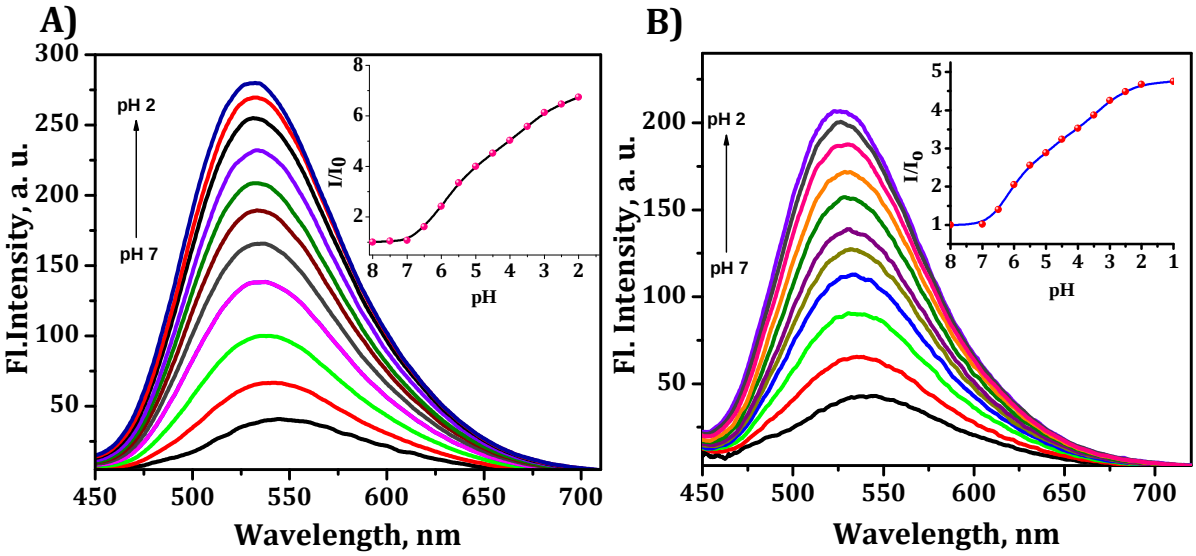

Figure 2.21. Change in fluorescence of A) **GO-NI** and B) **rGO-NI** with change in pH from 7 to 2. The inset shows a corresponding change in fluorescence intensity (I/I_o) with pH.

At lower pH conditions, the N-atoms in the **NI** chromophore and all the oxygen-containing functional groups on the **GO** surface gets protonated, which perturb the strong interaction between **GO** and the **NI** chromophore. In addition, protonation of N-atoms render the **NI** chromophores more hydrophilic and solvated in aqueous media, facilitating the dynamic dislocation of the chromophores from the **GO** surface. Both these effects contribute to the observed enhancement in the fluorescence emission. The lower extent of interaction between **GO** and the protonated **NI** chromophores at pH 2

was confirmed *via* titration experiments using **GO** and **NI** which showed a lesser extent of fluorescence quenching (~29%) upon addition of 30 μg/mL of **GO**, with no indication of ground state complex formation in the corresponding absorption spectra (Figure 2.22).

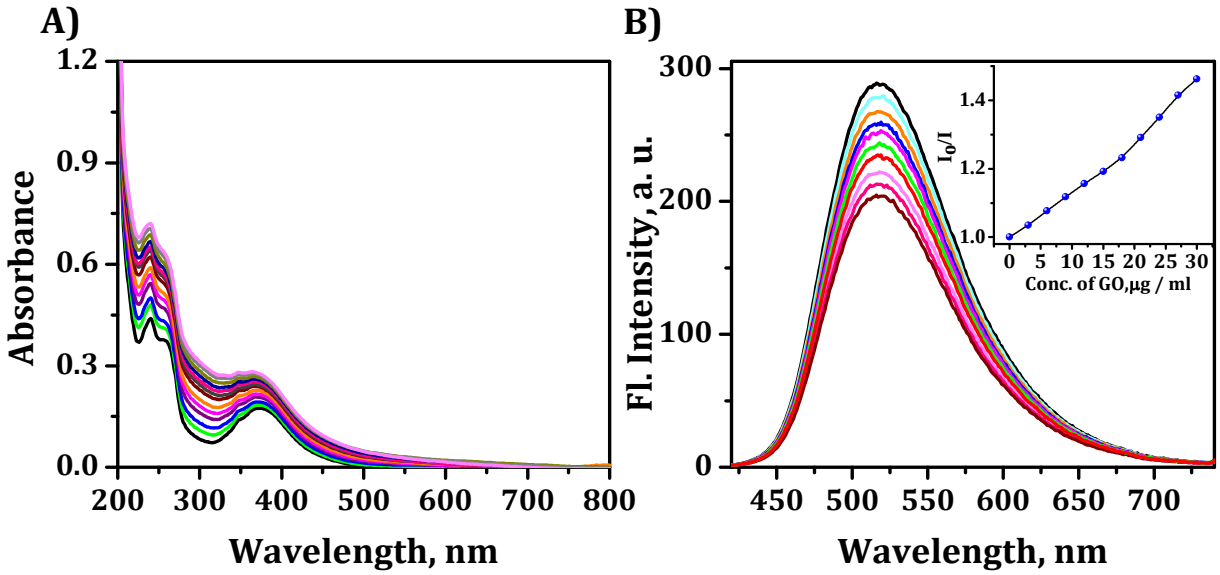

Figure 2.22. A) Absorption and B) fluorescence spectra of aqueous solutions of **NI** (22 μM) upon addition of increasing **GO** concentration, up to of 30 μg/mL (λ_{ex}= 420 nm) at pH 2. The inset shows the corresponding Stern-Volmer plot.

Another contributing factor in the observed fluorescence enhancement is the change in the intramolecular fluorescence quenching pathways in the **NI** chromophore upon protonation of the picolylamine units. At pH 7, the possible photoinduced electron transfer from the picolylamine moiety to naphthalimide fluorophore is responsible for the reduction of the fluorescence quantum yield of **NI**. At lower pH conditions, the protonation of N-atoms of the picolylamine moiety blocks possible PET pathways, resulting in an enhancement in the **NI** fluorescence. Thus, the observed enhancement in

the fluorescence of the nanoconjugates at lower pH conditions could be attributed to the synergistic effects of reduced π-π interactions between **GO** and **NI** chromophore and perturbation in the internal electron transfer pathways within the chromophore (Figure2.23).

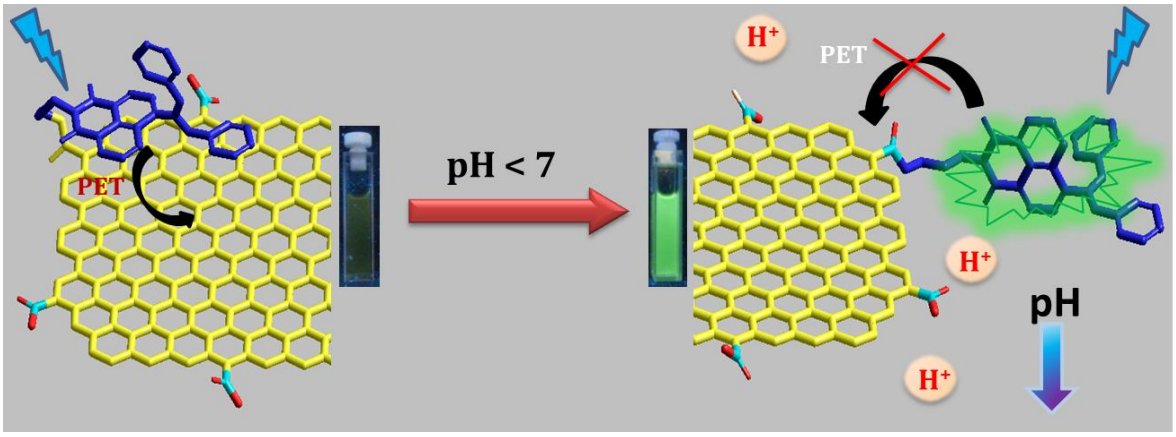

Figure 2.23. Schematic representation of pH-dependent fluorescence enhancement in **GO-NI**.

2.3.8. Interaction of GO-NI with metal ions

The observed pH-responsive fluorescence behavior of **GO-NI** nanoconjugate was further demonstrated to report the pH changes of aqueous solutions due to salt hydrolysis. The presence of picolylamine units in the **NI** chromophore facilitates interactions with various metal ions such as Zn^{2+}, $Hg^{2+,}$ etc leading to subtle enhancement in the fluorescence properties (Figure 2.24). On the other hand, the addition of micromolar amounts of $FeCl_3$ in aqueous solutions of **GO-NI** resulted in significant enhancement of fluorescence (~10 times enhancement compared to **GO-NI** at pH 7) as shown in Figure 2.24B.

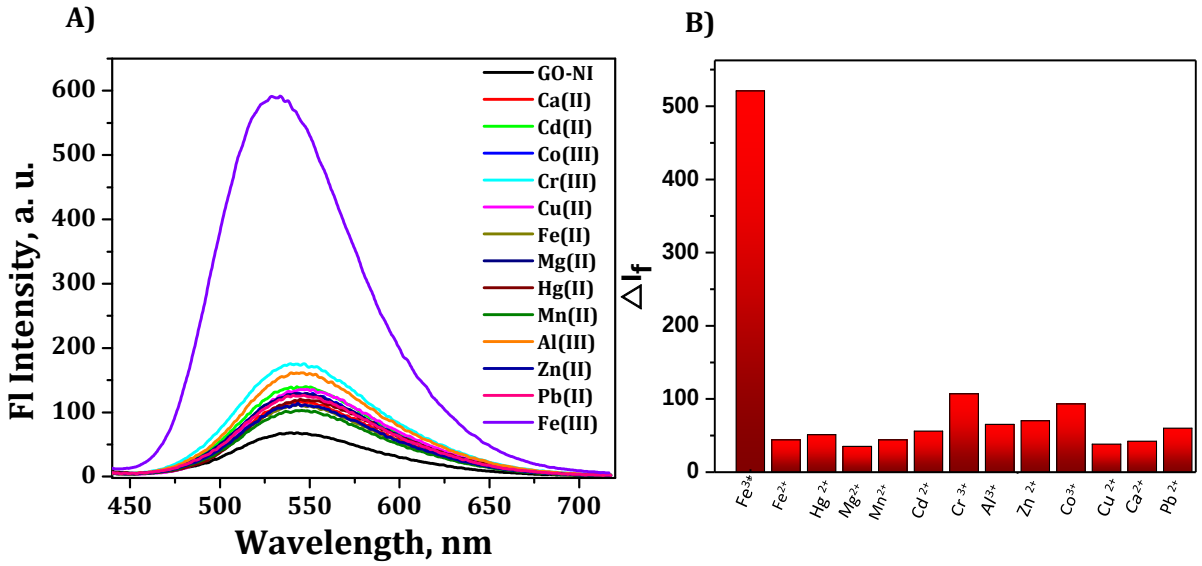

Figure 2.24. A) Emission spectra of **GO-NI** in presence of various metal ions and B) corresponding bar diagram.

GO and its covalently and non-covalently modified derivatives are known to have selective interactions with Fe^{3+} ions leading to changes in optical and electrochemical properties.[38,39] Along with the chances of the interaction of Fe^{3+} ions with **GO** surface and picolylamine units, we also have considered the pH changes upon hydrolysis of $FeCl_3$ in aqueous solutions. As shown in Figure 2.25, the concentrations of $FeCl_3$ used in aqueous solutions would significantly lower the pH of the system which in turn would cause the observed fluorescence enhancement of **GO-NI** nanoconjugate. **GO-NI** exhibited a significant enhancement in fluorescence intensity upon addition of increasing concentration of Fe^{3+} up to 75 µM, which is equivalent to the pH of 2. These results indicate the usefulness of this material for "turn on" sensing of Fe^{3+} in aqueous solution indirectly by sensing pH of the medium.

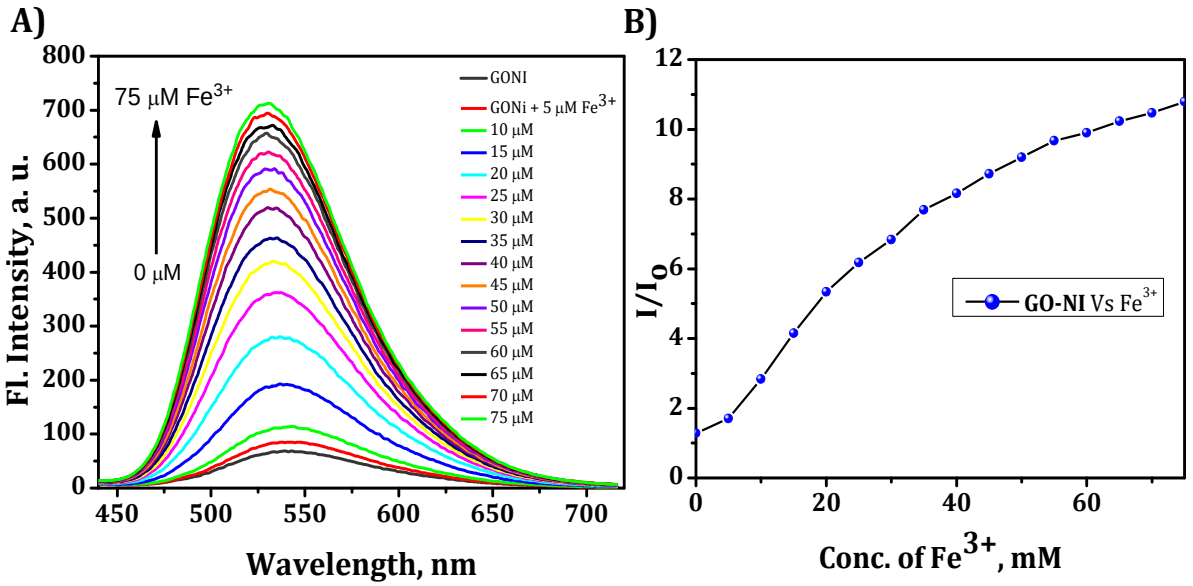

Figure 2.25. A) Change in fluorescence of **GO-NI** with an increase in Fe^{3+} concentration up to 75 μM and B) shows a corresponding change in fluorescence intensity (I/I_o) with Fe^{3+} concentration up to 75 μM.

2.3.9. Sensing of Acetylcholine using GO-NI

Acetylcholine (ACh) is an important neurotransmitter and its abnormalities in the brain are related to the neuropsychiatric disorders, such as Alzheimer's disease. The excessive accumulation of ACh in synaptic clefts can cause fatal health problems and its sensing is of greatest interest. Enzyme-based sensors are widely used owing to its specificity towards the substrate, acetylcholine.[40-44] Enzymatic sensing of graphene oxide nanosheets is highly desirable due to its excellent colloidal stability in aqueous medium and also it provides a suitable platform for enzyme immobilization.[45]

The potential of these nanoconjugates in reporting physiological pH changes was further demonstrated using the fluorescence response of **GO-NI** towards enzymatic hydrolysis of acetylcholine (**ACh**) in the presence of acetylcholine esterase (**AChE**),

which convert **ACh** to choline and acetic acid.[13a, 13b] Under optimized concentration of enzyme (3 U/mL, Figure 2.26A), and reaction time (10 min, Figure 2.26B), we have observed a significant enhancement in the fluorescence intensity of the nanoconjugate with increasing concentration (0 - 60 mM) of **ACh** (Figure 2.27A).

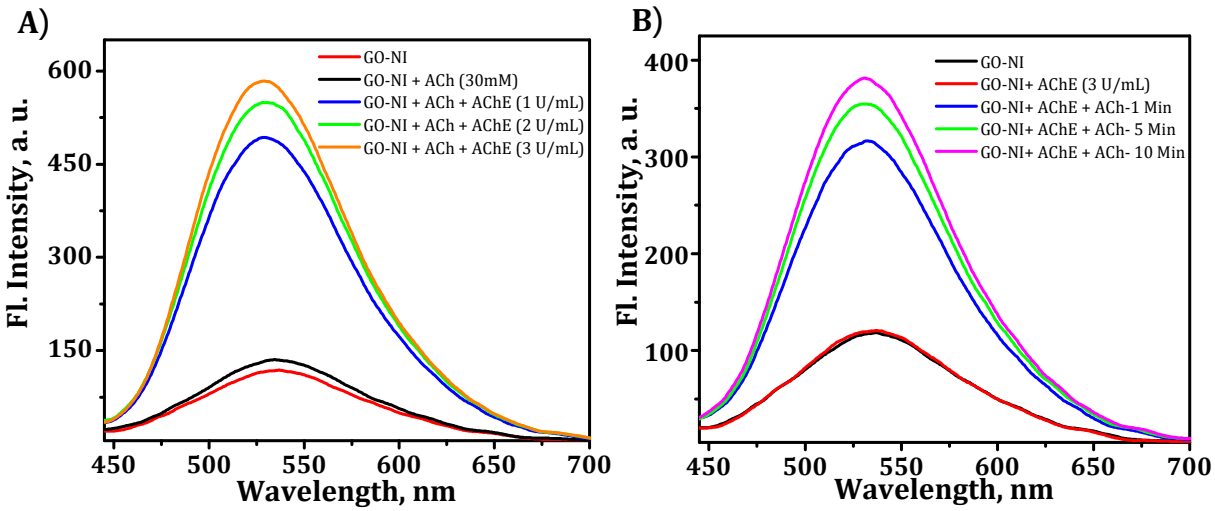

Figure 2.26. A)Fluorescence spectra of **GO-NI – ACh** (30 mM) mixture at various concentrations of **AChE** (1 - 3 U/mL). Each measurement has taken after incubation of the sample mixture at 25 °C for 10 mins. B) Fluorescence spectra of **GO-NI – ACh** (20 mM)-**AChE** (3 U/mL) mixture after incubation for the various time scale.

The fluorescence response (I/I_0) of **GO-NI** towards **ACh** concentration and the corresponding pH change are shown in Figure 2.27B, which directly correlate the observed fluorescence enhancement with the pH changes of the medium. Separate control experiments were carried out without the enzyme and the substrate under otherwise similar reaction conditions showed negligible fluorescence response. **GO-NI** exhibited nearly linear fluorescence response at lower **ACh** concentrations (0 to 500 μM) and the lower limit of detection is calculated to be 50 μM, which shows the ability of our sensor to detect **ACh** in neurophysiological range.

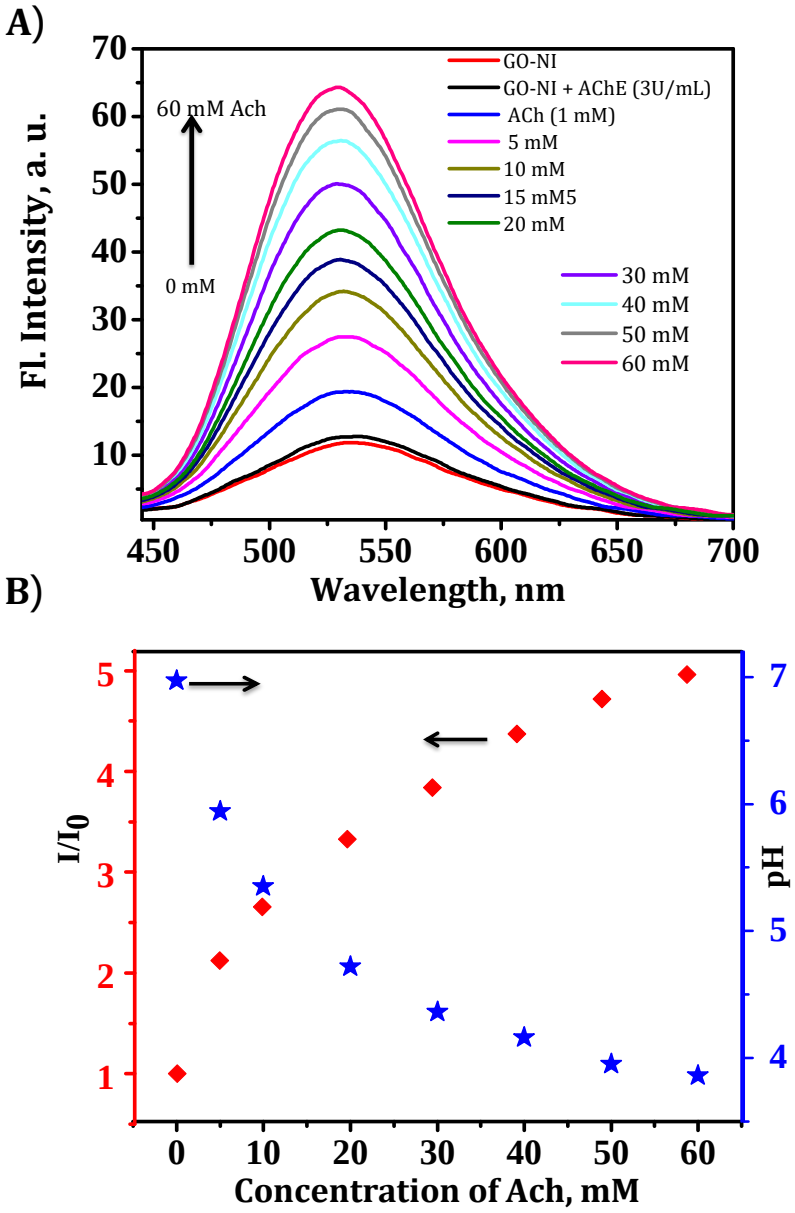

Figure 2.27. A) Fluorescence spectra of **GO-NI** in presence of **ACh** at various concentrations from 1 to 60 mM. **AChE** (3 U/mL) was used for hydrolysis. Each measurement has taken after incubation of the sample mixture at 37 ^{0}C for 10 mins. B) Fluorescence intensity changes (I/I_0) of **GO-NI** – **AChE** mixture at 540 nm (red squares) with various concentrations of **ACh** and pH change in the solution (blue stars). I_0 and I are the fluorescence intensity of **GO-NI** – **AChE** mixture before and after treatment with Ach.

2.4. Conclusions

In summary, we demonstrated the design and synthesis of two novel graphene nanoconjugates, **GO-NI** and **rGO-NI** with appended 1,8-naphthalimide based fluorophores. In aqueous solutions, both **GO-NI** and **rGO-NI** exhibited highly quenched fluorescence emission consequent to the strong π-π interaction of the chromophores with the **GO** surface and possible internal PET processes. At lower pH conditions, these nanoconjugates exhibited a unique fluorescence enhancement due to the synergistic effects of reduced π-π interactions between **GO** and **NI** chromophore and perturbation in the internal electron transfer pathways within the chromophore. The potential of these nanoconjugates in reporting real time pH reduction *via* a fluorescence 'turn on' response was demonstrated using salt hydrolysis of $FeCl_3$ and enzymatic hydrolysis of acetylcholine, as representative examples.

2.5. Experimental Section

2.5.1. Synthesis and Characterization

Graphene oxide (**GO**) was synthesized from graphite powder (400 nm APS) by modified Hummers' method. The reagents and materials for synthesis were purchased from Sigma-Aldrich, Alfa-Aesar and Spectrochem. Acetylcholinesterase from *Electrophorus electricus* (electric eel), acetylcholine and all metal salts used were purchased Sigma-Aldrich. ^{1}H-NMR & ^{13}C-NMR spectra were recorded using DPX 500 MHz spectrometer using tetramethylsilane (TMS) as the internal standard and deuterated solvents were used for the measurements. Absorption spectra were

recorded on a Shimadzu UV-2600 UV-Visible spectrophotometer. Fluorescence spectra were collected using SPEX-Fluorolog F112X Spectrofluorimeter equipped with a 450 W Xenon arc lamp and spectra obtained were corrected using the program supplied by the manufacturer. Measurements of solution state quantum efficiency were carried out using a calibrated integrating sphere in the SPEX Fluorolog spectrofluorimeter. A Xenon-arc lamp was used to excite the samples placed in the sphere, with 420 nm as the excitation wavelength. This experimental setup and the integrating sphere system calibrated using the solid state fluorescence quantum yield of the standard sodium salicylate (white powder) was determined to be 60 ± 10%, which is consistent with previously reported values.[46] FT-IR spectra were recorded on a Shimadzu IRPrestige-21 Fourier Transform Infrared Spectrophotometer. Raman analysis was carried out in a WITec Raman instrument (Witec Inc. Germany, alpha 300R) with a laser beam directed to the sample through 60× water immersion objective and a Peltier-cooled CCD detector. Samples were excited with a 532 nm excitation wavelength laser and Stokes-shifted Raman spectra were recorded from 500 to 3000 cm^{-1} with 1 cm^{-1} resolution. Prior to every measurement, a calibration with a silicon standard 4 was performed. WITec Project Plus (v 2.1) software was used for data evaluation.

Electron microscopic observations (TEM) of the morphology were performed with a FEI Tecnai G2-30 Transmission Electron Microscope operating at 120 kV. AFM images were recorded using a NTEGRA (NT-MDT) instrument operating with a tapping mode regime. Micro-fabricated TiN cantilever tips (NSG10) with a resonance frequency of 299 kHz and a spring constant of 20-80 Nm^{-1} were used. AFM section analysis was

carried out offline. Samples for the analysis were prepared by drop casting the sample solution (0.1 mg/mL) on freshly cleaved mica substrate at ambient conditions. Zeta potential of samples (0.1 mg/mL in water) was measured using Malvern Zetasizer Nano-ZS. pH of the solutions was measured using Metler Toledo FiveGo pH analyzer. Thermogravimetric analysis of samples was carried out using Shimadzu DTG-60 TG analyzer, and the samples were heated from room temperature to 900 ˚C at a heating rate of 5 ˚C/min in N_2 atmosphere. Fluorescence lifetimes were measured using an IBH Picosecond single photon counting system. The fluorescence decay profiles were deconvoluted using IBH data station software V2.1, fitted with exponential decay and minimizing the chi-square values of the fit to 1 ±0.1. (1.194).

Responsiveness of the sensor was analyzed over a range of acetylcholine concentrations from 0.1 mM to 1 mM. The lower limit of detection is determined based on standard deviation of the response (σ_y) of the curve and the slope of the calibration curve (m), according to the formula LOD = 3.3(σ_y/m). The standard deviation of the response can be determined based on the standard deviation of y-intercepts of regression lines.

2.5.2. Synthesis of graphene oxide (GO)

Graphite oxide was synthesized from graphite powder by a modified Hummers' method.[47] To a solution of potassium metabisulfite (2.5 g) and phosphorous pentoxide (2.5 g) in concentrated sulfuric acid (12 mL) at 80 °C was added graphite powder (3 g). The mixture was stirred at 80 °C for 4.5 h, cooled to room temperature, diluted with de-ionized water (500 mL) and left overnight. Then the mixture was filtered using a 0.2-

micron nylon Millipore filter and washed with deionized water to remove the residual acid. The product was dried under ambient conditions overnight. This pre-oxidized graphite was then further oxidized by Hummers' method. To a solution of pretreated graphite powder in concentrated sulfuric acid (120 mL) at 0 ˚C, was added potassium permanganate (15 g) gradually, under stirring keeping the temperature below 20 °C. Successively, the mixture was stirred at 40 °C for 1h and then diluted cautiously with 250 mL of de-ionized (DI) water maintaining the temperature below 50 °C. Stirring was continued for 2h, and then additional 0.7 L of DI water was added. Shortly after this dilution hydrogen peroxide (30%, 20 mL) was added to the mixture. The mixture was filtered and washed with aqueous hydrochloric acid (1M, 1L) followed by DI water. The resulting solid was dried at ambient temperature and diluted with water to make a **GO** dispersion. It was further purified by dialysis for one week to remove the remaining metal species and acid impurities. The graphite oxide thus obtained was dried under ambient conditions.

Synthesis of graphene oxide (**GO**) was carried out by exfoliation of graphite oxide (10 mg) by sonication in water (100 mL) under ambient condition for 20 min. The resulting homogeneous brownish-yellow water suspension was found to be stable for several months and used for further characterization and synthesis of nanoconjugates.

2.5.3. Synthesis of reduced graphene oxide (rGO)

Graphene oxide (200 mg) was added to 100 mL water and sonicated for 1 h until it becomes a clear solution. To this solution added 6 mL of hydrazine hydrate and refluxed for 24 h with constant stirring. The solution was cooled and centrifuged. The

residue was washed with water and then washed with methanol for many times and then dried at room temperature.

2.5.4. Synthetic procedure for NI

2.5.4.1. Synthesis of 6-(bis(pyridin-2-ylmethyl)amino)benzo[de]isochromene-1,3-dione (3)

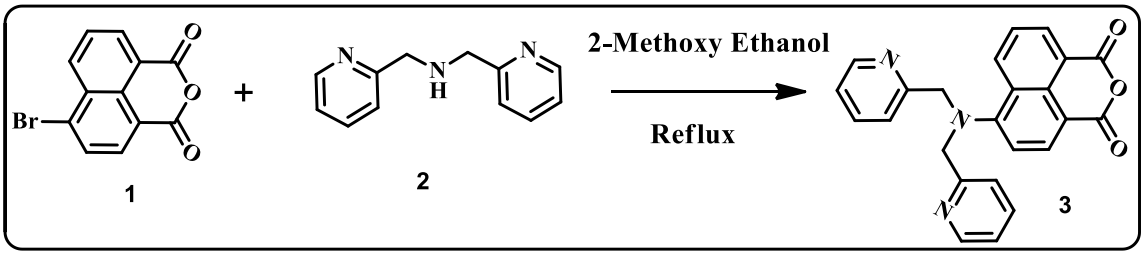

A solution of 4-bromo-1,8-naphthalic anhydride (**1**, 1.8 g) and di-(2-picolyl)amine (**2**, 1.8 g) in 2-methoxyethanol (50 mL) was refluxed for 48 h. The mixture was concentrated by rotatory evaporation and dissolved in CH_2Cl_2 (150 mL). The organic layer was washed with water and dried over anhydrous Na_2SO_4 and filtered. Further purification of the crude mixture by column chromatography (Silica gel, Ethyl acetate) yielded 2.1 g (81%) of the product.

^{1}HNMR: ($CDCl_3$, 500 MHz) , δ (ppm): 4.796 (s, 4H), 7.215 (t, J = 6.5 Hz, 3H), 7.369 (d, J = 8 Hz, 2H), 7.634 (t, J = 7.5 Hz, 2H), 7.734 (t, J = 8 Hz, 1H), 8.389 (d, J = 8.5 Hz, 1H), 8.611 (d, J = 6.5 Hz, 3H), 9.028 (d, J = 8.5 Hz, 1H). MS (FAB): 395.1 (M^+).

2.5.4.2. Synthesis of tertbutyl(3-aminopropyl)carbamate (4)

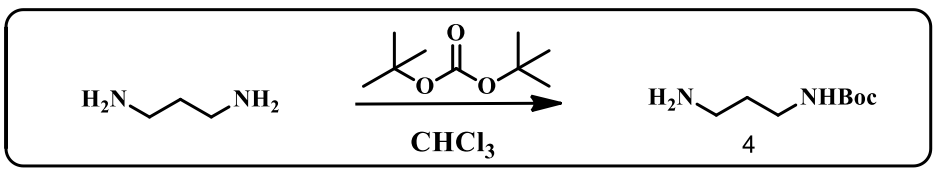

To an ice-cooled solution of 1,3-diaminopropane (3.7 g, 0.05 mol) in chloroform (50 mL) was added a solution of di-*tert*-butyl bicarbonate (10.9 g, 0.05 mol) in chloroform (250 mL) over 3h. After the addition of reagent, the reaction mixture was brought to room temperature and the stirring was continued for 16 h. The precipitate formed was filtered off and the filtrate was washed with water followed by brine. The organic phase was separated, and the solvent was removed under reduced pressure to give the product (2 g, 37%) which was sufficiently pure for further synthesis.

^{1}H NMR ($CDCl_3$, 500 MHz): δ (ppm) 1.4 (s, 9H), 1.63 (qt, J = 6.5 Hz, 2H), 2.77 (t, J = 6.5 Hz, 2H), 3.21 (q, J = 6 Hz, 2H), 4.89 (s, 1H, NH). MS (FAB): 174.2 (M^+).

2.5.4.3. Synthesis of tert-butyl (3-(6-(bis(pyridin-2-ylmethyl)amino)-1,3-dioxo-1H-benzo[de]isoquinolin-2(3H)-yl)propyl)carbamate (5)

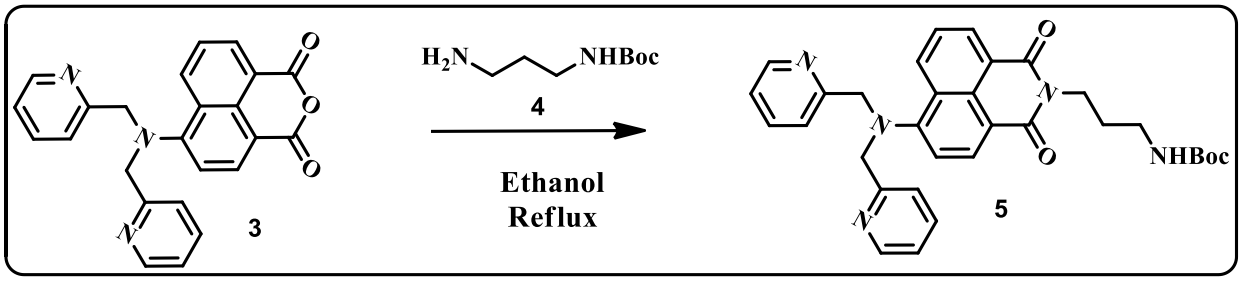

To a solution of compound **3** (2.1 g, 5.3 mmol) in ethanol (30 mL) added 1.74 g (10 mmol) of *tert*-butyl(3-aminopropyl)carbamate **(4)** and refluxed for 24 hrs. Completion of the reaction was confirmed by TLC and the reaction mixture was cooled to room temperature. The solvent was removed in vacuum and the crude mixture obtained was purified further by column chromatography (Silica gel, 1:4 mixture of Ethyl acetate: Hexane) to give 1.8 g of **5** (61%).

^{1}HNMR ($CDCl_3$, 500 MHz); δ (ppm) 1.440 (s, 9H), 1.899 (t, J = 6 Hz, 2H), 3.138 (d, J = 5.5 Hz, 2H), 4.234 (t, J = 6.5 Hz, 2 H), 4.749 (s, 4H), 5.319 (s, 1H), 7.201 (t, J = 9 Hz, 3H), 7.37 (d, J = 7.5 Hz, 2H), 7.611 (t, J = 7.5 Hz, 2H), 7.726 (t, J = 7.5 Hz, 1H), 8.376 (d, J = 8 Hz, 1H), 8.595 (t, J = 8 Hz, 3H), 8.904 (d, J = 8.5 Hz, 1H). MS (FAB): 550.1 (M^+).

2.5.4.4. Synthesis of NI

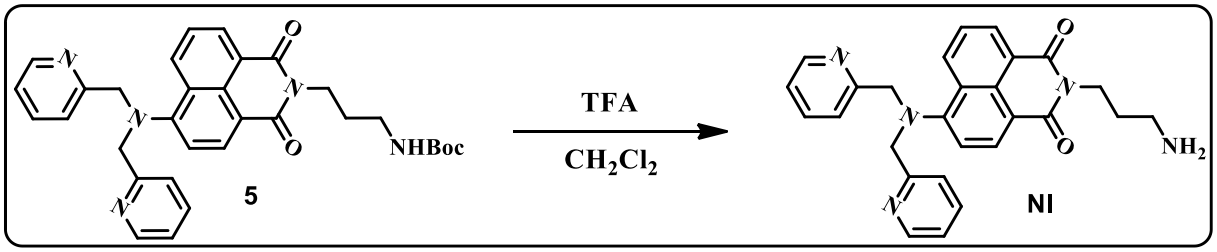

To a solution of **5** (1.7 g, 3.18 mmol) in 6 mL CH_2Cl_2, added 4 mL of TFA drop wise at 0 °C and stirred overnight. After evaporation of the solvent the crude mixture is dissolved in water and organic impurities were removed by extraction with CH_2Cl_2. The remaining aqueous solution was basified with 1M NaOH solution and extracted with CH_2Cl_2 to get 0.95 g of **NI** (70 %).

^{1}HNMR ($CDCl_3$, 500 MHz): δ (ppm), 1.876 (q, J = 6.5 Hz, 2H), 2.742 (t, J = 6.5 Hz, 2H), 4.250 (t, J = 7 Hz, 2H), 4.743 (s, 4H), 7.189 (q, J = 6.5 Hz, 3H), 7.359 (d, J = 7.5 Hz, 2H), 7.594 (t, J = 7.5 Hz, 2H), 7.720 (t, J = 7.5 Hz, 1H), 8.357 (d, J = 8 Hz, 1H), 8.586 (q, J = 4 Hz, 3H), 8.907 (d, J = 8.5 Hz, 1H).

^{13}C NMR ($CDCl_3$, 125MHz), δ (ppm): 37.47, 59.56, 115.27, 117.28, 122.42, 122.59, 126.10, 129.91, 131.50, 136.89, 149.44, 154.25, 157.04, 164.21, 164.72. MS (FAB): 451.2 (M^+).

2.5.5. Synthesis of GO-NI

GO (20 mg) is dispersed in 20 mL H_2O by sonication for 1hr. To this solution added 115 mg of NHS (1 mmol) and 191 mg of (1 mmol) EDC and stirred for 1 hr. 45 mg (0.1 mmol) of **NI** dissolved in 10 mL H_2O was added to this mixture, slowly over 1 hr and the mixture was stirred for 24 h at room temperature. The mixture was then centrifuged at 12000 rpm for 8 min and the residue was washed many times with water, DCM and water-acetone mixture (1:1) to remove unreacted reagents and other byproducts. Further, the product was washed many times with aqueous HCl (2M) to achieve complete removal of the adsorbed chromophore. Finally, the residue is dispersed in 10 mL H_2O and sonicated for 1h and used for further characterization.

2.5.6. Synthetic procedure for rGO-COOH

2.5.6.1. Synthesis of tert-butyl 3-((2-(benzyloxy)-2-oxoethyl)amino)propanoate

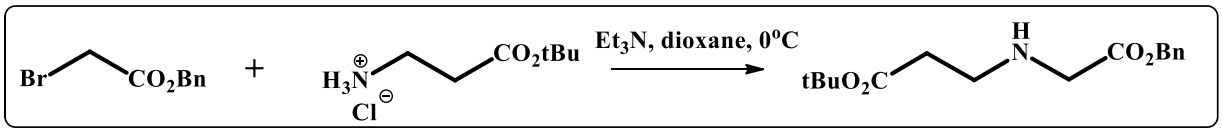

Triethylamine (0.75 mL, 5.5 mmol) was added to a suspension of β-alanine tert. butyl ester hydrochloride (500 mg, 2.75 mmol) in dioxane (20 mL) and the reaction mixture was stirred at room temperature for 20 minutes. The suspension was then cooled in an ice bath and a solution of benzyl bromoacetate (0.35 mL, 2.2 mmol) in dioxane (5 mL) was added dropwise and the mixture was stirred at room temperature for 24 h. Formation of the product was confirmed by TLC. The mixture was filtered and the filtrate was concentrated under reduced pressure and purified by column

chromatography on silica gel (20% Ethylacetate – Hexane) to yield 0.585 g (71%) of the product.

^{1}HNMR: ($CDCl_3$, 500 MHz) , δ (ppm): 1.454 (s, 9H), 2.464 (t, J = 6.5 Hz, 2H), 2.887 (t, J = 6.5 Hz, 2H), 3.496 (s, 2H), 5.180 (s, 2H), 7.352 (q, J = 2.5 Hz, 5H). MS (FAB): Calculated = 293.16 , Found = 294.39 $(M+H)^+$.

2.5.6.2. Synthesis of 2-((3-(tert-butoxy)-3-oxopropyl)amino)acetic acid

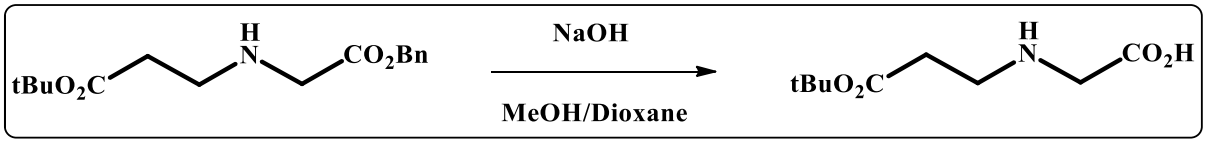

To a solution of compound **3** (200mg, 0.68 mmol) in a mixture of dioxane and methanol (4 mL, 3:1) was added 4N NaOH (0.177 mL). The mixture was stirred at room temperature for 1 h. The solvent was then removed under vacuum and the product is purified by column on silica gel eluted with 20% methanol- chloroform solvent to yield 0.105 g (73%) of the product.

^{1}HNMR: ($CDCl_3$, 500 MHz), δ (ppm): 1.456 (s, 9H), 2.803 (t, J = 7 Hz, 2H), 3.242 (t, J = 7 Hz, 2H), 3.533 (s, 2H). MS (FAB): Calculated = 203.12, Found = 204.22 $(M+H)^+$.

2.5.6.3. Synthesis of rGO-COOH (1,3-Dipolar addition reaction)

To a dispersion of **rGO** (5 mg) in DMF (4 mL), Boc-protected α-aminoacid (25 mg, 0.123 mmol) and formaldehyde (5 mg, 0.166 mmol) were added. The mixture was stirred at 130 °C for 72 hrs with successive similar additions of reactants every 24 h. The resulting solution was filtered and washed several times with DMF. The

functionalized **rGO** was dispersed in DMF, then trifluoroacetic acid (1 mL) was added. The mixture was kept under magnetic stirring overnight at room temperature. The suspension was filtered and the filtrate washed with DMF several times.

2.5.7. Synthesis of rGO-NI

rGO-COOH (5 mg) is dispersed in 5 mL H_2O by sonication for 1h. To this solution added 115 mg of NHS (1 mmol) and 191 mg of EDC (1 mmol) and stirred for 1 h. **NI** (45 mg, 0.1 mmol), dissolved in 10 mL H_2O was added to this mixture, slowly over 1 hr and the mixture was stirred for 24 hours at room temperature. The mixture was then centrifuged at 12000 rpm for 8 min and the residue was washed many times with water, DCM and water-acetone mixture (1:1) to remove unreacted reagents and other byproducts. Further, the product was washed many times with aqueous HCl (2M) to achieve complete removal of the adsorbed chromophore. Finally, the residue is dispersed in 10 mL H_2O and sonicated for 1hr and used for further characterization.

2.6. References

(1) Rao, C. N. R.; Sood, A. K.; Subrahmanyam, K. S.; Govindaraj, A. *Angew. Chem. Int. Ed.* **2009**, *48*, 7752.

(2) Allen, M. J.; Tung, V. C.; Kaner, R. B. *Chem. Rev.* **2010**, *110*, 132.

(3) Geim, A. K.; Novoselov, K. S. *Nat. Mater.* **2007**, *6*, 183.

(4) Wu, X.; Ding, S.-J.; Lin, K.; Su, J. *J. Mater. Chem. B* **2017**.

(5) Dreyer, D. R.; Park, S.; Bielawski, C. W.; Ruoff, R. S. *Chem. Soc. Rev.* **2010**, *39*, 228.

(6) Chen, D.; Feng, H.; Li, J. *Chem. Rev.* **2012**, *112*, 6027.

(7) Mao, S.; Pu, H.; Chen, J. *RSC Adv.* **2012**, *2*, 2643.

(8) Chua, C. K.; Pumera, M. *Chem. Soc. Rev.* **2014**, *43*, 291.

(9) Georgakilas, V.; Tiwari, J. N.; Kemp, K. C.; Perman, J. A.; Bourlinos, A. B.; Kim, K. S.; Zboril, R. *Chem. Rev.* **2016**, *116*, 5464.

(10) Georgakilas, V.; Otyepka, M.; Bourlinos, A. B.; Chandra, V.; Kim, N.; Kemp, K. C.; Hobza, P.; Zboril, R.; Kim, K. S. *Chem. Rev.* **2012**, *112*, 6156.

(11) Kasry, A.; Ardakani, A. A.; Tulevski, G. S.; Menges, B.; Copel, M.; Vyklicky, L. *J. Phys. Chem. C* **2012**, *116*, 2858.

(12) Swathi, R. S.; Sebastian, K. L. *J. Chem. Phys.* **2008**, *129*, 054703.

(13) Liu, Z.; Liu, B.; Ding, J.; Liu, *Anal. Bioanal. Chem* **2014**, *406*, 6885.

(14) Luo, W.; Feng, Y. Y.; Cao, C.; Li, M.; Liu, E. Z.; Li, S. P.; Qin, C. Q.; Hu, W. P.; Feng, W. *J. Mater. Chem. A* **2015**, *3*, 11787.

(15) Melucci, M.; Treossi, E.; Ortolani, L.; Giambastiani, G.; Morandi, V.; Klar, P.; Casiraghi, C.; Samori, P.; Palermo, V. *J. Mater. Chem.* **2010**, *20*, 9052.

(16) Liu, Z.; Chen, S.; Liu, B.; Wu, J.; Zhou, Y.; He, L.; Ding, J.; Liu, J. *Anal. Chem.* **2014**, *86*, 12229.

(17) Lu, C.; Jimmy Huang, P.-J.; Ying, Y.; Liu, J. *Biosens. Bioelectron.* **2016**, *79*, 244.

(18) Melucci, M.; Durso, M.; Zambianchi, M.; Treossi, E.; Xia, Z.-Y.; Manet, I.; Giambastiani, G.; Ortolani, L.; Morandi, V.; De Angelis, F.; Palermo, V. *J. Mater. Chem.* **2012**, *22*, 18237.

(19) Sohn, I.-Y.; Kim, D.-J.; Jung, J.-H.; Yoon, O. J.; Nguyen Thanh, T.; Tran Quang, T.; Lee, N.-E. *Biosens. Bioelectron.* **2013**, *45*, 70.

(20) Kuila, A.; Maity, N.; Layek, R. K.; Nandi, A. K. *J. Mater. Chem. A* **2014**, *2*, 16039.

(21) Kundu, A.; Layek, R. K.; Nandi, A. K. *J. Mater. Chem.* **2012**, *22*, 8139.

(22) Paek, K.; Yang, H.; Lee, J.; Park, J.; Kim, B. J. *ACS Nano* **2014**, *8*, 2848.

(23) Kang, T. W.; Jeon, S.-J.; Kim, H.-I.; Park, J. H.; Yim, D.; Lee, H.-R.; Ju, J.-M.; Kim, M.-J.; Kim, J.-H. *ACS Nano* **2016**, *10*, 5346.

(24) Talesa, V. N. *Mech. Ageing Dev.* **2001**, *122*, 1961.

(25) Inestrosa, N. C.; Alvarez, A.; Pérez, C. A.; Moreno, R. D.; Vicente, M.; Linker, C.; Casanueva, O. I.; Soto, C.; Garrido, J. *Neuron*, *16*, 881.

(26) Stankovich, S.; Dikin, D. A.; Dommett, G. H. B.; Kohlhaas, K. M.; Zimney, E. J.; Stach, E. A.; Piner, R. D.; Nguyen, S. T.; Ruoff, R. S. *Nature* **2006**, *442*, 282.

(27) Loh, K. P.; Bao, Q.; Eda, G.; Chhowalla, M. *Nat Chem* **2010**, *2*, 1015.

(28) Li, D.; Muller, M. B.; Gilje, S.; Kaner, R. B.; Wallace, G. G. *Nat. Nanotechnol.* **2008**, *3*, 101.

(29) Quintana, M.; Spyrou, K.; Grzelczak, M.; Browne, W. R.; Rudolf, P.; Prato, M. *ACS Nano* **2010**, *4*, 3527.

(30) Quintana, M.; Montellano, A.; del Rio Castillo, A. E.; Tendeloo, G. V.; Bittencourt, C.; Prato, M. *Chem. Commun.* **2011**, *47*, 9330.

(31) Pimenta, M. A.; Dresselhaus, G.; Dresselhaus, M. S.; Cancado, L. G.; Jorio, A.; Saito, R. *Phys. Chem. Chem. Phys* **2007**, *9*, 1276.

(32) Georgakilas, V.; Bourlinos, A. B.; Zboril, R.; Steriotis, T. A.; Dallas, P.; Stubos, A. K.; Trapalis, C. *Chem. Commun.* **2010**, *46*, 1766.

(33) Zhang, X.; Hou, L.; Cnossen, A.; Coleman, A. C.; Ivashenko, O.; Rudolf, P.; van Wees, B. J.; Browne, W. R.; Feringa, B. L. *Chem. Eur. J.* **2011**, *17*, 8957.

(34) Liang, H. F.; Smith, C. T. G.; Mills, C. A.; Silva, S. R. P. *J. Mater. Chem. C* **2015**, *3*, 12484.

(35) Duke, R. M.; Veale, E. B.; Pfeffer, F. M.; Kruger, P. E.; Gunnlaugsson, T. *Chem. Soc. Rev.* **2010**, *39*, 3936.

(36) Matte, H. R.; Subrahmanyam, K.; Rao, K. V.; George, S. J.; Rao, C. *Chem. Phys. Lett.* **2011**, *506*, 260.

(37) Bozkurt, E.; Acar, M.; Onganer, Y.; Meral, K. *PCCP* **2014**, *16*, 18276.

(38) Liu, Z. D.; Zhao, H. X.; Huang, C. Z. *PLoS ONE* **2012**, *7*, e50367.

(39) Şenol, A. M.; Onganer, Y.; Meral, K. *Sens. Actuators. B Chem.* **2017**, *239*, 343.

(40) Dai, N.; Teo, Y. N.; Kool, E. T. *Chem. Commun.* **2010**, *46*, 1221.

(41) Wang, C. I.; Chen, W. T.; Chang, H. T. *Anal. Chem.* **2012**, *84*, 9706.

(42) Garai-Ibabe, G.; Saa, L.; Pavlov, V. *Analyst* **2014**, *139*, 280.

(43) Mathew, M. S.; Baksi, A.; Pradeep, T.; Joseph, K. *Biosens. Bioelectron.* **2016**, *81*, 68.

(44) Walsh, R.; Morales, J. M.; Skipwith, C. G.; Ruckh, T. T.; Clark, H. A. *Sci. Rep.* **2015**, *5*, 14832.

(45) Jin, L.; Yang, K.; Yao, K.; Zhang, S.; Tao, H.; Lee, S.-T.; Liu, Z.; Peng, R. *ACS Nano* **2012**, *6*, 4864.

(46) Carlos, L. D.; De Mello DonegÁ, C.; Albuquerque, R. Q.; Alves, S.; Menezes, J. F. S.; Malta, O. L. *Mol. Phys.* **2003**, *101*, 1037.

(47) Hummers, W. S.; Offeman, R. E. *J. Am. Chem. Soc.* **1958**, *80*, 1339.

Chapter 3

Design, Synthesis and Characterization of Graphene Quantum Dot - BODIPY Nanoconjugates for PDT Applications

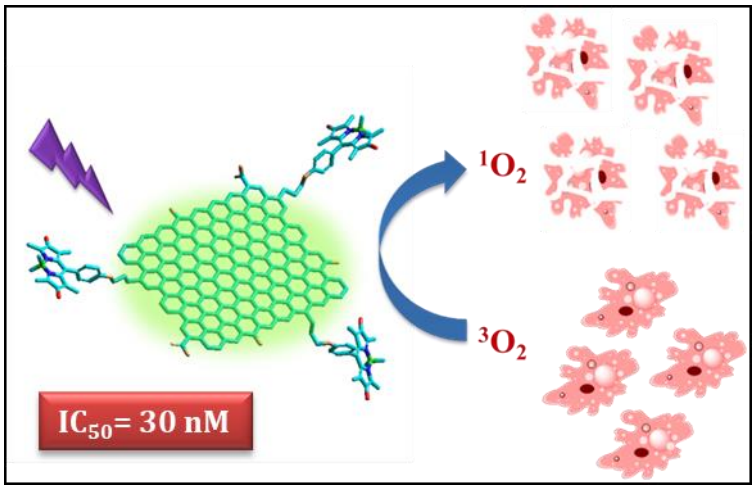

3.1. Abstract

*Photodynamic therapy (PDT), a non-invasive modality for the treatment of cancer, involves the combined interaction of oxygen, light and a photosensitizing agent and cause local destruction of cancerous cells through the generation of reactive oxygen species (ROS). Use of nano-carriers for the delivery of photosensitizer molecules to the target cells is a promising strategy to improve the efficacy of PDT based clinical treatment. Graphene Quantum Dots (GQDs), by virtue of its size in the nano domain, physiological solubility, high photostability, easy accumulation in tumor cells and low cytotoxicity, can be used as a suitable platform for the delivery of PDT agents conjugated through covalent and non-covalent strategies. In this context, we synthesized Graphene Quantum Dots (**GQD**s) – diiodo-BODIPY nanoconjugates (**GQD-BDPA**) and studied their photophysical properties*

and ability to generate singlet oxygen in detail. Here diiodo-BODIPY derivative serve as the photosensitizer with high singlet oxygen generation efficiency, whereas GQD counterpart can act as a nanocarrier to enhance cellular internalization, and as a solubilizing agent for photosensitizer in aqueous media. Green luminescent ***GQDs*** *were synthesized from graphene oxide (****GO****) via a modified acid treatment method and the amino BODIPY derivative (****BDPA****) was covalently attached to the* ***GQDs*** *via EDC/NHS coupling with a loading efficiency of ~4.4 wt %. These nanoconjugates, with average lateral dimensions of ~50 nm and excellent water solubility, exhibited characteristic absorption and fluorescence properties of both* ***GQDs*** *and* ***BDPA****. Nanoconjugates showed a strong absorption band around 550 nm, corresponding to the* ***BDPA*** *absorption and exhibited similar green luminescence properties of* ***GQDs****. Triplet quantum yield of* ***GQD-BDPA*** *was found to be 0.94±0.02 with high singlet oxygen generation efficiency (>90%), demonstrating the potential of these nanoconjugates for PDT applications. In vitro PDT activity of this nanoconjugate was investigated using MDA-MB-231 cancer cell lines and* ***GQD-BDPA*** *is found to be an efficient system for PDT treatment with an* IC_{50} *value of 30 nM (sensitizer concentration). The apoptotic cell death was characterized and confirmed by various assays such as Annexin, TMRM assay, nuclear condensation, etc. on MDA-MB-231 cell lines.*

3.2. Introduction

Photodynamic Therapy (PDT) is an emerging therapeutic technique for the treatment of cancer in which a photosensitizing molecule destroys malignant tumors under the influence of light.[1-3] Photo-excited drugs generate reactive oxygen species

(ROS) to the cellular environment, which in turn triggers the cell death.[4,5] This treatment is a widely accepted and successful therapy for various kinds of cancers, with several advantages over other existing therapies regarding relatively lower side effects and rapid recovery. Currently, nanomaterial assisted delivery of drugs are getting more attention in cancer therapies, owing to its high specificity as well as enhanced cellular distribution.[6] Among various nanomaterials, graphene has been demonstrated as an ideal platform for drug delivery applications.[7]

Graphene has a polyaromatic surface structure with an ultrahigh surface area, which is available for efficient loading of aromatic drug molecules *via* non-covalent as well as covalent approaches.[8-10] Chemical modifications can be done easily by introducing functional groups *via* oxidation. Functional groups, such as hydroxyl, epoxy and carboxylic acid moieties, attached to graphene oxide (**GO**) sheets facilitate easy modification with biomolecules that could improve the stability, solubility, and biocompatibility.[11] Graphene and its nanoconjugates have been widely used for the targeted delivery of PDT sensitizers both *in vitro* and *in vivo*.[12-15]

Daxiang Cui and co-workers demonstrated the use of nanomaterials as carriers of photosensitizers as a promising approach to improve the efficiency of PDT in clinical medicine (Figure 3.1).[15] In his study, a novel folic acid-conjugated graphene oxide was strategically designed and prepared for targeting drug delivery system. The second generation photosensitizer Chlorin e6 (Ce6) was efficiently loaded into the hybrid *via* π-π stacking. The nanocarrier, **GO** can significantly enhances the accumulation of Ce6 in tumor cells *via* the folate receptors mediated pathway and lead to a remarkable

photodynamic efficacy on MGC803 cells upon irradiation. Their studies suggested that folic acid-conjugated **GO** loaded Ce6 had great potential as effective drug delivery system in targeting PDT.

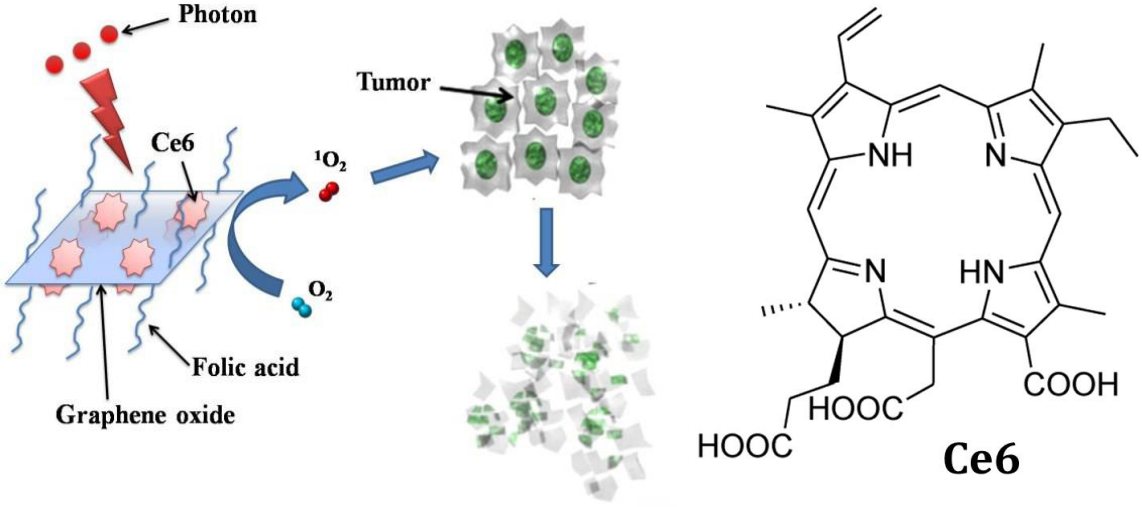

Figure 3.1. Photosensitizers Ce6 loaded on folic acid-conjugated graphene oxide used for PDT applications (Adapted from reference 15).

Graphene Quantum Dots (**GQDs**), by virtue of its size in the nanodomain, physiological solubility, high photostability, easy accumulation in tumor cells and low cytotoxicity, can be used as a suitable platform for the delivery of PDT agents conjugated through covalent and non-covalent strategies.[16-18] Recently, Jiechao and coworkers developed **GQDs** by hydrothermal reaction of thiophene, with high singlet oxygen generation of ~1.3, *via* a multistate sensitization process.[19] The mechanism of high singlet oxygen generation in the **GQDs** is schematically shown in Figure 3.2. Through *in vitro* and *in vivo* studies, they demonstrated that as-synthesized **GQDs** could be used as PDT agents, simultaneously allowing imaging and providing a highly efficient cancer therapy. However, most of the **GQDs** reported in the literature are not showing

much higher singlet oxygen efficiencies without covalent/non-covalent substitution with photosensitizers.

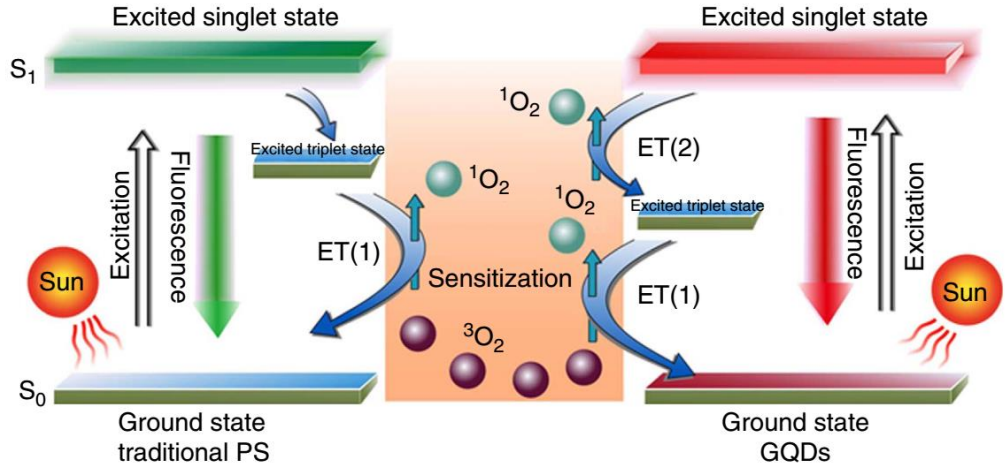

Figure 3.2. Schematic illustration of the $^1O_2$ generation mechanisms by conventional PDT agents (left) and as synthesized **GQDs** (right) from thiophene (Adapted from reference 19).

Markovic *et al.* reported that electrochemically produced **GQDs** irradiated with blue light (470 nm) generate reactive oxygen species, including singlet oxygen, and kill U251 human glioma cells by causing oxidative stress.[20] The cell death induced by photoexcited **GQDs** displayed morphological and biochemical characteristics of both apoptosis (phosphatidylserine externalization, caspase activation, DNA fragmentation) and autophagy. Recently Yongyong Li and coworkers reported **GQD** - Ce6 nano-assembly with a disulfide spacer for GSH responsive drug release and subsequent photodynamic therapy.[21,22] These reports indicate the potential usefulness of **GQDs** in photodynamic therapy applications.[20]

In the present study, we have synthesized a **GQD**-BODIPY nanoconjugate with efficient singlet oxygen generation capability. BODIPY dyes are known for its high molar

extinction coefficient (ε >50000 $M^{-1}cm^{-1}$), insensitivity to solvent polarity and pH, good photo and chemical stability and high singlet oxygen generation efficiency.[23-26] Despite high singlet oxygen generation efficiency, aqueous solubility is one of the main factors which limit its use as an efficient PDT sensitizer for practical applications.[27,28] In this context, we synthesized a diiodo-BODIPY derivative with an active aliphatic amino group by modifying the reported procedures. It is further coupled covalently to acid functionalized **GQDs** *via* EDC-mediated amide coupling. This covalent attachment can overcome some of the drawbacks of physisorbed PDT systems by avoiding premature release of drug molecules in blood and can reduce the risk of undesirable side effects. The covalent nanoconjugate formed have high triplet quantum yield of 0.94±0.02 and highly efficient in generating singlet oxygen (>90%). The enhanced cell permeability along with excellent photo-cytotoxicity indicates their potential as efficient sensitizers for PDT applications.

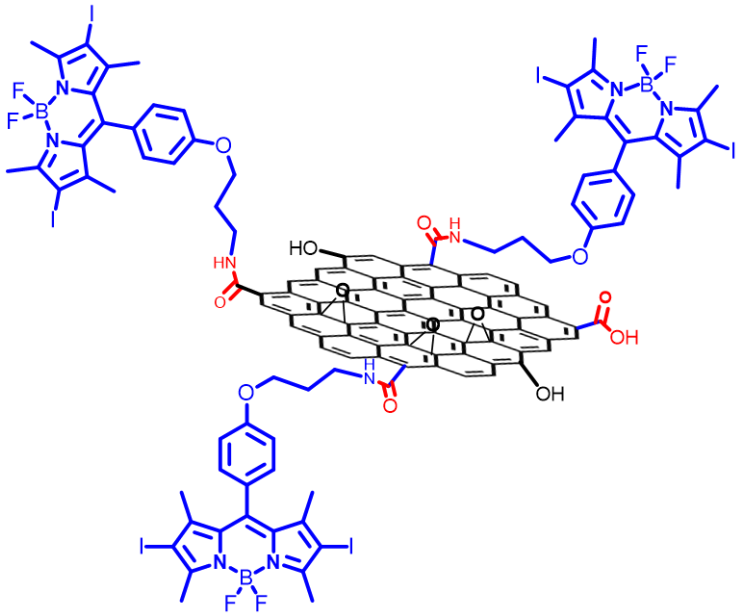

Figure 3.3. Schematic representation of **GQD-BDPA** nanoconjugates (Structures are not drawn to scale).

3.3. Results and Discussion

3.3.1. Synthesis and Characterization of GQDs

Graphene oxide (**GO**) is used as a precursor for the top-down synthesis of graphene quantum dots. **GO** is synthesized from graphite *via* well-known modified Hummers' method, where bulk graphite is reacted with strong oxidizing agent such as $KMnO_4$ in presence of concentrated H_2SO_4. The **GO** thus obtained upon treatment with concentrated nitric acid resulted in the further oxidation of **GO** and this oxidative cutting eventually leads to the formation of smaller sheets of graphene termed as graphene quantum dots (**GQDs,** Scheme 3.1). Excessive oxidation imparts various oxygen functionalities such as carboxylic acids and hydroxyl groups on the surface of **GQDs**, which impart aqueous solubility and make them an ideal nanomaterial for chemical conjugation with sensitizers for drug delivery applications.

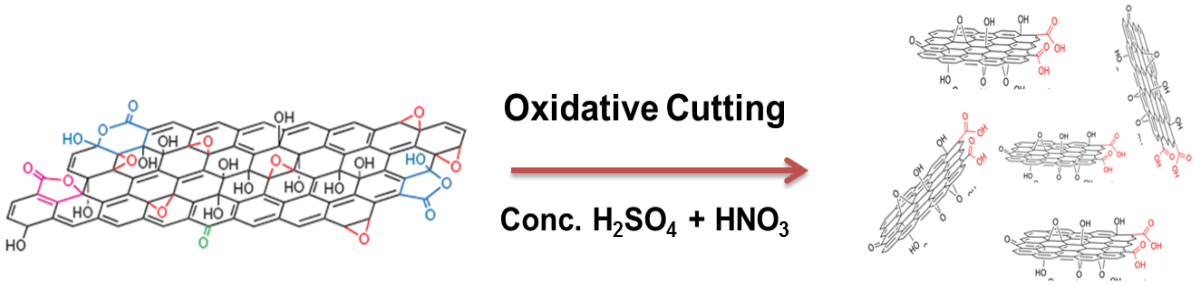

Scheme 3.1. Synthesis of **GQDs** (Structures are not drawn to scale).

As synthesized **GQDs** have been characterized using UV-visible and emission spectroscopy. Absorption and emission spectra of the prepared samples are shown in Figure 3.4. **GQDs** are showing almost similar broad absorption like graphene oxide (**GO**) starting from 800 nm to 200 nm with a shoulder band around 300 nm, which is

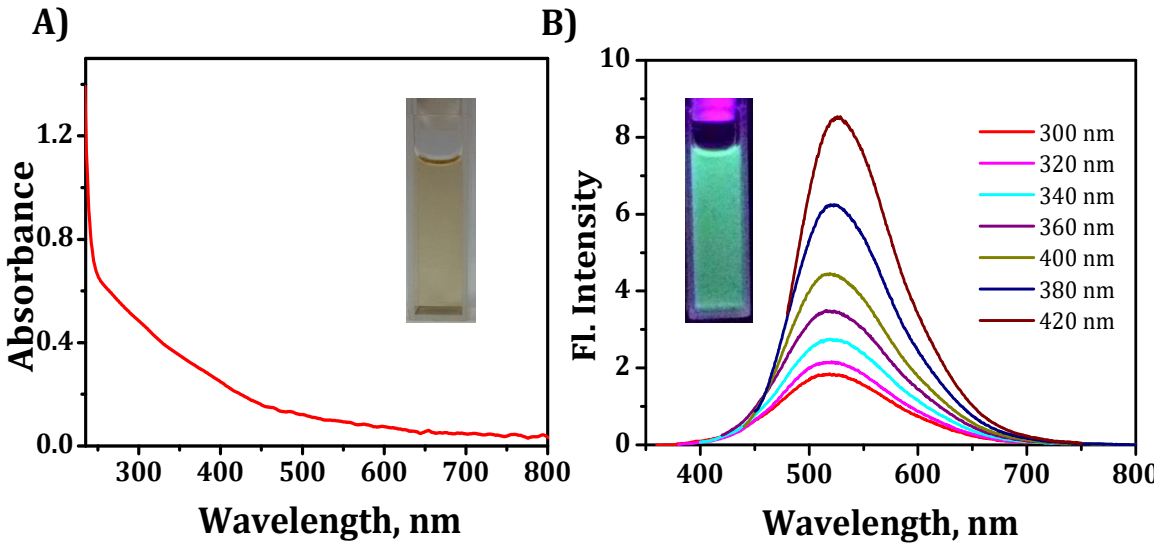

Figure 3.4. A) Absorption spectra of **GQDs** in water and B) Emission spectra of **GQDs** at various excitations from 300 to 420 nm.

assigned to the π - π* transition of aromatic sp^2 domains. The most interesting property of **GQDs** over **GO** is its bright luminescence by excitation with suitable wavelength. Our samples showed a broad emission from 400 nm to 700 nm upon exciting at 350 nm light, which is shown in Figure 3.4B. Emission maximum was found to be independent of the excitation wavelength indicating that the synthesized **GQDs** have a narrow lateral size distribution which further confirmed using other imaging techniques. The as synthesized **GQDs** exhibited a fluorescence quantum yield of 1.1% (comparative method, quinine sulphate as standard) which is comparable with GQDs synthesized *via* similar methods.[29]

GQDs have been further characterized by microscopic techniques such as AFM and TEM analysis. A representative AFM image of as-prepared **GQDs** in tapping mode is shown in Figure 3.5A, which was obtained by coating **GQDs** on a freshly cleaved mica surface using 0.1 mg/mL water solution of **GQDs**. The average size of prepared particles

is found to be less than 100 nm as expected from the emission characteristics.[30] TEM images of **GQDs** are obtained by drop casting 0.05 mg/ml water suspension on TEM copper grid and images obtained are shown in Figure 3.5B. The images confirmed the successful formation of nano-sized graphene sheets.

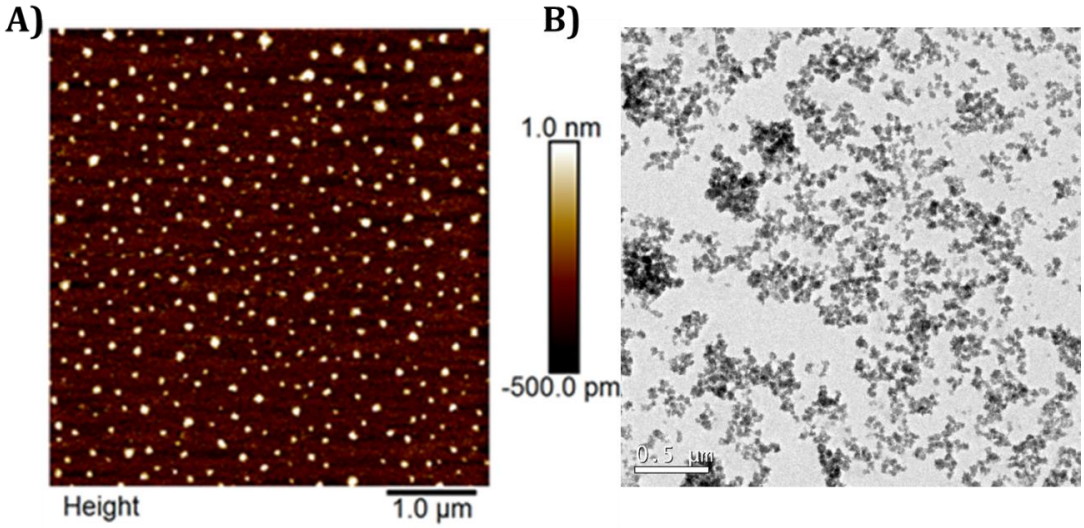

Figure 3.5. A) AFM image of as synthesized **GQDs**. The images were obtained by coating **GQDs** on a freshly cleaved mica surface using 0.1 mg/mL water solution of **GQDs**. B) High resolution TEM images of **GQDs**.

GQDs were further characterized by FTIR and DLS analysis. FTIR spectra of GQDs confirm the presence of several oxygen functionalities such as carboxylic acid (1735 cm^{-1}) and aldehydic groups present mainly on the edges (Figure 3.6A).[31] It also shows a prominent peak corresponding to C=C at 1600 cm^{-1} and a broad peak around 3200 cm^{-1} corresponding to O-H stretching arising from carboxyl and hydroxyl functionalities. Zeta potential of **GQDs** were measured using DLS analysis and is found to be -41 mV, which also indicate the presence of oxygen functionalities on the **GQD** surface (Figure 3.6B).

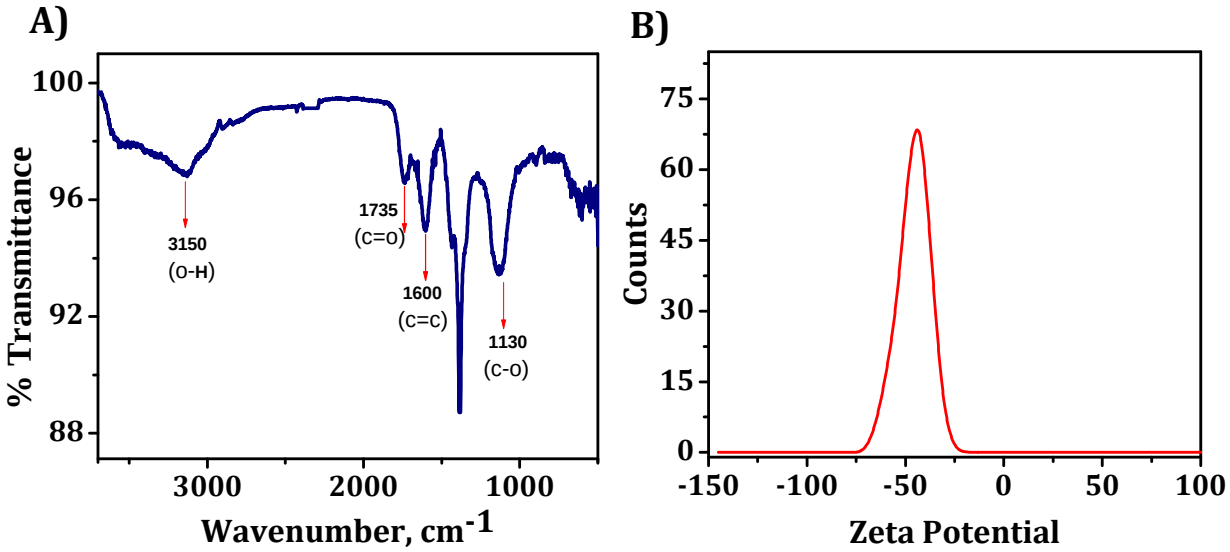

Figure 3.6. A) FTIR and B) Zeta potential analysis of **GQDs**

3.3.2. Synthesis of BDPA

The synthesis of diiodo-BODIPY derivative, **BDPA** is carried out as per Scheme 3.2. The synthesis started from the 4-hydroxy benzaldehyde which upon reaction with N-phthalimide protected 3-bromopropan-1-amine to five compound **2.**[32] This derivative upon reaction with 2,4 dimethyl pyrrole in presence of TFA, DDQ and BF_3-Etherate in DCM under room temperature gave the corresponding BODIPY derivative **3**, in moderate yield. [32] This BODIPY core is iodinated using NIS in chloroform / acetic acid mixture (3:1) and then the amino moiety was introduced by subsequent deprotection of the phthalimide protecting group using hydrazine.[33] **BDPA** was characterized using ^{1}H NMR and mass analysis and used for further reaction with **GQDs**. **BDPA** was found to be soluble in organic solvents such as chloroform, methanol, DMF, DMSO and partially soluble in water. The molar extinction coefficient of **BDPA** at 530 nm in methanol was calculated as 66000 $M^{-1}cm^{-1}$.

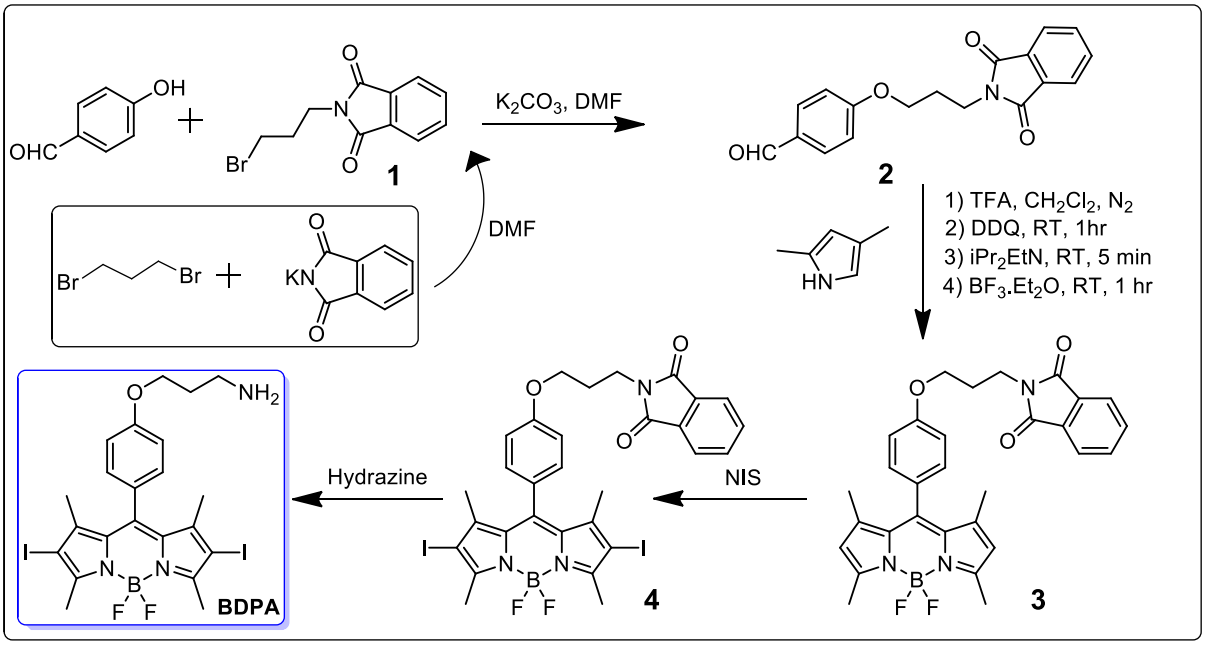

Scheme 3.2. Synthesis of **BDPA**

3.3.3. Synthesis and characterization of GQD-BDPA

Graphene Quantum Dot-BODIPY nanoconjugate, **GQD-BDPA** was synthesized by EDC-mediated coupling of **GQDs** with an amino functionalized BODIPY derivative, **BDPA** as shown in Scheme 3.3. **GQDs** contain several carboxylic acid functional groups on the edges and basal planes of graphene, which can form amide linkages with amine functionalized substrates. The reaction was carried out in water / DMF mixture (9:1) and the product was isolated by centrifugation at 13000 rpm. The product was further purified by subsequent washings with chloroform and methanol to remove traces of starting material (mainly free **BDPA**) adsorbed on the **GQDs** surface. After drying under ambient conditions, **GQD-BDPA** nanosheets were re-suspended in water by sonication to give a stable colloidal solution of **GQD-BDPA**. Suspension of **GQD-BDPA** in water was found to be stable for several days compared to poorly soluble **BDPA**. As prepared

nanoconjugate also form stable suspensions in organic solvents such as methanol, DMF and DMSO.

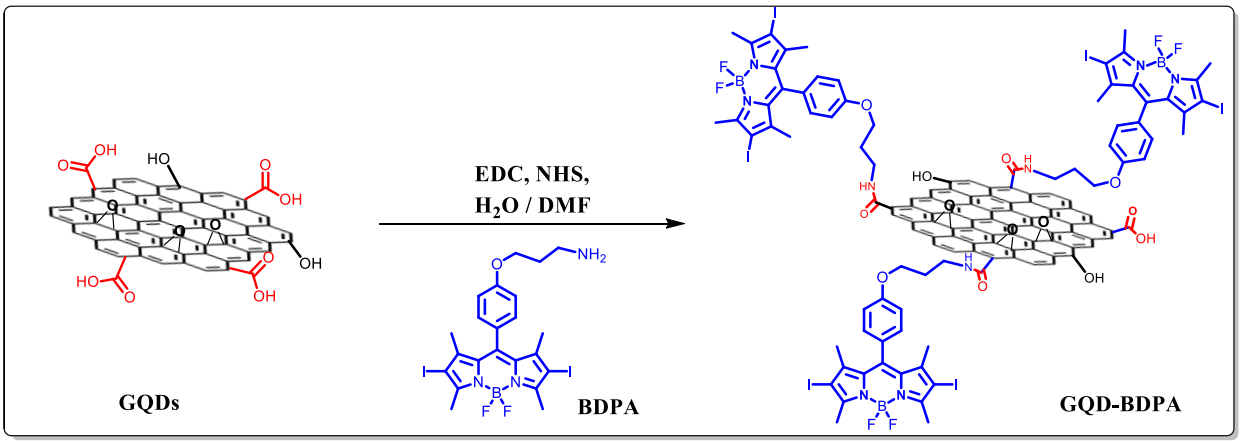

Scheme 3.3. Synthesis of **GQD-BDPA** nanoconjugate.

3.3.4. Material Characterization of GQD-BDPA

Covalent functionalization of **BDPA** on **GQDs** was confirmed by FT-IR spectroscopy and DLS analysis. The FT-IR spectrum of **GQDs** (Figure 3.7A) confirms the presence of several oxygen functionalities such as carboxylic acid (1735 cm^{-1}) and aldehydic groups present mainly on the edges. EDC coupling of **BDPA** with **GQDs** resulted in the conversion of carboxylic acid functionalities of **GQDs** to amide linkages, the formation of which is evident from the new 1650 cm^{-1} IR broad absorption peak of the synthesized nanoconjugate. FT-IR spectra of the sample also show other peaks corresponding to that of **BDPA** indicating the successful attachment of the sensitizer to the **GQD** sheets.

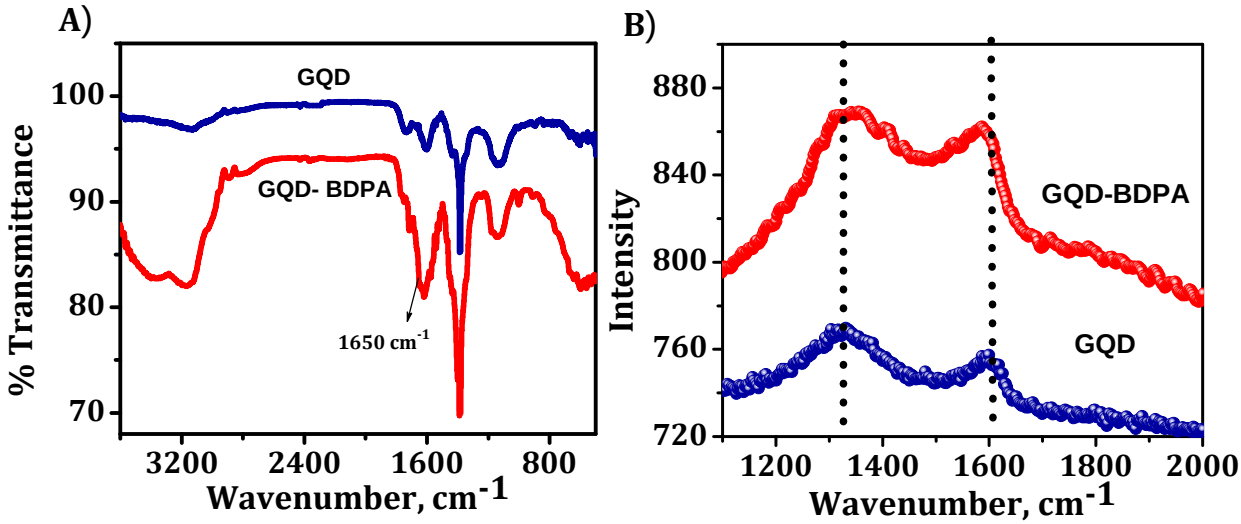

Figure 3.7. A) FT-IR and B) Raman spectra of **GQDs** and **GQD-BDPA**

The Raman spectra of **GQDs** and **GQD-BDPA** are shown in Figure 3.7B. The graphitic materials show two typical bands at 1350 cm^{-1} (D band) due to defects and 1580 cm^{-1} (G band) corresponding to the in-plane vibration of sp^2 C atoms. **GQDs** and the nanoconjugate exhibit both characteristic bands with I_D/I_G value of 1.28 and 1.30 respectively. Compared to **GQDs**, the **GQD-BDPA** showed significant redshift for G bands (~15 cm^{-1}) from 1602 cm^{-1} to 1587 cm^{-1}. The red-shift in Raman band could be attributed to the functionalization of **GQDs** with **BDPA** molecules.[34]

Average sizes of prepared **GQDs** particles were found to be 60-80 nm, obtained from TEM and AFM analysis (Figure 3.8). HRTEM image (Inset) of a single nanosheet with clearly visible lattice fringes, indicates the graphene-like atomic arrangement in the synthesized nanoparticles. The microscopic characterization of **GQD-BDPA** confirms the intact nanosheets structures even after the reaction with **BDPA** and have a similar size distribution as that of the precursor, **GQDs**.

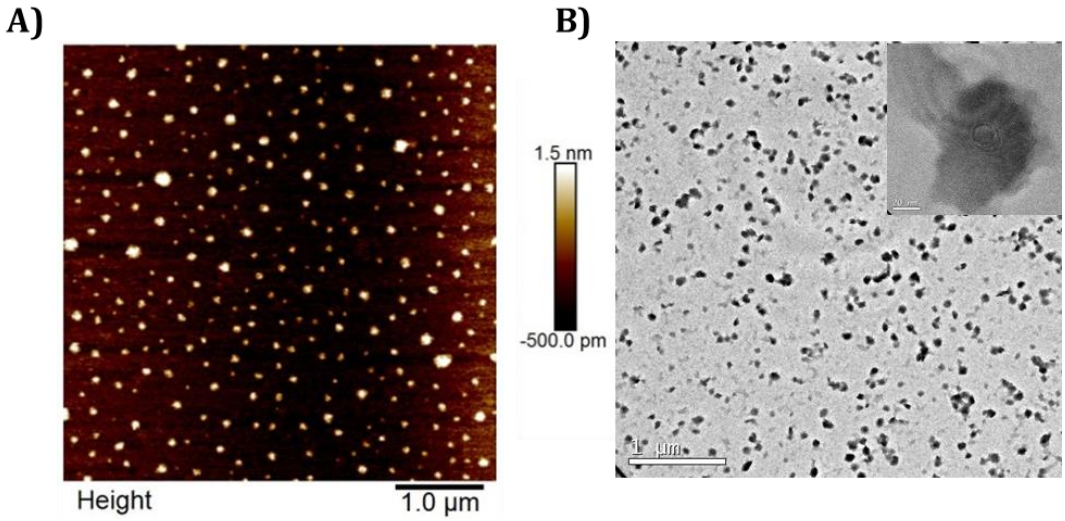

Figure 3.8. A) AFM and B) TEM images of **GQD-BDPA**.

3.3.5. Photophysical Characterization of GQD-BDPA

The synthesized **GQDs** and its nanoconjugates are further subjected to photophysical characterization using UV-Visible and fluorescence spectroscopy. UV-Vis spectra of the nanoconjugate, **GQD-BDPA** shows considerable absorption corresponding to **BDPA** in the 480-600 nm region even after the extensive washing process indicating the successful attachment of **BDPA** on **GQDs** (Figure 3.9A). Notably, the absorption maximum of **BDPA** in **GQD-BDPA** is red shifted from 530 nm to 550 nm (shift ~20 nm), which indicate the presence of strong electronic interaction between them. The **BDPA** loading content in the nanoconjugate was determined through absorption spectroscopy and the weight of the sensitizer is calculated to be ~4.4%.

Normalized emission spectra of the **GQDs**, and the nanoconjugate recorded by 350 nm excitation in water, are shown in Figure 3.9B. **GQD-BDPA** in water showed a broad emission from 400 nm to 700 nm with a maximum at 530 nm upon excitation at

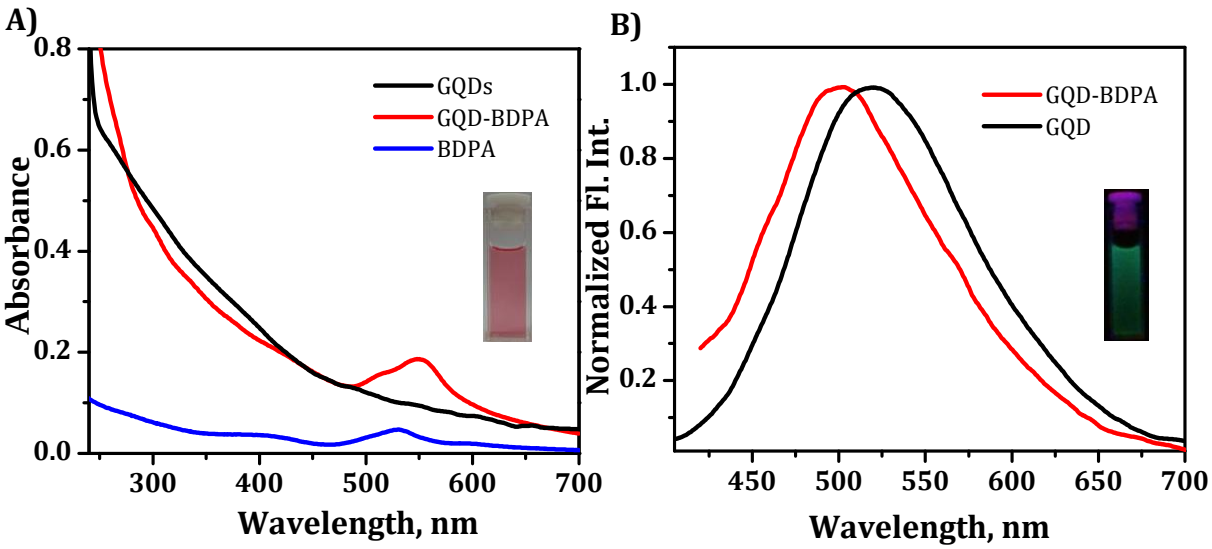

Figure 3.9. A) Absorption spectra of **GQDs, BDPA** and **GQD-BDPA** in water. B) fluorescence spectra of **GQD** and **GQD-BDPA**. Fluorescence spectra are normalized and recorded by excited at 350 nm light.

350 nm. Fluorescence quantum yield of nanoconjugate (1.02%) is found to be slightly quenched compared to that of **GQDs** (1.1%) with a considerable blueshift of 20 nm. This is in accordance with reported literature that surface modifications can alter the luminescence properties of **GQDs**.[35] Surface passivation of **GQDs** can result in the blue shift in emission, which further confirms the successful formation of the covalent conjugate. It is noted that the **GQDs** alone contribute to the entire observed fluorescence in nanoconjugate, whereas, BODIPY derivative shows only negligible fluorescence.

3.3.6. Quantification of Triplet Excited States

To understand the transient intermediates involved during the excitation of **BDPA** and **GQD-BDPA** conjugates, we have carried out nanosecond laser flash photolysis studies using a 532 nm laser pulse excitation. Figure 3.10 shows the

transient absorption spectrum of the **BDPA** and **GQD-BDPA** obtained after the laser excitation in methanol. The transient absorption spectrum showed a maximum at 460 nm with bleach at 530 nm, where the compound has significant ground state absorption. The lifetime of the transient was determined from the decay profile (Inset, Figure 3.10) and it was found to be 0.49 μs and 0.55 μs for **BDPA** and **GQD-BDPA** respectively. The triplet excited state yields (Φ_T) of the samples, **BDPA** and **GQD-BDPA**

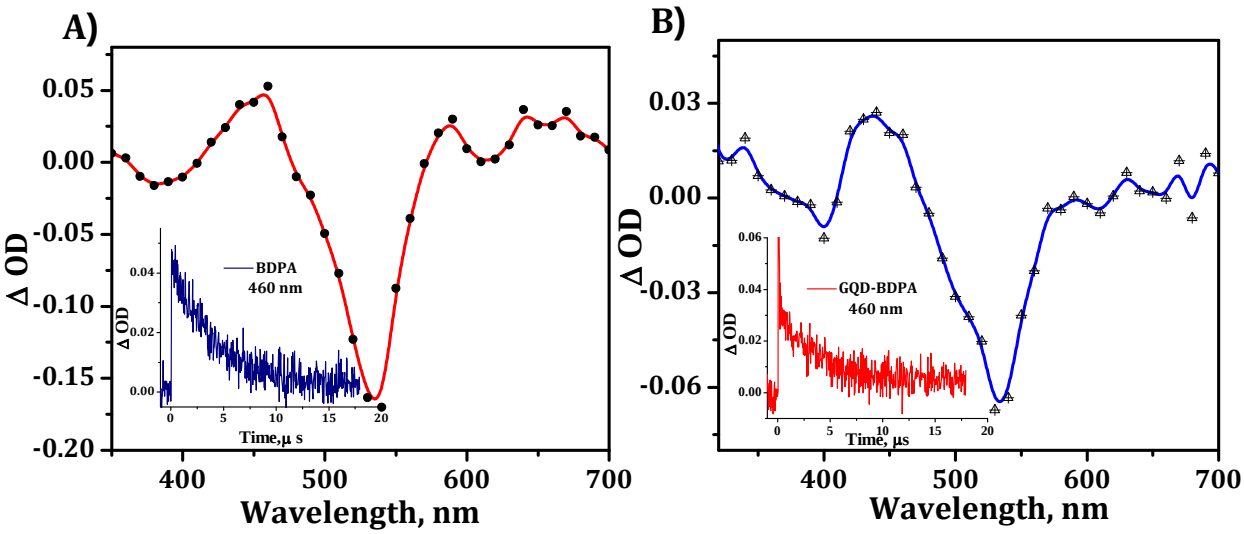

Figure 3.10. Transient absorption spectra of A) **BDPA** and B) **GQD-BDPA** excited at 532 nm LASER. Triplet decay at 460 nm is shown in inset.

were determined to be 0.90±0.01 and 0.94±0.02 respectively, by an earlier reported procedure of energy transfer to β-carotene, using $Ru(bpy)_3^{2+}$, as the reference molecule. The transient absorbance of the β–carotene triplet, generated by the energy transfer from $Ru(bpy)_3^{2+}$ or the triplet of the sample, was monitored at 510 nm. Comparison of plateau absorbance (ΔA) following the completion of sensitized triplet formation, properly corrected for the decay of the donor triplet excited state in competition with energy transfer to β-carotene, enabled us to estimate Φ_T of the triplet excited states.

3.3.7. Quantification of Singlet Oxygen Generation

In order to check the efficacy of nanoconjugates for PDT applications, we have studied the singlet oxygen generation efficiency of free sensitizer, **BDPA** and **GQD-BDPA** conjugate using 1,3-diphenylbenzofuran (DPBF) as a singlet oxygen trapping agent. An optically matching solution of the sample and the standard were irradiated using oriel lamp fitted with a 475 nm long pass filter at regular intervals followed by absorption measurements. Singlet oxygen generation efficiency of **BDPA** and **GQD-BDPA** were calculated as 85% and 91% respectively using Rose Bengal (80%) as a standard (Figure 3.11A & 3.11B).[36] The observed singlet oxygen efficiencies of **BDPA** and the nanoconjugate are comparable to the reported diiodo-BODIPY based sensitizers,[24] whereas **GQD** alone is not showing singlet oxygen generation under similar experimental setup. Generation and efficiency of singlet oxygen by samples were further confirmed by observed phosphorescence at 1270 nm, which is characteristic of singlet oxygen (Figure 3.11D). By comparing the peak area of optically matching solutions of samples and Rose Bengal as a reference, it is found that **GQD-BDPA** is showing more singlet oxygen generation ability. The iodinated core of **BDPA** could increase the rate of ISC *via* heavy atom effect which in turn sensitizes more triplet oxygen. Results indicate that our nanoconjugate is highly efficient in producing singlet oxygen which is a key requirement of a sensitizer for PDT applications.

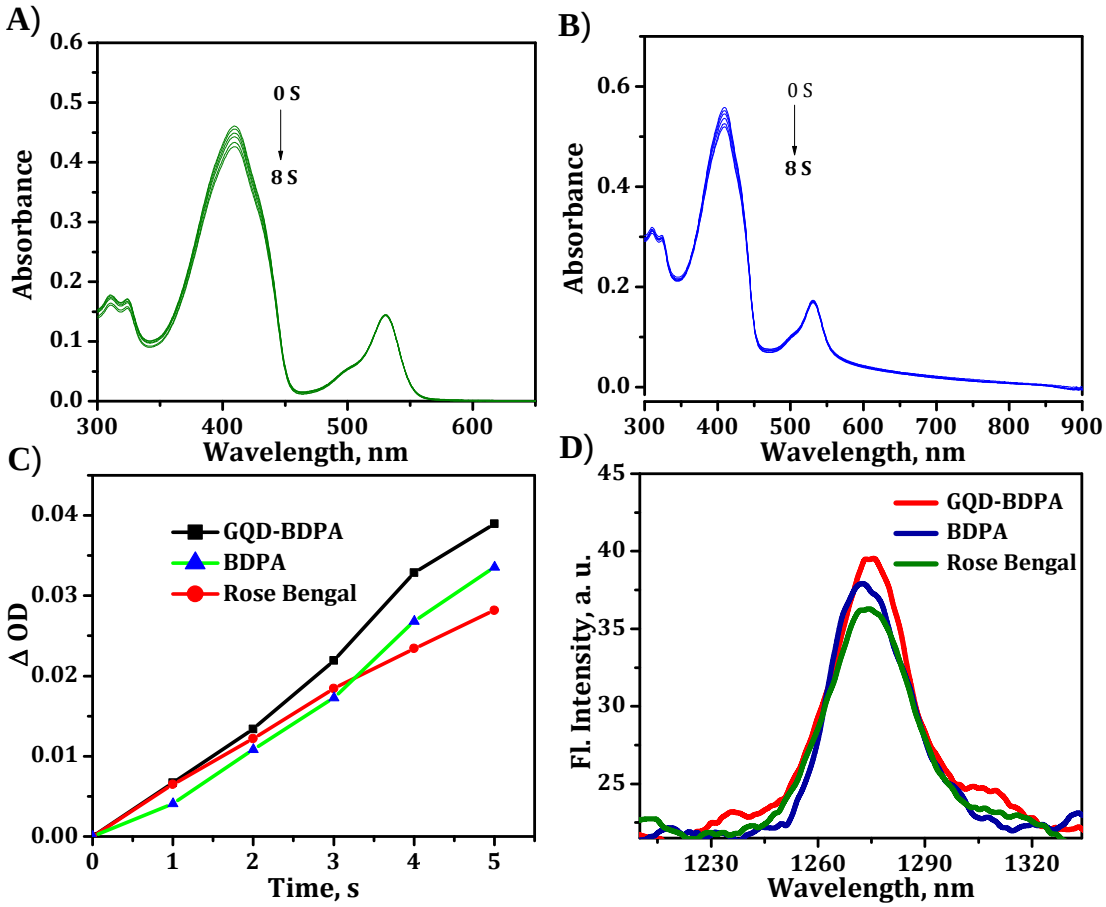

Figure 3.11. A) The decrease in the absorption of DPBF (410 nm) of **BDPA**, B) **GQD-BDPA** sample upon 1 s irradiation using 200 W mercury lamp (model 3767) on an Oriel optical bench (model 11200) fitted with 475 nm long pass filter. C) Relative plot of singlet oxygen generation efficacy of **BDPA** and **GQD-BDPA** with the standard Rose Bengal. D) Singlet oxygen luminescence spectrum of the **BDPA**, **GQD-BDPA** and the Rose Bengal after the excitation at 530 nm.

3.3.8. DNA Interaction Studies of BDPA and GQD-BDPA

We have further analyzed the interaction of this nanoconjugate with DNA, which is vital for the better understanding of the extent of dark toxicity of nanomaterials in normal cells and it can give insight to their PDT mechanism. Here we studied the interactions of sensitizer (**BDPA**) alone and its graphene conjugate with CT-DNA.

Binding properties of **BDPA** and **GQD-BDPA** toward CT-DNA was studied by absorption titration experiments. Absorption titration is one of the simplest and most useful methods to investigate the binding interactions of molecules, particularly towards DNA. Figure 3.12A shows the absorption changes of **BDPA** by addition of upto 31.5 μM CT-DNA. The decrease in the **BDPA** absorbance indicates its interaction with DNA, possibly through intercalation. On the other hand **GQD-BDPA** doesn't show much change in absorbance upon interaction with even high concentration of CT-DNA. This decreased interaction of conjugate is expected as the **BDPA** chromophore is now part of the **GQD-BDPA** nanoconjugate and steric interaction may hinder the binding of **BDPA** moiety to CT-DNA (Figure 3.12B).

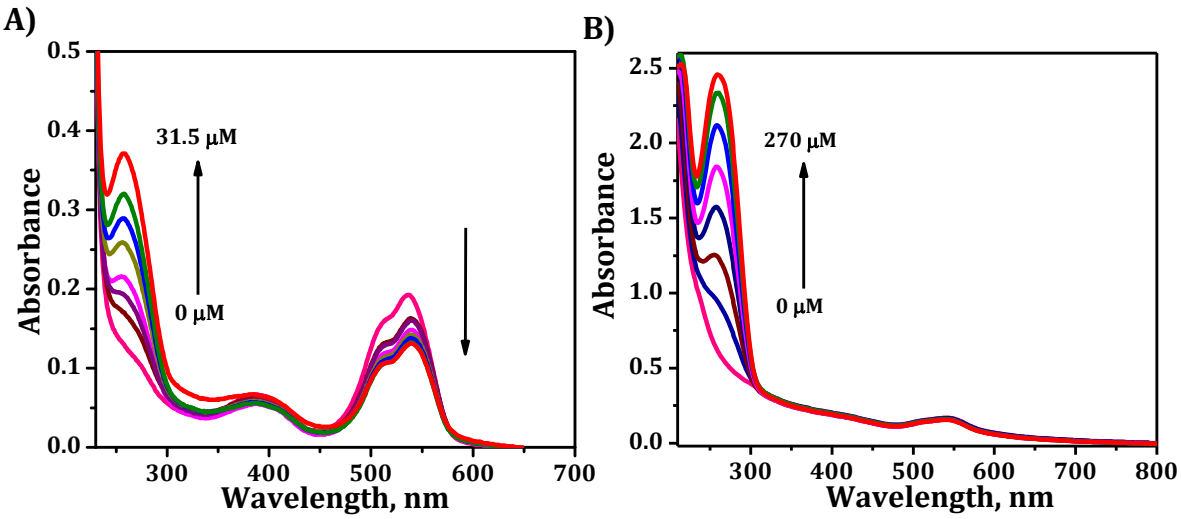

Figure 3.12. A) Absorption changes of BDPA (9 μM) on titration of CT-DNA (0-31.5 μM) in PBS buffer 0.01 mM. B) Absorption changes of GQD-BDPA (100 μg/mL) on titration with CT-DNA (0-270 μM)

An ethidium bromide displacement assay was carried out to determine the mode of interaction as well as the apparent binding constant K_{app} of **BDPA** and its GQD

conjugate towards CT-DNA. Ethidium bromide is a well-known intercalator for DNA helix which can give an enhanced emission upon binding with DNA. Another efficient intercalator can displace EtBr from DNA leads to decrease in fluorescence intensity of EtBr. On addition of **BDPA** to EtBr/DNA solution, EtBr fluorescence was quenched effectively due to its displacement from DNA (Figure 3.13A). The apparent binding affinity K_{app} of **BDPA** is calculated as 1.2 x 10^7 M^{-1}, from the concentration of the **BDPA** at 50% reduction of EtBr fluorescence and from the binding constant of EtBr towards CT-DNA (1 x 10^7 M^{-1}).[37] In order to compare this interaction with that of **GQD-BDPA**, similar titration experiment with a higher concentration of conjugate (100 µg/mL) was carried out. Nanoconjugate exhibited only negligible decrease in the EtBr fluorescence intensity, which indicates **GQD-BDPA** cannot intercalate to DNA for EtBr displacement. This result is obvious from the bigger size of **GQD-BDPA** compared to a small molecule like **BDPA**. These results provide an insight that conjugation with **GQDs** not only

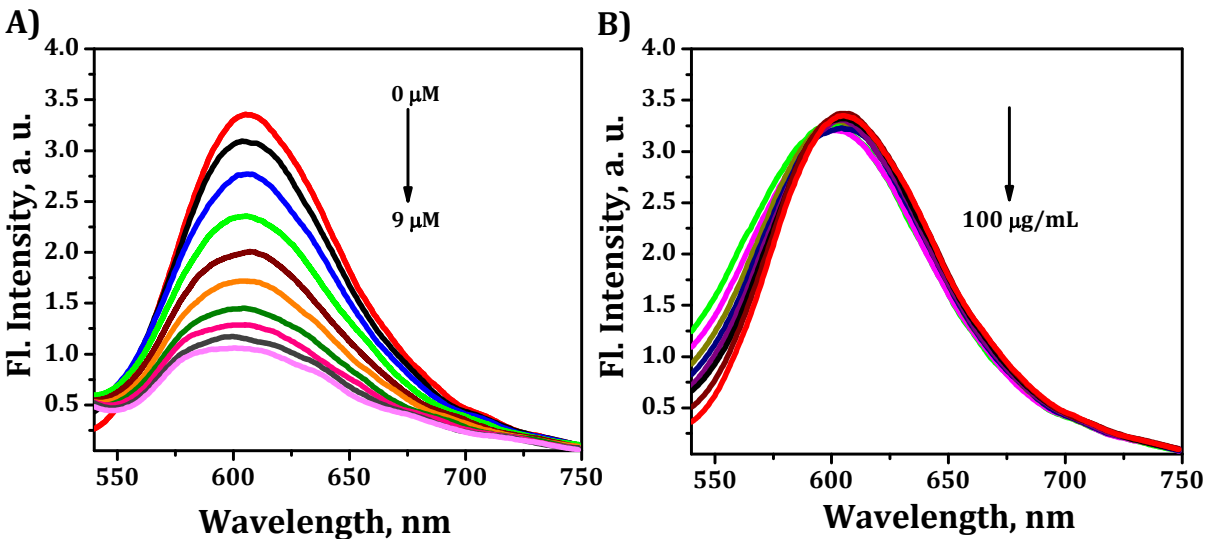

Figure 3.13. A) Fluorescence quenching of EtBr (6 uM) – CT-DNA (22 µM) in 0.01 mM PBS by **BDPA** (up to 9 µM) and B) Fluorescence changes by **GQD-BDPA** (upto 100 µg/mL).

enhances the solubility and cellular internalization, also can effectively reduce the chance of interaction with DNA present in normal cells thereby decreasing the dark toxicity of the drug.

3.3.9. Investigation of *in vitro* Photobiological Properties

To investigate the photodynamic activity of the synthesized nanoconjugate in cancer cells, *in vitro* studies on cancer cell lines were carried out. MTT assay was done in MDA-MB-231 cells (Breast cancer cells) and the percentage of growth inhibition of cells in the presence of **GQD-BDPA** and the control samples such as **GQD** and **BDPA**

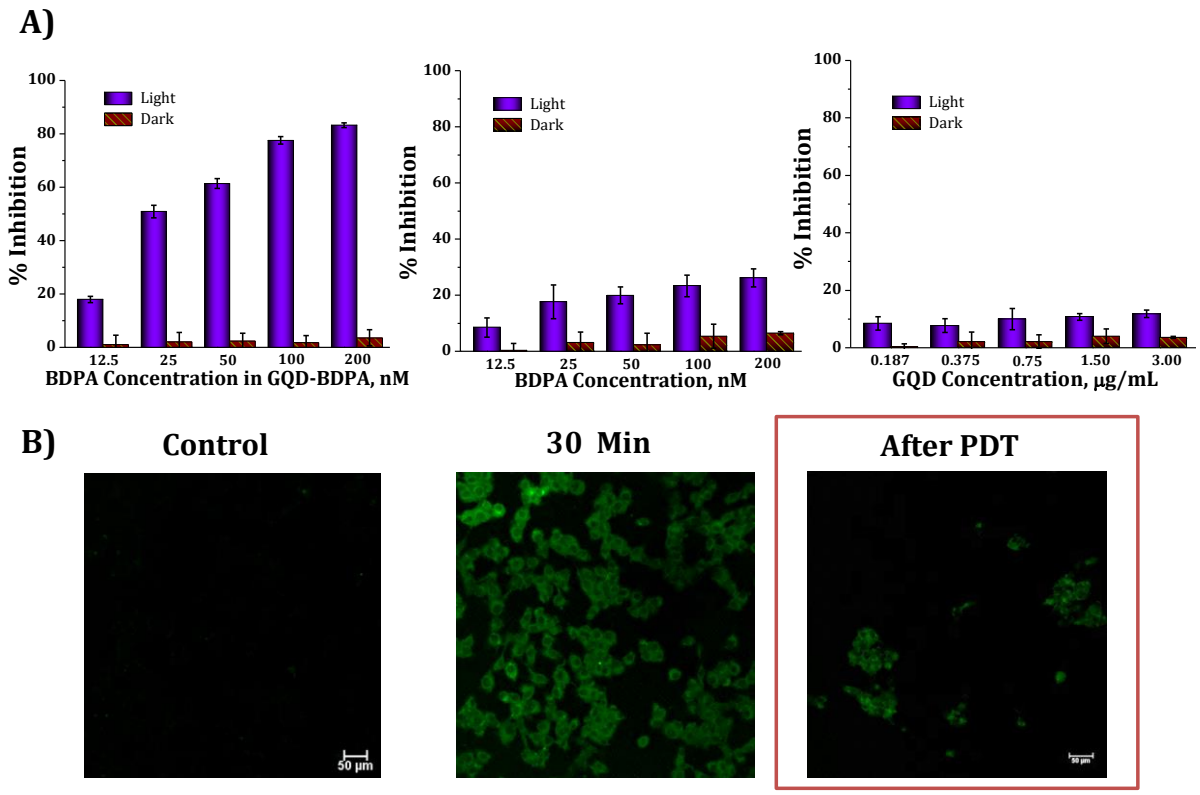

Figure 3.14. A) MTT assay showing photocytotoxicity of **GQD-BDPA**, **BDPA** and **GQD** in MDA-MB 231 breast cancer cells. B) Confocal microscopic images of MDA-MB-231 cell lines using **GQD-BDPA** before and after PDT.

alone were determined with and without irradiation (PDT lamp, 540 nm, Green LED array with a total fluence rate of 100 J/cm^2, Figure 3.14 A). The result shows that **GQD-BDPA** is a better candidate for PDT with an IC_{50} value of 30 nM (sensitizer concentration) whereas a negligible change in growth inhibition was observed in both **GQD** and **BDPA** alone at similar concentration range. We have further examined cellular internalization and the fluorescence imaging capability of this nanoconjugate on MDA-MB-231 cell lines. Green luminescent **GQD-BDPA** is found to be efficient in imaging these cell lines upon excitation at 360 nm (Figure 3.14B), which confirms the efficacy of these conjugate for imaging guided PDT applications.

The cytotoxic effect of a photosensitizer is predominately through ROS mediated cell death. Hence we studied cellular oxidative stress in **GQD-BDPA** based PDT using

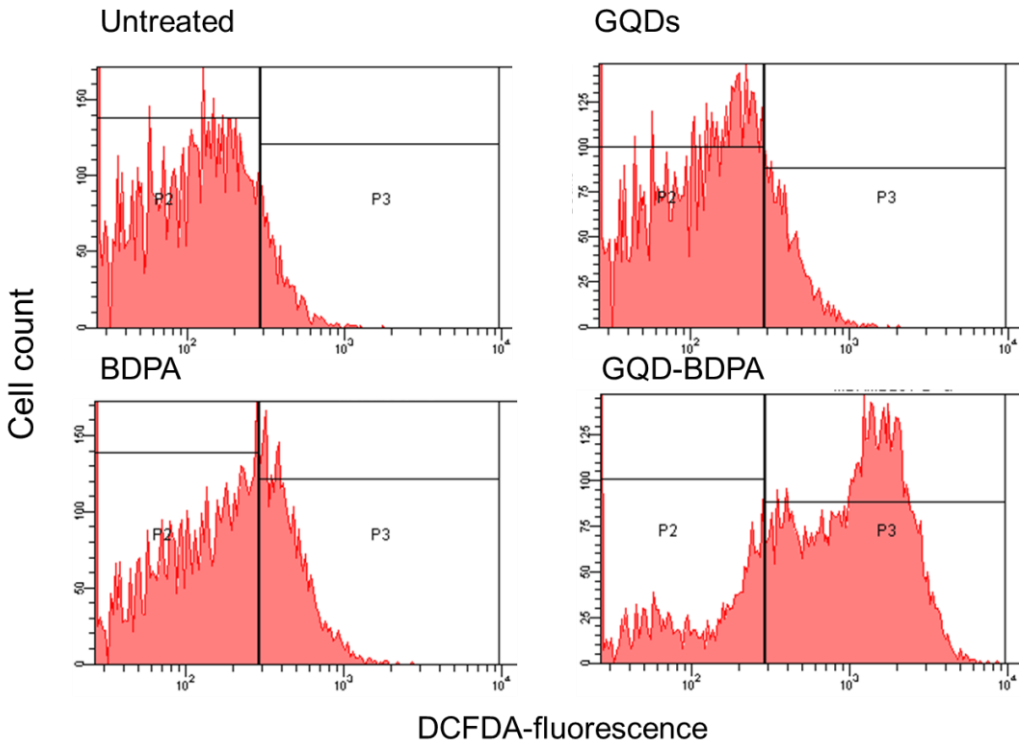

Figure 3.15. Flow cytometry analysis of MDA-MB-231 cells, showing induction of intracellular ROS by untreated, **GQD**, **BDPA** and **GQD-BDPA** after PDT.

flow cytometric analysis with CM-H2DCFDA probe. In the reduced form, CM-H2DCFDA is non-fluorescent, but after cellular oxidation followed by esterases mediated hydrolysis of acetate groups, results in a green fluorescent derivative.[38] When MDA-MB-231 cells were treated with **GQD-BDPA** and irradiated, followed by the addition of CM-H2DCFDA, we observed fluorescence in 76.9% of cells, In contrast, **GQD** alone and **BDPA** alone showed background values of 15.1% and 30.7%, respectively (Figure 3.15). These results demonstrate that PDT with **GQD-BDPA** nanoconjugate induced a significant subcellular ROS generation leading to oxidative stress in MDA-MB-231 cells.

In order to understand the mechanism of cell death as well as the efficiency of our nanoconjugate for PDT treatment, we carried out a nuclear condensation assay using MDA-MB-231 human breast cancer cells. The cell lines were stained with Hoechst dye, specific dye for viable cells. The decrease in blue fluorescence intensity after PDT treatment with **GQD-BDPA** (30 nM, sensitizer concentration) was observed to be augmented compared to free **BDPA** sensitizer and **GQD**s alone, which further confirms the greater efficiency of the nanoconjugate (Figure 3.16A). The nature of cell death was confirmed through tetramethylrhodaminemethyl ester (TMRM) staining experiment, as shown in Figure 3.16B. The apoptotic cell death causes decrease in the mitochondrial inner membrane potential, which will result in further decrease of red fluorescence of TMRM. Photodynamic treatment of nanoconjugate with MDA-MB-231 cell lines caused a decrease in red fluorescence of TMRM, which confirms the cell death through the mitochondria-mediated apoptotic pathway. Added to this, the cell viability test has been done using Acridine orange / propidium iodide (AO/ PI) staining. AO/PI staining which

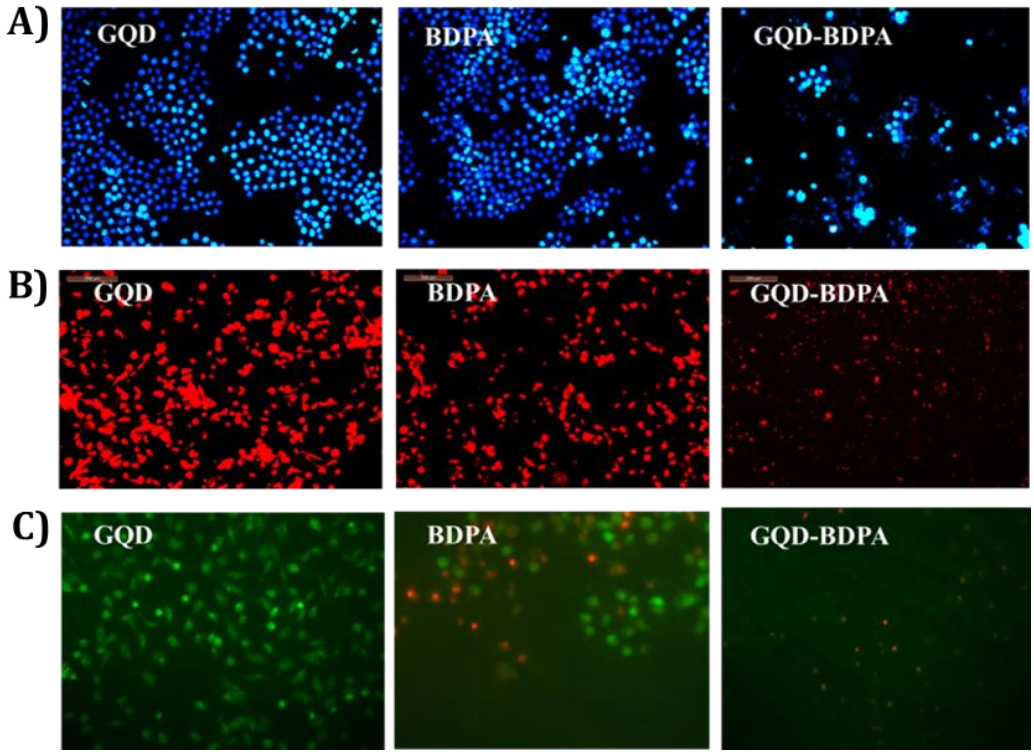

Figure 3.16. A) Hoechst staining and B) TMRM assay and C) propidium iodide assay, with MDA-MB-231 cell lines, each panel showed the cells under **GQD**, **BDPA** and **GQD-BDPA** after PDT analysis (30 nM sensitizer concentration).

has been used to visualize the nuclear changes and apoptotic body formation that forms the characteristic feature of apoptosis. Acridine orange permeated in all live cells and appeared green, while propidium iodide was taken up only by cells when cytoplasmic membrane integrity is lost and stains the nucleus red. However, an increase in the red fluorescence intensity after the PDT treatment with GQD-BDPA was identified, compared to free BDPA sensitizer and GQD alone indicating that the cell has undergone apoptosis and this could be easily monitored by inverted fluorescent microscopy (Figure 3.16C).

To understand the mechanism behind PDT activity and cellular damage induced by **GQD-BDPA**, we investigated the apoptotic potential of the nanoconjugate using

Annexin V-FITC/PI flow cytometric analysis as shown in Figure 3.17. The lower left quadrant (Q3) of the panel shows the viable cells, negative for both Annexin V– FITC and PI. The lower right quadrants (Q4) represent the early apoptotic cells Annexin V– FITC and Propidium iodide (PI). The upper right quadrants (Q2) represent the late apoptotic cells positive for Annexin V– FITC and Propidium iodide (PI).[39] Cell populations at different phases of cell death, namely, viable (AnnexinV-FITC (– ve)/PI (– ve)), early apoptotic (Annexin V-FITC (+ ve)/PI (– ve)) and necrotic or late-stage apoptotic (Annexin V-FITC(+ ve)/PI(+ ve) were examined using different drug concentration after 24 hours of PDT and the results revealed that PDT using

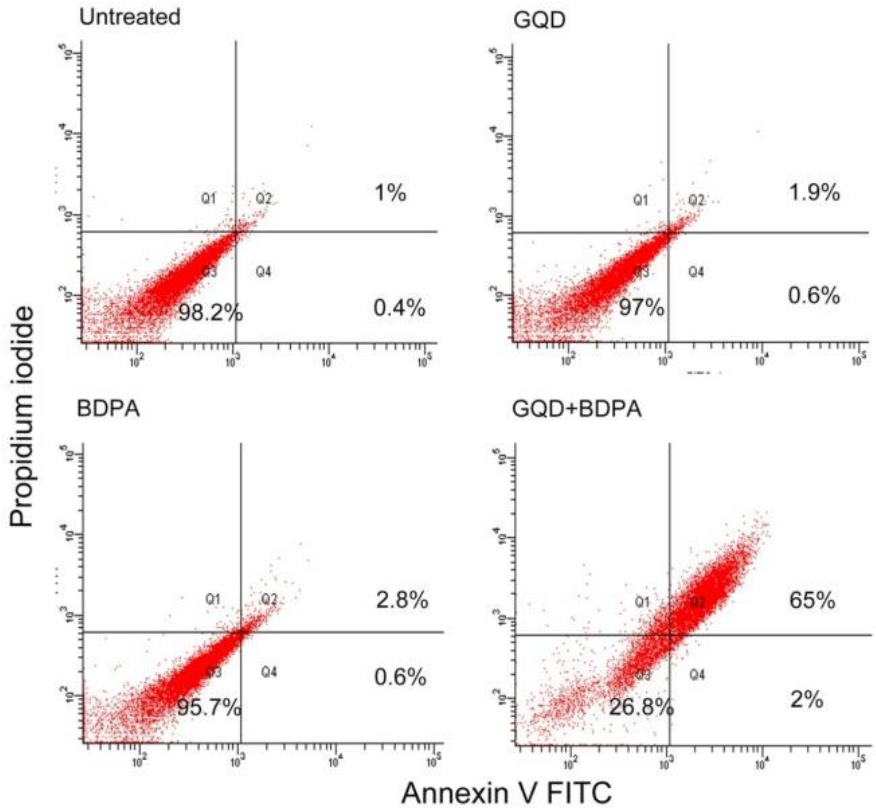

Figure 3.17. Apoptotic induction of **GQD-BDPA** after PDT treatment. Annexin Flow cytometric analysis of MDA-MB-231 cells after PDT treatment with light control and dark control and in presence of **GQD**, **BDPA** and **GQD-BDPA** at a concentration of 30 nM.

GQD-BDPA (30 nM) induces late apoptosis of about 65% whereas, **GQD** and **BDPA** alone showed only 1.9% and 2.8% late apoptotic cells respectively. This result confirmed that major cell death induced by **GQD-BDPA** is *via* apoptosis.

3.3.10. Synthesis and Characterization of GQD- BODIPY Mixed Derivatives

In order to improve the luminescence properties of this nanoconjugate for image-guided PDT applications, we have adopted a mixed BODIPY derivative (**GQD-BDPA-MIX**) coupling strategy by incorporating fluorescent BODIPY derivative (**BDPA-FL**) along with **BDPA** on **GQDs** *via* EDC-NHS reaction (Figure 3.18A). Presence of **BDPA-FL** can make conjugate more fluorescent and **BDPA** efficiently generate singlet oxygen upon excitation. We have synthesized three types of derivatives by varying the ratio of **BDPA-FL** and **BDPA** (1:5, 1:1 and 5:1) on reaction with **GQDs** and carried out its photophysical characterization as well as singlet oxygen generation studies in detail.

As synthesized GQD-BODIPY derivatives were characterized using UV-Visible absorption and fluorescence spectroscopy. Absorption spectra of nanoconjugates show considerable absorption corresponding to both BODIPY derivatives in the 480-600 nm regions even after extensive washing process indicating the successful attachment of BODIPY derivatives on **GQDs** (Figure 3.18B). Emission spectra of all derivatives are recorded by exciting at 350 nm light. Emission intensity is found to be accordance with the amount of fluorescent **BODIPY** derivative present in the sample (Figure 3.18C).

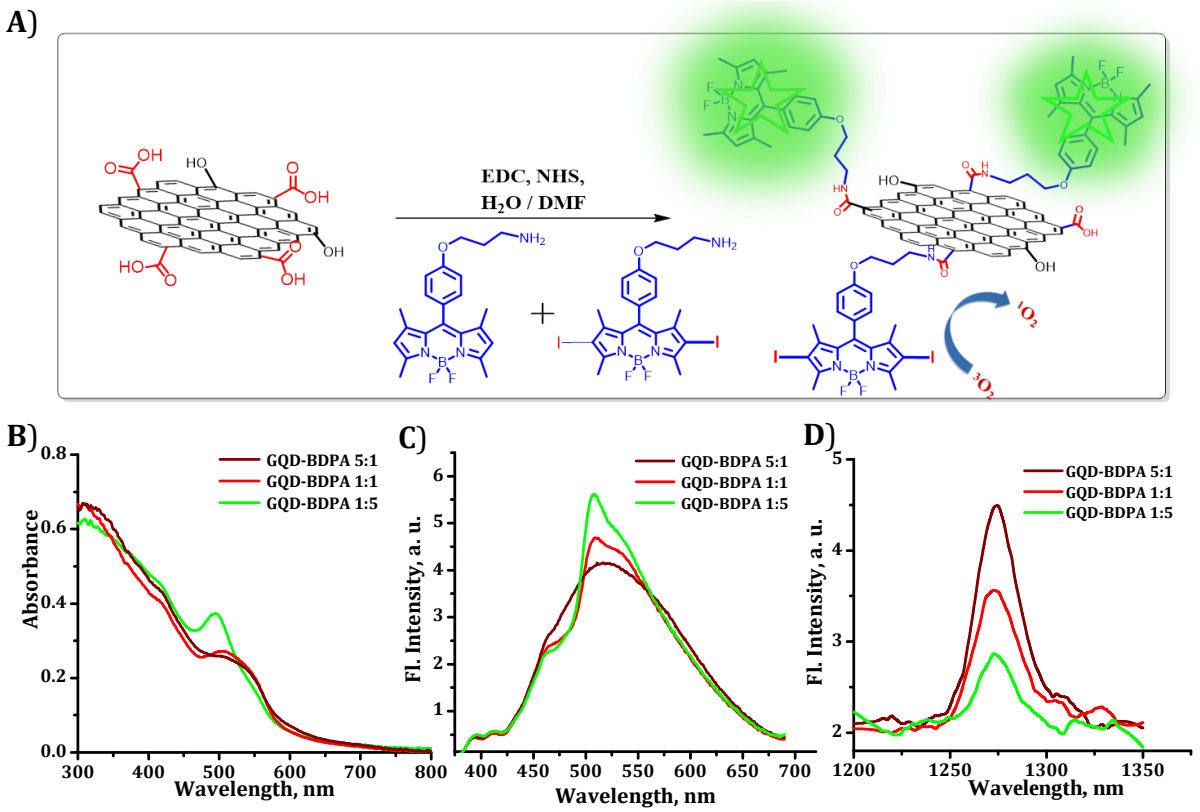

Figure 3.18. A) Schematic representation for the synthesis of **GQD-BDPA-MIX**. B) Absorption C) Emission and D) singlet oxygen luminescence spectrum of **GQD-BDPA-MIX** derivatives.

Singlet oxygen generation ability of synthesized nanoconjugates was confirmed using NIR-fluorescence spectrometer by recording phosphorescence emission of singlet oxygen at 1270 nm. All derivatives showed emission peak at 1270 nm due to the presence of **BDPA** and intensity increases with **BDPA** concentration in the sample (Figure 3.18D). These results show that these mixed derivatives can be used for image guided PDT applications. We have successfully utilized this green luminescent material for *in vitro* cellular imaging applications on MDA-MB-231 cells. The images obtained before and after PDT treatment is shown in Figure 3.19. Nanoconjugate is exhibiting

excellent cellular internalization even at 30 minutes of incubation of samples and which could be easily tracked by confocal fluorescence imaging techniques.

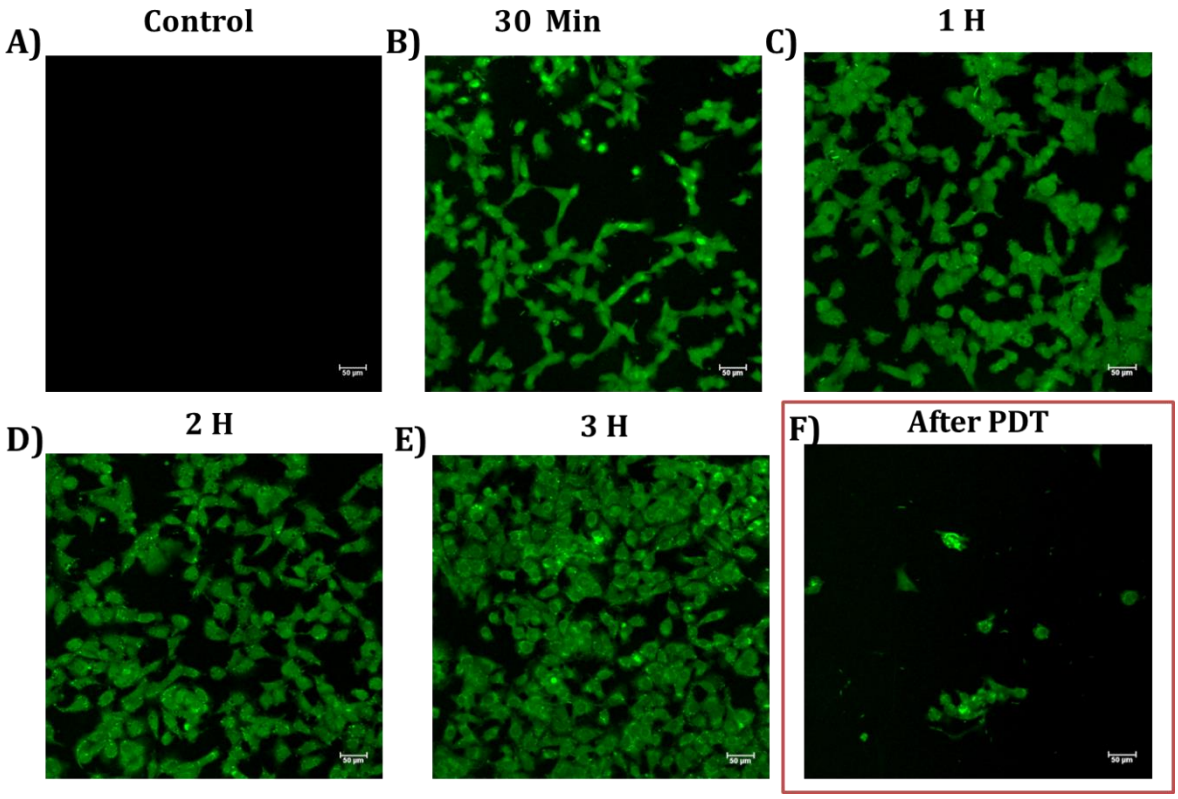

Figure 3.19. Confocal images of MDA-MB-231 cells after incubation with **GQD-BDPA-MIX**. A) Control, B) after 30 mins, C) after 1 hours, D) after 2 hours, E) after 3 hours and F) after PDT treatment. (540 nm, Green LED array with a total fluence rate of 100 J/cm^2)

3.4. Conclusions

In summary, we have designed and synthesized a graphene quantum dot-BODIPY sensitizer nanoconjugate, **GQD-BDPA** and characterized the structural and photophysical properties through spectroscopic, analytic and microscopic techniques. **GQDs** with lateral dimensions of ~50 nm were prepared *via* oxidative cutting of larger as-prepared graphene oxide sheets using concentrated nitric acid. Further conjugation of **GQDs** with core iodine substituted BODIPY amine derivative, **BDPA** was achieved

through EDS-NHS coupling. The nanoconjugate, **GQD-BDPA** was thoroughly characterized and preliminary photophysical investigations confirmed successful conjugation of the sensitizer with **GQDs**. **GQD-BDPA** exhibited higher singlet oxygen generation quantum yield of 90%, compared to that of free **BDPA** (85%), demonstrating the potential of these nanoconjugates for PDT applications. *In vitro* PDT activity of this nanoconjugate was investigated using MDA-MB-231 cell lines and is found to be an efficient system for PDT treatment with an IC_{50} value of 30 nM (sensitizer concentration). Annexin, TMRM and nuclear condensation assay on MDA-MB-231 human breast cell lines confirmed the cell death through the late apoptotic pathway. Further modification of the nanoconjugate with fluorescent BODIPY derivative (**GQD-BDPA-MIX**) exhibited enhanced emission properties and excellent cellular imaging characteristics make it suitable for image guided PDT applications.

3.5. Experimental Section

3.5.1. Synthesis and Characterization

The reagents and materials for synthesis were purchased from Sigma-Aldrich and Spectrochem Chemical suppliers. Dry solvents were used wherever necessary and were prepared using reported drying procedures. Annexin V-FITC Apoptosis Detection Kit, CMH2DCFDA, Tetramethylrhodaminemethyl ester, hoechst, 3(4,5-dimethylthiazol-2-yl)-2,5 diphenyltetrazolium bromide (MTT), Rose Bengal (RB) were purchased from S.D. Fine chemicals, India; Sigma-Aldrich; U.S.A and Merk Chemicals, Germany.

^{1}H-NMR spectra were recorded using DPX 500 MHz spectrometer using tetramethyl silane (TMS) as the internal standard and deuterated solvents were used for the measurements. Absorption spectra were recorded on a Shimadzu UV-3101 PC UV-Vis-NIR spectrophotometer. Fluorescence spectra were collected using HORIBA SPEX-Flurolog Spectrofluorimeter and FT-IR spectra were recorded on a Shimadzu IR Prestige-21 Fourier Transform Infrared Spectrophotometer. Electron microscopic observations (TEM) of the samples were performed with a FEI Tecnai G^2-30 Transmission Electron Microscope operating at 120 kV. Atomic Force Microscopy images were recorded under ambient conditions using a BRUKER (Multimode AFM 3COCF) operating with a tapping mode regime. Micro-fabricated TiN cantilever tips (NSG10) with a resonance frequency of 299 kHz and a spring constant of 20-80 Nm^{-1} were used. AFM section analysis was done offline. Samples for the imaging were prepared by drop casting the **GQD** solution (0.05 mg/ mL) on freshly cleaved mica surface at ambient conditions. Thermo gravimetric analysis of samples is carried out using Shimadzu DTG-60 TG analyzer and the samples were heated from room temperature to 900 ˚C at a heating rate of 5 ˚C/ min in the N_2 atmosphere.

Raman analysis was carried out in a WITec Raman instrument (Witec Inc. Germany, alpha 300R) with a laser beam directed to the sample through 60× water immersion objective and a Peltier cooled CCD detector. Samples were excited with a 532 nm excitation wavelength laser and Stokes-shifted Raman spectra were recorded with 1 cm^{-1} resolution. WITec Project plus (v 2.1) software was used for data evaluation.

3.5.1.1. Synthesis of Graphene Quantum Dots (GQDs) by acid treatment

Graphene oxide (GO) was used as a precursor for the synthesis of graphene quantum dots. GO was synthesized from graphite via well-known modified Hummers method as explained in the previous Chapter.[40] Graphite Oxide (50 mg) was added to 20 ml water and ultra-sonicated for 1 hour until it became a clear solution. To this, added concentrated nitric acid (50 ml) and concentrated sulphuric acid (10 ml) and heated to 120 ˚C, fitted with water cooled condenser. It is kept for stirring over 48 hrs. The solution was cooled and the clear brown solution obtained is neutralized with NaOH flakes. The excess salt formed was removed by filtration and the resulting solution was purified by dialysis for 3 days with frequent change of water. Desalted **GQDs** were dried and used for further reactions.

3.5.2. *Synthesis of BODIPY amine, BDPA*

3.5.2.1. *Synthesis of Bromopropylphthalimide*

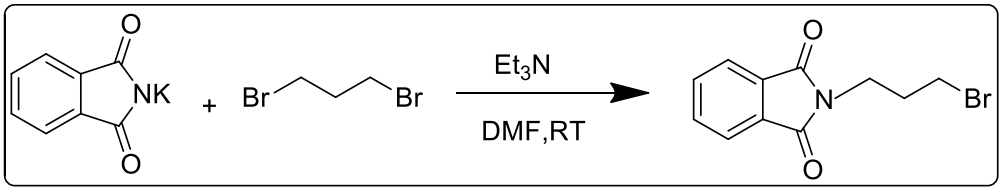

To the solution of 1,3 dibromo propane (3.287 ml, 32.39 mmol) in DMF (5 mL) added potassium derivative of phthalimide (2 g, 10.79 mmol) and few drops of *tert* - butylamine and stirred for 24 hrs. Formation of the product was confirmed by TLC. DMF was removed by evaporation and then purified by column chromatography (20% ethylacetate-hexane) over silica gel to yield 1.9 g (65 %) compound as a white powder.

^{1}HNMR: ($CDCl_3$, 500 MHz) , δ (ppm): 2.26 (q, J =6.5 Hz , 2H), 3.42 (t, J =6.5 Hz, 2H), 3.84 (t, J = 7 Hz, 2H), 7.73 (m , J= 2.5 Hz , 2H), 7.85 (m , J =3 Hz , 2H), MS (HRMS) : Calculated =268 , Found =267.997 $(M+H)^+$

3.5.2.2. *Synthesis* of *4-(3-(1,3 dioxoisoindoline-2-yl)propoxy)benzaldehyde*.

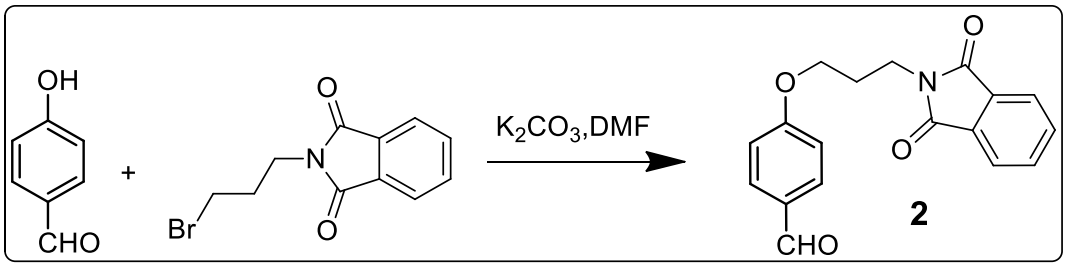

To a solution of 3-bromopropyl phthalimide (400 mg, 1.49 mmol) and 4-hydroxy benzaldehyde (180 mg,1.49 mmol) in DMF (5 ml) was added anhydrous K_2CO_3 (440 mg, 3.18 mmol). The mixture was stirred at 70 ^{0}C for 4 h and at room temperature overnight. The solvent was removed under reduced pressure and the residue was taken up in chloroform. The organic layer was washed with 5% aqueous NaOH and the product is purified by column on silica gel eluted with 30% ethylacetate-hexane solvent to yield 318 mg (70%) of the product.

^{1}HNMR: ($CDCl_3$, 500 MHz) , δ (ppm): 2.230 (m, J =6.5 Hz , 2H), 3.929 (t, J = 7 Hz, 2H), 4.122 (t, J = 6 Hz, 2H), 6.896 (q, J= 5 2H), 7.726 (q, J = 2.5 ,2H), 7.783 (q, J = 2 Hz, 2H), 7.840 (m, J = 3 , 2H), 9.866 (s, 1H). MS (FAB): Calculated =309, Found =309.090 $(M+H)^+$.

3.5.2.3. *Synthesis* of *3*

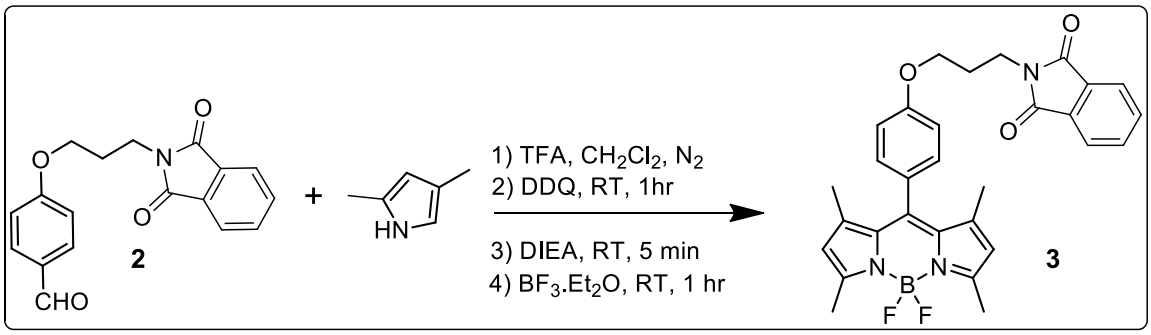

To the solution of compound **2** in DCM (250 mL) added 2 drops of TFA and 2,4-dimethyl pyrrole (0.2 ml, 1.29 mmol) and stirred overnight under argon atmosphere. Then DDQ (170 mg, 0.647 mmol) is added and continued stirring for 15 minutes followed by DIEA (3 ml) and stirred again for 5 minutes. Finally $BF_3.OEt_2$ was added and stirred for one hour. The reaction mixture washed with water and the organic layer is passed over Na_2SO_4 and concentrated. The compound was purified by column chromatography with 30% ethyl acetate / hexane to yield 225 mg (68%) of product.

^{1}HNMR: ($CDCl_3$, 500 MHz) , δ (ppm): 1.415(s, 6H), 2.233 (m, J = 6.5 Hz, 2H), 2.545 (s, 6H), 3.944 (t, J = 7 Hz, 2H), 4.096 (t, J = 6 Hz, 2H), 6.883 (d, J = 8.5 Hz, 2H),7.123 (d, J =8.5 Hz,2H), 7.264 (s, 2H), 7.729 (m, J = 2.5 Hz, 2H), 7.840 (m, J = 2.5 Hz, 2H),

MS (HRMS) : Calculated =527.22 , Found = 528.12 $(M+H)^+$.

3.5.2.*4. Synthesis of 4*

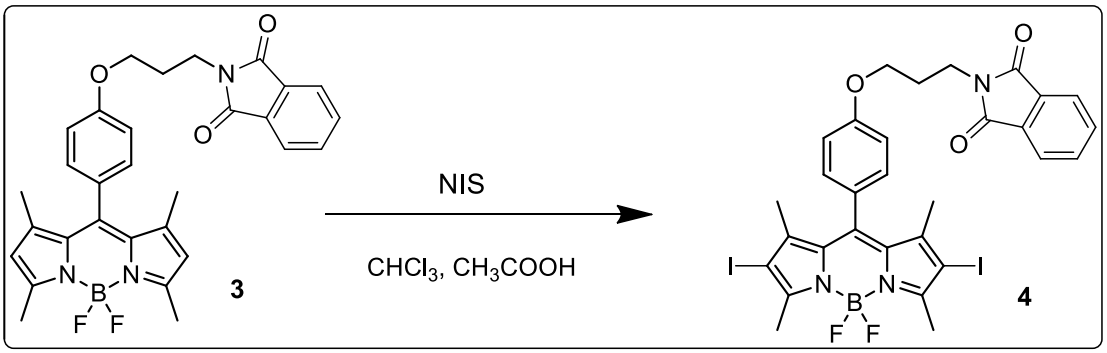

To a solution of Compound **3** (50 mg, 0.1 mmol) in 15 ml chloroform added N-iodosuccimide (56.24 mg, 0.25 mmol) and glacial acetic acid (5 ml) and stirred for overnight. The reaction mixture was washed with sodium bicarbonate and sodium thiosulphate. The resulting compound was purified by column chromatography using 20% ethylacetate-hexane to yield 28 mg (40%) of the product.

^{1}HNMR: ($CDCl_3$, 500 MHz) , δ (ppm): 1.427 (s, 6H), 2.248 (m, J = 6.5 Hz, 2H), 2.636 (s, 6H), 3.955 (t, J = 7 Hz, 2H), 4.113 (t, J = 6 Hz, 2H), 6.925 (d, J = 8.5 Hz, 2H),7.090 (d, J =8.5 Hz ,2H), 7.738 (q, J = 3 Hz, 2H), 7.850 (q, J = 2.5 Hz, 2H),

MS (HRMS) : Calculated= 778.01, Found = 778.09 $(M)^+$.

3.5.2.5. *Synthesis of BDPA*

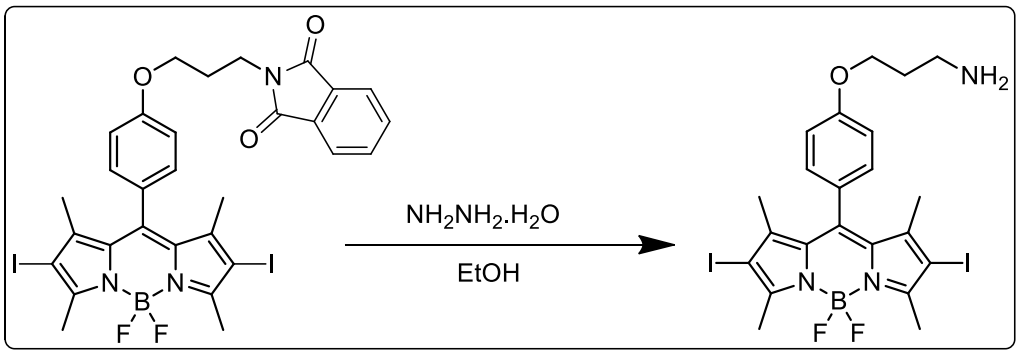

To a solution of compound **4** (50 mg, 0.066 mmol) in 10ml ethanol, hydrazine monohydrate (0.2 ml) was added and stirred for 1 hr. Formation of the product was confirmed by TLC. The solvent was removed and then the compound was purified by column chromatography using 10% methanol-chloroform mixture to yield 33 mg product (78%).

^{1}HNMR: (MeOD, 500 MHz) , δ (ppm): 1.490(s, 6H), 2.193 (m, J = 7 Hz, 2H), 2.59 (s, 6H),

3.17 (t, J = 7 Hz, 2H), 4.22 (t, J = 6 Hz, 2H), 7.196 (d, J = 8.5 Hz, 2H), 7.274 (q, J =5 Hz,2H), MS (HRMS) : Calculated = 649.02 , Found =650.01 $(M+H)^+$.

3.5.3. *Synthesis of GQD-BDPA conjugates*

GQD (10 mg) is dispersed in 2 ml H_2O by sonication for 5 minutes. To this solution added NHS (8 mg, 0.0661 mmol) and EDC (12 mg, 0.0628 mmol) and stirred for 1 hr. Then a solution of **BDPA** (2 mg, 1.54 mmol) dissolved in 300µL H_2O and 200µL DMF was added to this mixture and was stirred for 24 hours at room temperature. The mixture was then heated to remove water and then washed many times with methanol and chloroform to remove unreacted reagents and other byproducts. The product is then kept for dialysis for 3 days with the frequent change in water. Finally, the residue is dispersed in water and used for further characterization.

3.5.4. *Synthesis of GQD-BODIPY-Mixed derivatives*

GQD (10 mg) is dispersed in 2 ml H_2O by sonication for 5 minutes. To this solution added NHS (11.5 mg, 0.01 mmol) and EDC (19 mg, 0.01 mmol) and stirred for 1 hr. Then a solution of Diiodo-**BDPA** (6.5 mg, 0.01 mmol) and **BDPA** (4 mg, 0,01 mmol) dissolved in 300 µL H_2O and 200 µL DMF were added to this mixture and was stirred for 24 hours at room temperature. The mixture was then heated to remove water and then washed many times with methanol and chloroform to remove unreacted reagents and other byproducts. The product is further purified by dialysis for 2 days. Finally, the residue is dispersed in water and used for further characterization.

3.5.5. Description of Experimental Techniques

3.5.5.1. Optical Measurements

Electronic absorption spectra were recorded on a Shimadzu UV-2600 spectrophotometer and the emission spectra were measured on a SPEX-Fluorolog F112X spectrofluorimeter. Measurements of solution state fluorescence quantum efficiency were carried out using a calibrated integrating sphere connected to SPEX Fluorolog-3 spectrofluorimeter. A Xenon-arc lamp was used to excite the samples placed in the sphere, with 350 nm as the excitation wavelength. This experimental setup and the integrating sphere system calibrated using the solid state fluorescence quantum yield of the standard sodium salicylate (white powder) was determined to be 60 ± 10%, which is consistent with previously reported values.

3.5.5.2. Nanosecond Laser Flash Photolysis Studies

Nanosecond laser flash photolysis experiments were performed by using an Applied Photophysics model LKS-20 laser kinetic spectrometer using OCR-12 Series Quanta Ray Nd: YAG laser. The triplet excited state yields (Φ_T) of the samples, **BDPA** and **GQD-BDPA** were determined by an earlier reported procedure of energy transfer to β-carotene, using $Ru(bpy)_3^{2+}$, as the reference molecule. For these experiments, optically matched solutions of $Ru(bpy)_3^{2+}$ and the samples at 532 nm, were mixed with a known volume of β-carotene solution (end concentration of β-carotene was fixed at *ca.* 2.0 x 10^{-4} M). The transient absorbance of the β–carotene triplet, generated by the energy transfer from $Ru(bpy)_3^{2+}$ or the sample's triplet excited state, was monitored at 510 nm. Comparison of plateau absorbance (ΔA) following the completion of sensitized

triplet formation, properly corrected for the decay of the donor triplet excited state in competition with energy transfer to β-carotene, enabled us to estimate Φ_T of the triplet excited states based on Eqn 1.

$$\phi_T^{sam} = \phi_T^{ref} \frac{\Delta A^{sam} K_{obs}^{sam} (K_{obs}^{ref} - K_0^{ref})}{\Delta A^{ref} (K_{obs}^{sam} - K_0^{sam}) K_{obs}^{ref}} \qquad \text{Eqn (1)}$$

wherein, superscripts sam and ref designate various samples and $Ru(bpy)_3^{2+}$, respectively, K_{obs}, is the pseudo-first-order rate constant for the growth of the β-carotene triplet and K_0 is the rate constant for the decay of the donor triplet, in the absence of β- carotene, observed in solutions containing $Ru(bpy)_3^{2+}$ or a sample at the same optical density (OD = 0.1) as those used for sensitization.

3.5.5.3. Determination of singlet oxygen generation efficiency

Singlet oxygen generation quantum yields in methanol solution were determined by monitoring the photo-oxidation of 1,3-diphenylisobenzofuran (DPBF) sensitized by **BDPA/GQD-BDPA**.[41] DPBF can form *o*-dibenzoylbenzene through a [4 + 2] cycloaddition with $^1O_2$. The disappearance of DPBF and the formation of the product *o*-dibenzoylbenzene can be monitored by absorption decrease at 410 nm. Optically matching solution of the sample and the standard was irradiated using oriel lamp (200 W xenon lamp, model 3767) fitted with a suitable filter (475 nm long pass) at regular intervals followed by UV-visible absorption measurements. The singlet oxygen generation quantum yields (Φ $^1O_2$) were calculated as per Eqn (2), where m is the slope of a plot of change in absorbance of DPBF (at 410 nm) with the irradiation time and F is

the absorption correction factor, which is given by F = 1 – 10^{-OD} (OD at the irradiation wavelength).

$$\Phi\Delta^{com} = \Phi\Delta^{ref}\frac{m^{com}\ F^{ref}}{m^{ref}\ F^{com}} \qquad \text{Eqn(2)}$$

3.5.5.4. Cell culture and Photodynamic treatment.

Human breast cell lines (MDA-MB-231) were purchased from ATCC (USA). The photosensitizer nanoconjugate, **GQD-BDPA** was synthesized as previously described and 150 µg/mL (10µM, sensitizer concentration) stock solutions in water were prepared for further studies.

3.5.5.5. Cytotoxicity assay (IC_{50} value)

MTT (3-(4,5-dimethylthiazol-2-yl)-2,5-diphenyltetrazolium bromide) reduction assay was performed to assess cell viability. Briefly, cells (10000 cells) were seeded in two 96 well cluster plate and allowed to reach the exponential phase of growth (18 hours). Later, both plates were treated using **GQD-BDPA** (5–200nM), incubated for 1 hour and photo-irradiated with PDT lamp (540 nm, Green LED array with a total fluence rate of 100 J/cm^2 for 10 minutes. Another plate was kept in dark for assessing dark cytotoxicity. The amount of formazan crystals formed was measured after 4 h of MTT addition. The crystals were dissolved in isopropyl alcohol and the OD was measured at 570 nm. Graphs were plotted using Microsoft Excel, percentage inhibition was calculated by the formula (OD value of control - OD value of test)/OD value of control * 100).

3.5.5.6. Assay for cellular reactive oxygen species (ROS) content

ROS stress studies, approximately 5× 10^5 MDA-MB-231 cells were seeded in 60 mm culture dishes and 10000 cells were plated in 60 mm and 96 well Opti-bottom plates (BD Falcon) with serum-containing media. After 18 hours, the cells were treated with **GQD-BDPA (**30 nM, sensitizer concentration) for 1 h and photo-irradiation was done using PDT lamp (Green LED array, 540 nm with a total fluence rate of 100 J/cm^2) for 10 minutes. In one plate 30 nM nanoconjugate was added and the plate was kept in the dark to be taken as Dark control. Another plate was irradiated with a laser without drug treatment and was taken as Light control. After 1 hour of PDT the cellular reactive oxygen content was determined using a CM-H2DCFDA probe, according to the manufacturer's instructions (Invitrogen). The confocal images and differential interference contrast (DIC) images were acquired (Nikon A1R), merged, and processed using Nikon Imaging Software. Further, we analyzed the fluorescence of CM-H2DCFDA using flow cytometry (FACS Aria, Special order system, BD, USA) and analysis was done using DIVA software.

3.5.5.7. Measure of mitochondrial membrane potential

Mitochondrial membrane potential was measured using TMRM dyes from molecular probes (Life Technology, USA). Approximately 5 × 10^5 MDA-MB-231 cells were seeded in 60 mm culture dishes. After 18 h, the cells were treated with **GQD-BDPA** (30 nM, sensitizer concentration) for 1 h and photo irradiation was done using PDT lamp (540 nm, Green LED array with a total fluence rate of 100 J/cm^2) for 10 minutes and incubated for 3, 6, 12 and 24 hours. Light and Dark control were taken as

mentioned earlier. For fluorescence, cyto-chemical study 10^5 MDA-MB-231 cells were seeded in a 96 well plate and subjected to **GQD-BDPA** PDT treatment as mentioned earlier. Post treatment, the cells were washed with PBS and incubated with 10 nm TMRM in PBS for 30 minutes. Images were taken using a fluorescent microscope (Leica DMI 4000 B, Germany). Further, the fluorescence of TMRM corresponding to mitochondrial membrane potential was analyzed using flow cytometry.

3.5.5.8. Chromatin Condensation Assay by Hoechst Staining

To study chromatin condensation, approximately 10^5 MDA-MB-231 cells were seeded in 96 well culture dishes and incubated for 24 h. Then, cells were incubated with 30 nM **GQD-BDPA** for 24 h followed by photoirradiation using PDT lamp (540 nm, Green LED array with a total fluence rate of 100 J/cm^2). Light and Dark control were taken as previously described. After 24 h of treatment MDA-MB-231 cells were rinsed twice with PBS and stained with 5 µg/mL Hoechst dye for 15 min at room temperature. Cells were then washed twice with PBS and visualized under an inverted fluorescence microscope.

3.5.5.9. Acridine orange/Ethidium Bromide Assay (AO/EB)

Apoptotic cell morphology was assessed by Acridine orange/ Ethidium Bromide Assay for **GQD**, **BDPA** and **GQD-BDPA** nanoconjugates in MDA MB 231 cell lines. Approximately 10000 cells were seeded in 96 well plates and the following day nanoconjugates was added and incubated for 24 h. After that PDT treatment was administered and incubated for 48 h. 1µl acridine orange stock (5mg/ml) and 1µl ethidium bromide stock (3 mg/ml) was added to 1ml PBS and mixed well. This was

used as AO-EB working solution. Then media was removed from cell plate and 100µl of AO-EB working solution was added to each well and immediately viewed under an inverted fluorescence microscope.

3.5.5.10. Annexin binding assay

PDT treatment was done as mentioned earlier in TMRM assay. Annexin binding the assay was performed as per manufacturer's instructions provided in Annexin VFITC Apoptosis Detection Kit (Sigma) and flow cytometric analysis carried out using FACS Aria (BD, USA).

3.6. References

(1) Celli, J. P.; Spring, B. Q.; Rizvi, I.; Evans, C. L.; Samkoe, K. S.; Verma, S.; Pogue, B. W.; Hasan, T. *Chem. Rev.* **2010**, *110*, 2795.

(2) Dolmans, D. E. J. G. J.; Fukumura, D.; Jain, R. K. *Nature Reviews Cancer* **2003**, *3*, 380.

(3) Saini, R.; Poh, C. *Oral Dis.* **2013**, *19*, 440.

(4) Robertson, C. A.; Evans, D. H.; Abrahamse, H. *J. Photochem. Photobiol.* **2009**, *96*, 1.

(5) Kinsella, T. J.; Colussi, V. C.; Oleinick, N. L.; Sibata, C. H. *Expert Opin. Pharmacother.* **2001**, *2*, 917.

(6) Lucky, S. S.; Soo, K. C.; Zhang, Y. *Chem. Rev.* **2015**, *115*, 1990.

(7) Liu, J.; Cui, L.; Losic, D. *Acta Biomaterialia* **2013**, *9*, 9243.

(8) Chen, D.; Feng, H.; Li, J. *Chem. Rev.* **2012**, *112*, 6027.

(9) Georgakilas, V.; Otyepka, M.; Bourlinos, A. B.; Chandra, V.; Kim, N.; Kemp, K. C.; Hobza, P.; Zboril, R.; Kim, K. S. *Chem. Rev.* **2012**, *112*, 6156.

(10) Georgakilas, V.; Tiwari, J. N.; Kemp, K. C.; Perman, J. A.; Bourlinos, A. B.; Kim, K. S.; Zboril, R. *Chem. Rev.* **2016**, *116*, 5464.

(11) Quintana, M.; Vazquez, E.; Prato, M. *Acc. Chem. Res.* **2013**, *46*, 138.

(12) Wang, Y. H.; Wang, H. G.; Liu, D. P.; Song, S. Y.; Wang, X.; Zhang, H. J. *Biomaterials* **2013**, *34*, 7715.

(13) Li, F.; Park, S.; Ling, D.; Park, W.; Han, J. Y.; Na, K.; Char, K. *J. Mater. Chem. B* **2013**, *1*, 1678.

(14) Tian, B.; Wang, C.; Zhang, S.; Feng, L. Z.; Liu, Z. *Acs Nano* **2011**, *5*, 7000.

(15) Huang, P.; Xu, C.; Lin, J.; Wang, C.; Wang, X. S.; Zhang, C. L.; Zhou, X. J.; Guo, S. W.; Cui, D. X. *Theranostics* **2011**, *1*, 240.

(16) Chong, Y.; Ma, Y.; Shen, H.; Tu, X.; Zhou, X.; Xu, J.; Dai, J.; Fan, S.; Zhang, Z. *Biomaterials* **2014**, *35*, 5041.

(17) Li, L.; Wu, G.; Yang, G.; Peng, J.; Zhao, J.; Zhu, J.-J. *Nanoscale* **2013**, *5*, 4015.

(18) Shen, J.; Zhu, Y.; Yang, X.; Li, C. *Chem. Commun.* **2012**, *48*, 3686.

(19) Ge, J.; Lan, M.; Zhou, B.; Liu, W.; Guo, L.; Wang, H.; Jia, Q.; Niu, G.; Huang, X.; Zhou, H.; Meng, X.; Wang, P.; Lee, C.-S.; Zhang, W.; Han, X. *Nat. Commun.* **2014**, *5*.

(20) Markovic, Z. M.; Ristic, B. Z.; Arsikin, K. M.; Klisic, D. G.; Harhaji-Trajkovic, L. M.; Todorovic-Markovic, B. M.; Kepic, D. P.; Kravic-Stevovic, T. K.; Jovanovic, S. P.; Milenkovic, M. M.; Milivojevic, D. D.; Bumbasirevic, V. Z.; Dramicanin, M. D.; Trajkovic, V. S. *Biomaterials* **2012**, *33*, 7084.

(21) Li, Y.; Wu, Z. Y.; Du, D.; Dong, H. Q.; Shi, D. L.; Li, Y. Y. *Rsc Adv.* **2016**, *6*, 6516.

(22) Du, D.; Wang, K.; Wen, Y.; Li, Y.; Li, Y. Y. *ACS Appl. Mater. Interfaces* **2016**, *8*, 3287.

(23) Verwilst, P.; David, C. C.; Leen, V.; Hofkens, J.; de Witte, P. A. M.; De Borggraeve, W. M. *Bioorg. Med. Chem. Lett.* **2013**, *23*, 3204.

(24) Kamkaew, A.; Lim, S. H.; Lee, H. B.; Kiew, L. V.; Chung, L. Y.; Burgess, K. *Chem. Soc. Rev.* **2013**, *42*, 77.

(25) Awuah, S. G.; You, Y. *Rsc Adv.* **2012**, *2*, 11169.

(26) Cakmak, Y.; Nalbantoglu, T.; Durgut, T.; Akkaya, E. U. *Tetrahedron Lett.* **2014**, *55*, 538.

(27) Roby, A.; Erdogan, S.; Torchilin, V. P. *Eur. J. Pharm. Biopharm.* **2006**, *62*, 235.

(28) Nishie, H.; Kataoka, H.; Yano, S.; Kikuchi, J.-i.; Hayashi, N.; Narumi, A.; Nomoto, A.; Kubota, E.; Joh, T. *Oncotarget* **2016**, *7*, 74259.

(29) Jiang, D.; Chen, Y.; Li, N.; Li, W.; Wang, Z.; Zhu, J.; Zhang, H.; Liu, B.; Xu, S. *Plos ONE* **2016**, *10*, e0144906.

(30) Zhang, F.; Liu, F.; Wang, C.; Xin, X.; Liu, J.; Guo, S.; Zhang, J. *ACS Appl. Mater. Interfaces* **2016**, *8*, 2104.

(31) Yoon, Y.; Lee, Y. B.; Kim, S. K.; Song, W.; Myung, S.; Lim, J.; Lee, S. S.; Yoo, H.; An, K. S. *ChemistrySelect* **2018**, *3*, 321.

(32) Galeotti, F.; Calabrese, V.; Cavazzini, M.; Quici, S.; Poleunis, C.; Yunus, S.; Bolognesi, A. *Chem. Mater.* **2010**, *22*, 2764.

(33) Fu, G.-L.; Pan, H.; Zhao, Y.-H.; Zhao, c.-h. *Org. Biomol. Chem.,* **2011**,9, 8141

(34) Kudin, K. N.; Ozbas, B.; Schniepp, H. C.; Prud'homme, R. K.; Aksay, I. A.; Car, R. *Nano Lett.* **2008**, *8*, 36.

(35) Shen, J.; Zhu, Y.; Chen, C.; Yang, X.; Li, C. *Chem. Commun.* **2011**, *47*, 2580.

(36) Krieg, M. *J. Biochem. Bioph. Methods* **1993**, *27*, 143.

(37) Wang, J.; Hou, Y.; Lei, W.; Zhou, Q.; Li, C.; Zhang, B.; Wang, X. *ChemPhysChem* **2012**, *13*, 2739.

(38) Oparka, M.; Walczak, J.; Malinska, D.; van Oppen, L. M. P. E.; Szczepanowska, J.; Koopman, W. J. H.; Wieckowski, M. R. *Methods* **2016**, *109*, 3.

(39) Karunakaran, S. C.; Babu, P. S. S.; Madhuri, B.; Marydasan, B.; Paul, A. K.; Nair, A. S.; Rao, K. S.; Srinivasan, A.; Chandrashekar, T. K.; Rao, C. M.; Pillai, R.; Ramaiah, D. *ACS Chem. Biol.* **2013**, *8*, 127.

(40) Hummers, W. S.; Offeman, R. E. *J. Am. Chem. Soc.* **1958**, *80*, 1339.

(41) Wozniak, M.; Tanfani, F.; Bertoli, E.; Zolese, G.; Antosiewicz, Biochim. Biophys. Acta **1991**, *1082*, 94.

Chapter 4

BODIPY Functionalized MoS_2 Quantum Dots for Efficient PDT Applications

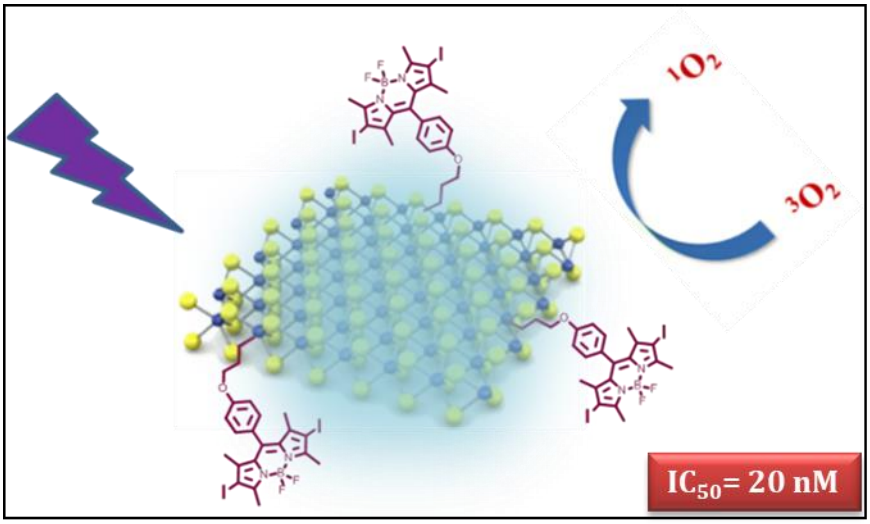

4.1. Abstract

*Transition metal dichalcogenides, like MoS_2 have received much attention in recent years, because of the unique properties associated with their ultra-thin thickness and 2D morphology, which makes them promising candidates for biomedical applications. MoS_2 nanosheets with few nanometers lateral dimension are termed as MoS_2 quantum dots (**MQDs**), which is known for its bright luminescence, excellent biocompatibility and aqueous solubility. Surface of MoS_2 nanosheets and **MQDs** can be easily functionalized with photosensitizes via various strategies, which will enhance their aqueous solubility as well as cellular internalization of photosensitizer, and enhance their photodynamic therapeutic performance. In this Chapter, we describe synthesis and characterization of*

*blue luminescent **MQDs** conjugated with a diiodo-BODIPY derivative (**MQD-BDSH**) which show high triplet quantum yields, excellent singlet oxygen generation efficiencies and aqueous solubility favourable for PDT applications. We followed an ultra-sonication assisted mixed solvent exfoliation method for the synthesis of few layered MoS_2 nanosheets from bulk MoS_2. These nanosheets were further cut into smaller dimensions (**MQDs**) via heat treatment method (120 °C in DMF). Both MoS_2 nanosheets and **MQDs** were characterized by AFM, TEM and EDX analysis. As synthesized **MQDs** were covalently functionalized with thiol modified diiodo-BODIPY derivative (**BDSH**) via thiol ligand conjugation method with ~8.2 wt.% sensitizer loading. As synthesized nanoconjugate, (**MQD-BDSH**) with average lateral dimensions of 30 nm - 80 nm and excellent water solubility, exhibited characteristic absorption and fluorescence properties of both **MQD** and **BDSH**. Triplet quantum yield of this nanoconjugate was found to be 0.91±0.02 with high singlet oxygen generation efficiency of 81%. In vitro PDT activity of this nanoconjugate was investigated on HSC4 oral cancer cell lines, which shows that **MQD-BDSH** is an efficient system for PDT with IC_{50} values in low nanomolar concentration range (20 nM, sensitizer concentration). The apoptotic cell death was characterized and confirmed by various assays such as Annexin, TMRM assay, nuclear condensation, etc. on HSC4 oral cancer cell lines. These results demonstrate the potential of these nanoconjugates for efficient PDT applications.*

4.2. Introduction

The past few years has seen great development in the field of 2D nanomaterials like graphene and its inorganic analogues, mainly transition metal dichalcogenides.[1-3]

Among various transition metal chalcogenides, MoS_2 shows superior properties with easy synthesis and functionalization.[4-6] The 2D planar structure and diverse chemical compositions lead to unique properties of these nanomaterials for biomedical applications such as drug delivery,[7,8] photothermal/photodynamic therapy,[9,10] diagnostic imaging,[11,12] and biosensing.[8,13,14] Moreover, the biological effect and behaviour of these 2D nanosheets are also now under extensive exploration.[15] It has been demonstrated that MoS_2 nanosheets present relatively high biocompatibility and low cytotoxicity even lower than graphene and other analogues.[16-20] MoS_2 is rather inert and thus face problems for chemical functionalization. Hence, to further modify the properties of these nanomaterials for various applications, routes towards their chemical functionalization must be identified. Various groups recently demonstrated the importance of functionalization of MoS_2 using variety of chromophores and used for applications ranging from energy harvesting to biosensing.[21,22] Surface imperfections created as a result of exfoliation procedure provides sufficient sites for incoming ligands to attach covalently to MoS_2 nanosheets.[23]

Due to quantum confinement and edge effects, MoS_2 nanosheets with lateral dimensions below 100 nm, have been found to be highly luminescent and termed as, MoS_2 QDs (**MQDs**).[6,24-26] This excellent luminescence property, along with good biocompatibility motivates researchers to explore this material in biomedical field for sensing as well as cellular imaging applications.[27-30] Presence of thiol-reactive defect sites of MQDs can be utilized for conjugation with various small molecules or biomaterials for several applications.[22,31]

MoS_2 nanosheets are recently explored by many research groups as a biocompatible nanocarrier for PDT drugs. Jun-Sheng Yu and coworkers designed a MoS_2 nanoplate-based nanoprobe for fluorescence imaging of intracellular ATP and photodynamic therapy *via* ATP-mediated controllable release of singlet oxygen (Figure 4.1).[32] The nanoprobe was prepared by non-covalently assembling chlorine e6 (Ce6) labelled ATP aptamer on MoS_2 nanoplates, which has a strong affinity towards single-stranded DNA and good fluorescence quenching ability. After the nanoprobe was internalized into the cells and entered into the ATP-abundant lysosomes, its recognition to ATP led to the release of the single- stranded aptamer from MoS_2 nanoplates and is evident by the fluorescence recovery of Ce6, and is capable of singlet oxygen eneration upon excitation with 660 nm laser.

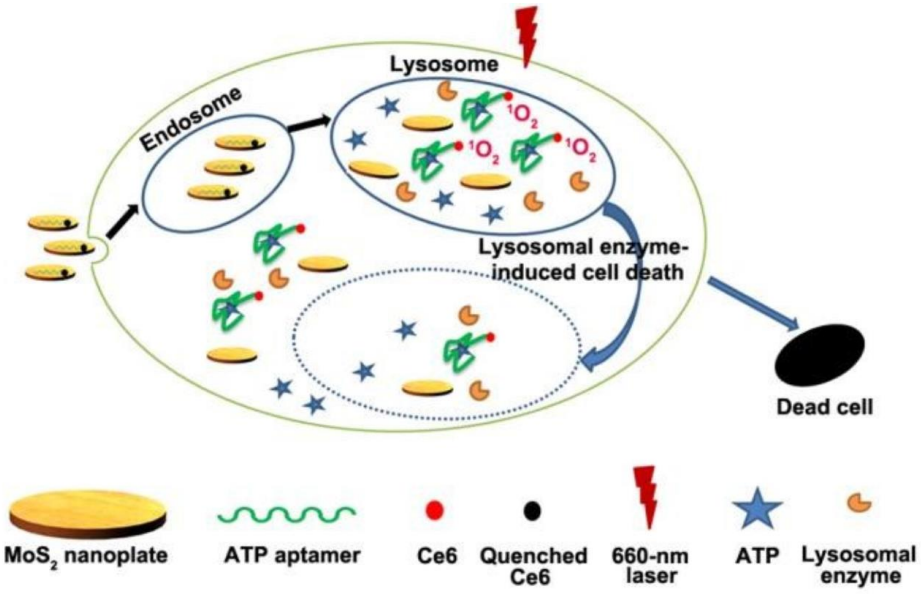

Figure 4.1. Schematic illustration of Ce6-aptamer loaded MoS_2 nanoprobe for $^1O_2$ production upon target binding (Adapted from reference 32).

Thiol ligand conjugation method is a well explored covalent functionalization strategy for effective modification of MoS_2 nanosheets. Liu *et al*., recently modified MoS_2

nanosheets for the simultaneous photothermal and chemotherapy of cancer (Figure 4.2).[33] Lipoic acid (LA) provided strong attachment of PEG to the chemically exfoliated 2D material through double thiol bonding, thus ensuring excellent dispersibility in aqueous solutions. The nanoconjugate did not agglomerate after centrifugation at 3000 rpm in phosphate buffer saline (PBS) or serum, while the unmodified MoS_2 nanosheets precipitate under same conditions due to charge masking by the phosphate buffer. The efficacy of the photodynamic treatment was enhanced by the localized increase in temperature due to the high absorption of near-infrared (NIR) radiation from the MoS_2.

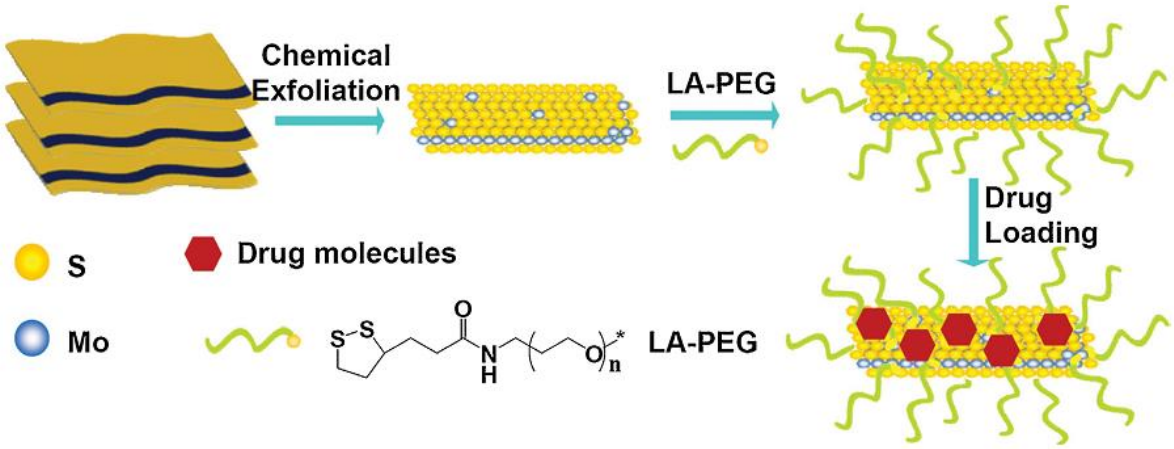

Figure 4.2. Scheme depicting the fabrication of the drug-loaded MoS_2-PEG conjugate. (Adapted from reference 33).

Recently, Xueji Zhang and coworkers developed fluorescent MoS_2 Quantum Dots using tetrabutylammonium-assisted ultrasonication of multilayered MoS_2 powder *via* OH mediated chain-like Mo-S bond cleavage mode (Figure 4.3).[34] The –OH group in tetrabutylammonium is suggested to intercalate and cleave the bulk MoS_2 by substituting S moieties. The synthesized MoS_2 QDs showed good down conversion as well as up-conversion photoluminescence behaviors, suitable for bioimaging

applications. This material also exhibit reasonable singlet oxygen generation ability compared to commercial photosensitizer PpIX, which could be utilized for PDT applications. No obvious cytotoxicity was observed to MoS_2 QDs-treated HeLa cells when the concentration of MoS_2 QDs ranges from 15 to 100 μg/mL, but showing prominent cytotoxicity after a 60 min irradiation under a 500 W xenon lamp.

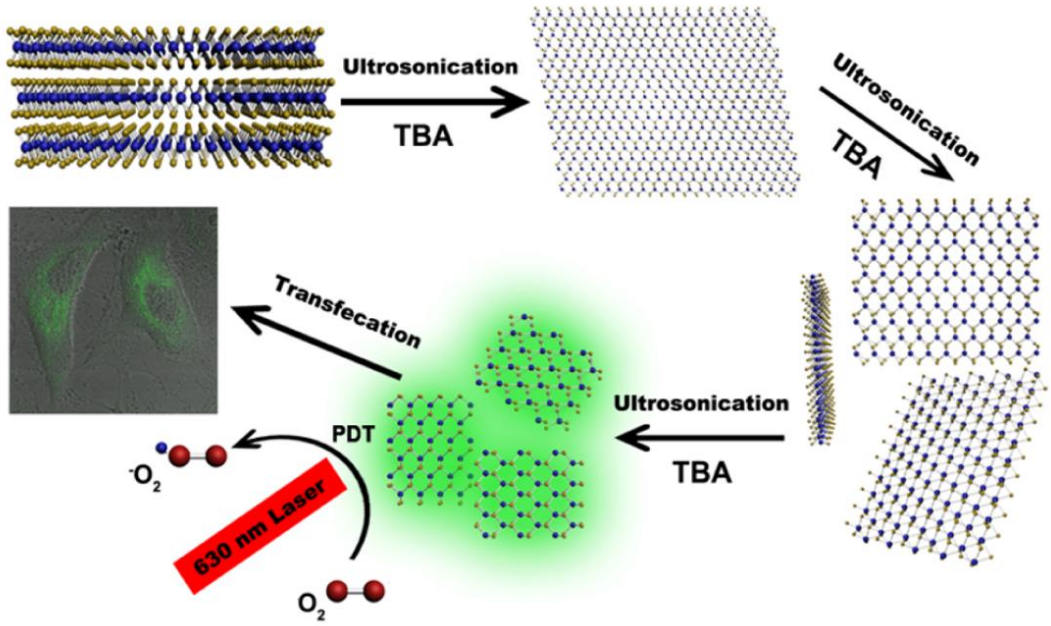

Figure 4.3. Schematic representation of synthetic method and resultant MoS_2 QDs for bioimaging and PDT applications (Adapted from reference 34).

In the present study we explore the covalent conjugation strategy for efficient functionalization of MoS_2 quantum dots using a diiodo-BODIPY photosensitizer with an alkyl thiol moiety (Figure 4.4). In this design, the presence of **MQD** conjugation can enhances the solubility in aqueous media and the presence of two iodines in the core structure of BODIPY increase the triplet quantum yield as well as singlet oxygen generation efficiency of the molecule, owing to heavy atom effect. These nanoconjugates

are stable in aqueous media and showed superior triplet quantum yields, singlet oxygen generation and efficient cancer cell death *via* apoptotic pathway, demonstrating their potential as PDT agent.

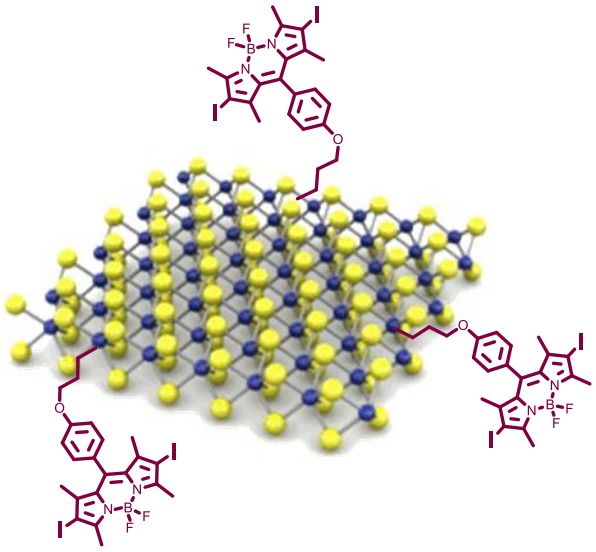

Figure 4.4. Schematic representation of **MQD-BDSH**

4.3. Results and Discussion

4.3.1. Synthesis and Characterization of MoS_2 nanosheets

MoS_2 nanosheets were synthesized by sonication assisted exfoliation from multi-layered bulk MoS_2 (Scheme 4.1). Here we followed a mixed solvent liquid exfoliation of MoS_2 in ethanol/ water (55:45).[35] Mixed-solvent dispersion method is considered as a general approach toward the dispersion of various nanomaterials with advantages such as low cost, lower toxicity, freedom from additives, and easy removal. Pure ethanol and pure water can hardly disperse MoS_2, but it exhibits significantly different dispersion properties in ethanol/water mixtures with different compositions. At an appropriate ethanol/water ratio (55:45), dark green dispersions of MoS_2 were obtained, which is

further sonicated for 24 hours to make it mono or few layered nanosheets. The supernatant of the resulting solution contains nanosheets of smaller dimension, which is separated by centrifugation at 2000 rpm. The material obtained could be successfully dispersed in the mixtures of ethanol and water. These suspensions were highly stable and showed no precipitation after being stored for few weeks under ambient conditions.

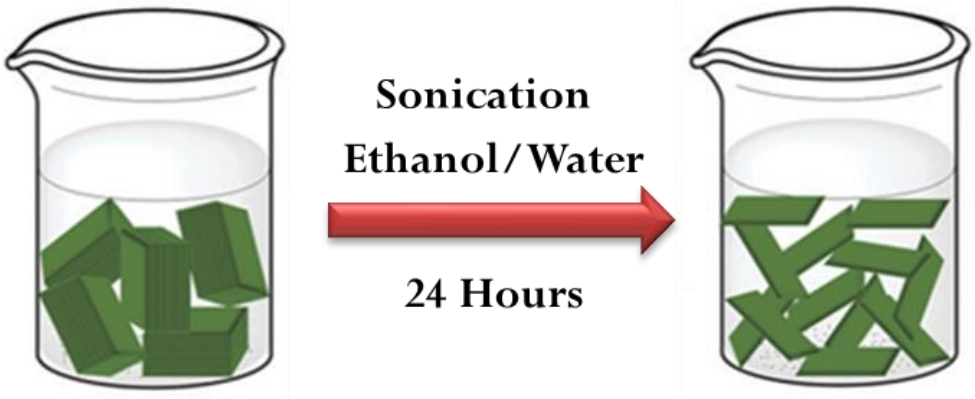

Scheme 4.1. Synthesis of MoS_2 nanosheets.

As synthesized nanosheets have been characterized using UV-Visible spectroscopy and the absorption spectra recorded in ethanol is shown in Figure 4.5A. Typical characteristic absorption bands of MoS_2 located at 680 nm, 619 nm, 470 nm, and 397 nm are observed in our sample, which is in good agreement with few-layered 2H-MoS_2 obtained from a liquid-based exfoliation method. The absorption peaks at 680 nm and 619 nm can be assigned to the direct excitonic transitions, A and B respectively, at the K point with the energy difference arising due to spin–orbital splitting of the valence band. Peaks at 470 nm and 397 nm correspond to the direct excitonic transitions of M point between higher density of state regions of the band structure.[36]

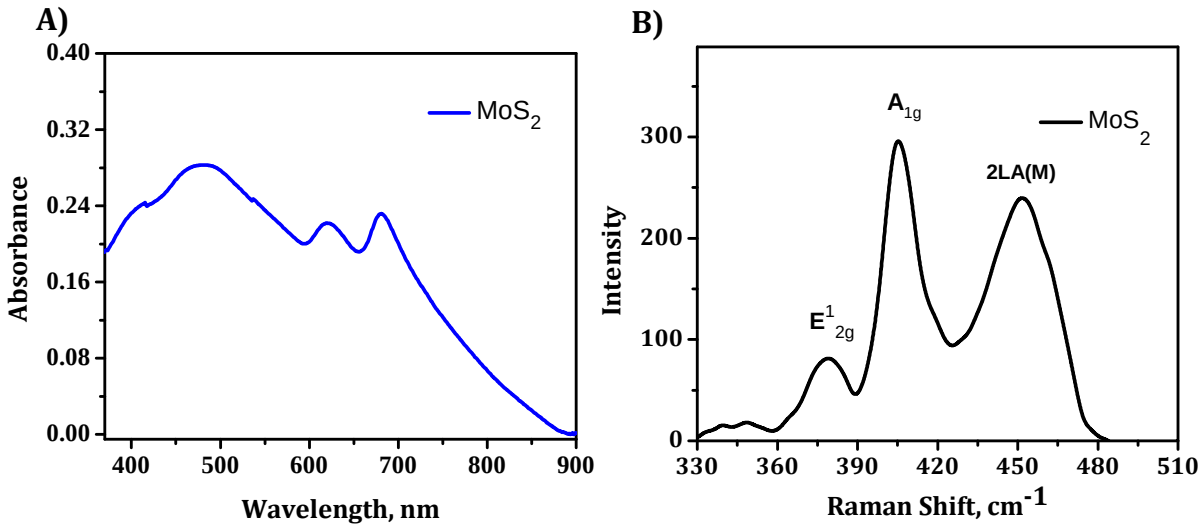

Figure 4.5. A) Absorption spectra of **MoS_2** nanosheets in ethanol and B) Raman spectra of **MoS_2** nanosheets

Raman spectroscopy is a powerful nondestructive technique for characterization of 2D nanomaterials materials like MoS_2, which will give characteristic bands, corresponds to various vibrational modes. The main bands include E^1_{2g} band around 380 cm^{-1} and A_{1g} band around 410 cm^{-1} corresponding to in-plane and out-of- plane vibrations of S atoms opposite to Mo, respectively. On resonance, MoS_2 exhibits a most prominent mode around 460 cm^{-1} arising from a second-order process involving the longitudinal acoustic phonons at M point (2LA(M)).[37] We have recorded Raman spectra using 633 nm laser on glass substrate (Figure 4.5B). As synthesized MoS_2 nanosheets showed bands at 379 cm^{-1}, 405 cm^{-1}, and 455 cm^{-1} corresponding to E^1_{2g}, A^1_g, and 2LA(M) modes respectively, indicates the formation of few layer MoS_2, which is in good agreement with microscopic analysis.

MoS_2 nanosheets have been further characterized by SEM, AFM and TEM analysis. A representative SEM image of as-prepared **MoS_2** in silicon wafer is shown in

Figure 4.6A, which clearly shows the formation of few layered MoS_2 nanosheets. AFM image was obtained by drop casting 0.05 $mgmL^{-1}$ water/ethanol (1:1) solution of MoS_2 on a freshly cleaved mica surface (Figure 4.6B). Micrometer-sized particles are observed in AFM with an average height of 1-2 nm. This is a typical value for mono or few layered MoS_2 nanosheets prepared using similar kind of methods.[38]

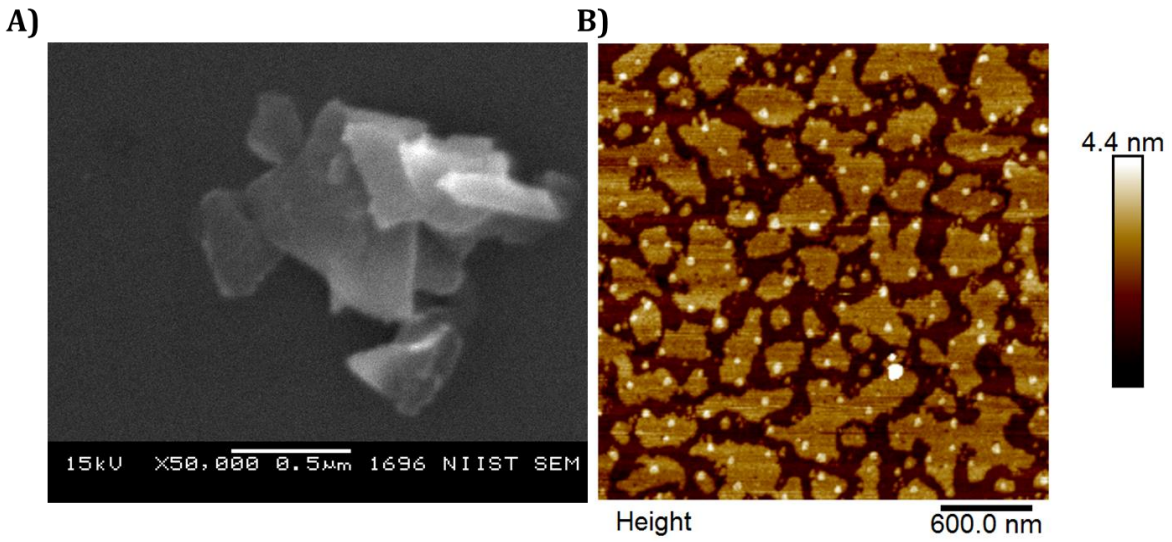

Figure 4.6. A) SEM and B) AFM images of MoS_2 nanosheets

TEM images were obtained by drop casting 0.05 mg/ml ethanol suspension on TEM copper grid and images obtained are shown in Figure 4.7. The images confirmed the successful formation of nano-sized MoS_2 sheets. Figure 4.7C shows the high resolution-TEM (HR-TEM) image of a single nanosheet with clearly visible lattice fringes, which again confirms the crystalline arrangement in the synthesized nanosheets. Hexagonal live FFT pattern further confirms the 2H phase of nanosheets (Figure 4.7D).[39]

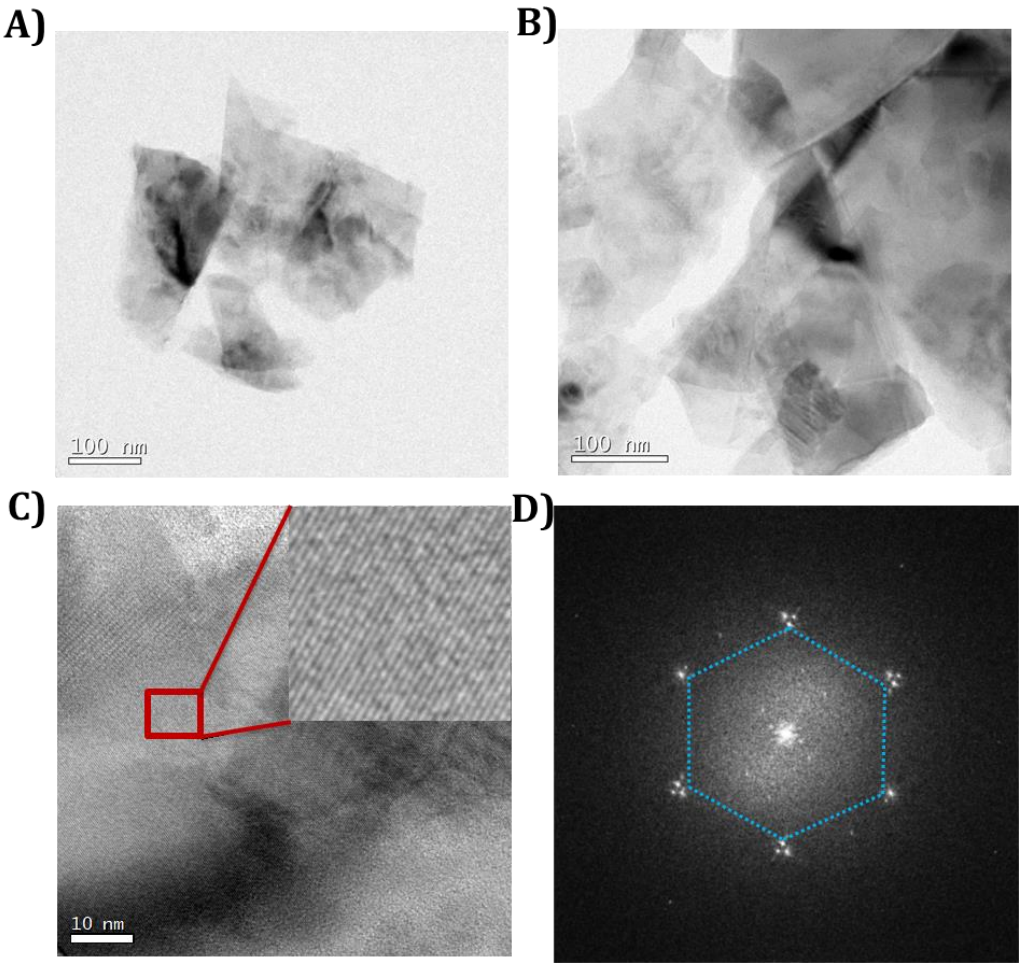

Figure 4.7. A) & B) TEM bright field images of **MoS_2** nanosheets. C) HR-TEM images of sample (enlarged portion with clearly visible lattice fringes are shown in inset). D) Live FFT pattern of the same sample.

4.3.2. Synthesis and Characterization of MQDs

Here we followed a modified synthetic strategy for the preparation of MoS_2 quantum dots (**MQDs**) by the combination of ultra-sonication and solvothermal treatment of exfoliated MoS_2 at a mild temperature (Figure 4.8).[40] As synthesized MoS_2 nanosheets upon heat treatment at higher temperature (120 °C in DMF for 12 hours) leads to the breaking of larger sheets to small nanosheets with various surface

defects.[40] These small sized blue luminescent particles (**MQDs**) are highly water soluble and are ideal nanomaterials for chemical conjugation with sensitizers for drug delivery applications.

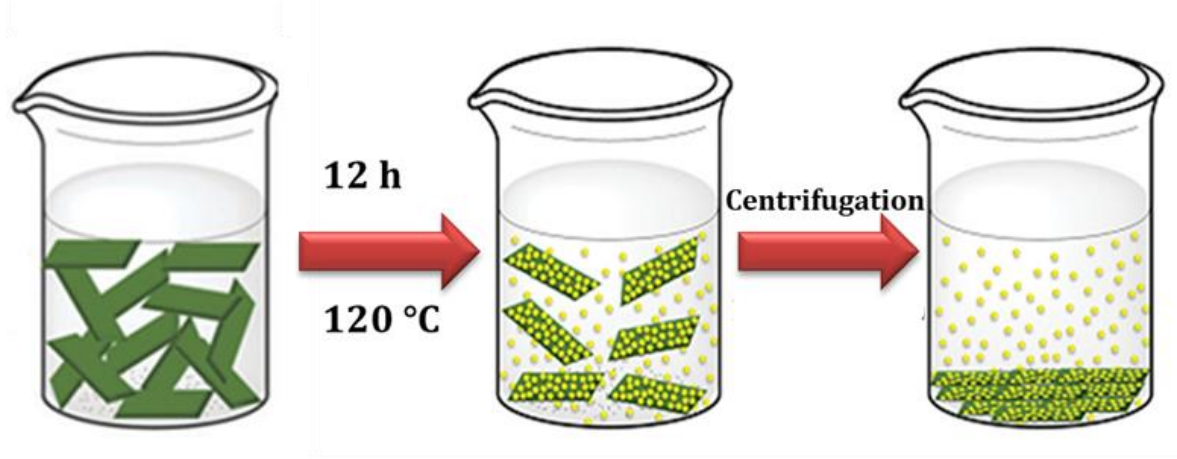

Figure 4.8. Schematic representation of synthesis of **MQDs**

We have characterized the synthesized **MQDs** also by AFM and TEM analysis. AFM samples are prepared by drop casting 0.05 mg/ml aqueous solution of MoS_2 quantum dots on mica substrate and images are shown in Figure 4.9A. AFM analysis of **MQDs** showed small sheets with average lateral dimensions of less than 50 nm with average thicknesses of ~1 nm. TEM images are also consistent with the AFM analysis, where nearly monodispersed particles with an average size of less than ~50 nm is observed for **MQDs** (Figure 4.9B). Energy-dispersive X-ray spectroscopy (EDX) measurements further confirmed the presence of Mo and S throughout the particles (Figure 4.9C).

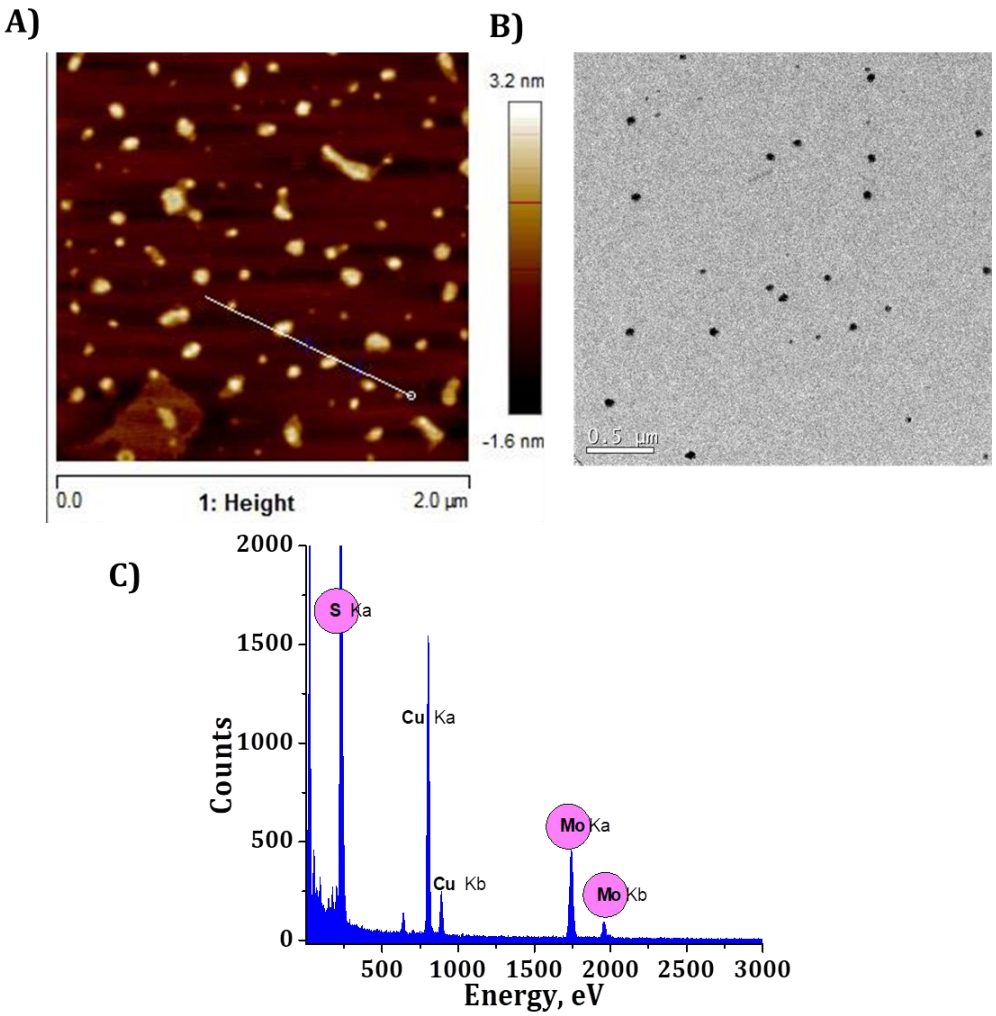

Figure 4.9. A) AFM, B) TEM, and C) EDX analysis of **MQDs**.

As synthesized **MQDs** have been characterized using UV-Visible and Emission spectroscopy. Absorption and emission spectra of the prepared samples are shown in Figure 4.10A. **MQDs** showed broad absorption starting from 450 nm to 200 nm with a shoulder band around 300 nm. The absorption peaks in the near-UV region ($\lambda < 300$ nm) can be attributed to the excitonic features of MoS_2 quantum dots in the sample.[41] The most interesting property of **MQDs** is its bright blue luminescence by irradiation of

suitable wavelength, which can be associated with the surface recombination of excitons that is generally observed in quantum-confined MoS_2 quantum dots. Our sample showed a broad emission from 380 nm to 700 nm by irradiating at 350 nm light, which is shown in Figure 4.10B. These particles are showing excitation dependent emission properties similar to other nanomaterials of same family. Emission maxima is changing from 350 nm to 550 nm by exciting at 300 to 500 nm, which indicates the possibility of various size distribution in the synthesized samples as observed in the imaging analysis (30 - 80 nm). The fluorescence quantum yield is calculated as 4.1% from absolute method using integrating sphere and is comparable with those of reported **MQDs** synthesized by similar methods.[40]

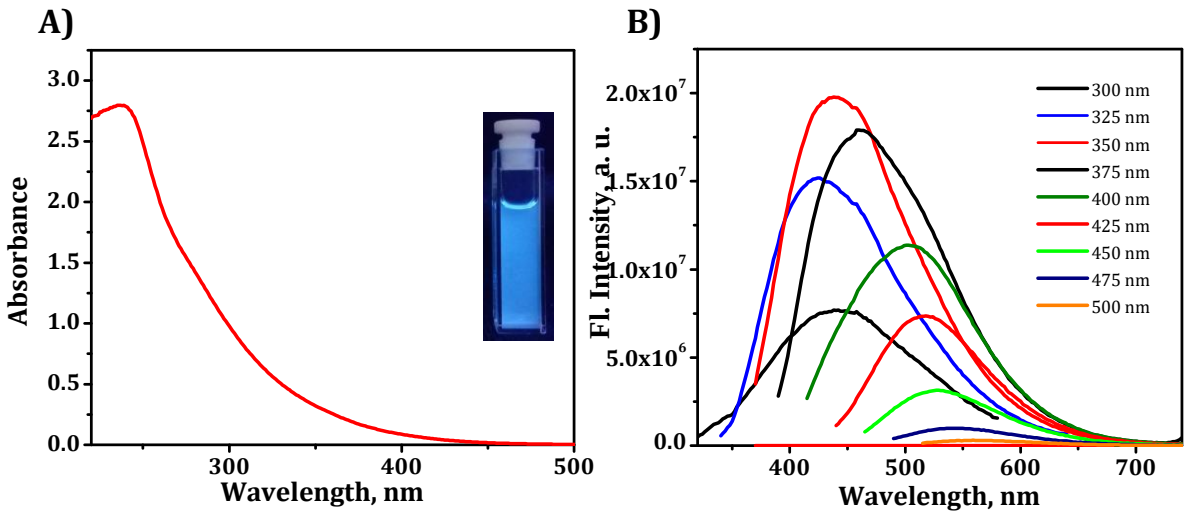

Figure 4.10. A) Absorpton spectra of **MQDs** in water and B) excitation dependent emission spectra of **MQDs** (excited from 300 to 500 nm).

4.3.3. Synthesis of BDSH

The diiodo-BODIPY core has been reported to have high triplet quantum yields, singlet oxygen generation efficiencies and excellent PDT activity. Major limitation of

most of the small molecule based diiodo-BODIPY derivative was their poor solubility and cellular availability. We have a conjugation strategy to covalently bind the diiodo-BODIPY derivative to **MQDs** *via* an alkyl thiol spacer, which is expected to enhance the solubility and bioavailability. The thiol derivative of diiodo-BODIPY (**BDSH**) was synthesized as per **Scheme 4.2**. The synthesis started from the 4-hydroxy benzaldehyde which upon reaction with 1,3-dibromopropane gave compound **1**, which upon reaction with 2,4 dimethyl pyrrole in presence of TFA, DDQ and BF_3-Etherate in DCM under room temperature gave the corresponding BODIPY derivative **3**, in moderate yield.[42] This BODIPY core is iodinated using NIS in 3:1 chloroform / acetic

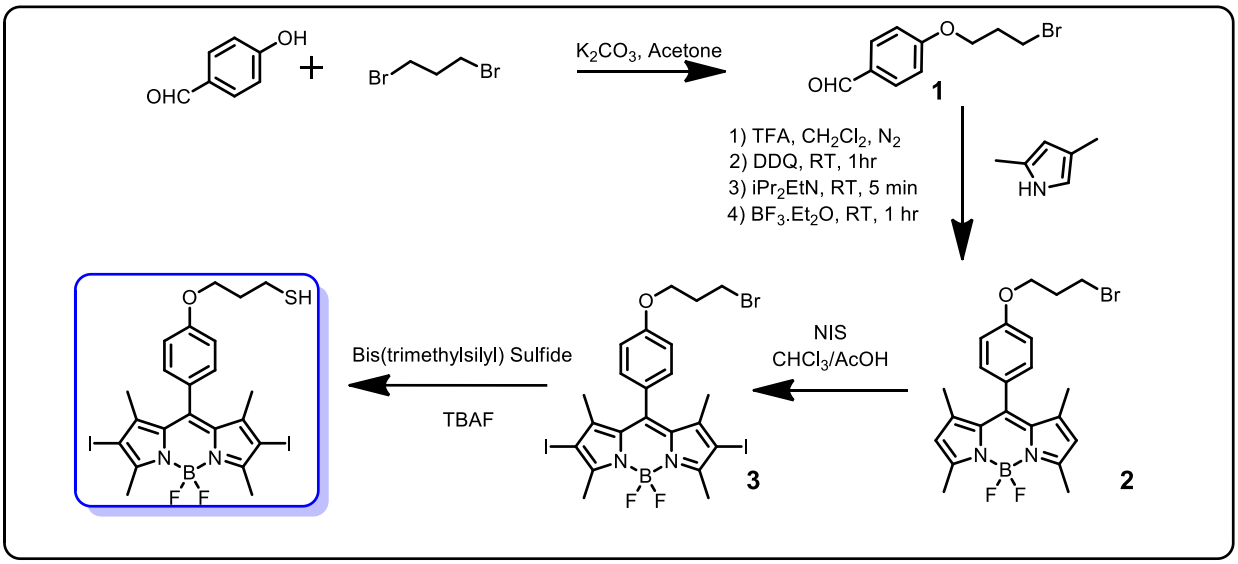

Scheme 4.2. Synthesis of BDSH

acid mixture and then the thiol moiety was introduced by subsequent reaction with bis(trimethylsilyl) sulfide in presence of TBAF. **BDSH** was characterized using ^{1}H NMR and mass analysis and used for further conjugation with **MQDs**. **BDSH** is found to be

soluble in organic solvents such as chloroform, methanol, DMF, DMSO and partially soluble in water. The molar extinction coefficient of **BDSH** at 530 nm in DMSO is calculated as 64000 $M^{-1}cm^{-1}$.

4.3.4. Synthesis and Characterization of MQD-BDSH

MoS_2 quantum dots - BODIPY nanoconjugate, **MQD-BDSH** was synthesized by using thiol ligand conjugation of **BDSH** with MoS_2 QDs as shown in Scheme 4.3. MoS_2 nanosheets contain several sulphur vacancies on the interior planes as well as on the edges, which can act as a coordinating site for incoming thiols. The reaction was carried out in water / DMF mixture (10:1) and the product was purified by subsequent washings with dichloromethane to remove traces of starting material, adsorbed on the

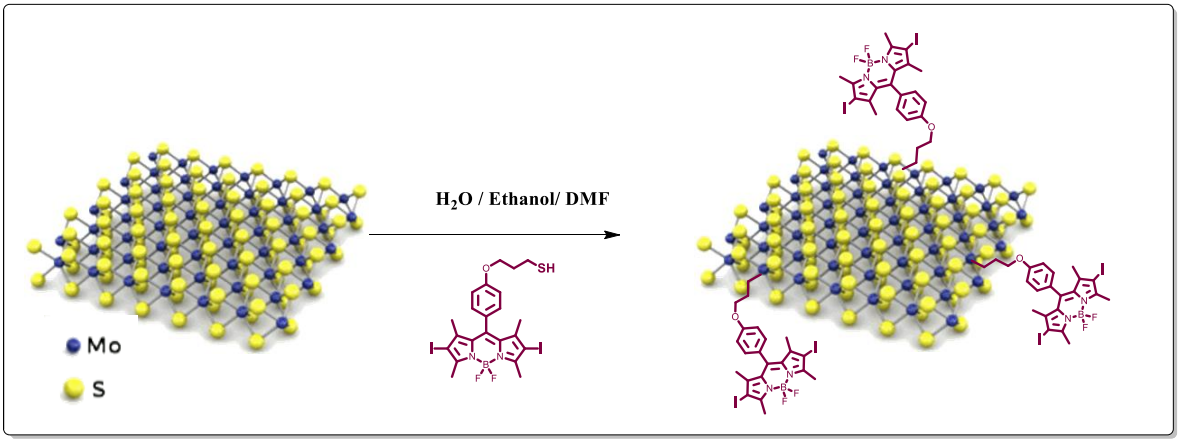

Scheme 4.3. Synthesis of **MQD-BDSH** nanoconjugate.

MQD surface. After drying under ambient conditions, **MQD-BDSH** nanoconjugates were re-suspended in water by sonication to give a stable colloidal solution. As prepared nanoconjugate also form stable suspensions in organic solvents such as methanol,

ethanol, DMF and DMSO. The amount of chromophore loading on the nanosheets was estimated to be about ~8.2% through UV-visible absorption technique.

4.3.5. Material Characterization of MQD-BDSH

MQD-BDSH nanoconjugate was characterized using AFM and TEM analysis. TEM images clearly shows the nanosheets in the size range of 30 nm - 80 nm with an average size of ~50 nm, similar distributions of that of **MQDs**. Efficient functionalization of **BDSH** on **MQDs** were confirmed from EDX analysis. Presence of Mo, S and I is obtained from EDX spectra as shown in Figure 4.11. AFM analysis further

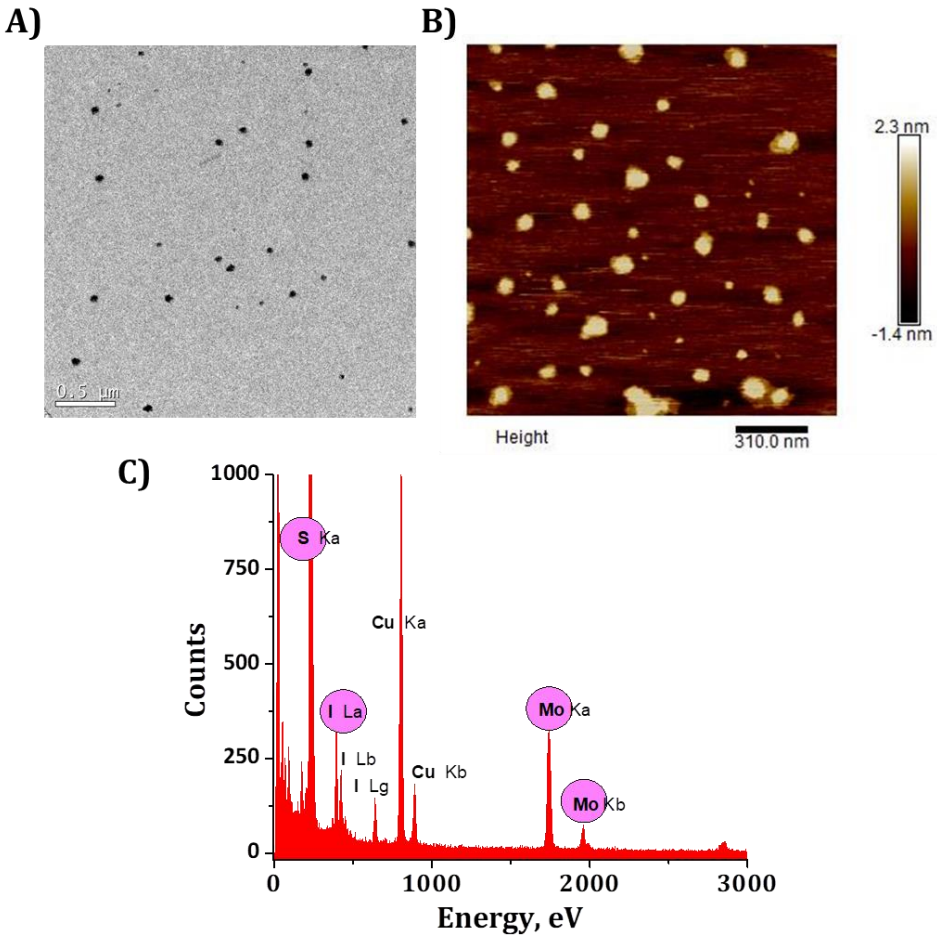

Figure 4.11. A) TEM, B) EDX and C) AFM images of **MQD-BDSH**

confirms the size and morphology of the synthesized nanoconjugate (Figure 4.11B). The microscopic characterization of **MQD-BDSH** confirms that the nanosheets are intact even after functionalization with **BDSH** and have similar size distribution that of the precursor, **MQDs**.

4.3.6. Photophysical Characterization of MQD-BDSH

The synthesized **MQDs** and its nanoconjugates are further subjected to photophysical characterization using UV-Visible and fluorescence spectroscopy. UV-Vis spectra of the nanoconjugate, **MQD-BDSH** shows considerable absorption corresponding to **BDSH** in the 480-600 nm region even after extensive washing process indicating the successful covalent attachment of **BDSH** on **MQDs** (Figure 4.12A). The drug loading content in the nanoconjugate is determined through absorption spectroscopy using the extinction coefficient of **BDSH** at 530 nm (64000 $M^{-1}cm^{-1}$) and the weight of the sensitizer is calculated to be ~8.2%.

Fluorescence intensity of nanoconjugate is found to be quenched to 3.4% compared to that of bare **MQDs** (4.1%). This is in accordance with the reported literature that surface modifications can alter the luminescence properties of **MQDs**. Surface functionalization can result in the observed quenching in fluorescence, which further confirms the successful formation of the covalent nanoconjugate. Normalized emission spectra of the **MQDs**, as well as the nanoconjugate recorded by 350 nm excitation in water, are shown in Figure 4.12B. Interestingly, we observed a quenching

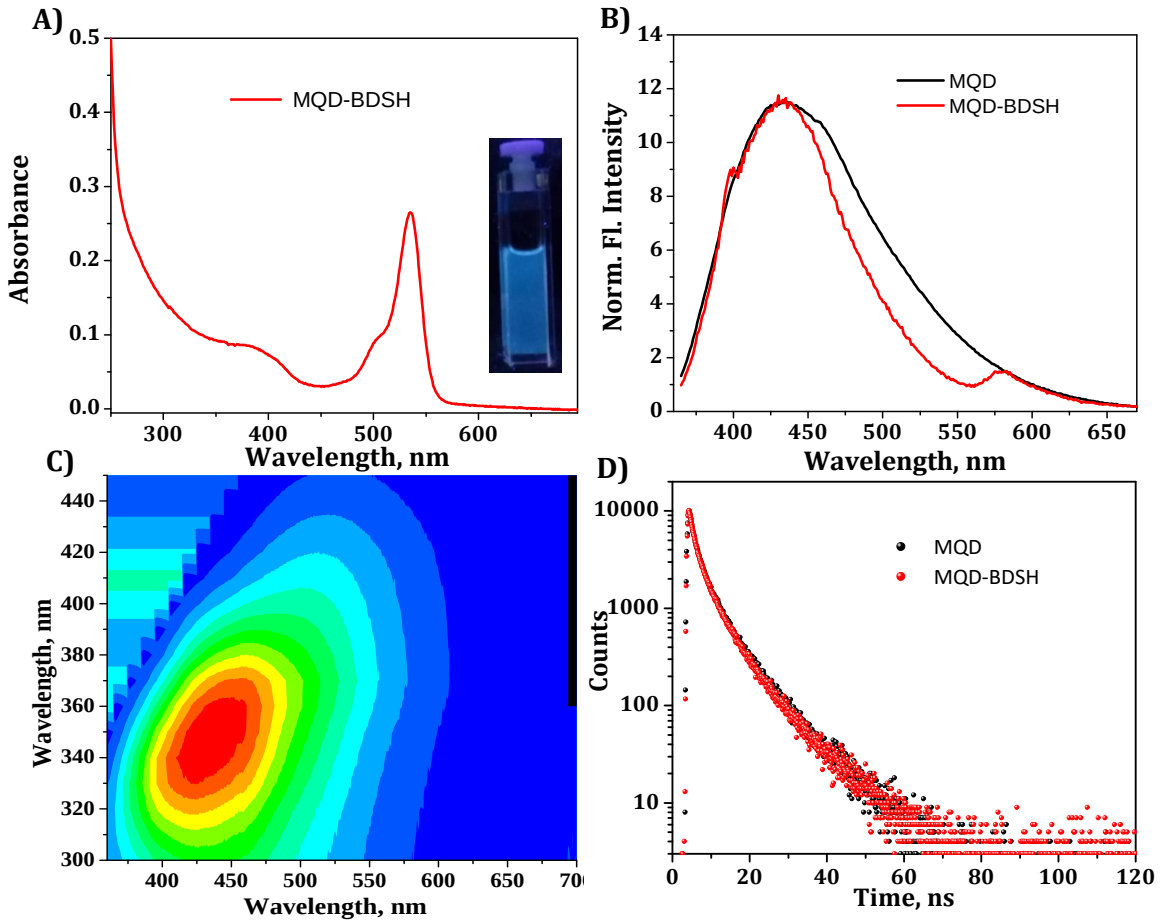

Figure 4.12. A) Absorption and B) fluorescence spectra of **MQD** and **MQD-BDSH** in water. Fluorescence spectra are normalized and recorded by excited at 350 nm light. C) Excitation dependent emission of **MQD-BDSH** and D) fluorescence lifetime of **MQDs** and **MQD-BDSH**.

of fluorescence band between 450 nm and 550 nm in the nanoconjugate, where **BDSH** has considerable overlapped absorption indicating the possibility of energy transfer from **MQDs** to the **BDSH**. Nanoconjugate is also exhibiting excitation dependent emission properties, similar to that of **MQDs** (Figure 4.12C). Fluorescence lifetime analysis of **MQDs** showed tri-exponential decay characteristics with an average lifetime of 8.64 ns. Nanoconjugate also exhibits similar fluorescence decay curve with a reduced average lifetime of 8.27 ns (Figure 4.12D).

4.3.7. Quantification of Triplet Excited States

To understand the transient intermediates involved during the excitation of **BDSH** and **MQD-BDSH** conjugates, we have carried out nanosecond laser flash photolysis studies using a 532 nm laser pulse excitation. Figure 4.13 shows the transient absorption spectrum of the **BDSH** and **MQD-BDSH** obtained after the laser excitation in methanol. The transient absorption spectrum showed maximum at 450 nm with bleach at 530 nm, where the compound has significant ground state absorption. The lifetime of the transient was determined from the decay profile (Inset, Figure 4.13) and it was found to be 0.78 μs and 0.33 μs for **BDSH** and **MQD-BDSH** respectively.

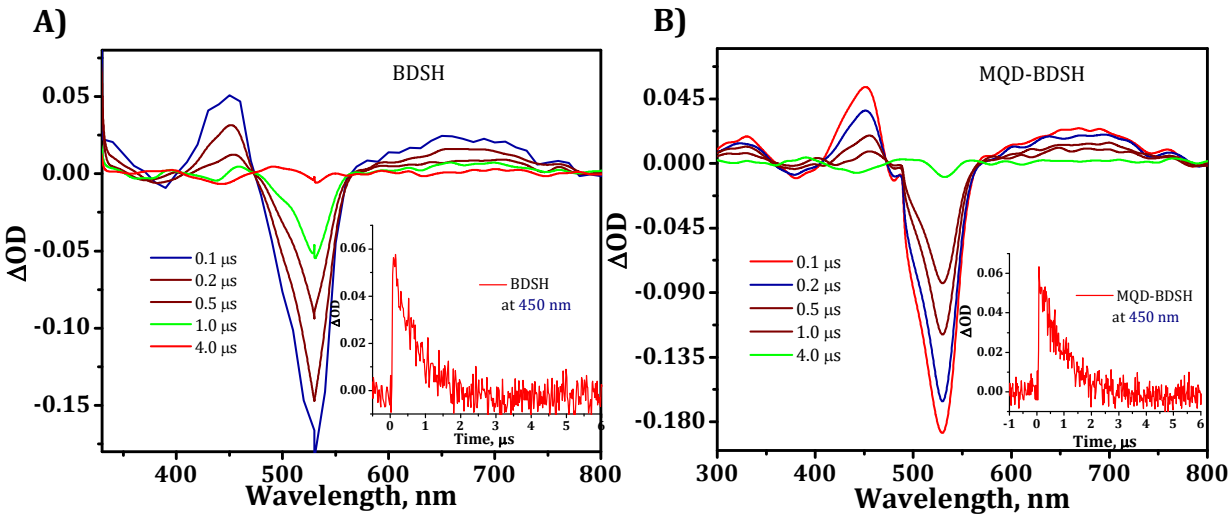

Figure 4.13. Transient absorption spectra of A) **BDSH** and B) **MQD-BDSH** excited at 532 nm laser. Triplet decay at 450 nm is shown in the inset.

The triplet excited state yields (Φ_T) of the samples, **BDSH** and **MQD-BDSH** were determined to be 0.90±0.03 and 0.91±0.02 respectively, by an earlier reported procedure of energy transfer to β-carotene, using $Ru(bpy)_3^{2+}$, as the reference molecule.[43] The transient absorbance of the β–carotene triplet, generated by the energy

transfer from $Ru(bpy)_3^{2+}$ or the triplet of the sample, was monitored at 510 nm. Comparison of plateau absorbance (ΔA) following the completion of sensitized triplet formation, properly corrected for the decay of the donor triplet excited state in competition with energy transfer to β-carotene, enabled us to estimate Φ_T of the triplet excited states.

4.3.8. Quantification of Singlet Oxygen Generation Efficiency

In order to check the efficacy of nanoconjugates for PDT applications, we have studied the singlet oxygen generation efficiency of free sensitizer (**BDSH**) and **MQD-BDSH** conjugate using 1,3-diphenylbenzofuran (DPBF) as a singlet oxygen trapping agent. Optically matching solution of the sample and the standard were irradiated using oriel lamp fitted with a 475 nm long pass filter at regular intervals followed by absorption measurements. The singlet oxygen generation quantum yields ($\Phi\ ^1O_2$) were calculated as per standard procedure using Rose Bengal as standard.[44] Singlet oxygen generation efficiency of **BDSH** and **MQD-BDSH** were calculated as 85% and 81%, respectively using Rose Bengal as a standard (Figure 4.14C). The iodinated core of **BDSH** can increase the rate of ISC *via* heavy atom effect which in turn sensitizes more triplet oxygen. Generation and efficiency of singlet oxygen by samples were further confirmed by observed phosphorescence at 1270 nm, which is characteristic of singlet oxygen (Figure 4.14D). By comparing the peak area of optically matching solutions of samples and Rose Bengal as reference, it is found that **BDSH** and **MQD-BDSH** are

showing comparable singlet oxygen generation efficiencies similar to that reported by DPBF method. The iodinated core of **BDSH** could increase the rate of ISC *via* heavy atom effect which in turn sensitizes more triplet oxygen. Results indicate that our nanoconjugate is highly efficient in producing singlet oxygen which is a key requirement of a sensitizer for PDT applications.

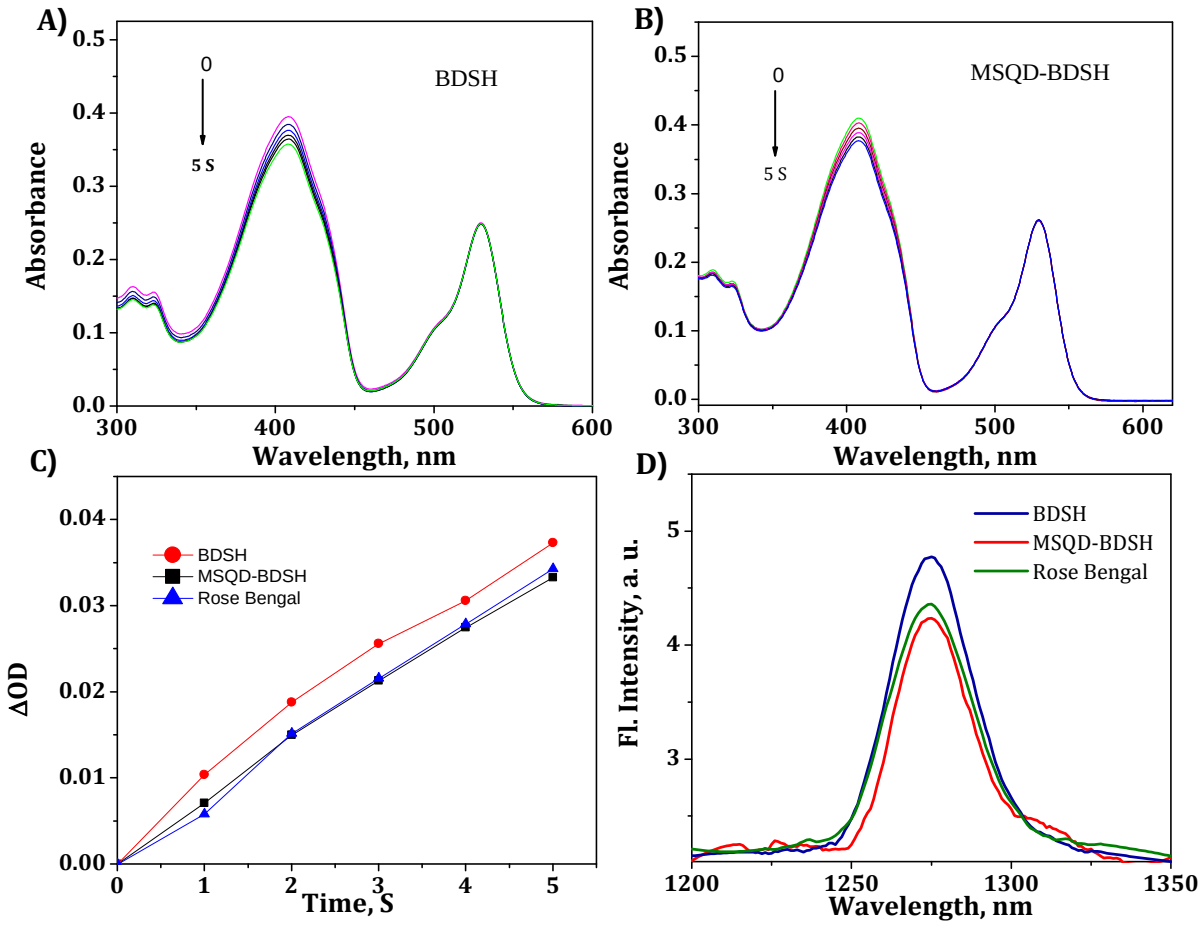

Figure 4.14. A) & B) Decrease in absorption of DPBF (410 nm) of **BDSH** sample upon 1 s irradiation using 200 W mercury lamp (model 3767) on an Oriel optical bench (model 11200) fitted with 475 nm long pass filter. C) Relative plot of singlet oxygen generation efficacy of **BDSH, MQD-BDSH** and the standard Rose Bengal. D) Singlet oxygen luminescence spectrum of the **BDSH**, **MQD-BDSH** and the Rose Bengal after the excitation at 530 nm.

4.3.9. Investigation of *in vitro* Photodynamic Efficiency

To investigate the photodynamic activity of the synthesized nanoconjugate in cancer cells *in vitro*, we have carried out MTT assay in HSC4 cells (Oral cancer). The percentage of growth inhibition of cells in presence of **MQD-BDSH** and the control samples such as **MQDs** and **BDSH** alone were determined using MTT assay with and without irradiation (PDT lamp, 540 nm, Green LED array with a total fluence rate of 100 J/cm^2). Result shows that **MQD-BDSH** is a better candidate for PDT with an IC_{50} value of 20 nM (sensitizer concentration), whereas a negligible change in growth inhibition was observed in **BDSH** alone at similar concentration range (Figure 4.15).

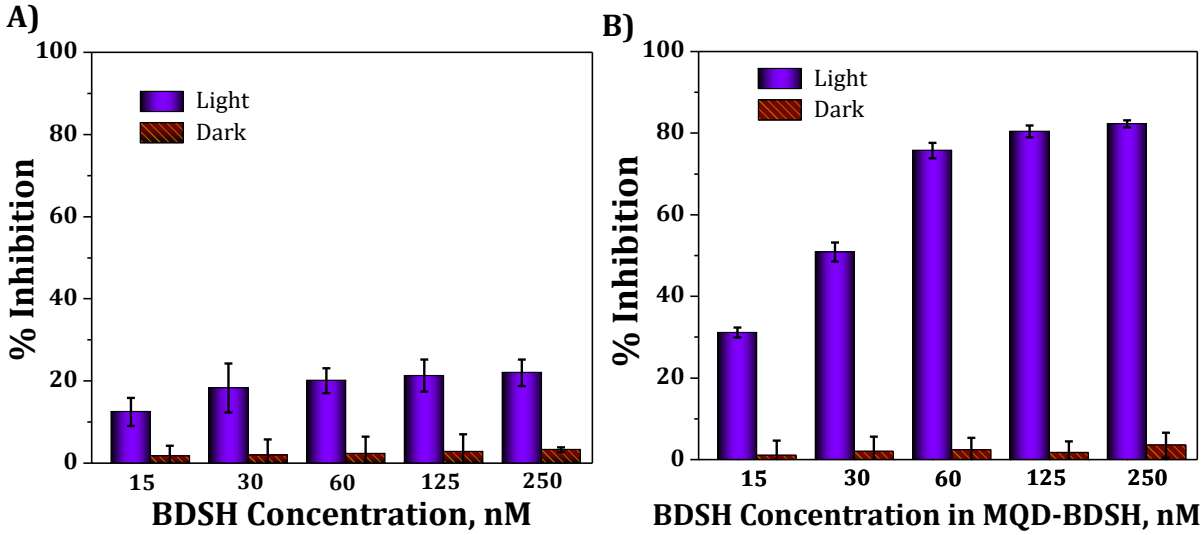

Figure 4.15. MTT assay showing photocytotoxicity of A) **BDSH** and B) **MQD-BDSH** in HSC4 oral cancer cells.

In general, the cytotoxic effect of a photosensitizer in PDT is predominately through ROS mediated cell death. Hence we studied cellular oxidative stress in **MQD-BDSH** based PDT using flow cytometric analysis with CM-H2DCFDA probe. In the reduced form, CM-H2DCFDA is non-fluorescent, but the cellular oxidation followed by

esterases mediated hydrolysis of acetate groups, results in a green fluorescent derivative. When HSC4 cells were treated with **MQD-BDSH** and irradiated, followed by the addition of CM-H2DCFDA, we observed fluorescence in 73.6% of cells, in contrast, **BDSH** alone showed background values of 18.7% (Figure 4.16). These results demonstrate that PDT with **MQD-BDSH** nanoconjugate induced a significant subcellular ROS generation leading to oxidative stress in HSC4 cells.

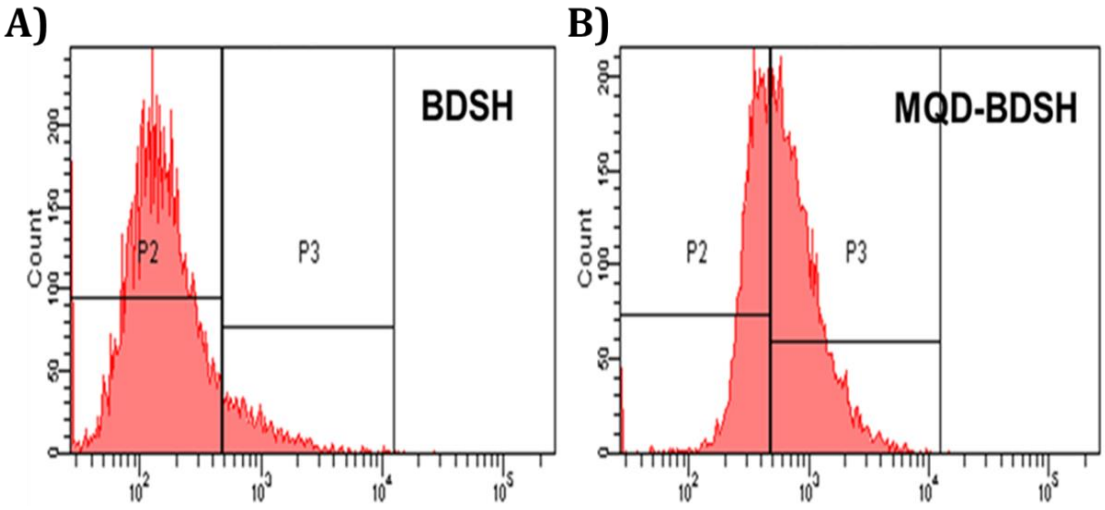

Figure 4.16. Sub cellular ROS induction after PDT using CM-H2DCFDA probe. Flow cytometry analysis of HSC4 cells, showing induction of intracellular ROS by, A) **BDSH** and B) **MQD-BDSH** after PDT.

In order to understand the mechanism of cell death as well as the efficiency of our nanoconjugate for PDT treatment, we have carried out a tetramethylrhodaminemethyl ester (TMRM) staining experiment, as shown in Figure 4.17A. The apoptotic cell death causes decrease in the mitochondrial inner membrane potential, which will result in further decrease of red fluorescence of TMRM. Photodynamic treatment of nanoconjugate with HSC4 cells caused a decrease in red fluorescence of TMRM, which confirms the cell death through mitochondria-mediated

apoptotic pathway. The nature of cell death was further confirmed through a nuclear condensation assay using HSC4 human oral cancer cells (Figure 4.17B). The cell lines are staining with Hoechst dye, which can stain only viable cells. The decrease in blue fluorescence intensity after PDT treatment with **MQD-BDSH** (20 nM) is more compared to free sensitizer and **MQDs** alone, which further confirms the better efficiency of the nanoconjugate.

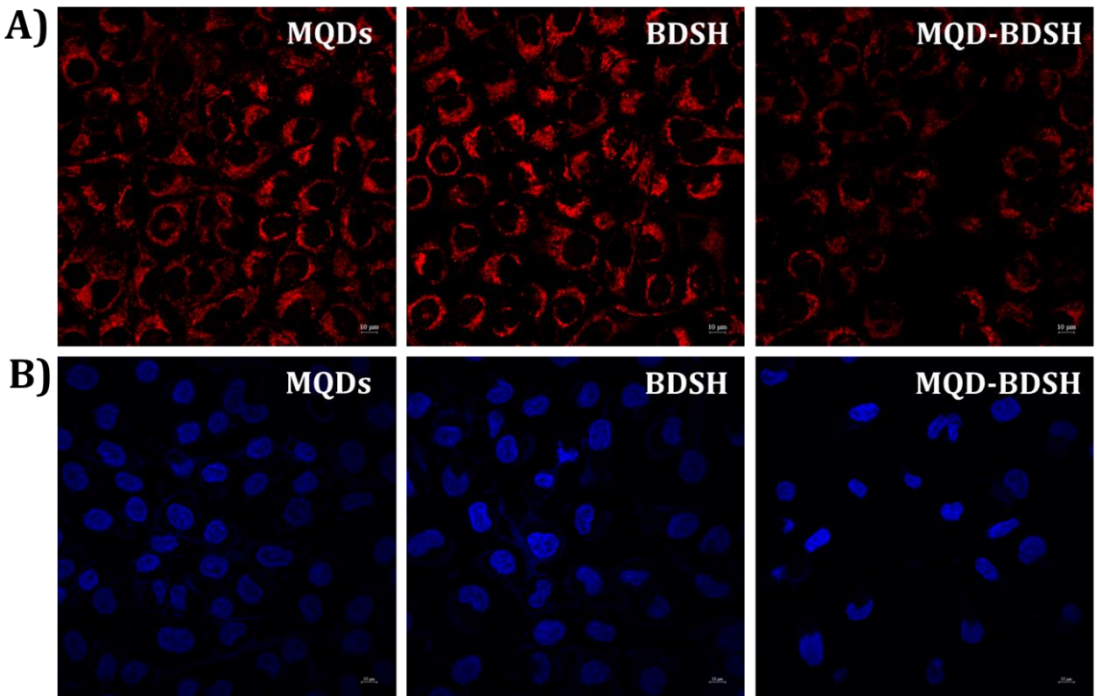

Figure 4.17. A) TMRM assay and B) Hoechst staining of HSC4 cell lines, each panel showed the cells under **MQD**, **BDSH** and **MQD-BDSH** after PDT analysis (20 nM sensitizer concentration).

The mechanism of the PDT activity of the conjugate can be evaluated by using Annexin V-FITC assay since it is an excellent indicator for the early stages of programmed cell death. This assay was based on the translocation of phosphatidylserine from the inner face of the plasma membrane to the cell surface, thus

exposing it to the external cellular environment and the Annexin V- FITC has high affinity for phosphatidylserine. To quantify the formation of apoptotic cells, we employed Annexin V-FITC through fluorescence microscopy and flow cytometry. The lower right quadrants (Q4) represent the early apoptotic cells Annexin V– FITC and propidium iodide (PI). The upper right quadrants (Q2)

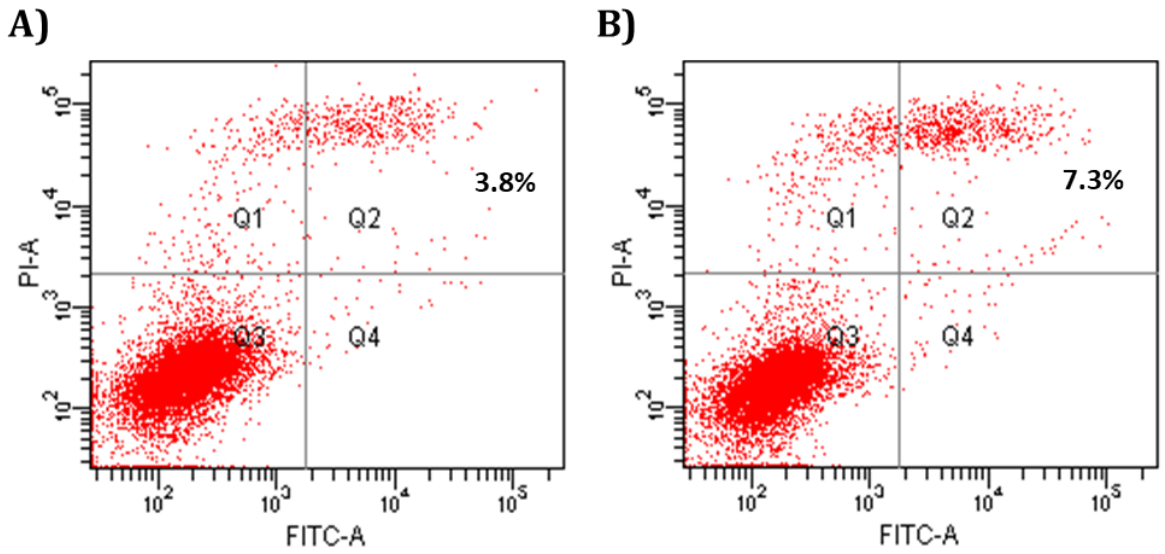

Figure 4.18. Annexin Flow cytometric analysis of HSC4 cells after PDT treatment with light control and dark control and in presence of A) **BDSH and** B) **MQD-BDSH** at concentration of 20 nM.

represent the late apoptotic cells positive for Annexin V– FITC and propidium iodide (PI). We carried out the assay using different drug concentration after 24 hours of PDT and the results revealed that PDT using **MQD-BDSH** (20 nM) induces late apoptosis of about 7.3% whereas, **BDSH** alone showed only 3.8% late apoptotic cells at same concentration range (Figure 4.18). This result confirmed that major cell death induced by **MQD-BDSH** is via apoptosis.

4.4. Conclusions

In summary, we have designed and synthesized a MoS_2 quantum dot-BODIPY sensitizer nanoconjugate, MQD-BDSH and characterized the structural and photophysical properties through spectroscopic, analytic and microscopic techniques. **MQDs** with lateral dimensions below 50 nm were prepared *via* temperature assisted cutting of larger as-prepared MoS_2 nanosheets in DMF. Further conjugation of **MQDs** with core iodine substituted BODIPY thiol derivative, **BDSH** was achieved through thiol ligand conjugation method. The nanoconjugate, **MQD-BDSH** was thoroughly characterized and preliminary photophysical investigations confirmed successful conjugation of the sensitizer with **MQDs**. **MQD-BDSH** exhibited good singlet oxygen generation quantum yield of 81%, demonstrating the potential of these nanoconjugates for PDT applications. *In vitro* PDT activity of this nanoconjugate was investigated using HSC4 oral cancer cell lines and is found to be an efficient system for PDT treatment with an IC_{50} value of 20 nM (sensitizer concentration). TMRM assay and nuclear condensation and Annexin assay on HSC4 cell lines confirmed the cell death through apoptotic pathway. These results demonstrate the potential of these nanoconjugates for PDT applications.

4.5. Experimental Section

4.5.1. Synthesis and Characterization

The reagents and materials for synthesis were purchased from Sigma-Aldrich and Spectrochem Chemical suppliers. Dry solvents were used wherever necessary and were prepared using reported drying procedures. ^{1}H-NMR spectra were recorded using

DPX 500 MHz spectrometer using tetramethyl silane (TMS) as the internal standard and deuteriated solvents were used for the measurements. Absorption spectra were recorded on a Shimadzu UV-2600 PC UV-Vis spectrophotometer.

Electron microscopic observations (TEM) of the morphology were performed with a FEI Tecnai G^2-30 Transmission Electron Microscope operating at 120 kV. Atomic Force Microscopy images were recorded under ambient conditions using a BRUKER (Multimode AFM 3COCF) operating with a tapping mode regime. Micro-fabricated TiN cantilever tips (NSG10) with a resonance frequency of 299 kHz and a spring constant of 20-80 Nm^{-1} were used. AFM section analysis was done offline. Samples for the imaging were prepared by drop casting the sample solution (0.05 mg/ mL) on freshly cleaved mica surface at ambient conditions.

4.5.2. *Synthesis of MoS_2 nanosheets*

The MoS_2 nanosheets were prepared by a modified liquid exfoliation method. MoS_2 powder (300 mg) was mixed with 100 mL of ethanol/water with ethanol volume fraction of 45% in a 250mL flask. The mixture was taken in a sealed flask and ultra-sonicated for 24 h to form a dark green suspension. After that, the dispersion was centrifuged at 6000 rpm for 20 min three times to remove the aggregates. Then the supernatant was collected and dried at ambient conditions.

4.5.3. *Synthesis of MoS_2 Quantum Dots (MQDs) by heat treatment*

MoS_2 (20 mg) was added to 10 ml water and ultra-sonicated for 1 hour until it became a clear solution. This solution is further heated to 120 ^oC, fitted with water cooled condenser. It is kept for stirring over 12 h. The solution was cooled and the clear

yellow solution obtained is neutralized with NaOH. Excess salt formed was removed by filtration and the resulting solution was purified by dialysis for 3 days with frequent change of water. Desalted **MQDs** were dried and used for further reactions.

4.5.4. Synthesis of diiodo-BODIPY thiol, BDSH

4.5.4.*1. Synthesis of 4-(3-bromopropoxy)benzaldehyde, 1*

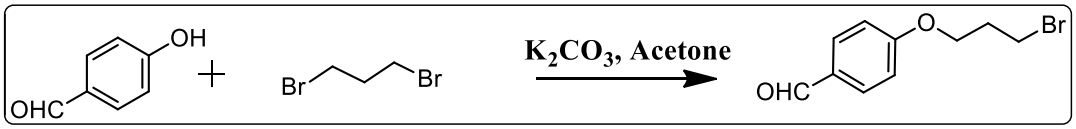

A suspension of 1, 3-dibromopropane (4g, 20 mmol), p-hydroxybenzaldehyde (1.22 g, 10 mmol), and K_2CO_3 (2.76 g, 10 mmol) was refluxed in acetone (25 mL) for 12h. The reaction mixture was cooled, filtered, and concentrated under reduced pressure. The crude product was chromatographed over silica gel (200-400mesh) and eluted with chloroform to give 67% of compound.

^{1}HNMR: ($CDCl_3$, 500 MHz), δ (ppm): 2.35 (q, J = 6Hz, 5H), 3.61 (t, J= 6.5Hz, 2H), 4.19 (t, J =6Hz, 2H), 7.01 (d, J =8.5Hz, 2H), 7.83 (d, J =8.5Hz, 2H), 9.88 (s, 1H),

MS (HRMS): Calculated =241.99, Found = 241.98 (M^+).

4.5.4.*2 Synthesis of 2*

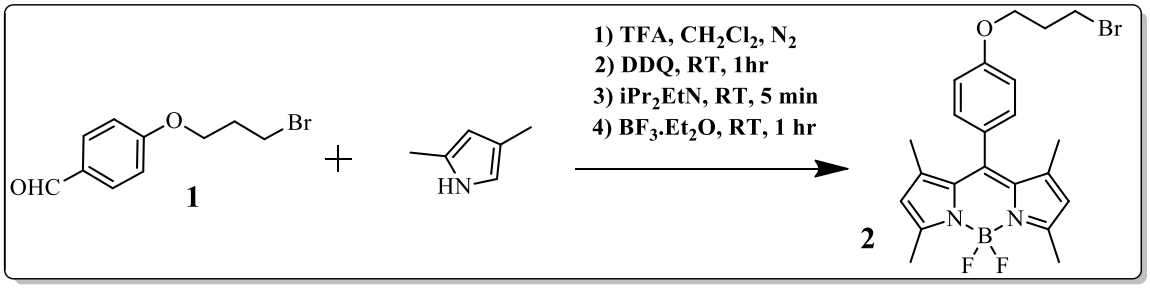

To the solution of compound **1** (400 mg, 1.6 mmol) in DCM (250 mL), added 2,4-dimethyl pyrrole (313 mg, 3.2 mmol) under Argon atmosphere. One drop of TFA was added and the solution was stirred at room temperature for overnight. When TLC monitoring shows complete consumption of the aldehyde, solution of DDQ (373 mg, 2 mmol) in DCM was added and stirring was continued for 20 min. Then 4 mL of *N,N*-diisopropylethylamine (DIEA) added and stirred for 5 min. Then BF_3-OEt_2 (4 mL) was added and stirring was continued for 30 minutes. The reaction mixture was washed with water three times and the organic layer is dried over Na_2SO_4 and reduced under vacuum. The compound was purified by column chromatography (silica gel) with 20% ethyl acetate / hexane to yield 494 mg (67%) of the product.

^{1}HNMR: ($CDCl_3$, 500 MHz), δ (ppm): 1.43 (s, 6H), 2.37 (q, J= 6 Hz, 2H), 2.55 (s, 6H), 3.64 (t, J= 6.5 Hz, 2H), 4.16 (t, J= 5.5 Hz, 2H), 5.9 (s, 2H), 7.01 (d, J= 8.5Hz, 2H), 7.17(d, J= 8.5 Hz, 2H).

MS (HRMS): Calculated = 460.11, Found =483.10 (M+23).

4.5.4.3. ***Synthesis of 3***

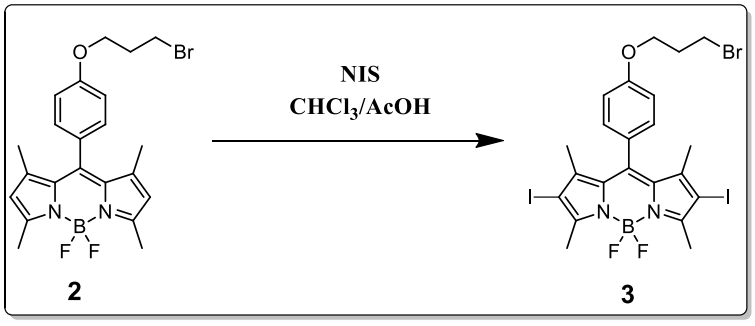

Compound **2** (400 mg) was dissolved in 40 mL $CHCl_3$: AcOH (3:1) mixture. Then NIS (486.84 mg, 2.5 eq) was added and stirred at room temperature for 1 h. After completion of the reaction, the excess acetic acid was neutralized by washing with

$NaHCO_3$ solution and then washed with sodium thiosulphate to quench excess iodine. The reaction mixture was concentrated and purified using silica gel and eluted with 10% ethylacetate-hexane to obtain 70% of compound.

^{1}HNMR: (CDCl3, 500 MHz), δ (ppm): 1.44 (s, 6H), 2.38 (q, J= 6Hz, 2H), 2.64 (s, 6H), 3.65(t, J= 6.5 Hz, 2H), 4.18 (t, J= 5.5Hz, 2H), 7.04(d, J= 8.5 Hz, 2H), 7.14 (d, J= 8.5 Hz).

MS (HRMS): Calculated =711.90, Found = 711.91 $(M)^+$.

4.5.4.4. *Synthesis of BDSH*

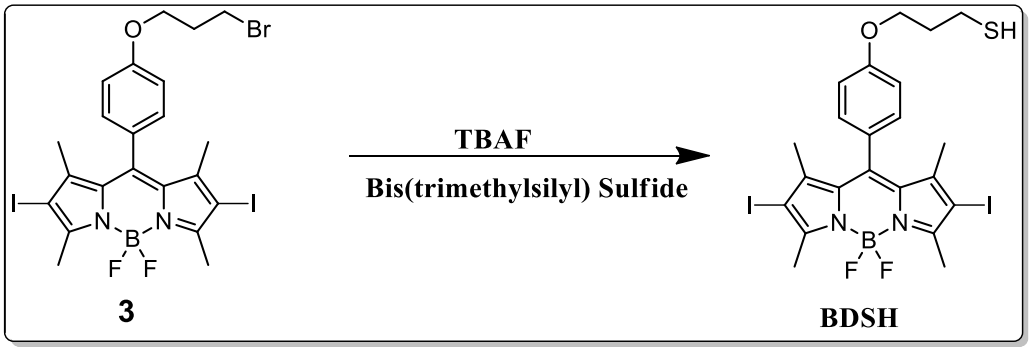

To a stirred solution of compound **3** (100 mg, 0.140 mmol) in freshly distilled THF (2 mL), a mixture of bis(trimethylsilyl)sulfide (30.07 mg~35.38 µL, 0.1685 mmol, 1.2 eq) and tetrabutylammoniumflouride (TBAF, 48.58 mg, 0.154 mmol, 1.1eq) dissolved in THF (1 mL) was added. The resulting mixture was stirred at room temperature for 12 h, diluted with dichloromethane, and washed with saturated NH_4Cl solution. The crude product when chromatographed over silica gel (200-400 mesh) and eluted with 5% ethylacetate-hexane to obtain 46% of compound.

^{1}HNMR: (CDCl3, 500 MHz), δ (ppm): 1.44 (s, 6H), 2.34 (q, J= 6.5Hz, 2H), 2.64 (s, 6H), 3.19 (t, J= 7Hz, 2H), 4.17 (t, J= 6 Hz,2H), 7.03 (d, J= 8.5Hz,2H), 7.13 (d, J= 8.5Hz, 2H)

MS (HRMS): Calculated =664.90, Found = 664.91 $(M).^+$

4.5.5. *Synthesis of MQD-BDSH conjugates*

BDSH (5 mg) dissolved in 200 µL DMF was added to aqueous solution of **MQDs** (10 mg in 2 mL). The reaction was carried out in water / DMF mixture (1:0.1) under stirring for 24 hours and the product was purified by subsequent washings with dichloromethane to remove traces of starting material, adsorbed on the **MQD** surface. Product is further purified by dialysis for 12 hours. After drying under ambient conditions, **MQD-BDSH** nanosheets were re-suspended in water by sonication to give a stable colloidal solution.

4.5.6. Description of Experimental Techniques

4.5.6.1. Optical Measurements

Electronic absorption spectra were recorded on a Shimadzu UV-2600 PC spectrophotometer and the emission spectra were measured on a SPEX-Fluorolog F112X spectrofluorimeter. Measurements of solution state fluorescence quantum efficiency were carried out using a calibrated integrating sphere connected to SPEX Fluorolog-3 spectrofluorimeter. A Xenon-arc lamp was used to excite the samples placed in the sphere, with 350 nm as the excitation wavelength. This experimental setup and the integrating sphere system calibrated using the solid state fluorescence quantum yield of the standard sodium salicilate (white powder) was determined to be 60 ± 10%, which is consistent with previously reported values.[45]

4.5.6.2. Nanosecond Laser Flash Photolysis Studies

Nanosecond laser flash photolysis experiments were performed by using an Applied Photophysics model LKS-20 laser kinetic spectrometer using OCR-12 Series

Quanta Ray Nd: YAG laser. The detailed experimental procedure was described in Chapter 3 of this thesis. The triplet excited state yields (Φ_T) of the samples, **BDSH** and **MQD-BDSH** were determined by an earlier reported procedure of energy transfer to β-carotene, using $Ru(bpy)_3^{2+}$, as the reference molecule.[43] For these experiments, optically matched solutions of $Ru(bpy)_3^{2+}$ and the samples at 532 nm, were mixed with a known volume of β-carotene solution (end concentration of β-carotene was fixed at *ca.* 2.0 x 10^{-4} M). The transient absorbance of the β–carotene triplet, generated by the energy transfer from $Ru(bpy)_3^{2+}$ or the sample's triplet excited state, was monitored at 510 nm. Comparison of plateau absorbance (ΔA) following the completion of sensitized triplet formation, properly corrected for the decay of the donor triplet excited state in competition with energy transfer to β-carotene, enabled us to estimate Φ_T of the triplet excited states based on Eqn 1.

$$\phi_T^{sam} = \phi_T^{ref} \frac{\Delta A^{sam} K_{obs}^{sam} (K_{obs}^{ref} - K_0^{ref})}{\Delta A^{ref} (K_{obs}^{sam} - K_0^{sam}) K_{obs}^{ref}} \qquad \text{Eqn (1)}$$

wherein, superscripts sam and ref designate various samples and $Ru(bpy)_3^{2+}$, respectively, K_{obs}, is the pseudo-first-order rate constant for the growth of the β-carotene triplet and K_0 is the rate constant for the decay of the donor triplet, in the absence of β- carotene, observed in solutions containing $Ru(bpy)_3^{2+}$ or a sample at the same optical density (OD = 0.1) as those used for sensitization.

4.5.6.3. Determination of singlet oxygen generation efficiency

Singlet oxygen generation quantum yields in methanol solution were determined by monitoring the photo-oxidation of 1,3-diphenylisobenzofuran (DPBF)

sensitized by **BDSH/MQD-BDSH**.[46] DPBF can form *o*-dibenzoylbenzene through a [4 + 2] cycloaddition with $^1O_2$. The disappearance of DPBF and the formation of the product *o*-dibenzoylbenzene can be monitored by absorption decrease at 410 nm. Optically matching solution of the sample and the standard were irradiated using oriel lamp (200 W xenon lamp, model 3767) fitted with a suitable filter (475 nm long pass) at regular intervals followed by UV-visible absorption measurements. The singlet oxygen generation quantum yields (Φ $^1O_2$) were calculated as per Eqn (2), where m is the slope of a plot of change in absorbance of DPBF (at 410 nm) with the irradiation time and F is the absorption correction factor, which is given by $F = 1 - 10^{-OD}$ (OD at the irradiation wavelength).

$$\Phi\Delta^{com} = \Phi\Delta^{ref}\frac{m^{com}\,F^{ref}}{m^{ref}\,F^{com}} \qquad \text{Eqn(2)}$$

4.5.6.4. Cell culture and Photodynamic treatment.

The cell biology experiments were conducted in RGCB, Trivandrum, with collaboration with Dr. Asha S. Nair's group. Human oral cancer cell lines (HSC4) were purchased from ATCC (USA). The photosensitizer nanoconjugate, **MQD-BDSH** was synthesized as previously described and 100 µg/mL (12µM, sensitizer concentration) stock solutions in water was prepared for further studies.

4.5.6.5. Cytotoxicity assay (IC_{50} value)

MTT (3-(4,5-dimethylthiazol-2-yl)-2,5-diphenyltetrazolium bromide) reduction assay was performed to assess cell viability. Briefly, cells (10000 cells) were seeded in

two 96 well cluster plate and allowed to reach the exponential phase of growth (18 hours). Later, both plates were treated using **MQD-BDSH** (5–200nM), incubated for 1 hour and photo-irradiated with PDT lamp (540 nm, Green LED array with a total fluence rate of 100 J/cm^2 for 10 minutes. Another plate was kept in dark for assessing dark cytotoxicity. The amount of formazan crystals formed was measured after 4 h of MTT addition. The crystals were dissolved in isopropyl alcohol and the OD was measured at 570 nm. Graphs were plotted using Microsoft Excel, percentage inhibition were calculated by the formula (OD value of control - OD value of test)/OD value of control * 100).

4.5.6.6. Assay for cellular reactive oxygen species (ROS) content (CM-H2DCFDA)

ROS stress studies, approximately 5× 10^5 MDA-MB-231 cells were seeded in 60 mm culture dishes and 10000 cells were plated in 60 mm and 96 well Opti-bottom plates (BD Falcon) with serum-containing media. After 18 hours, the cells were treated with **MQD-BDSH (**20 nM, sensitizer concentration) for 1 h and photo-irradiation was done using PDT lamp (Green LED array, 540 nm with a total fluence rate of 100 J/cm^2) for 10 minutes. In one plate 20 nM nanoconjugate was added and the plate was kept in the dark to be taken as Dark control. Another plate was irradiated with a laser without drug treatment and was taken as Light control. After 1 hour of PDT the cellular reactive oxygen content was determined using a CM-H2DCFDA probe, according to the manufacturer's instructions (Invitrogen). Further, we analyzed the fluorescence of CM-H2DCFDA using flow cytometry (FACS Aria, Special order system, BD, USA) and analysis was done using DIVA software.

4.5.6.7. Measure of mitochondrial membrane potential

Mitochondrial membrane potential was measured using TMRM dyes from molecular probes (Life Technology, USA). Approximately 5 × 10^5 MDA-MB-231 cells were seeded in 60 mm culture dishes. After 18 hours, the cells were treated with **MQD-BDSH** (20 nM, sensitizer concentration) for 1 hour and photo irradiation was done using PDT lamp (540 nm, Green LED array with a total fluence rate of 100 J/cm^2) for 10 minutes and incubated for 3, 6, 12 and 24 hours. Light and Dark control were taken as mentioned earlier. For fluorescence cyto-chemical study 10^5 HSC4 cells were seeded in a 96 well plate and subjected to **MQD-BDSH** PDT treatment as mentioned as earlier. Post treatment, the cells were washed with PBS and incubated with 10 nm TMRM in PBS for 30 minutes. Images were taken using a fluorescent microscope (Leica DMI 4000 B, Germany). Further, the fluorescence of TMRM corresponding to mitochondrial membrane potential was analyzed using flow cytometry.

4.5.6.8. Chromatin Condensation Assay by Hoechst Staining

To study chromatin condensation, approximately 10^5 MDA-MB-231 cells were seeded in 96 well culture dishes and incubated for 24 h. Then, cells were incubated with 20 nM **MQD-BDSH** for 24 h followed by photo-irradiation using PDT lamp (540 nm, Green LED array with a total fluence rate of 100 J/cm^2). Light and Dark control were taken as previously described. After 24 h of treatment on HSC4 cells were rinsed twice with PBS and stained with 5 µg/ml Hoechst dye for 15 min at room temperature. Cells were then washed twice with PBS and visualized under an inverted fluorescence microscope.

4.5.6.9. Annexin binding assay

PDT treatment was done as mentioned earlier in TMRM assay. Annexin binding assay was performed as per manufacturer's instructions provided in Annexin VFITC Apoptosis Detection Kit (Sigma) and flow cytometric analysis carried out using FACS Aria (BD, USA).

4.6. References

(1) Rao, C. N. R.; Matte, H. S. S. R.; Subrahmanyam, K. S. *Acc. Chem. Res.* **2013**, *46*, 149.

(2) Tan, C.; Cao, X.; Wu, X.-J.; He, Q.; Yang, J.; Zhang, X.; Chen, J.; Zhao, W.; Han, S.; Nam, G.-H.; Sindoro, M.; Zhang, H. *Chem. Rev.* **2017**, *117*, 6225.

(3) Chen, Y.; Tan, C.; Zhang, H.; Wang, L. *Chem. Soc. Rev.* **2015**, *44*, 2681.

(4) Chhowalla, M.; Liu, Z.; Zhang, H. *Chem. Soc. Rev.* **2015**, *44*, 2584.

(5) Li, X.; Zhu, H. *J. Materiomics* **2015**, *1*, 33.

(6) Arul, N. S.; Nithya, V. D. *RSC Adv.* **2016**, *6*, 65670.

(7) Zeng, G.; Chen, T.; Huang, L.; Liu, M.; Jiang, R.; Wan, Q.; Dai, Y.; Wen, Y.; Zhang, X.; Wei, Y. *J. Taiwan Inst. Chem. Eng.* **2018**, *82*, 205.

(8) Li, B. L.; Setyawati, M. I.; Chen, L.; Xie, J.; Ariga, K.; Lim, C.-T.; Garaj, S.; Leong, D. T. *ACS Appl. Mater. Interfaces* **2017**, *9*, 15286.

(9) Liu, L.; Wang, J.; Tan, X.; Pang, X.; You, Q.; Sun, Q.; Tan, F.; Li, N. *J. Mater. Chem. B* **2017**, *5*, 2286.

(10) Huang, H.; Du, C.; Shi, H.; Feng, X.; Li, J.; Tan, Y.; Song, W. *Part. Part. Syst. Charact.* **2015**, *32*, 72.

(11) Chen, S. C.; Lin, C. Y.; Cheng, T. L.; Tseng, W. L. *Adv. Funct. Mater.* **2017**, *27*, 1702452.

(12) Sweet, C.; Pramanik, A.; Jones, S.; Ray, P. C. *ACS Omega* **2017**, *2*, 1826.

(13) Li, Z. B.; Wong, S. L. *Mater. Sci. Eng. C Mater. Biol. Appl.* **2017**, *70*, 1095.

(14) Dong, X.; Yin, W.; Zhang, X.; Zhu, S.; He, X.; Yu, J.; Xie, J.; Guo, Z.; Yan, L.; Liu, X.; Wang, Q.; Gu, Z.; Zhao, Y. *ACS Appl. Mater. Interfaces* **2018**, *10*, 4271.

(15) Chimene, D.; Alge, D. L.; Gaharwar, A. K. *Adv. Mater.* **2015**, *27*, 7261.

(16) Gu, Z. L.; Plant, L. D.; Meng, X. Y.; Perez-Aguilar, J. M.; Wang, Z. G.; Dong, M. D.; Logothetis, D. E.; Zhou, R. H. *Acs Nano* **2018**, *12*, 705.

(17) Appel, J. H.; Li, D. O.; Podlevsky, J. D.; Debnath, A.; Green, A. A.; Wang, Q. H.; Chae, J. *ACS Biomater. Sci. Eng.* **2016**, *2*, 361.

(18) Pratikkumar, S.; Tharangattu, N. N.; Chen-Zhong, L.; Subbiah, A. *Nanotechnology* **2015**, *26*, 315102.

(19) Wang, S.; Li, K.; Chen, Y.; Chen, H.; Ma, M.; Feng, J.; Zhao, Q.; Shi, J. *Biomaterials* **2015**, *39*, 206.

(20) Hossain, R. F.; Deaguero, I. G.; Boland, T.; Kaul, A. B. *NPJ 2D Mater. Appl.* **2017**, *1*, 28.

(21) Canton-Vitoria, R.; Sayed-Ahmad-Baraza, Y.; Pelaez-Fernandez, M.; Arenal, R.; Bittencourt, C.; Ewels, C. P.; Tagmatarchis, N. *NPJ 2D Mater. Appl.* **2017**, *1*, 13.

(22) Chen, X.; Berner, N. C.; Backes, C.; Duesberg, G. S.; McDonald, A. R. *Angew. Chem. Int. Ed.* **2016**, *55*, 5803.

(23) Zhou, L.; He, B.; Yang, Y.; He, Y. *RSC Adv.* **2014**, *4*, 32570.

(24) Gopalakrishnan, D.; Damien, D.; Li, B.; Gullappalli, H.; Pillai, V. K.; Ajayan, P. M.; Shaijumon, M. M. *Chem. Commun.* **2015**, 51, 6293.

(25) Lin, H.; Wang, C.; Wu, J.; Xu, Z.; Huang, Y.; Zhang, C. *New J. Chem.* **2015**, *39*, 8492.

(26) Gan, Z. X.; Liu, L. Z.; Wu, H. Y.; Hao, Y. L.; Shan, Y.; Wu, X. L.; Chu, P. K. *Appl. Phys. Lett.* **2015**, *106*, 233113.

(27) Gan, Z.; Gui, Q.; Shan, Y.; Pan, P.; Zhang, N.; Zhang, L. *J. Appl. Phys.* **2016**, *120*, 104503.

(28) Wu, J.-Y.; Zhang, X.-Y.; Ma, X.-D.; Qiu, Y.-P.; Zhang, T. *RSC Adv.* **2015**, *5*, 95178.

(29) Gu, W.; Yan, Y.; Zhang, C.; Ding, C.; Xian, Y. *ACS Appl. Mater. Interfaces* **2016**, *8*, 11272.

(30) Yan, L.; Shi, H.; Sui, X.; Deng, Z.; Gao, L. *RSC Adv.* **2017**, *7*, 23573.

(31) Presolski, S.; Pumera, M. *Mater. Today* **2016**, *19*, 140.

(32) Jia, L.; Ding, L.; Tian, J.; Bao, L.; Hu, Y.; Ju, H.; Yu, J.-S. *Nanoscale* **2015**, *7*, 15953.

(33) Liu, T.; Wang, C.; Gu, X.; Gong, H.; Cheng, L.; Shi, X.; Feng, L.; Sun, B.; Liu, Z. *Adv. Mater.* **2014**, *26*, 3433.

(34) Dong, H.; Tang, S.; Hao, Y.; Yu, H.; Dai, W.; Zhao, G.; Cao, Y.; Lu, H.; Zhang, X.; Ju, H. *ACS ACS Appl. Mater. Interfaces* **2016**, *8*, 3107.

(35) Zhou, K.-G.; Mao, N.-N.; Wang, H.-X.; Peng, Y.; Zhang, H.-L. *Angew. Chem. Int. Ed.* **2011**, *50*, 10839.

(36) Zhang, W.; Wang, Y.; Zhang, D.; Yu, S.; Zhu, W.; Wang, J.; Zheng, F.; Wang, S.; Wang, J. *Nanoscale* **2015**, *7*, 10210.

(37) Li, H.; Zhang, Q.; Yap, C. C. R.; Tay, B. K.; Edwin, T. H. T.; Olivier, A.; Baillargeat, D. *Adv. Funct. Mater.* **2012**, *22*, 1385.

(38) Jawaid, A.; Nepal, D.; Park, K.; Jespersen, M.; Qualley, A.; Mirau, P.; Drummy, L. F.; Vaia, R. A. *Chem. Mater.* **2016**, *28*, 337.

(39) Muscuso, L.; Cravanzola, S.; Cesano, F.; Scarano, D.; Zecchina, A. *The Journal of Physical Chemistry C* **2015**, *119*, 3791.

(40) Xu, S.; Li, D.; Wu, P. *Adv. Funct. Mater.* **2015**, 25, 1127.

(41) Li, B.; Jiang, L.; Li, X.; Ran, P.; Zuo, P.; Wang, A.; Qu, L.; Zhao, Y.; Cheng, Z.; Lu, Y. *Scientific Reports* **2017**, *7*, 11182.

(42) Galeotti, F.; Calabrese, V.; Cavazzini, M.; Quici, S.; Poleunis, C.; Yunus, S.; Bolognesi, A. *Chem. Mater.* **2010**, *22*, 2764.

(43) Karunakaran, S. C.; Babu, P. S. S.; Madhuri, B.; Marydasan, B.; Paul, A. K.; Nair, A. S.; Rao, K. S.; Srinivasan, A.; Chandrashekar, T. K.; Rao, C. M.; Pillai, R.; Ramaiah, D. *ACS Chem. Biol.* **2013**, *8*, 127.

(44) Krieg, M. *J. Biochem. Bioph. Methods* **1993**, *27*, 143.

(45) Carlos, L. D.; De Mello DonegÁ, C.; Albuquerque, R. Q.; Alves, S.; Menezes, J. F. S.; Malta, O. L. *Mol. Phys.* **2003**, *101*, 1037.

(46) Wozniak, M.; Tanfani, F.; Bertoli, E.; Zolese, G.; Antosiewicz, *Biochim. Biophys. Acta* **1991**, *1082*, 94.

LIST OF PUBLICATIONS

1. pH Responsive Fluorescence Enhancement in Graphene Oxide - Naphthalimide Nanoconjugates: A Fluorescence Turn-on Sensor for Acetylcholine. **Sreejith Mangalath**, Silja Abraham, and Joshy Joseph, *Chem. Eur. J.* **2017**, 23, 11404–11409.

2. Transmissive-to-black Electrochromic Devices Based on Cross-linkable Tetraphenylethene-diphenylamine Derivatives. Silja Abraham, **Sreejith Mangalath**, Deepika Sasikumar and Joshy Joseph, *Chem. Mater.* **2017**, 29, 9877–9881.

3. A Study on Liposomal-Encapsulation of New BODIPY Sensitizers for Photodynamic Therapy. Gayathri Thumuganti, Vijayalakshmi A., **Sreejith Mangalath**, Joshy Joseph, Nalam Rao, Surya Singh, *ACS Med. Chem. Lett.* **2018**, 9, 323-327.

4. NIR Absorbing Aza-BODIPY Based Turn ON Fluorescent Sensor for the Selective Recognition of Bivalent Copper Ions. Yogesh Gawale, **Sreejith Mangalath**, N. Adarsh, Joshy Joseph, Danaboyina Ramaiah and Nagaiyan Sekar (Under Review).

5. Covalently Anchored BODIPY Photosensitizer on Graphene Quantum Dots for Highly Efficient Photodynamic Therapy. **Sreejith Mangalath**, P. S. Saneesh Babu, Prasad M. Manu, S. Asha Nair, and Joshy Joseph (To be communicated).

6. BODIPY Functionalized Water Soluble MoS_2 Quantum Dots for Efficient Photodynamic Therapy. **Sreejith Mangalath**, Rajshree R. Nair, Asha S. Nair and Joshy Joseph (To be communicated).

PAPERS/POSTERS PRESENTED IN CONFERENCE

1. "Can Fluorophores Glow on Graphene Oxide Surface? Stimuli Responsive Fluorescence Enhancement in GO-Naphthalimide Conjugates", **Sreejith Mangalath,** Mridula A. S. & Joshy Joseph, A **Poster** presented in the ACS on Campus programme, 29th November, **2013**, held at CSIR-NIIST, Thiruvananthapuram, India.

2. "Stimuli Responsive Fluorescence Enhancement of Graphene-Naphthalimide Nanoconjugates", **Sreejith Mangalath**, and Joshy Joseph, A **Poster** presented in the 8th Asian Photochemistry Conference, November 10-13, **2014**, Thiruvananthapuram, India.

3. *"*Design of Graphene Quantum Dot – BODIPY Nanoconjugates for PDT Applications*"*, **Sreejith Mangalath**, P. S. Saneesh Babu, Asha Nair and Joshy Joseph., A **Poster** presented in the 10th CRSI-RSC Joint Symposium, February 4-6, **2016**, Panjab University, Chandigarh, India.

4. *"*BODIPY Functionalized MoS_2 Quantum Dots for PDT Applications*"*, **Sreejith Mangalath,** P. S. Saneesh Babu, Asha Nair and Joshy Joseph, A **Poster** presented in the 8th East Asia Symposium on Functional Dyes and Advanced Materials, September 20-22, **2017**, CSIR-NIIST, Thiruvananthapuram, India.

5. "Iodo-BODIPY Anchored MoS_2 Quantum Dots for Efficient PDT Applications", **Sreejith Mangalath**, Rajashree R. Nair, P. S. Saneesh Babu, Asha S. Nair, and Joshy Joseph, A **Poster** presented in the 2nd Annual Conference of Indian Society of Nanomedicine, NANOBIOTEK-2017, December 6-8, **2017**, Thiruvananthapuram, India.

6. *"*Graphene Oxide - Naphthalimide Nanoconjugates as a Fluorescence "Turn-On" Sensor for Acetylcholine*",* **Sreejith Mangalath**, Silja Abraham and Joshy Joseph, A **Paper** presented in 30th Kerala Science Congress, January 28-30th, **2018**, held at Govt. Brennen College, Thalassery, India.

7. "pH Responsive Fluorescence "Turn-On" Sensor based on Graphene Oxide - Naphthalimide Nanoconjugates" **Sreejith Mangalath**, Silja Abraham and Joshy Joseph, A **Poster** presented in the National Conference on Luminescence and its Applications, NCLA-2018, February 14-16, **2018**, held at CSIR-NIIST, Thiruvananthapuram, India.

8. *"*Fluorescence "Turn-On" Sensor for Acetylcholine based on pH Responsive Graphene Oxide - Naphthalimide Nanohybrids*"* **Sreejith Mangalath** and Joshy Joseph, A **Paper** presented in the International Conference on Advances in Analytical Sciences, ICAAS-2018, March 15-17, **2018**, held at CSIR-IIP, Dehradun, India.